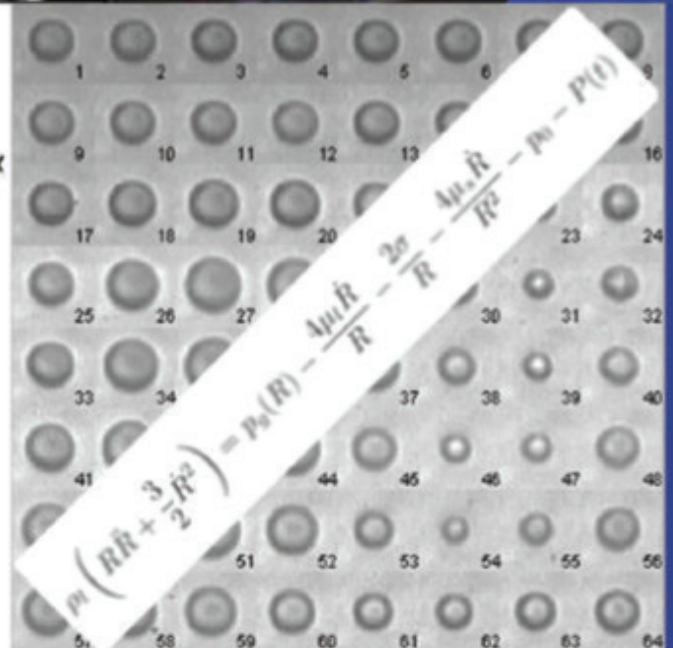
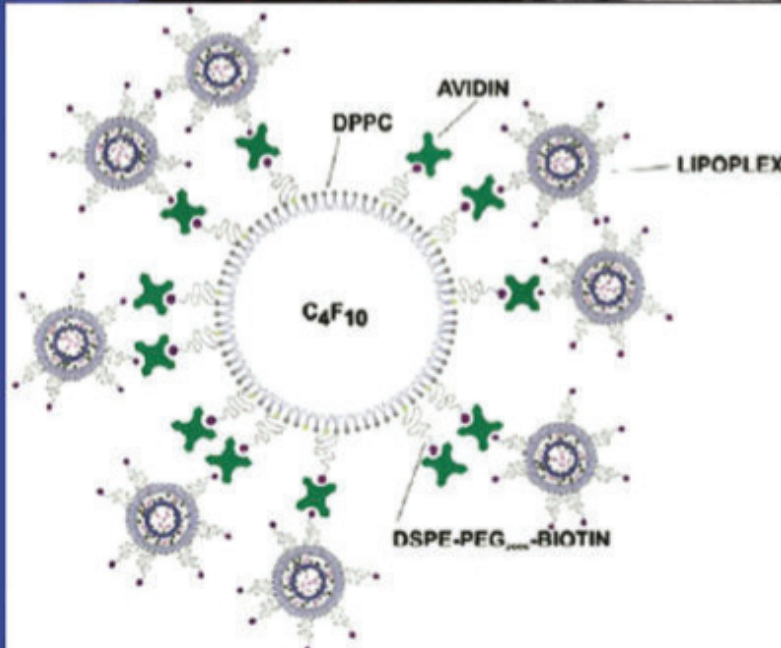
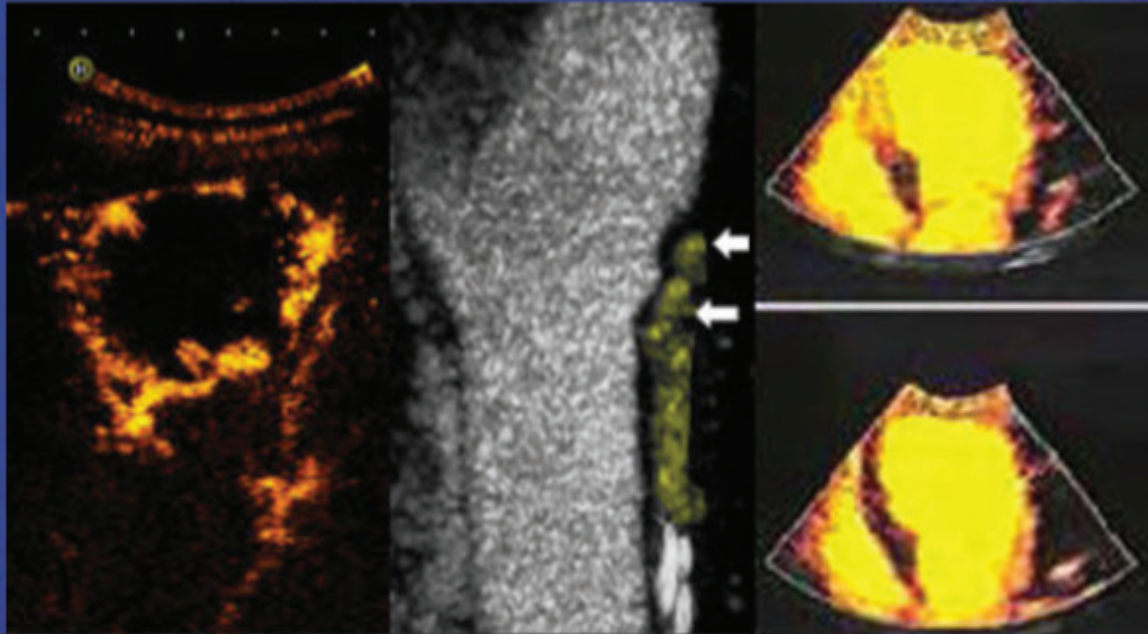


The 21st European Symposium on Ultrasound Contrast Imaging

- An ICUS Conference -



Abstract book

21-22 January 2016, Rotterdam, The Netherlands

Organized by Nico de Jong, Arend Schinkel, Folkert ten Cate, Rik Vos and Klazina Kooiman
Erasmus MC Rotterdam

21st EUROPEAN SYMPOSIUM ON ULTRASOUND CONTRAST IMAGING
21-22 JANUARY 2016, Rotterdam, The Netherlands

WEDNESDAY, 20 January 2016

11.30 15.30	PhD Defense (Erasmus MC) Jacopo Viti PhD Defense (Erasmus MC) Ilya Skachkov	High framerate Imaging of Ultrasound Contrast Agents Microbubbles for Molecular Imaging and Drug Delivery
18.00 – 20.00	Registration - Welcome Drinks	

THURSDAY, 21 January 2016

08.00 – 09.00	Registration
---------------	--------------

Oral program

09.00 – 09.10	Introduction and opening.....	Steve Feinstein	
09.10 – 10.40	STATE OF THE ART	Chairpersons: Peter Burns and Eleanor Stride	
Francois Tranquart	Current and future use of clinical ultrasound contrast agents		1
Christian Greis	Characteristics and Echogenicity of clinical Ultrasound Contrast Agents: An in vitro and in vivo comparison study		5
Steven Freear	Acoustic trapping of microbubbles at clinically relevant flow rates		9
Mangala Srinivas	Nanoparticles for multimodal imaging		12
Paul Sheeran	From bubbles to droplets to bubbles again: Applying microbubble condensation to aid translation		13
10.40 – 11.10	Intermission		
11.10 – 12.40	DRUG DELIVERY	Chairpersons: Michel Versluis and Klazina Kooiman	
Liza Villanueva	Studies of Endothelial Sonoporation Using Ultrafast Frame Rate Microscopy of Microbubble Oscillations and Confocal Microscopy		14
Per Sontum	Acoustic Cluster Therapy – A Novel Approach for Ultrasound Mediated Targeted Drug Delivery: Technology Basics and Proof of Concept.....		15
Dario Carugo	Modulation of Cell Membrane Properties by Lipid Transfer from Microbubbles - a potential mechanism for sonoporation?.....		19
Ine Lentacker	Real-time confocal and high-speed imaging to unravel microbubble-cell interactions involved in ultrasound triggered drug delivery with nanoparticle-loaded microbubbles		22
Joyce Wong	Direct Observation of Targeted Ultrasound-Assisted Liposomal Doxorubicin Delivery in Microvessels-on-a-Chip		24
12.40 – 13.45	LUNCH		
13.45 – 14.15	Dutch Heart Foundation lecture	Chairperson: Folkert ten Cate	
Christy Holland	Microbubble pumps: Ultrasound theragnostic agents		25
14.15 – 15.30	THERAPEUTICS	Chairpersons: Otto Kamp and Liza Villanueva	
Tom Porter	Effect of Longer Pulse Duration Transthoracic Ultrasound Induced Microbubble Cavitation on Coronary Artery ... Diameter In Different Pathophysiological Conditions		26
Robin Cleveland	Lithotripsy: a shocking blow to kidney stones		27
Francois Yu	Sonoreperfusion for microvascular obstruction: a clinically applicable approach		28
Heleen Dewitte	Ultrasound-mediated cancer immunotherapy		30
15.30 – 16.00	Intermission		
16.00– 17.30	NEW APPLICATIONS	Chairpersons: Edward Leen and Christy Holland	
Gaio Paradossi	Echogenic polymer platforms: toward a versatile diagnostic tool		32
Yvo Kusters	Impaired Muscle Microvascular Recruitment Contributes to Metabolic Insulin Resistance in Obesity		33
Katrien Vanderperren	Contrast-enhanced ultrasound imaging of the anti-angiogenic effects of interleukin 12 in pet dogs with spontaneous malignant tumors		35
Tom van Rooij	Contrast-enhanced ultrasound imaging of the renal cortex of pigs during hemorrhagic shock.....		40
Amit Livneh	Extracorporeal Acute Cardiac Pacing by a Multi Harmony High Intensity Focused Ultrasound: The Role of Cavitation, Insights from In-vivo Pacing and Modeling of a Left Ventricle Cardiomyocyte.....		43
18.30 – 22.30	EVENING PROGRAM (Incl. Dinner buffet)		

21st EUROPEAN SYMPOSIUM ON ULTRASOUND CONTRAST IMAGING
21-22 JANUARY 2016, Rotterdam, The Netherlands

FRIDAY, 22 January 2016

07.30 – 08.00 Registration

Poster sessions

07.30 – 09.00 MODERATED POSTER SESSION A: BIOLOGY Moderator: *Arend Schinkel*

A1)	Alexander Klibanov	Microbubbles electrostatically adherent to tumor vasculature: positively charged bubbles provide tumor-specific contrast ultrasound imaging	45
A2)	John Hossack	Empirical and theoretical study of the interaction between plasmonic-nanoparticle coated microbubbles and nanosecond pulsed laser excitation	47
A3)	Emmelie Stock	Quantitative differences are present between the first and second injection of contrast agent in contrast-enhanced ultrasonography of feline kidneys	48
A4)	Brandon Helfield	Bio-physical insight into the mechanisms of ultrasound-stimulated microbubble sonoporation	52
A5)	Marine Bezagu	In situ Activation of monomethylauristatin E (MMAE) using Ultrasound-Triggered Release of Composite Droplets	54
A6)	Yosra Toumia	Graphene PVA Microbubbles: a New Hybrid Ultrasound-Photoacoustic Imaging Contrast Agent	55
A7)	Simona Turco	Quantification of cancer angiogenesis by modeling the binding kinetics of targeted ultrasound contrast agents ...	57
A8)	Xucai Chen	Effect of viscosity and thrombus composition on sonoreperfusion efficacy in a model of microvascular obstruction	60

07.30 – 09.00 MODERATED POSTER SESSION B: TECHNOLOGY Moderator: *Nico de Jong*

B1)	Nick Ovenden	Ultrasound propagation through contrast agent suspensions	62
B2)	Matthieu Toulemonde	A Contrast Enhanced Ultrasound imaging system with diverging waves for cardiac imaging – initial evaluation on a beating phantom	65
B3)	Shengtao Lin	Acoustic quantification of microbubble populations in a branched microvasculature phantom	70
B4)	Charles Tremblay	Observations of the Doppler Twinkling Artifact of Kidney Stones are Bubble Related	72
B5)	Victoria Mico	Two-step, single chip, microfluidic production of hybrid Microbubble-Nanodroplet architectures for enhanced hydrophobic drug delivery	75
B6)	Marie de Saint Victor	Theoretical and Experimental Investigation of Magnetic targeting to Enhance Microbubble Delivery in an Occluded Microarterial Bifurcation	77
B7)	Fabio Domenici	Poly(vinyl alcohol) based microbubbles: A study on the chemical and mechanical ageing	79
B8)	Dario Carugo	High-throughput production of clinically-relevant microbubbles using microfluidic architectures	80

Wednesday–Friday POSTER SESSION C: NEW DIRECTIONS I Election by the audience

C1)	Kentaro Otani	Lactadherin specifically detects phosphatidylserine on the surface of clinically available ultrasound contrast agent	84
C2)	Sara Zullino	Sonophorable polyelectrolyte multi-layer shelled nanobubbles for enhancing 'on demand' drug release	86
C3)	Jennifer Wischhusen	Detection of tumoral Netrin-1 protein levels using ultrasound microbubble contrast agents: in vitro validation	87
C4)	Wing Keung Cheung	Reproducible quantification of active vascular density in human lower limbs through temporal and spatial analysis of contrast enhanced ultrasound images	89
C5)	Martynas Maciulevičius	Dosimetric assessment of calcein sonoextraction from cells in vitro	92
C6)	Tom van Rooij	Interaction of laser-activated polymeric microcapsules with cells	95
C7)	Jeff Bamber	In vivo activation, imaging dynamics and delivery effectiveness of an acoustic cluster therapy (ACT) agent	98
C8)	Avinoam Bar-Zion	High-resolution Estimation of Local Perfusion Parameters While Compensating for Substantial Respiratory Motion	102

Wednesday–Friday POSTER SESSION D: NEW DIRECTIONS II Election by the audience

D1)	Emma Kanbar	Impact of gas composition on subharmonic emission from phospholipid contrast agents	105
D2)	Antonis Pouliopoulos	The Superharmonic Microbubble Doppler Effect in Ultrasound Therapy: An Observation Useful for Monitoring .. Velocities	108
D3)	Miloslav Pekař	Study of the Colloidal Properties of Phospholipids Microbubbles	110
D4)	Naohiro. Sugita	Spherical and translational dynamics of a collapsing cavitation bubble cluster	111
D5)	Inés Beekers	Acoustic characterization of a novel cell culture platform for ultrasound-mediated drug delivery	113
D6)	Barbara Cerroni	Poly(vinyl alcohol) Microbubbles for Ultrasound Molecular Imaging	116
D7)	Edyta Swider	Polymeric nanoparticles for enhancing HIFU ablation	118
D8)	Dmitry Grishenkov	Investigation of Polymer-Shelled Microbubbles Motions in Acoustophoresis	119

21st EUROPEAN SYMPOSIUM ON ULTRASOUND CONTRAST IMAGING
21-22 JANUARY 2016, Rotterdam, The Netherlands

FRIDAY, 22 January 2016

Oral program

09.00 – 10.30	TECHNOLOGY <i>Chairpersons: Mike Averkiou and Rik Vos</i>	
James Choi	Contrast-Enhanced Ultrasound Elastography: A Novel Method for using Acoustic Particle Palpation (APP) to ... Image Tissue Elasticity.....	122
James Moore	Development of a branched microfluidic platform for acoustic quantification of microbubble populations.....	124
Steven Spencer	Estimation of Medical Microbubble and Liquids Properties by Acoustic Resonance Interference Spectroscopy ...	127
Paul Rademeyer	High Throughput Characterisation of Single Contrast Agent Microbubbles – Towards Optimisation of Contrast... Enhanced Imaging	128
Guillaume Lajoinie	Laser driven microbubbles as multimodal contrast agents	131
10.30 – 11.00	Intermission	
11.00 – 12.30	IMAGING CONCEPTS <i>Chairpersons: Steve Feinstein and Dan Adam</i>	
Mike Averkiou	Can bolus wash-in/washout analysis measure flow changes in the liver microvasculature?	132
Massimo Mischi	Contrast ultrasound dispersion imaging in prostate cancer: an update	134
Libertario Demi	Cumulative Phase Delay Imaging	136
Klazina Kooiman	The chicken embryo chorioallantoic membrane model for studying microbubbles <i>in vivo</i>	138
Vera Daeichin	Micro-ultrasound molecular imaging in mice: Live observation of atherosclerosis plaque disruption in ApoE ^{-/-} mouse	139
12.30 – 13.30	LUNCH	
13.30 – 14.00	COEUR LECTURE <i>Chairperson: Francois Tranquart</i>	
Ayache Bouakaz	Clinical oncology therapy with microbubbles and ultrasound: The future	142
14.00 – 16.00	COMPETITION: PLANE WAVE IMAGING OF ULTRASOUND CONTRAST AGENT	
 <i>Chairpersons: Nico de Jong and Tom Porter</i>	
Olivier Couture	Ultrafast and programmable ultrasound scanners, a new paradigm applied to contrast imaging	143
Charles Tremblay	Principal curvature analysis in plane-wave contrast-enhanced Doppler imaging	147
Yann Desailly	Contrast enhancement by real-time spatiotemporal filtering of ultrafast images.....	150
Avinoam Bar-Zion	Fast and Background Free Super-Resolution Ultrasound Based on Fluctuation Statistics	153
Claudia Errico	Ultrafast ultrasound localization microscopy of the living brain vasculature at the capillary scale	157
Antonio Stanzola	Temporal and spatial processing of high frame-rate contrast enhanced ultrasound data.....	160
16.00 – 16.10	DISCUSSION AND CONCLUSIONS <i>Nico de Jong & Arend Schinkel</i>	
16.10	ANNOUNCEMENT OF THE WINNERS OF THE COMPETITION AND POSTER PRIZES, AND ADJOURN	

Organised by: Nico de Jong, Arend Schinkel, Folkert ten Cate, Rik Vos and Klazina Kooiman
Scientific board: David Cosgrove, Edward Leen, Mike Averkiou, Eleanor Stride and Paolo Colonna



Thursday, 21 January 2016

Evening Program

Grillcafé Bar Bowling "DOK 99"

Straatweg 99 Rotterdam

Buffet: around 19:30

Coaches will be leaving from Hilton at 18:30 and will be back in Hilton around 22:30

Current and future use of clinical ultrasound contrast agents

François Tranquart

Advice-US, Nernier, France

Introduction

Ultrasound imaging (US) is in the front line to image various body parts to detect or characterize lesions, which are or not clinically suspected. Before the introduction of ultrasound contrast agents (UCA), the patient was referred to other imaging modalities, mainly CT-scan, MRI, which result in increased costs, limited access and possible adverse events. In this view, the use of UCA with modern ultrasound scanners offers a valuable alternative by simultaneously providing accurate results and eliminating renal risks, which forms a solid basis for the new and expanding modality of Contrast-Enhanced Ultrasound (CEUS).

Status of Ultrasound Contrast Agents

SonoVue® (Bracco, Milan, Italy) is the second UCA approved for cardiac and/or non-cardiac indications in Europe and other countries in the world (including USA, China, Brazil, Russia, Singapore, Hong Kong, Canada and India). Non-cardiac indications include assessment of diseases in large vessels (such as aorta, carotid and intracranial vessels, peripheral arteries, renal arteries...) and small vessels (breast tumors, focal liver lesions). In cardiology, SonoVue® allows the improvement of endocardial border delineation at rest and during stress and the recommended dosage is a 2 mL bolus.

Definity® or Luminity® (Avista-Lantheus, USA) is approved in Canada and USA for radiology and cardiac applications, and in Europe for cardiac applications.

Optison® (GE Healthcare, USA) is obtained by sonication of human albumin and octafluoropropane. This product is approved in USA and Europe for endocardial border delineation.

Sonazoid® (GE Healthcare, USA) consists of microbubbles of perfluorobutane (PFB) stabilized by a monomolecular membrane of hydrogenated egg phosphatidyl serine, embedded in an amorphous sucrose structure. This agent is only available in Japan for radiology applications.

While Definity® is mostly used in the US for cardiac indication, SonoVue® is largely used in radiology and cardiac indications in Europe, USA and Asia; Sonazoid® is currently less used due to its market limited to Japan. In spite of a positive sales trend for all agents in all countries, these agents remain considerably less used than other agents such as those for CT or MRI.

Which elements contribute to the adoption of UCA?

Globally, positive features of these agents can be listed as: very rare adverse events, real-time imaging feature of CEUS which is highlighted by physicians, the possible use at bedside and the specific patterns observed in many lesions. The specific characteristic of these agents as strict markers of the vascular bed is a great advantage for quantification in some indications, such as therapeutic treatment monitoring. In that perspective, the improvements in machine performances during the last ten years and the increased reliability of the results were greatly appreciated by the customers. The relative

stability in performances and the use of similar sequences in most of the scanners from that time has made the customers more confident with their results.

The adoption of CEUS varies significantly across countries in relation to the imaging scenario. Indeed, for radiology indications, in the countries where US imaging is preferably performed by radiologists, the penetration is limited due to a competition with other imaging modalities. Conversely, in countries where a large part of US imaging is performed by specialties other than radiology, CEUS is well adopted. For cardiac indications, the development of stress echo imaging is a real booster for this adoption.

In 2008, EFSUMB has published the results of a consensus conference in Guidelines and Good Clinical Practice for CEUS which highlight its value in liver, kidney, pancreas and transcranial indications, these guidelines being extended to many possible off-label indications in a new version published in 2011 [1,2].

Cardiac applications represent another large application of CEUS. This is used both for infarct size and myocardial viability assessment and for opacification of cardiac chambers with enhancement of left ventricular endocardial border delineation. All published studies have demonstrated an improvement in the quality of provided information for cardiac chambers, especially during stress studies for which the total number of segments, which are correctly examined, is significantly greater than without UCA. In the recently published European Association of Echocardiography (EAE) Guidelines, major indications for contrast agents for cardiac applications are clearly underlined [3,4].

The absence of ionizing radiation is of utmost importance for an imaging technique. There is more and more attention on that point since long-term deleterious effects have been recently reported due to an excessive radiation dose even with modern X-Ray machines. This is definitely a huge advantage for CEUS for pediatric indications, repeated examinations for monitoring some lesions or treatments. This point has been recently reinforced with the significant increase in life-expectancy for oncology patients. Therefore, a large part of the patients with known cancer will not die from that cancer, highlighting the need to avoid inducing additional cancer lesions by excessive radiation.

What are the barriers for a larger adoption ?

Despite the fact that the use of DCE-US has been expanded in clinics during the recent years, the adoption still remains below the expectations. After more than 15 years since its introduction, this modality is not available in all imaging departments. Therefore, behind the strict problem of UCA injection, the CEUS imaging itself has first to be adopted by the physicians. This implies the need to pursue education of physicians regarding the technique, the preparation of the agents, the injection and finally the US acquisition itself. It clearly appears that some of the key-elements during that educational chain are not perfectly known by the users inducing possible artefacts, disappointments or wrong interpretation.

Various points could be considered to explain the limited adoption of CEUS as a diagnostic tool in all departments. This could relate to the machines used, to the physicians and the authorities. Regarding the machines used, as said above, the adoption of similar contrast-specific imaging techniques in all machines has significantly improved the reproducibility between centres and patients. Nevertheless, it is noteworthy that some differences are still observed with more sensitivity or more penetration on some machines, limiting the confidence of the physicians and more importantly the clinicians. In addition, the use of different names for similar techniques implemented in systems of different ultrasound companies induces some confusion.

Workflow needs to be improved by providing customers with a simple solution more integrated to the systems. The need to have a nurse available to perform an injection represents a significant limitation

for some centres, in which nurses or technicians are lacking for that task. The additional cost could represent a significant limitation for some centres. The limited standardization of the technique must also be underlined: in addition to the operator dependence characteristics known for US imaging, the interpretation of contrast images remains in general at a subjective level. However we could consider the introduction of CEUS as a positive factor in improving standardization with strict recommendations for US acquisitions, well-defined enhancement phases and well-known patterns.

The reported adverse events cannot be considered as a limiting factor for the use of UCA. It is generally admitted that the rate of these events (around 0.01% for serious adverse events based on post-marketing safety data, with no significant differences between agents) is far below what is reported for iodinated compounds and in the range even below what is reported for MR agents [5-7]. However, the accuracy of the events with the latter agents is questionable since their adverse effects are well-known and so most of the physicians forget to report them. This bias could correspond to a rate of adverse events for UCA far below the rate reported for other agents. In any case, this point was never put in front line as an excuse for not using UCA.

The lack of reimbursement or a correct value for the procedure is considered as a limitation for a routine use. This is related to some points reported above for additional expenses such as additional personnel or specific equipment which could make the procedure less attractive for some physicians or institutions. Despite some efforts in some countries, there is no reimbursement for the procedure in the vast majority of countries in Europe and so no real incentive for radiologists to perform CEUS. Conversely in some countries, the reimbursement for the agent itself has a positive effect on its use.

The limited number of large multi-centric trials involving different countries and different continents for established indications or off-label indications is a limiting factor for larger use. This is expected by agencies to support new possible approvals or to tackle some contraindications. This could help in differentiating the agents if this exists, in establishing worldwide guidelines for such indications. At the same time, the long process required or the complexity of that process to get a new approved indication is a clear barrier for ultrasound and pharma companies.

How to tackle the current barriers ?

The limited acceptance of CEUS in all imaging departments raises the need to address some specific issues in a proper way, involving all the actors in that domain: pharma companies, ultrasound companies, medical community, patient groups, etc... The single chance to increase the market penetration is to have a coordinated effort from all actors. In that sense, the approach followed in the recent period by the International Contrast Ultrasound Society (ICUS) must be underlined. This is illustrated by the citizen petition, which has been filed early October to the FDA to lift some of the contraindications for the use of UCA.

First of all, education remains the key [8]. This concerns physicians not only from imaging departments but also administrative stakeholders and health authorities. It remains mandatory to demonstrate the real value of CEUS versus other imaging modalities not as a competition between modalities but as a convergence for a better diagnostic chart with an improved cost/benefit ratio. We have to inform all specialties of the strengths of CEUS to limit the costs, to improve the availability of the technique and in some cases to provide increased accuracy. This will drive recognition of the value of CEUS by both clinicians and authorities. Even though there are some available guidelines sponsored by US scientific societies, there is a need to work closely with professional societies to get their support as well.

Secondly, there is a need for standardization. This is required for image acquisition, for quantification, for training, but also for naming some US techniques. Sometimes, you need a lexicon to understand the technique that has been used by the physicians. In that perspective, more integration of some tools

will be of value to facilitate the use of these agents and the reproducibility between acquisitions. This is especially required for some new indications such as therapeutic treatment monitoring in which the conclusions drawn depend critically on standardization.

There is a need to reinforce the network between ultrasound and pharma companies to sponsor large multi-centric clinical trials. We need to build the strategy on well-established and approved indications to reinforce the use and acceptance of CEUS, before moving to new indications. In that sense, there are some discrepancies between academic centers and pharma companies. Even everybody could be easily convinced by the clear advantages of CEUS for many possible indications, the cost and time to get an approval from health authorities are a significant barrier for pharma companies. This is of crucial importance, since some physicians are so enthusiast for some indications that they may create expectations, which cannot be easily fulfilled. These hopes are frequently not reached, limiting the use of immediately available methods. This is specifically the case for 3D/4D techniques, local treatment with bubbles or molecular imaging.

Additional issues might be considered such as reimbursement procedures, which need to be improved or adopted, development of this method for difficult conditions such as those observed in intensive care units or emergency rooms, pediatric indications, etc. This has to be part of a global approach involving all actors with the objective to use CEUS in combination with other imaging techniques. However, if CEUS could replace other imaging techniques in relation to its particular value, then this should be done without hesitation. There is no more need to duplicate exams if previously published results are convincing when considering large multi-centric trials.

CONCLUSION

CEUS has proved its efficiency in many indications, this being reinforced by guidelines established by scientific societies. Despite this recognized value, CEUS still remains underutilized in relation to many factors. The increased adoption, which will be valuable for patients and healthcare system, needs to be emphasized and well addressed towards health authorities and physicians to simplify the procedures for adoption. In addition, the education of all players will be the leverage to use the currently available techniques but also to create the ground for future developments of the microbubble agents.

References

1. M Claudon, D Cosgrove, T Albrecht, et al. "Guidelines and good clinical practice recommendations for contrast enhanced ultrasound (CEUS) - update 2008." *Ultraschall Med*, vol 29, pp 28-44, 2008.
2. F. Piscaglia, C. Nolsøe, C. F. Dietrich, et al. "The EFSUMB Guidelines and Recommendations on the Clinical Practice of Contrast Enhanced Ultrasound (CEUS): Update 2011 on non-hepatic applications." *Ultraschall Med*. 2012 Feb;33(1):33-59
3. SL Mulvagh, H Rakowski, MA Vannan, et al. "American Society of Echocardiography Consensus Statement on the Clinical Applications of Ultrasonic Contrast Agents in Echocardiography." *J Am Soc Echocardiogr.*, vol 21, pp 1179-1201, 2008.
4. R Senior, H Becher, M Monaghan, et al. "Contrast echocardiography: evidence-based recommendations by European Association of Echocardiography." *Eur J Echocardiogr.*, vol 10, pp 194-212, 2009.
5. DL Miller, MA Averkiou, AA Brayman, et al. "Bioeffects considerations for diagnostic ultrasound contrast agents." *J Ultrasound Med.*, vol 27, pp 611-32, 2008.
6. C Jiménez, R de Gracia, A Aguilera, et al. "In situ kidney insonation with microbubble contrast agents does not cause renal tissue damage in a porcine model." *J Ultrasound Med.*, vol 27, pp 1607-1615, 2008.
7. F Piscaglia, L Bolondi. "The safety of SonoVue in abdominal applications: retrospective analysis of 23,188 investigations." *Ultrasound Med Biol.*, vol 32, pp 1369-1375, 2006.
8. SR Wilson, LD Greenbaum, BB Goldberg. "Contrast-enhanced ultrasound: what is the evidence and what are the obstacles?" *AJR Am J Roentgenol.*, vol 193, pp 55-60, 2009.

Characteristics and Echogenicity of clinical Ultrasound Contrast Agents: An *in vitro* and *in vivo* comparison study.

*Jean-Marc Hyvelin, Christian Greis, Emmanuel Gaud, Maria Costa, Alexandre Helbert
Philippe Bussat, Thierry Bettinger and Peter Frinking.*

*Bracco Suisse S.A., Geneva Research Center and Manufacturing Site, Plan-les-Ouates / Geneva,
Switzerland*

Objectives:

Contrast-enhanced ultrasound (CEUS) is a promising diagnostic imaging modality exploiting the unique acoustic properties of microbubble-based contrast agents. Due to their micrometer sizes, microbubbles (MB) are considered ideal blood tracers. Their strong echo signals or echogenicity improves the visualization and assessment of cardiac cavities, but also offers dynamic detection of blood flow in both the macro and microvasculature. The combination of ultrasound contrast agents with the latest equipment offers a flexible low-cost diagnostic imaging modality equivalent or superior to existing modalities such as X-ray computed tomography, Magnetic Resonance Imaging and Nuclear Medicine. Several ultrasound contrast agents (UCA) are commercially available, and their clinical use is expanding rapidly. The aim of this work was to compare *in vitro* and *in vivo* imaging performances of three of these agents, *viz.* SonoVue® (also marketed as Lumason™ in the USA), Definity® and Optison™.

Material and Methods:

Size distributions and microbubble (MB) concentrations were measured with a Multisizer™ Coulter Counter® (Beckman Coulter, Fullerton, CA) using an aperture tube with a 30- μm or 100- μm orifice (diameter range of 0.7-18 μm and 2-60 μm , respectively).

Two ultrasound systems, namely Toshiba Aplio500 and GE LogiqE9, were used with transducers having frequencies that are typically used for different clinical indications.

In vitro imaging performance of UCA was assessed using an in-house setup (Figure 1A) which consisted of a beaker filled with 800 mL of saline (0.9% NaCl). The beaker was placed on a magnetic stirrer to homogenize the UCA suspensions. A 1-cm thick acoustic absorber was placed at the bottom of the beaker to minimize acoustic reflections. An L-shape tissue-mimicking phantom was placed in the beaker directly below the transducer. The phantom had a depth of 33 mm on one side and 90 mm on the other side creating a cavity where contrast enhancement could be measured at different depths, in an upper region of interest (ROI) located directly below the phantom and in a lower ROI located approx. 3 cm deeper (Figure 1A).

In vivo comparison was performed in pigs (approx. 30 kg) and rabbits (3-4 kg). Briefly, anesthetized pigs (thiopental/fentanyl, FiO_2 21%) were pretreated with aspirin (10 mg/kg) to prevent the activation of pulmonary intravascular macrophages (PIM). Rabbits were anesthetized with isoflurane (2-3% in medical air). UCA were reconstituted according to the manufacturer's instruction, and were injected intravenously (auricular vein) followed by a saline flush. The agents were injected at full and half-clinical dose, *i.e.* 34 $\mu\text{L}/\text{kg}$ and 17 $\mu\text{L}/\text{kg}$ (2.4 mL and 1.2 mL per bolus for a 70 kg person) for SonoVue®; 3 $\mu\text{L}/\text{kg}$ and 1.5 $\mu\text{L}/\text{kg}$ (0.2 mL and 0.1 mL per bolus for a 70 kg person) for Definity®; 15 $\mu\text{L}/\text{kg}$ and 7.5 $\mu\text{L}/\text{kg}$, (1 mL and 0.5 mL per bolus for a 70 kg person) for Optison™ (dosage were determined according to literature). In each animal, injections at full and half the clinical dose were repeated twice, and injection order was randomized.

Quantification of contrast enhancement was performed using VueBox® software (Bracco Suisse SA).

Results:

Physicochemical characterization. The MB concentration of Definity® (120×10^8 MB/mL) is approximately 25 times higher than that of SonoVue®, and its mean MB diameter in number (D_N) is smaller (D_N of 1.2 μm and 1.9 μm for Definity® and SonoVue®, respectively). For Optison™, MB concentration is approximately twice that of SonoVue®, and its mean MB diameter is larger (D_N of 3.1 μm and 1.9 μm for Optison™ and SonoVue®, respectively). The fraction of MB with diameters larger than 10 μm is less than 1% for both SonoVue® and Definity® but it is 1.1% for Optison™ (all in accordance with the supplier leaflet). The MB volume concentrations (MVC), measured with the 30- μm orifice aperture tube were 6.5, 44.0 and 35.2 μL of gas per mL for SonoVue®, Definity® and Optison™. When MVC was measured using the 100- μm orifice aperture tube, values of both SonoVue® and Optison™ were similar to those obtained with the 30- μm orifice. However, for Definity® MVC is 3 times higher due to the presence of MB with diameters larger than 20 μm .

In vitro performance. Scattered echo signals were measured in the upper and lower ROI at the same time. For all three agents, scattered echo signals in the upper ROI (Figure 1B) increase proportionally with agent concentration (expressed in μL of encapsulated gas per mL) as indicated by a slope of 10 dB/decade. In the lower ROI (Figure 1B), proportionality between MB scattering and agent concentration is visibly affected by attenuation at concentrations higher than 10^{-3} $\mu\text{L}/\text{mL}$.

Both scattering and attenuation need to be considered when assessing the performance of UCA, since at higher concentrations imaging penetration may be limited and contrast enhancement may be affected by attenuation at larger depths. Figure 1C (left side) summarizes the results obtained in the upper ROI for all ultrasound systems and transducers used: note that all data were normalized to those of SonoVue®. The scattering of Definity® is similar or lower compared to that of SonoVue®. Compared to Optison™, SonoVue® scattering is substantially higher for all conditions used. As demonstrated in Figure 1B, in the lower ROI scattering is affected by attenuation. Therefore, an apparent scattering-to-attenuation ratio can be determined from data in this lower ROI; this ratio can also be considered as a measure of the performance of the agents. Figure 1C (right side) summarizes the results, normalized to those obtained with SonoVue® and shows that the performance of SonoVue® is similar or better than that of Definity®, but it is superior compared to that of Optison™ for all transducers tested.

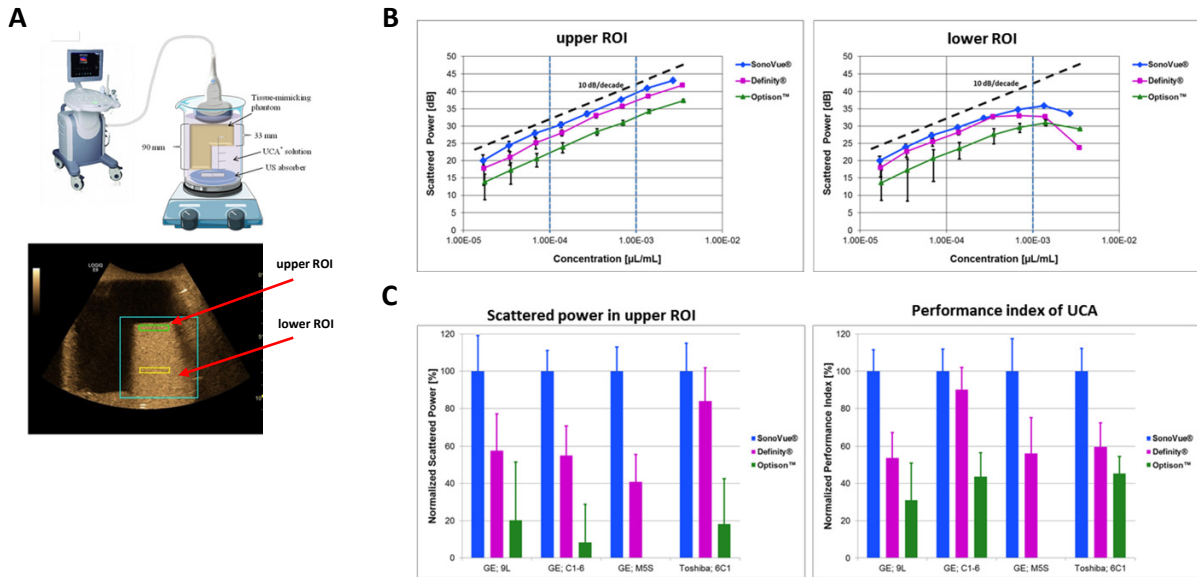


Figure 1: In vitro comparison of UCA imaging performance. A) Experimental setup; B) Scattered power as a function of agent concentration in the upper ROI (left) and lower ROI (right) obtained with LogiqE9 – 9L transducer. C) Normalized scattered power (left bar graph), based on the mean scattering for concentrations between 10^{-4} $\mu\text{L/mL}$ and 10^{-3} $\mu\text{L/mL}$ in the upper ROI. The right bar graph represents normalized performance index, which is based on an apparent scattering-to-attenuation ratio determined in the lower ROI at the concentration of 10^{-3} $\mu\text{L/mL}$. Data are normalized to those of SonoVue[®].

In vivo performance. In vivo imaging performances of SonoVue[®] and Definity[®] were assessed in the liver and heart of pigs. Despite premedication, a substantial number of Optison[™] MB can still be trapped within PIM limiting the trans-pulmonary passage of Optison[™], and thus imaging performances of Optison[™] were only compared in rabbits.

In pig, SonoVue[®] and Definity[®] showed uniform contrast enhancement in the liver at their clinical dose allowing adequate visualization of the complete liver, and contrast enhancement persisted for at least 3 min. At half and full clinical dose, both agents also demonstrated adequate and uniform contrast enhancement within the liver parenchyma. Peak enhancement (PE) measured in the liver parenchyma, using VueBox[®] quantification software, was similar or slightly higher for SonoVue[®] compared to Definity[®] (Figure 2A). In general, PE at full clinical dose reached twice the PE at half the clinical dose, confirming proportionality with agent concentration as expected.

Left ventricle (LV) endocardial border delineation could be assessed in pig with Definity[®] at the clinical dose for up to 1 min after injection; SonoVue[®], on the other hand, showed longer enhancement, and LV border delineation could be assessed up to 2 min after injection (Figure 2B). Contrast enhancement was quantified in the LV cavity for both agents at full and half the clinical dose, demonstrating that PE of SonoVue[®] was significantly higher compared to that of Definity[®].

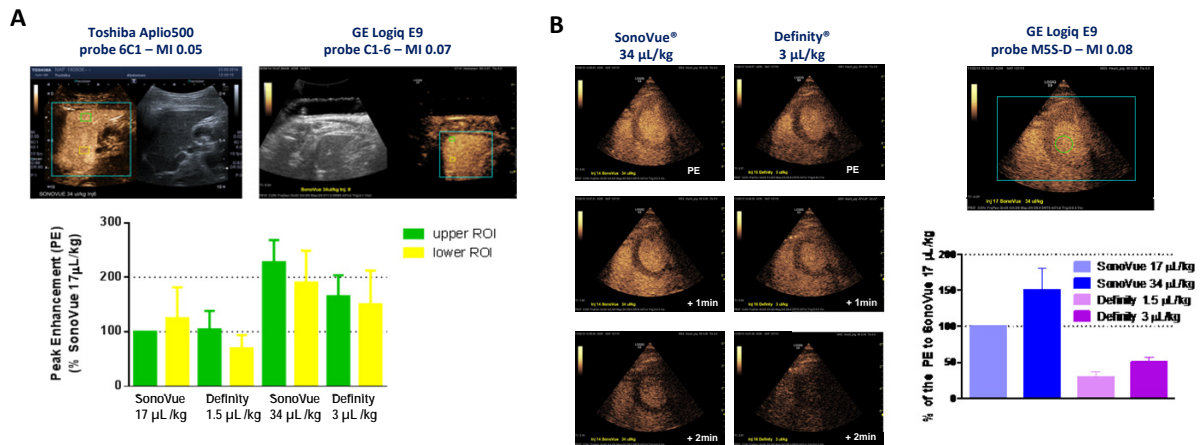


Figure 2: In vivo comparison of UCA imaging performance. A) Quantitative analysis of SonoVue[®] and Definity[®] contrast enhancement within the pig liver using VueBox[®] quantification software. Imaging was performed with Toshiba - Aplio500 (transducer 6C1) and GE - Logiq E9 (transducer C1-6). Data were normalized to the PE of SonoVue[®] at 17 μ L/kg measured within the upper part of liver parenchyma. B) Typical images of contrast enhancement in the LV of the pig after injection of SonoVue[®] and Definity[®]. Contrast imaging was performed with GE - Logiq E9 (transducer M5S-D). PE was measured in the LV for SonoVue[®] and Definity[®] at half and full clinical dose using VueBox[®]. Data were normalized to the PE of SonoVue[®] at 17 μ L/kg.

In rabbit, contrast enhancement of Optison[™] within the liver parenchyma is lower compared to that of SonoVue[®] at full and half the clinical dose. In particular, contrast enhancement of SonoVue[®] lasts longer than that of Optison[™], which is important, e.g. for the assessment of the portal-venous and late phase.

Conclusion:

At their clinical dose, Definity[®] may contain substantially more MB larger than 20 μ m compared to SonoVue[®] and Optison[™]. In pig, SonoVue[®] and Definity[®] showed similar contrast enhancement and duration of enhancement in liver. In the heart, both SonoVue[®] and Definity[®] produced efficient LV opacification, allowing endocardial border delineation particularly when using the highest clinical dose (i.e. 34 μ L/kg and 3 μ L/kg for SonoVue[®] and Definity[®], respectively). Interestingly, quantitative analysis revealed a significantly higher enhancement for SonoVue[®] compared to Definity[®], which is in agreement with *in vitro* results. Moreover, the duration of enhancement was longer with SonoVue[®] compared to that of Definity[®]. In rabbit, SonoVue[®] showed superior imaging performance compared to Optison[™] which is in agreement with *in vitro* results.

Acoustic trapping of microbubbles at clinically relevant flow rates

Sevan Harput¹, David Cowell¹, Thomas Carpenter¹, Ben Raiton¹, James McLaughlan^{1,2}, Steven Freear¹

¹School of Electronics and Electrical Engineering, University of Leeds, UK. LS2 9JT

²Division of Biomedical Imaging, University of Leeds, UK. LS2 9JT

Introduction

Considerable research effort is being devoted to the development of microbubbles with a therapeutic payload. To increase the efficacy of these agents, a number of strategies have been developed to improve localisation including targeting ligands, acoustic release, sonoporation [1] and magnetic targeting [2]. This study investigates an alternative approach using an array transducer for imaging, ultrasonically trapping, manipulating and increasing the population of microbubbles at a desired location in a vessel phantom [3, 4].

Methods

A 128 array element imaging transducer was configured with two sub apertures of 64 elements. This transducer was connected to the Leeds Ultrasound Array Research Platform (UARP) affording arbitrary excitation waveform control and ultra-fast image capture [5, 6 and 7]. To each aperture an ultrasound pulse sequence was applied but with opposite phase polarity. The beams destructively interfere along the central axis of the transducer, perpendicular to the vessel axis, creating a pressure null (figure 1). An acoustic trapping force (ATF) is resolved along the axis of the vessel and is directly proportional to the gradient of the pressure field. Two equal, out of phase, plane wave fields produce a beam profile as shown in figure 2. It can be seen there is a steep sided pressure gradient at 0mm with resolving forces in opposite directions along the vessel axis creating a trapping zone.

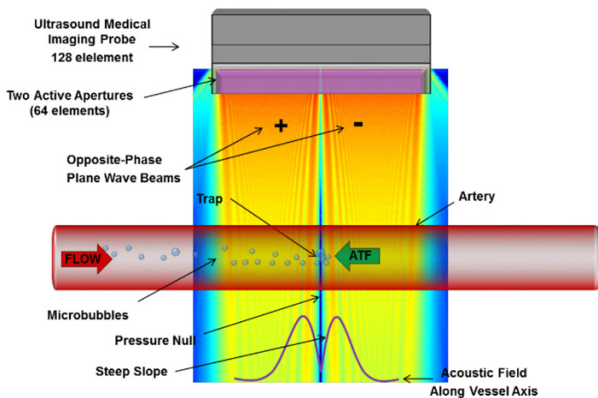


Figure 1 Schematic of transducer and alignment to flowing microbubbles in a vessel. Central null beam creates an Acoustic Trapping Force (ATF)

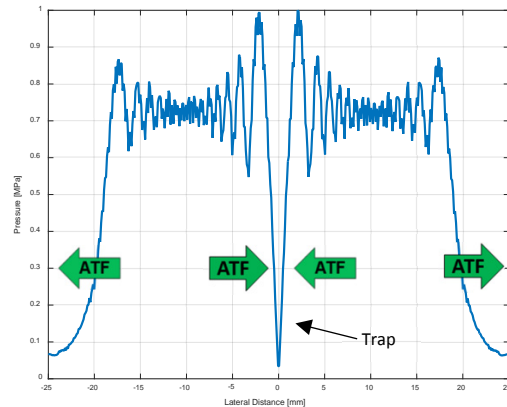


Figure 2 Beam profile of two plane wave trapping beams with π phase shift at 30mm depth

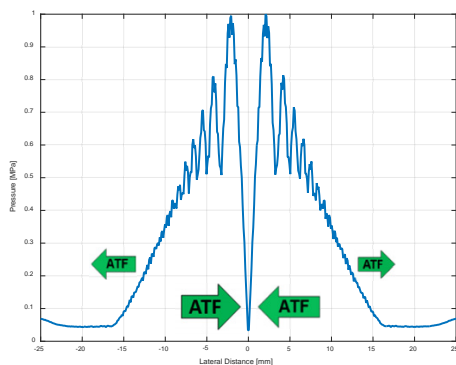


Figure 3 Beam profile of two plane wave trapping beams with π phase shift (apodization) at 30mm depth

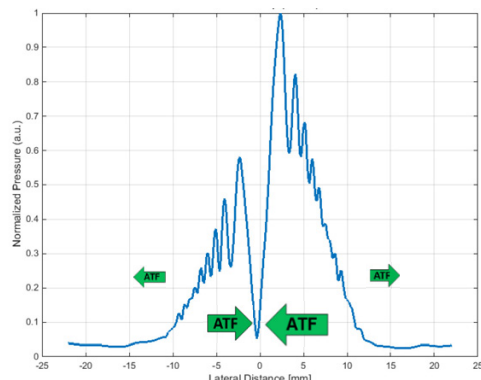


Figure 4 Beam profile of two plane wave trapping beams with π phase shift (apodization and lower pressure input beam) at 30mm depth

However there is also an equally significant gradient at -20mm, stopping SonoVue microbubbles entering the trap. This is corrected by applying apodization at the outer edges of the array and therefore reducing the pressure gradient at -20 and +20mm (figure 3). To further facilitate microbubble entrance to the trap and allow for the pulsatile nature of flow, the input beam is further reduced through the application of pulse width modulation [8, 9]. This beam profile is shown in figure 4 and resultant beam plot in figure 5.

Results and Discussion

Microbubble trap monitoring was performed with the same transducer utilizing high frame rate plane wave imaging (PWI). Trapping and imaging sequences required two different beam profiles and must be interlaced to achieve both. However with arterial blood flow rates in the region of 1m/s, time spent gathering an imaging frame must be kept to a minimum, otherwise the microbubbles will flow out of the trap region. With linear imaging and a typical frame rate of 25Hz, one frame requires 40ms to acquire. During this time, without the trapping beam, microbubbles can travel 40mm which is well outside the trapping region. With PWI a frame rate of 10kHz is achievable, each frame requiring 100 μ s to acquire. During this time period without the trap, microbubbles can travel 100 μ m, which is still within the trapping region. High frame rate plane wave imaging (PWI) was used to visualise microbubbles flowing and trapped within the flow phantom. When the UARP was switched into dual trapping and imaging an interlaced sequence begins, switching between PWI and trapping at 10kHz. In either mode the whole 128 element array was employed, this ensures optimal trapping control and the highest quality images. Electronic manipulation and transportation of the trapped microbubbles was observed when the central null zone was electronically shifted, figure 6 illustrates trapped microbubbles, in a wall-less vessel phantom, transported to -7mm. Once the interleaved trapping sequence was removed and the transducer only emits an imaging sequence the trapped microbubbles disperse and normal contrast agent flow returns.

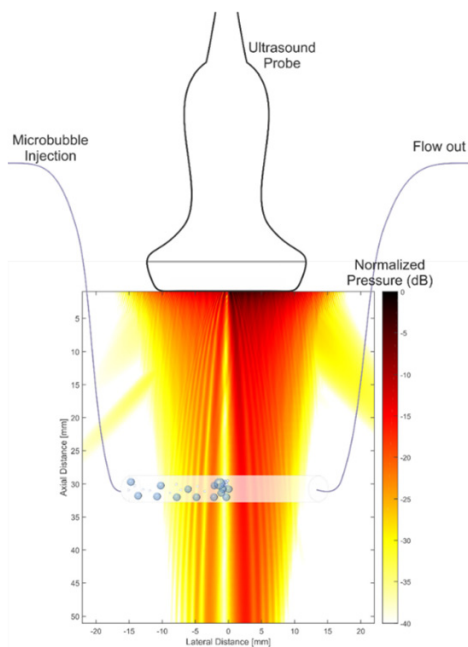


Figure 5 Schematic showing final trapping beam design (apodization and asymmetric beam pressure)

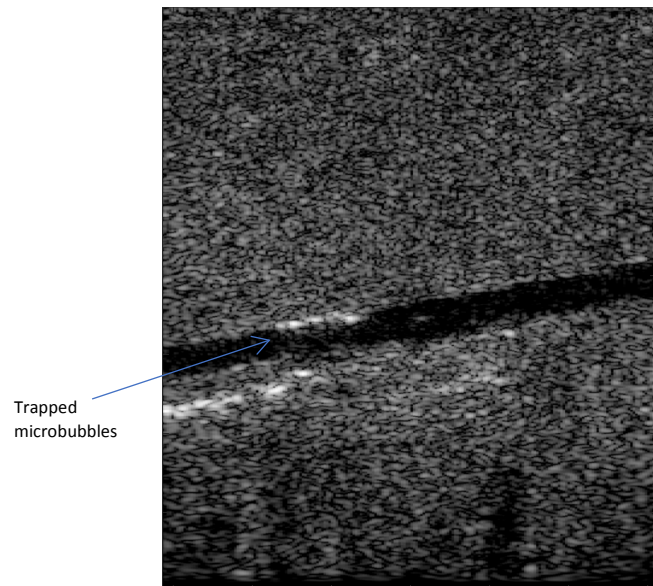


Figure 6 High Frame rate PWI interlaced with trapping sequence showing trapped microbubbles within an arterial phantom

Conclusions

This study shows the viability of trapping microbubbles in a tissue mimicking phantom with a linear array imaging transducer. A custom designed beam profile has been developed which can retain the microbubbles in the trapping zone and is resilient to pulsatile clinical flow rates. The trapped microbubbles can be simultaneously imaged using high frame rate plane wave imaging (PWI), interlaced with a trapping sequence. Finally the trapped microbubble population can be transported by electronically changing the trapping null zone of the transducer. For drug loaded microbubbles the study shows the potential to increase the volume of drug at a particular location. The drug volume can also be continually monitored using PWI. Further work will focus on destruction and imaging of the trapped microbubbles.

References

1. McLaughlan J; Ingram N; Smith PR; Harput S; Coletta PL; Evans S; Freear S Increasing the sonoporation efficiency of targeted polydisperse microbubble populations using chirp excitation. *IEEE Transactions on Ultrasonics, Ferroelectrics and Frequency Control*, vol. 60, pp.2511-2520. 2013.
2. J. Owen, P. Rademeyer, D. Chung, Q. Cheng, D. Holroyd, C. Coussios, P. Friend, Q. Pankhurst and E. Stride. *Magnetic Targeting of Microbubbles against Physiologically Relevant Flow Conditions*. *J. Roy. Soc. Interface Focus* 5: 20150001 (2015)
3. Raiton B; McLaughlan JR; Harput S; Smith PR; Cowell DMJ; Freear S The capture of flowing microbubbles with an ultrasonic tap using acoustic radiation force. *Applied Physics Letters*, vol. 101, pp.044102-044102-4. 2012.
4. Steven Freear, Ben Raiton, James McLaughlan, David Cowell, Peter Smith, Sevan Harput *Apparatus and Method for Manipulating Entrained Particles*. *International Application Number PCT/GB2013/050738*.
5. Cowell DMJ; Smith PR; Freear S Phase-inversion-based selective harmonic elimination (PI-SHE) in multi-level switched-mode tone-and frequency-modulated excitation. *IEEE Transactions on Ultrasonics, Ferroelectrics, and Frequency Control*, vol. 60, pp.1084-1097. 2013.
6. Harput S; Arif M; McLaughlan, J; Cowell DMJ; Freear S The Effect of Amplitude Modulation on Subharmonic Imaging with Chirp Excitation. *IEEE Transactions on Ultrasonics, Ferroelectrics and Frequency Control*, vol. 60, pp.2532-2544. 2013.
7. Smith PR; Cowell DMJ; Raiton B; Vo Ky C; Freear S Ultrasound array transmitter architecture with high timing resolution using embedded phase-locked loops. *IEEE Transactions on Ultrasonics, Ferroelectrics and Frequency Control*, vol. 59, pp.40-49. 2012.
8. Smith PR; Cowell DMJ; Freear S Width-modulated square-wave pulses for ultrasound applications. *IEEE Transactions on Ultrasonics, Ferroelectrics, and Frequency Control*, vol. 60, pp.2244-2256. 2013
9. Steven Freear, Peter Smith, David Cowell, *Hybrid Multi-Level Pulse Width Modulation Method*, *International Patent Application No PCT/GB2013/053289*.

Acknowledgements

The authors gratefully acknowledge funding from the Engineering and Physical Sciences Research Council (UK) via grant no. EP/K030159/1, EP/I000623/1 and the Leverhulme fellowship (ECF-2013-247).

Nanoparticles for multimodal imaging

Olga Koshkina, Edyta Swider, Eric van Dinther, Carl Figdor, Jolanda de Vries, Mangala Srinivas

Department of Tumor Immunology, Radboud Institute for Molecular Life Sciences, Nijmegen, The Netherlands

We developed polymer-entrapped perfluorocarbon (PFC) nanoparticles for ^{19}F MRI applications, particularly cell tracking. The nanoparticles can be made with different polymers and different PFCs, and typically we also add a fluorescent dye. The diameter and fluorine content of the particles varies dependent on the polymer and formulation parameters used. Most often, we work with a perfluoro-15-crown-5-ether entrapped in poly-lactic-co-glycolic acid (PLGA), and these particles can also be formulated at GMP-grade. The ultrasound contrast achieved by these nanoparticles varies with the polymer and the PFC used, and other factors. PFC emulsions and nanodroplets have been used previously to generate ultrasound contrast, albeit at relatively poor levels, and typically after vaporisation. However, we found that a formulation of PLGA and PFC results in particles which have relatively high ultrasound contrast, as well as excellent contrast with MRI. Furthermore, the contrast is stable to insonation for extended periods of time. We used these particles for applications including imaging migratory cells in mice, after labelling with the nanoparticles. A clinical trial with these nanoparticles for imaging therapeutic cells in melanoma patients using multimodal imaging is underway.

From bubbles to droplets to bubbles again: Applying microbubble condensation to aid translation

Paul S. Sheeran¹, Kimoon Yoo², Ross Williams², and Peter N. Burns^{1,2}

¹Department of Medical Biophysics, University of Toronto, Toronto, Ontario, Canada

²Sunnybrook Research Institute, Toronto, Ontario, Canada

Ultrasonically-activated phase-shift perfluorocarbon droplets that are vaporized to form microbubbles by externally applied ultrasound have been proposed for many applications of diagnosis and therapy. However, translation into the clinic has been slow: with a history of over 20 years of published patents and research, first-in-human use has yet to be reported. Unlike microbubbles, which allowed for simple imaging characterization even during the earliest reports, the requirement of high control over pulse sequence design and generally *in vivo* high activation pressures often precludes basic investigation of nanoscale phase-shift droplets. Furthermore, introducing a ‘new drug’ into the relatively small clinical ultrasound contrast agent market requires, in addition to compelling applications, significant commercial investment to develop manufacturing protocols, characterize safety, and fund clinical trials. In this talk, we discuss recent efforts in our group to address these issues and expedite clinical translation by using microbubble condensation in combination with low boiling point perfluorocarbons to generate phase-shift droplets¹.

First, we show that basic image-guided characterization of contrast-enhancement, circulatory kinetics, and biodistribution of low boiling point droplets can be accomplished with commercially available small animal imaging scanners using standard imaging sequences². Droplet vaporization in the kidney, liver, spleen, and in hindlimb tumour xenografts is evaluated in the context of droplet-aided anti-cancer drug delivery. Results show that these formulations are well tolerated at relatively high doses and clear from circulation over the course of 1-2 hours. Preliminary evidence suggests a higher concentration of droplets per tissue volume in the spleen compared to the liver after clearance from the circulation.

We next highlight a potential shortcut to translation: that phase-shift droplets can be generated by microbubble condensation directly from commercially available clinical and pre-clinical microbubbles. This bypasses the need to develop new manufacturing processes and provides an initial safety record in humans and animals from the same constitutive components with which to compare. Proof-of-principle is given using droplets created from Definity (Lantheus Medical Imaging) and MicroMarker (VisualSonics/Bracco). Activation as a function of ambient temperature and ultrasound pressure is characterized acoustically *in vitro* on both clinical diagnostic scanners and small animal scanners, with preliminary *in vivo* demonstrations in the rabbit kidney and mouse liver. Results demonstrate the impact of perfluorocarbon choice on overall thermal stability, in agreement with recent reports³, and suggest specific clinical microbubbles that may be suitable to convert to phase-shift droplets for applications in human imaging and therapy.

1. Sheeran, P. S., Luois, S. H., Mullin, L. B., Matsunaga, T. O. & Dayton, P. A. Design of ultrasonically-activatable nanoparticles using low boiling point perfluorocarbons. *Biomaterials* **33**, 3262–3269 (2012).
2. Sheeran, P. S. et al. Image-guided ultrasound characterization of volatile sub-micron phase-shift droplets in the 20-40 MHz frequency range. *Ultrasound Med. Biol.* In Press (2015).
3. Mountford, P. A., Thomas, A. N. & Borden, M. A. Thermal Activation of Superheated Lipid-Coated Perfluorocarbon Drops. *Langmuir* **31**, 4627–4634 (2015).

Studies of Endothelial Sonoporation Using Ultrafast Frame Rate Microscopy of Microbubble Oscillations and Confocal Microscopy

Brandon Helfield¹, Xucai Chen¹, Simon C. Watkins², Flordeliza S. Villanueva¹

¹*Center for Ultrasound Molecular Imaging and Therapeutics, University of Pittsburgh, PA, USA*

²*Department of Cell Biology, Center for Biologic Imaging, University of Pittsburgh, PA, USA*

Ultrasound-stimulated microbubbles are clinically employed for diagnostic imaging and have been shown to be a feasible therapeutic strategy for localized drug and gene delivery applications. However, the mechanisms by which circulating microbubbles oscillating in the microvasculature promote extravascular transit of macromolecules and subsequent target cell uptake are poorly understood. In order to investigate microbubble oscillation dynamics in relation to endothelium, the UPMC-Cam has been recently developed at the University of Pittsburgh Medical Center- an ultrafast imaging system capable of recording 128 frames at up to 25 million frames per second, one of two in the world currently dedicated for biological ultrasound research..

We have been interested in the effects of ultrasound induced microbubble oscillation specifically on endothelial cells, since these cells are the initial point of contact of vibrating microbubbles and represent the first anatomic barrier to the transfer of macromolecular therapeutic payloads (e.g. therapeutic nucleic acids). We have performed high speed imaging studies in which individual microbubbles lie adjacent to a monolayer of cultured human umbilical vein cells (HUVECS) and are exposed to short ultrasound pulses (1 MHz, 0.1-0.8 MPa) during simultaneous low frame rate fluorescence imaging of uptake of propidium iodide present in the medium (as an indicator of sonoporation). These studies have revealed a maximum microbubble expansion threshold above which sonoporation occurs, likely related to the associated shear stresses exerted by a microbubble on the adjacent cell membrane.

Additional complementary confocal microscopic studies of membrane-labeled HUVECS in the presence of extracellular propidium iodide have shown microbubble-induced pore formation extending through the entire cell thickness, pore healing in the z-plane, and variable persistence of the pore in the x-y plane, with retention of cellular viability. Further, a single microbubble oscillation event can induce tight junction opening between nearby HUVECS. These data suggest several physical mechanisms whereby ultrasound induced microbubble oscillations enhance endothelial permeability and facilitate non-endosomal uptake of therapeutic macromolecules, and that varied acoustic parameters can induce similar biophysical effects. Such insights should inform strategies to optimize ultrasound mediated delivery of therapeutic loads.

Acoustic Cluster Therapy – A Novel Approach for Ultrasound Mediated Targeted Drug Delivery: Technology Basics and Proof of Concept.

P. Sontum², A. Healey², S. Kvåle², N. Bush³, J. Bamber³, C. de Lange Davies¹ and A. van Wamel¹

¹Dept. of Physics, NTNU, Trondheim, Norway, ²Phoenix Solutions AS, Oslo, Norway, ³Joint Dept. of Physics, ICR, London, UK.

Introduction

A very basic dilemma is often encountered with drug molecules; upon systemic administration, they display an unacceptable safety profile at doses relevant for an effective treatment of the indicated pathology. For decades, the pharmaceutical industry has tried to solve this problem with various approaches designed for specific delivery or enhanced uptake of the drug in the *targeted* pathology (i.e. targeted drug delivery). If successful, such strategies may offer ways to increase the dose to the target and/or minimize systemic exposure, improving the therapeutic efficacy and reducing serious side effects. Even though huge resources have been spent over the last two decades in finding functional concepts for targeted drug delivery, there has been a very limited transition to clinical practice. In truth, the objective remains essentially unresolved in medical practice.

The current paper proposes a novel approach to ultrasound mediated, targeted drug delivery; Acoustic Cluster Therapy (ACT) [1][2][3][4]. It also presents interim results from a first proof of concept study where ACT has been investigated for treatment of human prostate adenocarcinoma in mice, in combination with paclitaxel and nab-paclitaxel (Abraxane™).

ACT Basic Concept

In brief, the ACT formulation comprises mixing negatively charged microbubbles with positively charged microdroplets, with the ensuing formation of microbubble/microdroplet clusters from the electrostatic attraction between the two components. The ACT Cluster Dispersion for Injection may be co-administered with a regular medicament (e.g. chemotherapeutic) to induce locally enhanced uptake of the systemically injected drug. The clusters are small enough to be free flowing in the microvasculature after i.v. injection. When insonated with US (activated) *within the targeted pathology*, the microbubble transfers energy to the microdroplet and acts as a vaporisation ‘seed’ initiating vaporisation of the oil droplet. In this way, the cluster construct enables the vaporisation process to occur at much lower acoustic powers than in the absence of a microbubble; the compound may be activated by regular, low MI medical US insonation (e.g. 1-10 MHz, MI < 0.4). Upon US activation, the oil component of the microdroplets instantly vaporise and subsequent inwards diffusion of blood gases produce a 20-30 µm large bubble that transiently deposit in the local microvasculature, stopping the blood flow for some 5-10 minutes. From the transient occlusion of the vessel, immediate wash out is avoided and the drug is kept locally at high concentration for a significant period of time. Post activation, low frequency (e.g. 0.3-1 MHz), low MI US is applied to induce controlled volume oscillations of the large, deposited bubbles with ensuing biomechanical effects to allow for enhanced extravasation and distribution of drug molecules to the targeted tissue. The concept is visualized in Figure 1.

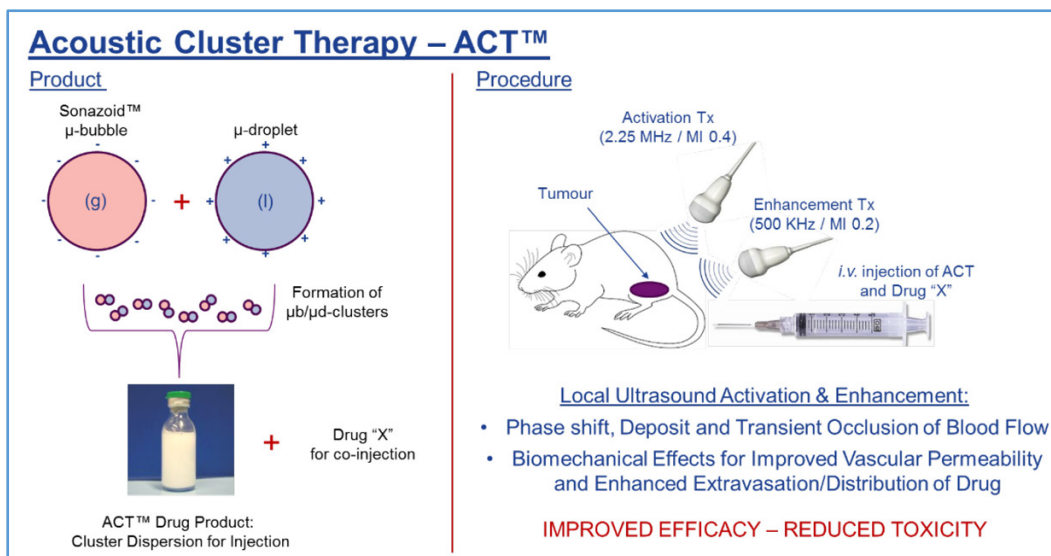


Figure 1 Schematic representation of Acoustic Cluster Therapy – ACT.

Materials and Methods

Animals and Tumor model

50- μ L suspension containing 3×10^6 PC-3 prostate adenocarcinoma cells was slowly injected subcutaneously on the lateral aspect of one hind leg in Balb/c mice. Tumors were allowed to grow for 3–6 wk until the diameter of the tumor was between 5 and 10 mm.

Test items

Details on the investigated ACT test item are provided in [1]. For the microbubble component, Sonazoid™ (GE Healthcare AS) [5] was utilised. The ACT Dispersion for Injection comprised Sonazoid™ reconstituted with 2 ml of an emulsion of perfluoromethyl-cyclopentane (PFMCP) microdroplets (3 μ l/ml) stabilized with a distearoylphosphatidyl-choline (DSCP) phospholipid membrane with 3% (mol/mol) stearylamine (SA), dispersed in 5 mM TRIS (2-Amino-2-hydroxymethyl-propane-1,3-diol) buffer.

Paclitaxel 6 mg/ml (Fresenius Kabi) and Abraxane™ 5 mg/ml (Celgene).

Treatment regime

The first study cohort comprised eight groups of animals, 3-5 in each, as detailed in Table 1. Treatment was given on days 0, 7, 14 and 21. Test items were injected i.v., drug immediately prior to ACT test item or Sonazoid™. For activation, the tumor was insonated for 45 s immediately after injection by regular diagnostic US using a clinical VScan™ system (GE Healthcare AS) with a transducer (Activation Tx, see Fig 1) center frequency of 2.25 MHz and at an estimated mechanical index (MI) of approximately 0.4 in the insonated tumor volume. After activation, the tumor tissue was insonated with low frequency US of 500 kHz at an estimated MI of 0.2 using a custom made transducer (Enhancement Tx, see Fig 1) (Imasonic SAS). ACT treatment was repeated three consecutive times at each cycle. Animals were monitored for body weight and tumour size by caliper twice weekly.

Table 1 – Study Design (N = number of animals in each group)

Group (N)	Test item	US procedure
Control (3)	Saline	45s 2.25 MHz/MI 0.4 + 5min 0.5 MHz/MI 0.2
Paclitaxel (5)	12 mg Ptx/kg <i>i.p.</i>	45s 2.25 MHz/MI 0.4 + 5min 0.5 MHz/MI 0.2
Abraxane (4)	12 mg Ptx/kg <i>i.v.</i>	45s 2.25 MHz/MI 0.4 + 5min 0.5 MHz/MI 0.2
ACT (4)	3 x 5 mg pFMCP/kg <i>i.v.</i>	45s 2.25 MHz/MI 0.4 + 5min 0.5 MHz/MI 0.2
ACT + Paclitaxel (4)	12 mg Ptx/kg <i>i.p.</i> + 3 x 5 mg pFMCP/kg <i>i.v.</i>	45s 2.25 MHz/MI 0.4 + 5min 0.5 MHz/MI 0.2
ACT + Abraxane (5)	12 mg Ptx/kg <i>i.p.</i> + 3 x 5 mg pFMCP/kg <i>i.v.</i>	45s 2.25 MHz/MI 0.4 + 5min 0.5 MHz/MI 0.2
Sonazoid™ + Paclitaxel (5)	12 mg Ptx/kg <i>i.p.</i> + 3 x 8 µl PFB/kg <i>i.v.</i>	5min 45s 2.25 MHz/MI 0.4
Sonazoid™ + Abraxane (5)	12 mg Ptx/kg <i>i.p.</i> + 3 x 8 µl PFB/kg <i>i.v.</i>	5min 45s 2.25 MHz/MI 0.4

Results and Discussion

As noted the results reported herein are interim; the study is performed in two, serial and identical cohorts and monitoring will continue until 90 days after study start. The results reported are from the first cohort up until 59 days. Results are visualized in Figure 2.

Abraxane showed a marked effect on tumour growth rate after the second treatment cycle, all animals responding with remission back to initial tumour size after 28 to 42 days. After 35 days, two of four animals in this groups display significant regrowth. When combining ACT with Abraxane™, marked remission is observed after first treatment and the reduction in tumour volume persists until complete, stable remission for all animals after 59 days. At the end of the treatment period (21 days) the average tumour volumes were $959 \pm 172 \text{ mm}^3$, $251 \pm 64 \text{ mm}^3$ and $71 \pm 69 \text{ mm}^3$ for the control, Abraxane™ and Abraxane™ + ACT groups, respectively. Remarkably, the Abraxane™ + Sonazoid™ group showed a complete lack of response with an average tumour volume of $912 \pm 306 \text{ mm}^3$ at the end of the treatment period (21 days). This was despite the fact that, in an effort to optimize biomechanical effects induced by Sonazoid™ microbubbles, the US enhancement step for this group was performed by continuous insonation with 2.25 MHz and an MI of 0.4. It is, however, possible that this regimen induced some kind of shut down or disruption of the tumour vasculature, as reported elsewhere [6]. If so, this could prevent the drug from penetrating tumour tissue and explain the lack of response in this group. Studies are under way to elucidate possible causes for this observation.

The ACT alone, paclitaxel and Sonazoid™ + paclitaxel groups did not show significant therapeutic effect vs. the saline control group. At a weekly dose of 12 mg/kg given *i.p.*, the paclitaxel plasma concentration apparently does not reach therapeutic levels. However, when combining ACT with paclitaxel, all animals responded markedly to treatment, with significant remission observed after first treatment. At the end of the treatment period the average tumour volumes were $959 \pm 172 \text{ mm}^3$ and $166 \pm 211 \text{ mm}^3$ for the control and paclitaxel + ACT groups, respectively. The observed remissions were stable for 14 to 28 days, when two of four animals started to display regrowth and were euthanized after 42 and 49 days. However, the two remaining animals in this group still show complete, stable remission after 59 days.

Conclusions

Combination with Acoustic Cluster Therapy (ACT) has been shown to markedly increase the therapeutic efficacy of paclitaxel and nab-paclitaxel (Abraxane®) for treatment of human prostate adenocarcinoma in mice.

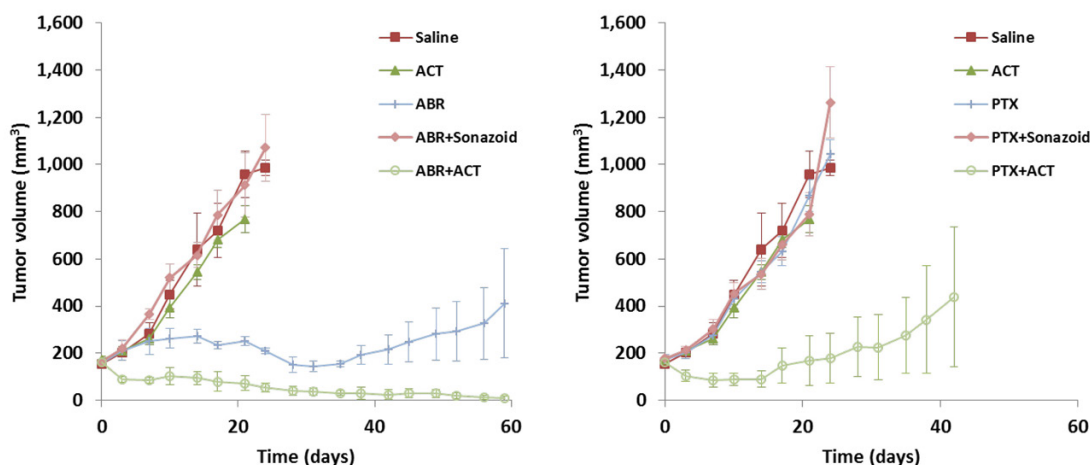


Figure 2 – Results for tumour volume in mice with human prostate adenocarcinoma, treated at days 0, 7, 14 and 21 as indicated in legends (PTX = paclitaxel, ABR = Abraxane®, ACT = Acoustic Cluster Therapy). Error bars designate standard error of the mean (SEM).

References

1. P.C. Sontum, A. J. Healey, S. Kvåle; *Ultrasound Mediated Delivery of Drugs*, patent application PCT/NO2014/050177
2. P.C. Sontum, S. Kvåle, A. J. Healey, R. Skurtveit, R. Watanabe, M. Matsumura, J. Østensen, *Acoustic Cluster Therapy (ACT) – a novel concept for ultrasound mediated, targeted drug delivery*, *Int J of Pharmaceutics*, Vol. 495 (2) (2015): 1019–1027. <http://dx.doi.org/10.1016/j.ijpharm.2015.09.047>
3. A. Van Wamel, A. Healey, P. C. Sontum, S. Kvåle, N. Bush, J. Bamber and C. de Lange Davies, *Acoustic Cluster Therapy (ACT) – pre-clinical Proof of Principle for local drug delivery and enhanced uptake effects*, submitted to *J Cont. Release*, 2015.
4. A. J. Healey, P. C. Sontum, S. Kvåle, M. Eriksen, R. Bendiksen, A. Tornes and J. Østensen, *Acoustic Cluster Therapy (ACT) – in-vitro and ex-vivo measurement of activated bubble size distribution and temporal dynamics*, *Ultrasound Med Biol*, 2015, in-press.
5. P.C. Sontum; *Physicochemical characteristics of Sonazoid™, a new contrast agent for ultrasound imaging*, *Ultrasound Med. Biol.*, Vol. 34 (5), (2008) 824-833.
6. D.E. Goertz, M. Todorova, O. Mortazavi, V. Agache, B. Chen, R. Karshafian, K. Hynynen; *Antitumor effects of combining docetaxel (taxotere) with the antivascular action of ultrasound stimulated microbubbles*, *PLoS one*, 7 (2012) e52307.

Modulation of Cell Membrane Properties by Lipid Transfer from Microbubbles - a potential mechanism for sonoporation?

Dario Carugo^{a†}, Miles Aron^{a†}, Erdinc Sezgin^b, Jorge Bernardino de la Serna^b, Marina Kuimova^c, Christian Eggeling^{b,d}, and Eleanor Stride^a

^aDepartment of Engineering Science, Institute of Biomedical Engineering, University of Oxford, Oxford OX3 7DQ, United Kingdom; ^bMRC Human Immunology Unit, Weatherall Institute of Molecular Medicine, University of Oxford, Headley Way, Oxford OX3 9DS, United Kingdom; ^cDepartment of Chemistry, Imperial College London, London SW7 2AZ, United Kingdom; ^dWolfson Imaging Centre, Weatherall Institute of Molecular Medicine, University of Oxford, Headley Way, Oxford OX3 9DS, United Kingdom

† Authors have equally contributed to the work in this study.

Sonoporation - the temporary permeabilisation of cell membranes following exposure to microbubbles and ultrasound - has been widely reported in the literature. Our understanding of the interaction between phospholipid-shelled microbubbles (MBs) and the cell membrane, however, is far from complete [1]. In this study we employed specially designed acoustofluidic systems and quantitative microscopy techniques to study this phenomenon with the following objectives: First, to investigate the effects of ultrasound and MBs on the arrangement of lipid molecules in cell membranes since this is the main determinant of membrane mechanical properties, protein dynamics, and permeability [2, 3]. Second, to investigate lipid transfer from the MB shell to the cellular membrane since this has previously been identified as a candidate mechanism for enhanced drug delivery with encapsulated MBs [4, 5].

Spectral imaging using C-Laurdan [6], a polarity-sensitive probe, was performed to quantify the packing or “order” of lipid molecules in A-549 cell membranes exposed to either a phosphate-buffered saline (PBS) sham, ultrasound only (970 kHz, ~210 kPa, 60 s continuous wave), MBs only, or ultrasound and MBs. Both DSPC and DSPC-PEG40S (9:1 molar ratio) microbubble formulations were investigated. Lipid order, as indicated by C-Laurdan generalized polarization (GP, ranging from -1 to 1), increased significantly following exposure to DSPC microbubbles ($\Delta GP = +0.044$) and decreased significantly following exposure to DSPC-PEG40S microbubbles ($\Delta GP = -0.051$) ($p < 0.01$ compared to PBS sham) (see Figure 1). Ultrasound did not significantly change the lipid order of A-549 cell membranes in comparison with exposure to MBs only (see Figure 1).

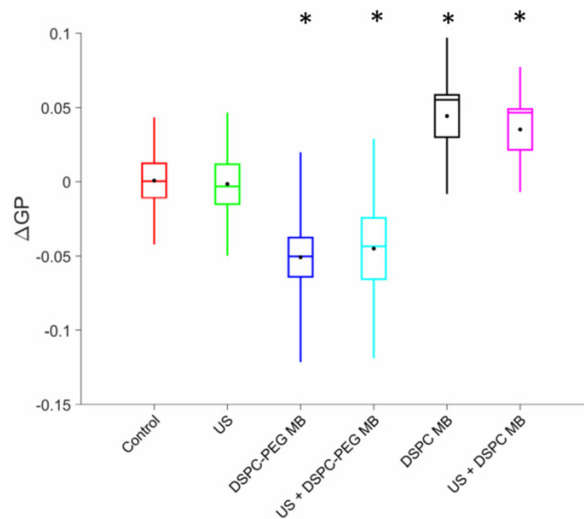


Figure 1. Changes in lipid packing (expressed as ΔGP) of A-549 cell membranes exposed to different experimental conditions. * = Indicates significance ($p < 0.01$) compared to control by Kruskal Wallis ANOVA with Mann-Whitney/Bonferroni-Holm post hoc.

In a complementary experiment, A-549 cells were exposed to DiI-loaded MBs of both formulations with or without ultrasound exposure (see Figure 2a-b). Fluorescent colocalization of cell membranes with DiI, a dye with lipidic molecular dynamics, was used to evaluate molecular transfer from microbubble shells to cell membranes. For DSPC MBs, DiI transfer was substantial, whereas transfer from DSPC-PEG40S MBs was negligible. Following ultrasound exposure, extensive transfer was observed for both MB formulations.

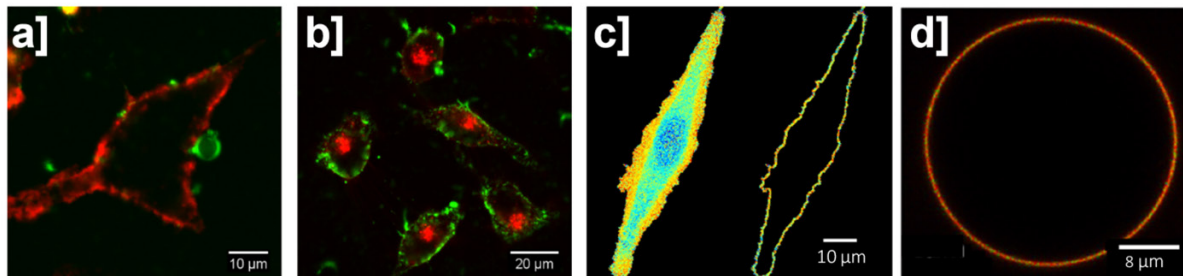


Figure 2. (a) DiI-loaded DSPC-PEG40S microbubble (green) attached to an A-549 cell membrane (red). (b) Extensive DiI transfer to A-549 cells following ultrasound exposure of DiI-loaded DSPC-PEG40S microbubbles. (c) An example C-Laurdan generalised polarization (GP) map and membrane segmentation of an A-549 cell. (d) A DOPC-GUV that has increased lipid order following ultrasound and DSPC-PEG40S microbubble exposure. In the final two images, red indicates high lipid order and blue indicates low lipid order.

Finally, to better understand the mechanisms underlying the change in lipid order in cells, we employed DOPC giant unilamellar vesicles (GUVs) as a simplified model system (see Figure 2d). GUVs membrane properties were evaluated by spectral imaging, fluorescence lifetime imaging microscopy (FLIM), and fluorescence correlation spectroscopy (FCS). For these GUVs, the presence of DSPC-PEG40S MBs increased lipid order, an effect that was dramatically enhanced by ultrasound. By comparing these results with our findings in cells, we determined that, in A-549 cells, the increase in lipid order from DSPC MBs results from lipid transfer, and the decrease in lipid order from DSPC-PEG40S MBs is a consequence of PEG40S.

Together these results provide strong evidence for the hitherto hypothetical mechanism of MB shell-to-cell membrane transfer, and suggest that MBs alter membrane properties in a formulation-

dependent manner. A critical finding of this study is that the PEG used in many MB formulations, including clinically-available Definity® and SonoVue®, has a major impact on lipid order *prior* to ultrasound exposure. We hypothesise that both these mechanisms may play an important role in ultrasound-mediated bio-effects.

References

1. I. Lentacker, I. De Cock, R. Deckers, S. De Smedt, C. Moonen, *Understanding ultrasound induced sonoporation: definitions and underlying mechanisms*, *Advanced drug delivery reviews*, 72 (2014) 49-64.
2. T.J. McIntosh, S.A. Simon, *Roles of bilayer material properties in function and distribution of membrane proteins*, *Annu. Rev. Biophys. Biomol. Struct.*, 35 (2006) 177-198.
3. W.J. Xia, H. Onyuksel, *Mechanistic studies on surfactant-induced membrane permeability enhancement*, *Pharmaceutical research*, 17 (2000) 612-618.
4. P. Dijkmans, L. Juffermans, R. Musters, A. van Wamel, F. Ten Cate, W. van Gilst, C. Visser, N. de Jong, O. Kamp, *Microbubbles and ultrasound: from diagnosis to therapy*, *European Heart Journal-Cardiovascular Imaging*, 5 (2004) 245-246.
5. C. Der Loughian, P.M. Seya, C. Pirat, C. Inserra, J.-C. Béra, J.-P. Rieu, *Jumping acoustic bubbles on lipid bilayers*, *Soft matter*, 11 (2015) 3460-3469.
6. E. Sezgin, D. Waite, J. Bernardino de la Serna, C. Eggeling, *Spectral Imaging to Measure Heterogeneity in Membrane Lipid Packing*, *ChemPhysChem*, 16 (2015) 1387-1394.

Real-time confocal and high-speed imaging to unravel microbubble-cell interactions involved in ultrasound triggered drug delivery with nanoparticle-loaded microbubbles

De Cock I.^{1}, Lajoinie G.^{2*}, De Smedt S.C.¹, Versluis M.², Lentacker I.¹*

*Ghent Research Group on Nanomedicines, University of Ghent, Ghent, Belgium.
Physics of Fluids Group and MIRA Institute for Biomedical Technology and Technical Medicine,
University of Twente, Enschede, The Netherlands.*

** Both first authors contributed equally.*

The amount of drug-loaded microbubbles for ultrasound triggered drug delivery applications is vastly expanding. Although several studies have proven the potential of drug-loaded microbubbles to enhance drug uptake, so far, very little is known on the biophysical microbubble-cell interactions resulting in drug delivery [1]. The relevant phenomena, however, involve a cascade of events: release of drugs during microbubble oscillations, subsequent drug transport and finally drug delivery to cells [2]. Therefore we used in this study three different imaging frame rates (2 frames per second, 1000 frames per second and 10 million frames per second) to unravel the complete chain of events.

In the first instance, we used real-time confocal microscopy to image nanoparticle-loaded microbubbles and cells during ultrasound radiation. Lipid microbubbles were loaded with fluorescent, 100nm polystyrene beads as model nanoparticles via avidin-biotin interaction. These recordings revealed that nanoparticle-loaded microbubbles directly deposited the nanoparticles in patches onto the cell membrane, a process that we termed 'sonoprinting' (**Figure 1 and 2**). This phenomenon resulted in the delivery of large amounts of nanoparticles onto the cellular membrane cells and is suggested not to correlate with the creation of cell membrane pores and enhanced endocytosis, which have been reported before to be responsible for ultrasound controlled drug delivery in cells.

The use of high-speed fluorescence imaging (Photron) and ultra-high-speed imaging (Brandaris128) to study nanoparticle release and transport at different acoustic settings revealed that at lower acoustic pressures, drug-loaded microbubbles transported the released drugs away from the cells by microstreaming. This was previously reported by Luan et al. and Lajoinie et al. [3,4]. In contrast, at higher acoustic pressures and longer ultrasound pulses, microbubbles were rapidly translating driven by secondary Bjerkness forces. As a result, the drugs released in the microbubble surroundings were dragged along with the travelling microbubble. Eventually this transport led to the deposition of the drugs in elongated patches onto the cell membrane (sonoprinting).

References

1. *Lentacker et al., Advanced Drug Delivery Reviews, 2014.*
2. *Kooiman et al., Advanced drug delivery reviews, 2014.*
3. *Luan et al., Ultrasound in Medicine & Biology, 2014. 40(8): p. 18341846.*
4. *Lajoinie, Ultrasound contrast agents-bubbles drops and particles, PhD thesis 2015, University of Twente.*

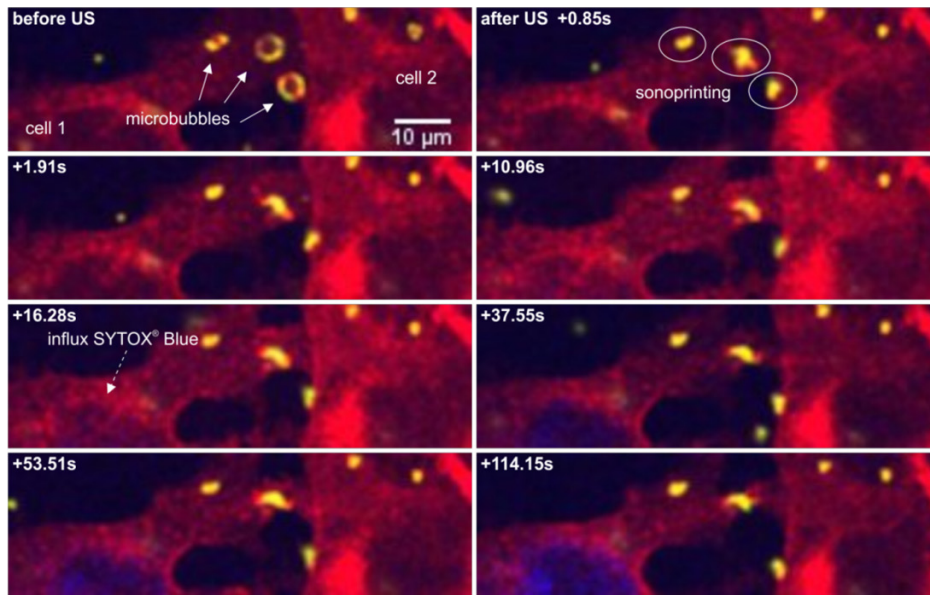


Figure 1. Sonoprinting by nanosphere-loaded microbubbles. Series of confocal images depicting three nanosphere-loaded microbubbles (arrows) that deliver their nanospheres to the cell membrane (sonoprinting) upon ultrasound exposure ($t=0$). Cell 1 shows influx of SYTOX[®] Blue (dashed arrow), indicating cell membrane poration, while this is not observed in cell 2. Cells were exposed to pulsed ultrasound with an acoustic pressure of 300 kPa (pulse length 10 cycles, PRP 0.01 s, duration 0.19 s). The cell membrane is labeled in red with CellMask[™] Orange Plasma membrane Stain, while green fluorescent 100 nm nanospheres are attached to the microbubble shell.

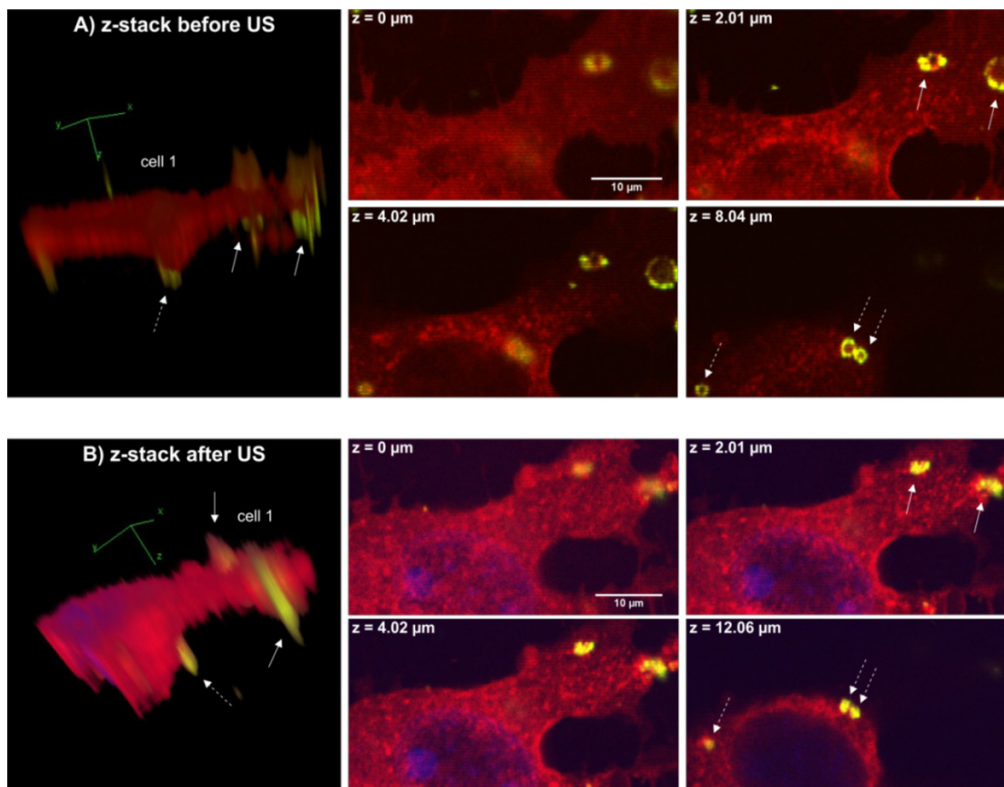


Figure 2. 3D image and corresponding Z-stacks of cell 1 in Figure 1, before (A) and after (B) ultrasound exposure. (left) 3D image of cell 1, (right) corresponding z-stacks at different focal depths. Microbubbles (A) and released nanospheres (B) are visible in the green channel and indicated with arrows.

Direct Observation of Targeted Ultrasound-Assisted Liposomal Doxorubicin Delivery in Microvessels-on-a-Chip

Yoonjee C. Park, Chentian Zhang, Sudong Kim, Grace Mohamedi, Carl Beigie, Robin O. Cleveland, Jon O. Nagy, R. Glynn Holt, Noo Li Jeon, and Joyce Y. Wong

Departments of Biomedical Engineering, Mechanical Engineering, and Division of Materials Science & Engineering, Boston University; School of Mechanical and Aerospace Engineering, Seoul National University, Seoul; Department of Engineering Science, Institute of Biomedical Engineering, University of Oxford; NanoValent Pharmaceuticals, Inc., Bozeman, Montana

Ultrasound-mediated drug delivery with microbubbles is increasingly being studied for targeted drug delivery to solid tumors. Clinical translation, however, has been slowed by the expense and technical challenges associated with in vivo mechanistic studies. To address this issues, we used microfluidic “microvessels-on-a-chip” to establish physical (microbubble oscillation) and biological (cell targeting) parameters for microbubble/ultrasound-dependent delivery of liposomal-encapsulated-doxorubicin (DOX-liposomes) to microvasculature in vitro. Acoustic emission signals showed that microbubbles perfused through microvessels-on-a-chip undergo modest, stable oscillations under low acoustic power ultrasound. Notably, we observed no microvessel damage when oscillating microbubbles or untargeted DOX-liposomes are perfused. In contrast, significant cytotoxicity is observed with perfused integrin-targeted DOX-liposomes, and this cytotoxic effect is significantly enhanced by ultrasound only when microbubbles are co-perfused. These results indicate DOX internalization that we observe is largely dependent on integrin receptor-mediated endocytosis, and this process is accelerated by stable-oscillating microbubbles. Our findings demonstrate potential utility for “microvessels-on-a-chip-model” in optimizing microvasculature-targeted drug delivery.

Microbubble pumps: Ultrasound theragnostic agents

Christy K. Holland, Ph.D.

Professor Internal Medicine, Division of Cardiovascular Health and Disease and Biomedical Engineering Program

*Director of Research, Heart, Lung, and Vascular Institute, University of Cincinnati
Cardiovascular Center 3935, 231 Albert Sabin Way, Cincinnati, Ohio 45267-0586
USA*

<http://www.ultrasound.uc.edu>

office: +1 513 558 5675

fax: +1 513 558 6102

Cardiovascular disease is the number one cause of death worldwide and thrombo-occlusive disease is a leading cause of morbidity and mortality. Ultrasound has been developed as both a diagnostic tool and a potent promoter of beneficial bioeffects for the treatment of cardiovascular disease. Ultrasound exposure can induce the release, delivery and enhanced efficacy of a thrombolytic drug (rt-PA) and bioactive gases from echogenic liposomes. By encapsulating drugs into micron-sized and nano-sized liposomes, the therapeutic can be shielded from degradation within the vasculature until delivery is triggered by ultrasound exposure. Insonification accelerates clot breakdown in combination with rt-PA and ultrasound contrast agents, which nucleate sustained bubble activity, or stable cavitation. Mechanisms for ultrasound enhancement of thrombolysis, with a special emphasis on cavitation and radiation force, will be reviewed. A non-invasive strategy for ultrasound-triggered local therapeutic gas delivery to treat ischemic injury, a sequela of thrombo-occlusive disease, is also under development. The delivery of bioactive gases, such as xenon and nitric oxide, from echogenic liposomes to promote vasodilation and cytoprotection will be discussed.

Effect of Longer Pulse Duration Transthoracic Ultrasound Induced Microbubble Cavitation on Coronary Artery Diameter In Different Pathophysiological Conditions

Thomas Porter, Feng Xie, John Lof

University of Nebraska Medical Center, Omaha, NE, USA

Background

Although ultrasound induced microbubble cavitation (UIMC) has been shown to dissolve intravascular and microvascular thrombi, the shear stress generated by cavitation has also altered endothelial function, which may result in different coronary artery (CA) vasomotor responses in different pathophysiologic settings. The purpose of this study was to determine regional CA responses to UIMC in three different pathophysiologic settings: normal conditions, regional endothelial dysfunction (ED), and regional ED with thrombus formation.

Methods

Intermittent high mechanical index (MI) impulses were applied with a diagnostic transthoracic ultrasound (TTU) transducer over the parasternal location. The high MI impulses were modified to be of longer pulse duration (1.7 MHz frequency, 1.3 MI, 20 μ s pulse duration), and applied in six pigs in a five seconds on, five seconds off sequence during a 3% intravenous Definity infusion. CA diameters of the proximal, mid (endothelial injury site), and distal left anterior descending (LAD), and proximal right coronary artery (RCA) were measured before and after the high MI TTU applications under (A): normal conditions, (B): after a 20 mm long balloon injury (BI) was performed in the mid LAD, and (C): after BI and introduction of 1.0 ml arterial thrombus at the BI site. Each intermittent high MI ultrasound application lasted for 10 minutes.

Results

CA diameter increased in the proximal and mid LAD following UIMC under normal conditions ($p=0.02$), and following BI ($p=0.02$), while no changes occurred in the distal LAD. After adding thrombus to the BI site, UIMC did not change proximal LAD CA diameters, but there was a *decrease* in mid and distal LAD diameter following UIMC ($p=0.008$ compared to baseline and post BI diameter changes; ANOVA). The degree of vessel diameter constriction ranged from 2% to 17%. No change in RCA CA diameter occurred in any setting.

Conclusion

CA vasomotor responses are primarily vasodilator in response to UIMC, but vasoconstrictor responses may occur in the presence of ED and active thrombus formation. This may affect the success of longer pulse duration high MI ultrasound in restoring coronary and microvascular flow in acute coronary syndromes.

Lithotripsy: a shocking blow to kidney stones

Robin Cleveland

*Institute of Biomedical Engineering
Department of Engineering Science
University of Oxford*

Shock wave lithotripsy (SWL) is a clinical procedure whereby shock waves, generated outside the body, are used to break-up kidney stones. First introduced in 1980 it revolutionized the treatment of renal calculi and at its peak about 85% of kidney stones in the Europe were treated by SWL. It remains a major technique for treating stones today. Despite the wide spread use of SWL there is no agreement in the literature as to the mechanism, or mechanisms, by which shock waves fragment kidney stones. In addition, it is now recognized that a clinical dose of shock waves will induce renal injury in most, if not all, treated kidneys. Both the significance of tissue damage, and the mechanisms that are responsible for the damage, are under dispute. This talk will address: how lithotripters generate shock waves, the mechanisms that likely play a role in stone fragmentation and tissue damage, the current state of lithotripsy and what its future may be.

Sonoreperfusion for microvascular obstruction: a clinically applicable approach

Francois TH Yu¹, Filip Istvanic¹, Xucai Chen¹, Flordeliza S Villanueva¹, Jeffrey Powers² and John J Pacella¹

1. Center for Ultrasound Molecular Imaging and Therapeutics, University of Pittsburgh School of Medicine, Pittsburgh, PA, USA
2. Philips Ultrasound, Bothell, WA, USA

Background

Microembolization during percutaneous coronary intervention for acute myocardial infarction causes microvascular obstruction (MVO), independent of patency of the supplying epicardial artery. We have shown that sonoreperfusion (SRP) therapy using ultrasound (US) and microbubbles (MB) specifically relieves MVO and restores microvascular perfusion *in vitro* and *in vivo* [1, 2], using an experimental single element ultrasound transducer delivering long tone burst ultrasound (US). To move toward clinical translation, we tested the effectiveness of a custom modified Philips clinical US scanner, a platform with potential theranostic capability, to deliver the therapeutic ultrasound in an animal model of MVO.

Methods

We used our previously developed rat hindlimb model of MVO [2]. Perfusion imaging of the rat hindlimb muscle was performed using a clinical Sequoia ultrasound scanner in contrast mode (CPS, 7 MHz, 0.2 MI) during jugular venous infusion of Definity (2 mL/hr). MVO was created by injecting microthrombi (< 200 μ m) into the hindlimb muscle microvasculature. Imaging was conducted at four time points: 1) baseline, 2) 10 minutes post-MVO, 3) post-treatment 1 (Tx1), and 4) post-treatment 2 (Tx2). For both treatments, the therapeutic ultrasound was delivered using a modified Philips EPIQ system (S1-5 probe, STL mode, 1.6 MHz, 1.1 MPa, 1 ms pulse length, 0.33 Hz framerate) to provide therapeutic impulses to the MBs in the obstructed hindlimb microvasculature for 10 minutes. “No Treatment” rats were injected with microthrombi to achieve MVO, but did not receive US therapy. A separate group of rats was treated with SRP with a single element transducer (1 MHz, 1.5 MPa, 5 ms pulse length, 0.33 Hz PRF), where the US power in the treatment area is estimated to be 5 times higher than with the Philips system. Image intensities of the acquired perfusion cine-loops were measured in regions of interest circumscribing the hindlimb microvasculature, and used to calculate microvascular blood volume (MBV). Data are expressed as mean \pm standard deviation. Results were analyzed using 2-way ANOVA and pairwise comparisons were obtained using Tukey’s post-hoc testing.

Results

MBV for all groups were similar at baseline. Imaging 10 minutes after microthrombi injection showed markedly reduced MBV in all groups, indicating successful MVO. In the Philips group, MBV increased to 36% of baseline after Tx1 (6.4 ± 5.7 dB, $p=0.07$ vs MVO). After Tx2, MBV increased to 89% of baseline (15.8 ± 1.9 dB, $p<0.05$ vs MVO) and was similar to baseline ($p=0.2$). In the “No Treatment” group, MBV remained reduced, respectively at 0.8 ± 1.3 dB (n.s. vs MVO) after Tx1 and 4.6 ± 5.2 dB (n.s. vs MVO) after Tx2.

Using the single element therapy transducer, MBV were respectively 12.8 ± 7.1 dB ($p < 0.05$ vs MVO) after Tx1 and 15.5 ± 7.6 dB ($p < 0.05$ vs MVO) after Tx2. There was a trend toward a higher MBV in the Single Element group vs the Philips group after Tx1 ($p = 0.15$). Both US configurations restored MBV after Tx2.

Conclusions

These results demonstrate the efficacy of a clinical system for SRP of MVO with theranostic capability. Compared to the Single Element system, the Philips system did not achieve the same degree of reperfusion after Tx1, but after Tx2, equivalent reperfusion was attained. This is likely due to a difference in total US energy and peak negative pressure delivered to the obstructed microvascular bed. Other differences, including US frequency, pulsing schemes and area covered by the beam cannot be excluded. This work represents progress toward clinical translation of this important therapeutic technique.

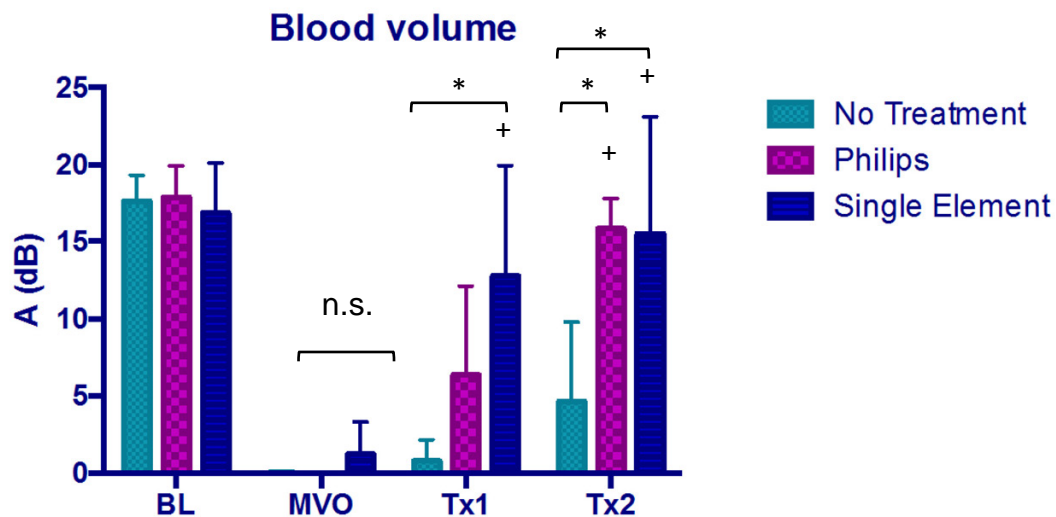


Figure 1: Blood volume assessed by perfusion contrast imaging in rat hindlimb at baseline (BL), after microvascular obstruction (MVO), and after 2 successive 10 minute sessions of sonoreperfusion therapy (Tx1 and Tx2) (* $p < 0.05$, + $p < 0.05$ vs MVO).

1. J. E. Leeman, J. S. Kim, F. T. Yu, X. Chen, K. Kim, J. Wang, et al., "Effect of acoustic conditions on microbubble-mediated microvascular sonothrombolysis," *Ultrasound Med Biol*, vol. 38, pp. 1589-98, Sep 2012.
2. J. J. Pacella, J. Brands, F. G. Schnatz, J. J. Black, X. Chen, and F. S. Villanueva, "Treatment of microvascular micro-embolization using microbubbles and long-tone-burst ultrasound: an in vivo study," *Ultrasound Med Biol*, vol. 41, pp. 456-64, Feb 2015.

Ultrasound-mediated Cancer Immunotherapy

Heleen Dewitte^{a,b}, Stefaan C. De Smedt^a, Karine Breckpot^b, Ine Lentacker^a

^aLaboratory for General Biochemistry and Physical Pharmacy, Faculty of Pharmacy, Ghent University, Ghent, Belgium. Heleen.Dewitte@UGent.be

^bLaboratory of Molecular and Cellular Therapy, Department of Biomedical Sciences, Vrije Universiteit Brussel, Brussels, Belgium

Introduction

Over the years it has become clear that ultrasound, for both imaging as well as therapy, is a versatile tool that finds its applications in many different types of diseases and treatments. One of the fields in which ultrasound has been investigated rather recently, is cancer immunotherapy. This relatively new and emerging research field aims to harness the patient's own immune system in the battle against cancer, by activating immune cells to target and destroy cancerous cells [1, 2]. As more and more immunotherapeutics are making it into the clinic, the number of reports on the use of ultrasound in/together with immunotherapy is also increasing.

Ultrasound & adoptive immune cell therapies

One way to boost a patient's immune responses against a tumor, is by adoptively transferring activated, tumor-reactive immune effector cells, such as cytotoxic T cells (CTLs) and Natural Killer cells (NK cells) [3]. The successes obtained with these cellular therapies are largely determined by the ability of the injected cells to reach and penetrate the tumor. The ability of microbubbles and ultrasound to temporarily open up biological barriers such as the blood-brain-barrier have been applied to improve the therapeutic outcome of NK cell therapy in metastatic brain tumors [4]. Even in case of more accessible solid tumors, low dose focused ultrasound was shown to improve the infiltration of adoptively injected cells [5].

HIFU and immune activation

Another therapeutic moiety based on ultrasound is the application of high intensity focused ultrasound (HIFU) to either mechanically or thermally disrupt solid tumors. However, it seems like the effect of HIFU is not limited to mere killing of cancerous cells. Studies showed that upon HIFU application to various tumor types, there was an increase in the number of circulating immune cells, as well as more tumor-infiltrating immune cells, compared to controls [6-9]. This could be attributed to *a.o.* the release of various *danger signals* which are released from the HIFU-treated tumor cells, such as heat shock proteins and ATP, which attract and activate peripheral immune cells. This indicates that by optimizing the HIFU parameters, it might be possible to use HIFU to disrupt a tumor in such a way that it can – as a matter of speaking – be turned into an antitumor vaccine.

Microbubble-mediated cancer vaccination

Finally, ultrasound has been used together with microbubbles for vaccination purposes. As such, microbubbles have been loaded with messenger RNA (mRNA) encoding tumor antigens as well as immune adjuvants, for the ultrasound-triggered transfection of dendritic cells (DCs), the key initiators of immune responses. As a result, the sonoporated DCs become highly efficient in presenting the antigens and activating anti-tumor T cell responses. When these mRNA-sonoporated DCs were injected as vaccines in tumor-bearing mice, this resulted in significant reductions in tumor-outgrowth

and even complete tumor regression in 2/6 treated animals [10]. Moreover, these microbubbles were shown to rapidly and extensively drain to the lymph nodes upon subcutaneous injections in dogs, as shown by contrast-enhanced ultrasound imaging [11]. This makes these mRNA-loaded microbubbles interesting agents for future *in vivo* intranodal vaccination. Alternatively, protein-loaded microbubbles, without ultrasound, have also shown potential as vaccines against bacterial infections *in vivo* [12]. Upon subcutaneous vaccination, the authors reported durable immune responses involving the two main arms of the immune system: the B cell antibody responses as well as the T cell-mediated immunity.

Conclusions

Despite the recent interest in the effect of (various types of ultrasound) on immune cells, there is still a large unexplored area of the possible applications for ultrasound (with or without cavitation agents) in cancer immunotherapy. Based on the abovementioned promising reports, further investigation is definitely warranted to elucidate the mechanisms behind the observed effects, and to confirm the synergy between ultrasound-based therapies and (various) immunotherapeutics.

Acknowledgements

Heleen Dewitte and Ine Lentacker are post-doctoral fellows of the Research Foundation-Flanders, Belgium (FWO-Vlaanderen). The authors also acknowledge funding through the FWO grant G016513N.

References

1. Dewitte, H., et al., *Nanoparticle design to induce tumor immunity and challenge the suppressive tumor microenvironment*. *Nano Today*, 2014. **9**(6): p. 743-758.
2. Coulie, P.G., et al., *Tumour antigens recognized by T lymphocytes: at the core of cancer immunotherapy*. *Nature reviews. Cancer*, 2014. **14**(2): p. 135-46.
3. Wayteck, L., et al., *A personalized view on cancer immunotherapy*. *Cancer letters*, 2013.
4. Alkins, R., et al., *Focused Ultrasound Delivers Targeted Immune Cells to Metastatic Brain Tumors*. *Cancer Research*, 2013. **73**(6): p. 1892-1899.
5. Sta Maria, N.S., et al., *Low Dose Focused Ultrasound Induces Enhanced Tumor Accumulation of Natural Killer Cells*. *PloS one*, 2015. **10**(11).
6. Lu, P., et al., *Increased infiltration of activated tumor-infiltrating lymphocytes after high intensity focused ultrasound ablation of human breast cancer*. *Surgery*, 2009. **145**(3): p. 286-293.
7. Wu, F., et al., *Expression of tumor antigens and heat-shock protein 70 in breast cancer cells after high-intensity focused ultrasound ablation*. *Annals of surgical oncology*, 2007. **14**(3): p. 1237-1242.
8. Wu, F., et al., *Activated anti-tumor immunity in cancer patients after high intensity focused ultrasound ablation*. *Ultrasound in Medicine and Biology*, 2004. **30**(9): p. 1217-1222.
9. Hoogenboom, M., et al., *Mechanical high-intensity focused ultrasound destruction of soft tissue: working mechanisms and physiologic effects*. *Ultrasound in medicine & biology*, 2015. **41**(6): p. 1500-1517.
10. Dewitte, H., et al., *The potential of antigen and TriMix sonoporation using mRNA-loaded microbubbles for ultrasound-triggered cancer immunotherapy*. *Journal of Controlled Release*, 2014. **194**(C): p. 28-36.
11. Dewitte, H., et al., *Theranostic mRNA-loaded microbubbles in the lymphatics of dogs: implications for drug delivery*. *Theranostics*, 2015. **5**(1): p. 97-109.
12. Bioley, G., et al., *Long-term persistence of immunity induced by OVA-coupled gas-filled microbubble vaccination partially protects mice against infection by OVA-expressing Listeria*. *Biomaterials*, 2015. **57**: p. 153-160.

Echogenic polymer platforms: toward a versatile diagnostic tool.

Gaio Paradossi

*Dipartimento di Scienze e Tecnologie Chimiche, Università di Roma Tor Vergata.
Via della Ricerca Scientifica 1, 00133-I, Rome.*

Ultrasound contrast agents (UCAs) have been used routinely in clinical diagnostics. The most used UCA is a saline suspension of lipid shells with a stabilizing hydrophobic gas core. However, focus on other UCAs have been also considered so far, including shells made of high molecular weight moieties. Polymer based shells¹ provide a unique platform supporting multimodality² (US, MRI for example) and multifunctionality³ (targeting, theranostics). The endurance of the polymer shells allows a long circulation life, although this feature can decrease the microbubble echogenicity. Bearing in mind such hurdles, this contribution will highlight the potentialities of polymer shelled microbubbles in supporting fast developing new methodologies such as photoacoustic imaging. It will also illustrate how “crosslinked polymer shells” concept can be advantageously used in the field of the “phase shift” microsystems.⁴ Insonification can transform microdroplets having crosslinked polymer shell into ultrasound active microbubbles via acoustic droplet vaporization (ADV). The viscoelasticity of the shell controls the expansion of the microbubble shell and is responsible for its return to the original droplet state in a time lapse of some minutes. The analysis of the time dependence of this retraction process provides an insight of the microrheology parameters of the polymer shell.⁵

References

1. F. Cavaliere, A. El Hamassi, E. Chiessi, G. Paradossi. *Langmuir*, , 21, 8758-8764 (2005)
2. T. B. Brismar, D. Grishenkov, B. Gustafsson, J. Härmark, Å. Barrefelt, S. V. V. N. Kothapalli, S. Margheritelli, L. Oddo, K. Caidahl, H. Hebert and G. Paradossi. *Biomacromolecules* 13 (5), 1390–1399 (2012)
3. R. Villa, B. Cerroni, L. Viganò, S. Margheritelli, G. Abolafio, L. Oddo, G. Paradossi, N. Zaffaroni *Colloids and Surfaces B: Biointerfaces* 110, 434 – 442 (2013)
4. S. Capece, E. Chiessi, R. Cavalli, P. Giustetto, D. Grishenkov, G. Paradossi. *Chem. Commun.*, 49, 5763 - 5765 (2013)
5. S. Capece, F. Domenici, F. Brasili, L. Oddo, B. Cerroni, A. Bedini, F. Bordi, E. Chiessi, G. Paradossi, to be submitted (2015)

Impaired Muscle Microvascular Recruitment Contributes to Metabolic Insulin Resistance in Obesity

Y.H.A.M. Kusters^{1,2,3}, C.G. Schalkwijk^{1,2,3}, A.J.H.M. Houben^{1,2}, J. Op 't Roodt^{1,3}, P.J. Joris^{3,4,5}, R.P. Mensink^{3,4,5}, E.J. Barrett⁶, C.D.A. Stehouwer^{1,2}

¹ Department of Internal Medicine, Maastricht University Medical Center, PO Box 616, 6200 MD, Maastricht, The Netherlands

² Cardiovascular Research Institute Maastricht (CARIM), PO Box 616, 6200 MD, Maastricht, The Netherlands

³ Top Institute Food and Nutrition, PO Box 557, 6700 AN, Wageningen, The Netherlands

⁴ Department of Human Biology, Maastricht University Medical Center, PO Box 616, 6200 MD, Maastricht, The Netherlands

⁵ School for Nutrition, Toxicology and Metabolism (NUTRIM), PO Box 616, 6200 MD, Maastricht, The Netherlands

⁶ Department of Medicine, Endocrinology and Metabolism, University of Virginia, PO Box 801410, Charlottesville, VA, 22908, United States of America

Background and aims

Obesity is associated with metabolic insulin resistance (characterized by impaired whole body glucose disposal (WBGD)), and an increased risk of type 2 diabetes (T2DM) and cardiovascular diseases (CVD). In skeletal muscle, insulin normally increases the number of perfused capillaries, enhancing its own delivery and that of glucose to myocytes. We hypothesize that impairments in insulin-induced muscle microvascular recruitment (MVR) may be responsible for the impaired WBGD in obese individuals. In addition, we investigate whether weight loss can restore MVR and whether this improves WBGD.

Materials and methods

In a randomized controlled trial with blinded analyses, 53 non-smoking, abdominally obese men (waist circumference 102-110 cm; aged 18-65; no CVD or T2DM) underwent either an 8-week weight loss program (6 weeks low calorie diet (LCD), 2 weeks weight stable) or maintained their usual diet for 8 weeks and were compared to 25 lean men (waist circumference <94 cm). During a 1 mU/kg/min euglycaemic insulin clamp, we determined WBGD and MVR as the change in microvascular blood volume using real-time contrast-enhanced ultrasound in forearm skeletal muscle. Abdominally obese men were studied at baseline and after completion of their 8-week program, whereas lean men were studied at baseline only.

Results

All 25 lean men and 50 abdominally obese men completed the study. Baseline BMI was 23.3 ± 1.8 kg/m² in lean men, 30.0 ± 1.7 kg/m² in the LCD group, and 29.9 ± 2.5 kg/m² in the control group. LCD reduced BMI by 3.0 ± 0.8 kg/m² ($p < 0.001$), whereas BMI in controls did not change ($+0.1 \pm 0.4$ kg/m²). Baseline WBGD was 6.76 ± 1.79 mg/kg/min in lean men; in both the LCD group (4.06 ± 1.28 mg/kg/min) and the control group (4.03 ± 1.39 mg/kg/min) WBGD was reduced ($p < 0.001$ for both). LCD increased WBGD by 1.31 ± 1.19 mg/kg/min ($p < 0.001$), whereas WBGD remained unaltered in

the control group (-0.05 ± 0.86 mg/kg/min; $p=0.761$). MVR at baseline was 44.4 ± 41.2 % in lean men; in both the LCD group (-5.6 ± 26.2 %) and the control group (0.7 ± 27.6 %) MVR was blunted ($p<0.001$ for both). LCD was able to restore part of this response, to 33.4 ± 39.6 % ($p<0.001$), whereas MVR remained unchanged in the control group (-0.3 ± 28.2 %; $p=0.952$). At baseline, MVR was associated with both BMI ($r=-0.414$; $p<0.001$) and WBGD ($r=0.577$; $p<0.001$). In addition, MVR mediated (18.3 %) the association between BMI and WBGD, independent of other contributors to metabolic insulin resistance. Moreover, changes in MVR were associated with changes in WBGD ($r=0.499$; $p<0.001$). These changes in MVR independently mediated (26.3 %) the association between the weight loss intervention and improvements in WBGD.

Conclusion

We conclude that both MVR and WBGD are impaired in abdominally obese men. In addition, MVR independently mediates the association between BMI and WBGD. Moreover, we conclude that weight loss improves both MVR and WBGD. Additionally, the improvement in MVR independently mediates the association between the weight loss intervention and improvements in WBGD. These findings indicate that impaired insulin-induced muscle microvascular recruitment contributes to metabolic insulin resistance in obesity and that improving muscle microvascular recruitment through weight loss improves metabolic insulin resistance. Future therapies aimed at improving muscle microvascular recruitment can be measured using contrast-enhanced ultrasound and may reduce the disease burden associated with obesity.

Contrast-enhanced ultrasound imaging of the anti-angiogenic effects of interleukin 12 in pet dogs with spontaneous malignant tumors

Laetitia Ciccheler¹, Katrien Vanderperren², Sofie Denies¹, Emmelie Stock², Hendrik Haers², Leen Van Brantegem³, Hilde de Rooster^{4} and Niek N Sanders^{1*}*

1 Laboratory of Gene Therapy, Department of Nutrition, Genetics and Ethology, Faculty of Veterinary Medicine, Ghent University, Heidestraat 19, B-9820 Merelbeke, Belgium

2 Department of Medical Imaging of Domestic Animals, Faculty of Veterinary Medicine, Ghent University, Salisburylaan 133, B-9820 Merelbeke, Belgium

3 Department of Pathology, Bacteriology and Poultry Diseases, Faculty of Veterinary Medicine, Ghent University, Salisburylaan 133, B-9820 Merelbeke, Belgium

4 Small Animal Hospital, Department of Medicine and Clinical Biology of Small Animals, Faculty of Veterinary Medicine, Ghent University, Salisburylaan 133, B-9820 Merelbeke, Belgium

** Both authors contributed equally*

Introduction & aim

One in every four dogs will develop cancer during their life.¹ Cancer is an important cause of canine death as nearly half of pet dogs over the age of 10 die from the consequences of cancer.¹

Interleukin 12 (IL-12) is an immunostimulatory cytokine, produced by antigen presenting cells, that has a key role in the regulation of inflammation by linking innate and adaptive immune responses. It has powerful antitumoral properties through immune stimulation and anti-angiogenesis. The inhibition of angiogenesis is obtained through the inhibition of new blood vessel formation by inducible protein 10.² As a result, the production of factors that facilitate new blood vessel formation such as vascular endothelial growth factor (VEGF) and metalloproteinase-9 is decreased.²

Contrast-enhanced ultrasound (CEUS), using microbubble contrast agents, has recently been proposed as a new imaging modality to quantify tissue perfusion.³ It uses tiny, gas-filled microbubbles, stabilized by an outer shell, that are injected intravenously. Microbubbles remain strictly intravascular, with no interstitial diffusion or urine excretion.³ Therefore, they can be used to portray phenotypical as well as functional differences in tumor vascularity.

The objective of this study was to describe whether CEUS can be used to detect the anti-angiogenic effects of IL-12 gene therapy in dogs with spontaneous malignant tumors.

Material and Methods

The study cohort consisted of 9 dogs, 5 castrated males and 4 spayed females of 8 different breeds (Golden Retrievers (n=2), Malinois, Bouvier, Maltese, Labrador Retriever, Bichon Frisé, French Bulldog, Bordeaux Dog). Their age ranged from 2.9 to 13.7 years (mean 9.5 years, SD 4.1). In all animals, screening for metastatic disease was accomplished by thoracic radiographs, abdominal ultrasonography and/or basic bloodwork. Other conventional therapies such as chemotherapy or radiation were not given prior to IL-12 gene therapy to the included patients, except in 2 dogs (radiotherapy and metronomic chemotherapy were discontinued 6 weeks and 1 month respectively prior to study entry in 1 dog and chemotherapy was discontinued 2 weeks prior to study entry in another dog), who did not complete the whole treatment cycle.

The IL-12 gene therapy treatment consisted out of three successive intratumoral injections (on day 1, 8 and 15) of a good manufacturing practices grade pDNA encoding IL-12 (Figure 1). Per session 1 mg of IL-12 plasmid, diluted with a saline solution to 1/6 of the tumor volume (with tumor volume = $a \times b \times c \times \pi / 6$), was intratumorally injected throughout the whole tumor mass. Subsequently, an 8-needle electrode connected to an electroporator (Agile Pulse generator, BTX® Harvard Apparatus) was inserted within 2 minutes after injection around the injection sites. Two pulses of 450 V/cm were given (pulse duration was 0.05 ms and the interval between the pulses was 0.2 ms). These 2 pulses were after 50 ms followed by 8 pulses of 100 V/cm (pulse duration was 10 ms and the interval between pulses was 20 ms).

Contrast-enhanced US was performed using a linear transducer of 12-5 MHz on a dedicated machine (Philips iU22 xMATRIX, Philips Medical systems, Bothell, Washington, USA) with contrast-specific software. Microbubble contrast agent SonoVue® (Bracco, Milan, Italy) was injected three times intravenously per treatment session as a 0.4 ml/10kg bolus followed by 1 ml of sterile saline flush (NaCl 0.9%). Ninety seconds digital video clips of the enhancement of the neoplastic tissue were obtained. The first injection with SonoVue® was not used for further evaluation. The following characteristics were evaluated on CEUS images: Peak Enhancement (PE), Time To Peak (TTP), Rise Time (RT), mean Transit Time (mTTI), Fall Time (FT), Wash-in Rate (WiR), Wash-out Rate (WoR), Wash-in Perfusion Index (WiPi), Wash-in Area Under the Curve (WiAUC), Wash-out Area Under the Curve (WoAUC) on day 1, 8 and 35 (Figure 1).

On top of CEUS, changes in angiogenesis were assessed for each patient by VEGF analysis of patient's tumor tissue and serum (Canine VEGF DuoSet ELISA Kit, R&D Systems, San Diego, USA) on days 1, 8 and 35 and days 1, 3, 8, 15 and 35 respectively (Figure 1).

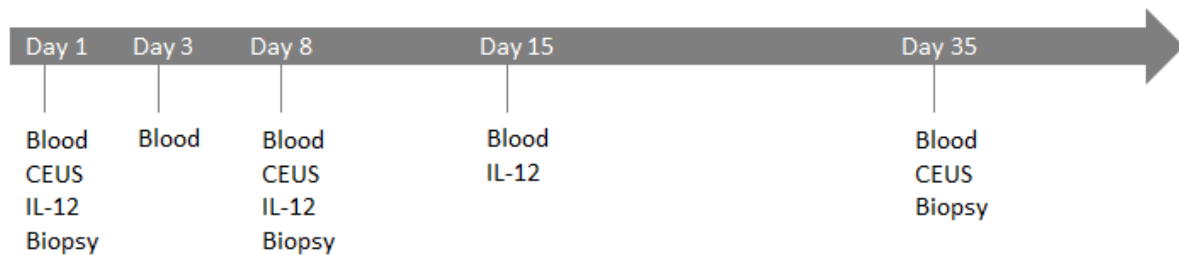
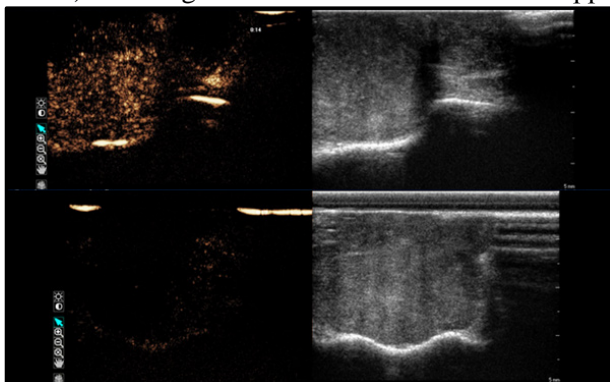


Figure 1: Schedule of IL-12 gene therapy, CEUS, blood collection and tumor biopsy.

Results

In total, 9 malignant tumors (schwannoma (2), fibrosarcoma, (2) (adeno)carcinoma (2), osteosarcoma, mastocytoma, squameus cell carcinoma) were evaluated in 9 dogs. CEUS showed that sarcoma's were less well-vascularized compared to (adeno)carcinomas. However, a difference in flow pattern could be observed in all tumor types. A trend for decrease for WiR was present between days 1 and 8 ($p=0.071$) and a significant decrease for WiR was apparent between days 8 and 35 of treatment ($p=0.04$).



A significant decrease of WiAU was present between days 1 and 8 ($p=0.018$) (Figure 2, 3 and 4). Two dogs demonstrated a clear decrease of intratumoral VEGF and all dogs a slight decrease of serum VEGF (data not shown).

Figure 2: Follow-up of tumor vascularization of a tumor treated with IL-12 gene therapy on day 1 (top) and 8 (bottom). The left plane of each image corresponds to the

CEUS-image of the tumor, the right plane to the ultrasound B-mode image. A decrease in contrast-uptake (represented by the amount of orange speckling) is discernable with the naked eye.

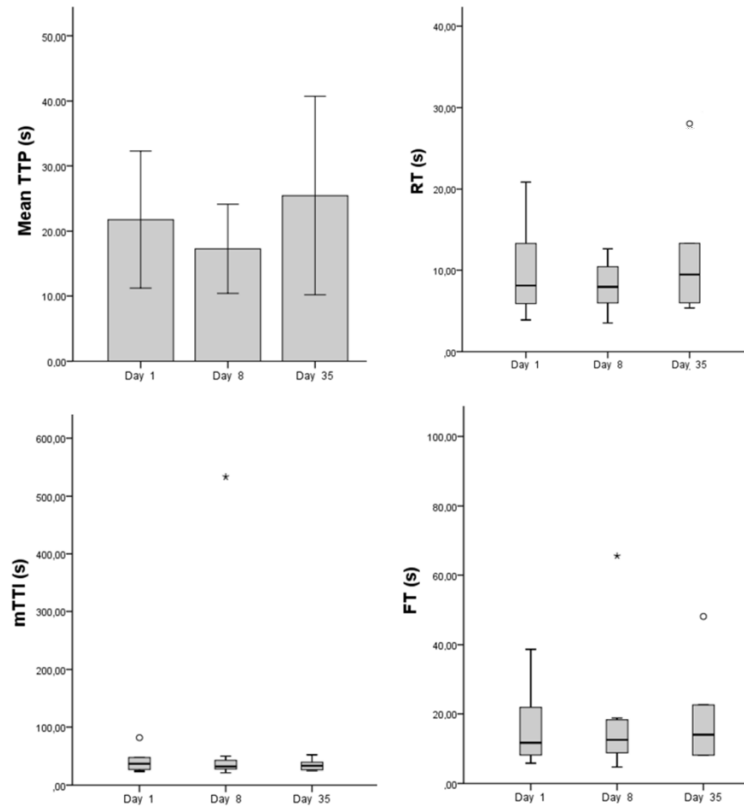


Figure 3: CEUS time parameters. TTP: Time To Peak, RT: Rise Time, mTTI: mean Transit Time, FT: Fall Time. Mean values \pm standard deviations are shown. * and ° indicate great and mild outliers respectively.

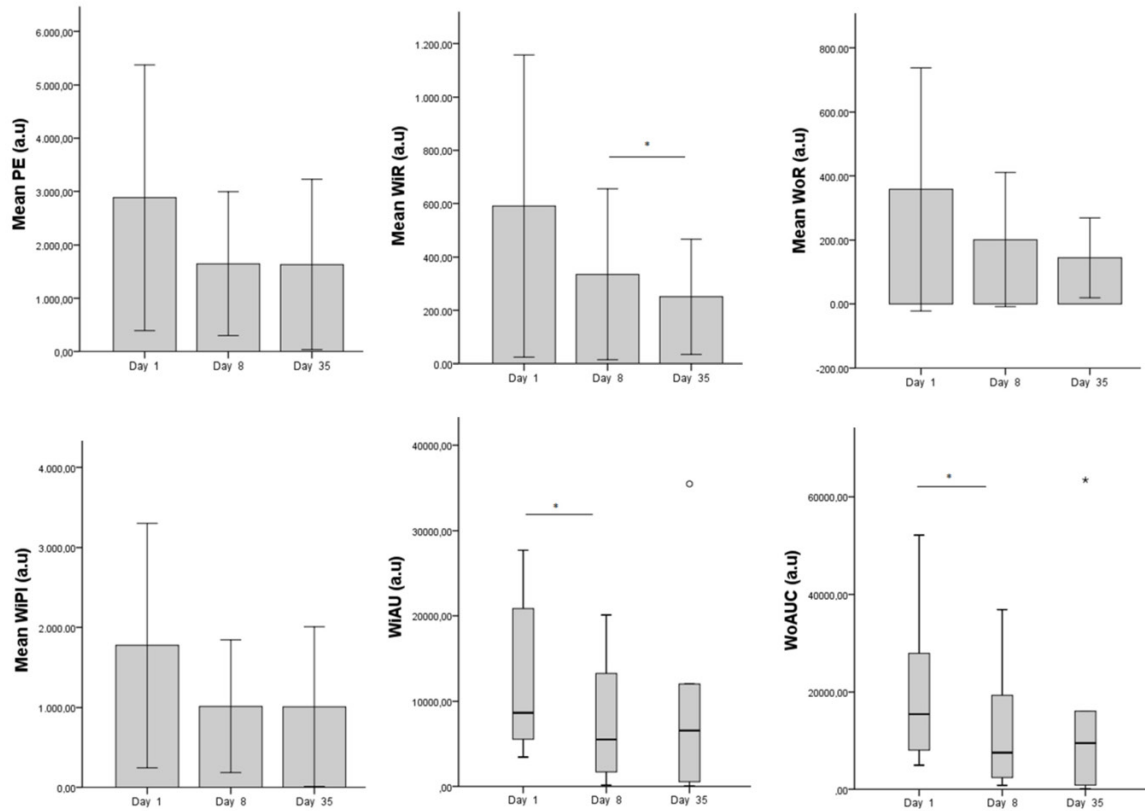


Figure 4: CEUS perfusion parameters. PE: Peak Enhancement, WiR: Wash-in Rate, WoR: Wash-out Rate, WiPi: Wash-in Perfusion Index, WiAU: Wash-in Area Under the Curve, WoAUC: Wash-out Area Under the Curve. Mean values \pm standard deviations are shown. *above horizontal line indicates $p < 0.05$. * and ° indicate great and mild outliers respectively.

Conclusions

In this study we monitored the effect of intratumoral IL-12 gene therapy on tumor vasculature with CEUS and followed the amount of VEGF by ELISA in serum and in tumoral tissue. A remarkable decrease in intratumoral VEGF was present in 2 dogs, but no decreases in VEGF amounts could be detected in the other treated dogs. Nevertheless, the CEUS findings did demonstrate an anti-angiogenic effect in all treated dogs. A significant decrease in blood volume and flow speed was present in all dogs after IL-12 gene therapy. Malignant and benign tumors are characterized by a rapid and slow increase of contrast uptake respectively.⁴ In similar terms, the observed decrease in blood flow speed could indicate a less aggressive behavior of the tumor after IL-12 treatment. Although the anti-angiogenic effects of IL-12 can be monitored in various ways (decrease in intratumoral VEGF and microvessel density^{5,6}, apoptosis of endothelial cells⁷), CEUS provides an excellent non-invasive quantitative and qualitative alternative for biopsies. CEUS has proven to be a more sensitive technique for angiogenesis monitoring than immunohistopathology⁸, as small biopsies are not likely representative for the whole tumor.⁹ Moreover, histological follow-up entails invasive and repetitive biopsies within short time spans, which is not required for CEUS.⁸ Therefore, CEUS has potential as diagnostic tool for the differentiation between benign and malignant lesions and the follow-up of the efficacy of anti-angiogenic treatments.

Bibliography

1. Impellizzeri JA, Ciliberto G, Aurisicchio L. Electro-gene-transfer as a new tool for cancer immunotherapy in animals. *Veterinary and comparative oncology* 2014; 12:310-8
2. Del Vecchio M, Bajetta E, Canova S, Lotze MT, Wesa A, Parmiani G, Anichini A. Interleukin-12: biological properties and clinical application. *Clinical cancer research : an official journal of the American Association for Cancer Research* 2007; 13:4677-85
3. Haers H, Saunders JH: Review of clinical characteristics and applications of contrast-enhanced ultrasonography in dogs. *Journal of American Veterinary Medicine Association* 2009; 234 (4): 460-470.
4. Kuhl CK, Mielcareck P, Klaschik S, Leutner C, Wardelmann E, Gieseke J, Schild HH. Dynamic breast MR imaging: are signal intensity time course data useful for differential diagnosis of enhancing lesions? *Radiology* 1999; 211:101-10
5. Li S, Zhang X, Xia X. Regression of tumor growth and induction of long-term antitumor memory by interleukin 12 electro-gene therapy. *Journal of the National Cancer Institute* 2002; 94:762-8
6. Lucas ML, Heller L, Coppola D, Heller R. IL-12 plasmid delivery by in vivo electroporation for the successful treatment of established subcutaneous B16.F10 melanoma. *Molecular therapy : the journal of the American Society of Gene Therapy* 2002; 5:668-75
7. Shibata MA, Ito Y, Morimoto J, Kusakabe K, Yoshinaka R, Otsuki Y. In vivo electrogene transfer of interleukin-12 inhibits tumor growth and lymph node and lung metastases in mouse mammary carcinomas. *The journal of gene medicine* 2006; 8:335-52
8. Paprottka PM, Rosspunt S, Ingrisich M, Cyran CC, Nikolaou K, Reiser MF, Mack B, Gires O, Clevert DA, Zengel P. Reducing tumor growth and angiogenesis using a triple therapy measured with Contrast-enhanced ultrasound (CEUS). *BMC cancer* 2015; 15:373
9. Chowdhury FZ, Ramos HJ, Davis LS, Forman J, Farrar JD. IL-12 selectively programs effector pathways that are stably expressed in human CD8+ effector memory T cells in vivo. *Blood* 2011; 118:3890-900

Contrast-enhanced ultrasound imaging of the renal cortex of pigs during hemorrhagic shock

Tom van Rooij¹, Alexandre Lima², Verya Daeichin¹, Patricia A.C. Specht³, Bulent Ergin⁴, Yasin Ince^{2,4}, Can Ince^{2,4}, Nico de Jong^{1,5}, Klazina Kooiman¹

¹ Department of Biomedical Engineering, Thorax Center, Erasmus MC, Rotterdam, the Netherlands

² Department of Intensive Care Adults, Erasmus MC, Rotterdam, the Netherlands

³ Laboratory of Experimental Anesthesiology, Department of Anesthesiology, Erasmus MC, Rotterdam, the Netherlands

⁴ Department of Translational Physiology, Academic Medical Center, Amsterdam, the Netherlands

⁵ Laboratory of Acoustical Wavefield Imaging, Faculty of Applied Sciences, Delft University of Technology, Delft, the Netherlands

Introduction

Contrast-enhanced ultrasound (CEUS) measurements could aid in early recognition of renal hypoperfusion, which may prevent the development of acute kidney injury. In this study we performed CEUS imaging to investigate the dynamic changes of the time-intensity curves (TICs) in a pig model of hemorrhagic shock. We hypothesize that the inflow-slope of the TICs is lower in shock as a result of decreased renal blood flow.

Materials & Methods

Surgery was performed on eight female pigs (30 kg) to expose the right kidney. An ultrasonic flow probe was placed around the renal artery to measure renal blood flow (RBF), which is considered as the golden standard for measuring the blood flow entering the kidney. In addition to the RBF, lactate levels, mean arterial pressure (MAP), heart rate (HR), and cardiac output (CO) were monitored during the entire procedure. Hemorrhagic shock was induced by withdrawing blood until MAP reached a steady-state value < 50 mmHg and blood lactate levels > 3 mmol/L. The animal was kept in shock for at least 60 minutes.

CEUS imaging was performed at baseline (t₀), 15 min after blood withdrawal (t₁ = early shock), and 60 min later (t₂ = late shock). At each of these time points a 1 mL bolus of microbubbles (C₄F₁₀ gas; lipid coating in mol%: 92.4 DSPC, 7.6 DSPE-PEG2000; made by Vialmix [1]) or Target-Ready MicroMarker (FUJIFILM VisualSonics Inc., Toronto, Ontario, Canada), was injected in the jugular vein followed by a 10 mL saline flush. The measurements were recorded using a Vevo2100 ultrasound scanner, equipped with a MS250 transducer (VisualSonics, 18 MHz transmit frequency, 10 frames per second, 10% power). Side-by-side B-mode and nonlinear contrast mode (amplitude modulation [2]) images were acquired using a wide beam-width in order to have a low and uniform transmit pressure over the imaging depth (~400 kPa, MI of 0.1). Immediately after injection of the microbubbles, the ventilation of the animal was paused to minimize movement due to breathing. Cine loops were stored and the TICs in a region of interest in the cortex were exported for further offline analysis using Matlab. After averaging over 15 frames the TICs for in-plane motion compensation, the inflow-slope (SL) or wash in rate was obtained. Others have shown that SL, for a given ultrasound contrast agent dose, is proportional to local blood flow rate [2] and that SL was mostly influenced by an increase in blood volume flow ratio [3].

Results

Due to hemorrhage, total blood volume decreased and consequently RBF decreased from 301 (287 – 366) mL/min at baseline (t0) to 90 (59 – 141) mL/min in early shock (t1) and decreased further to 61 (39 – 124) mL/min in late shock (t2), as expected (see Fig. 1). The median normalized SL increased 19% in early shock (t1) and 76% from t1 to t2 (see Fig 1). The normalized SL showed a trend opposite to the RBF measured with the flow probe: whereas RBF decreased in shock, SL increased.

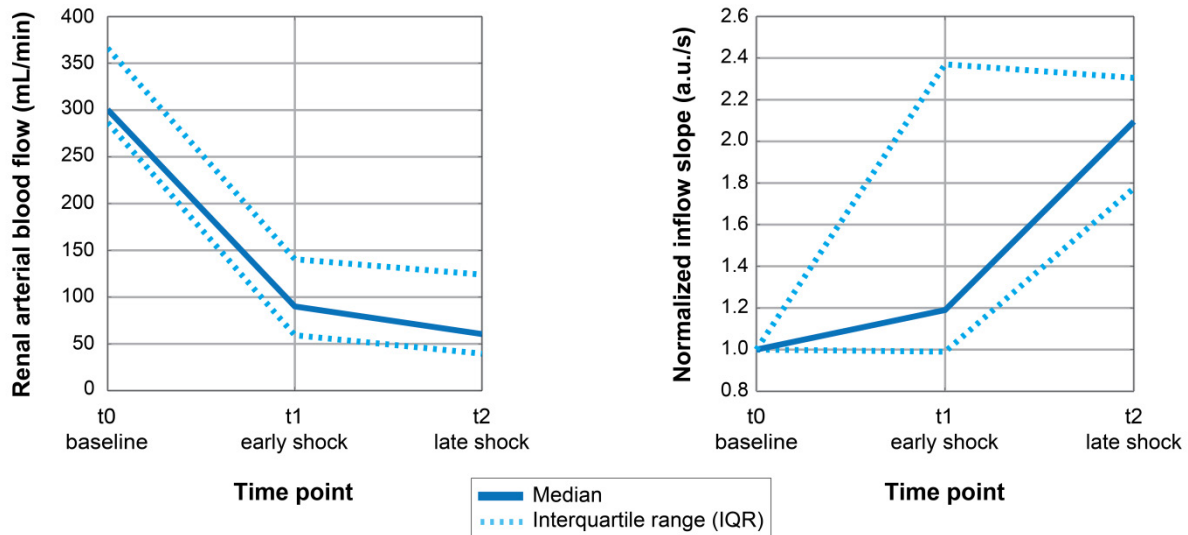


Fig. 1. Flow measured at different locations in the kidney (n = 8). **A)** Renal blood flow (RBF) was measured using a flow probe that was placed around the renal artery of the right kidney. RBF decreased in shock. **B)** Inflow-slope (SL) of the time-intensity curves (TICs) at every time point. Before calculating the median, measurements were normalized to the baseline measurement of that pig. In contrast to the RBF, SL increased during shock.

Conclusions

In this study we showed the feasibility of CEUS to measure blood flow changes in the exposed renal cortex during hemorrhagic shock. Due to the induced hemorrhage, blood flow decreased and it was hypothesized that this would result in a slower contrast inflow in the renal cortex. However, a disparity was observed between the flow measured in the renal artery using a flow probe and the flow in the cortex derived from the inflow-slope of the TIC. One explanation for this disparity is that the flow probe measured the flow in a large artery, whereas the inflow-slope is measured in multiple smaller vessels and capillaries. Lindner et al. [4] showed in vivo that the velocity of microbubbles (Definity) in arterioles and venules is similar to that of red blood cells at the centerline of the vessel.

However, MBs are smaller than red blood cells and may therefore also enter vessels where no red blood cells can enter. In these vessels only plasma is flowing, of which the velocity may be different than that of red blood cells. Alternatively, our results may reflect aspects of the hemodynamics of the kidney in hemorrhagic shock. Further research should focus on unraveling the underlying the origin of the increase in SL.

Acknowledgements

The authors thank Kirby Lattwein and Dr. Hans Bosch from the Dept. of Biomedical Engineering, Maaikete Lintel Hekkert and Prof. Dirk-Jan Duncker from the Dept. of Experimental Cardiology, Michele Sorelli from the Dept. of Intensive Care Adults and the Laboratory of Experimental Anesthesiology, Erasmus MC for their help with the animal experiments.

This work is supported by an Innovation Grant of the Dutch Kidney Foundation (14 OI 11) and NanoNextNL, a micro and nanotechnology consortium of the Government of the Netherlands and 130 partners.

References

1. Daeichin, V, et al., in *IEEE Ultrasonics Symposium Proceedings, Chicago, Illinois, USA, 2014*.
2. Needles, A, et al., *Ultrasound Med Biol*, vol. 36, pp. 2097-106, 2010.
3. Gauthier, TP, et al., *J Ultrasound Med*, vol. 30, pp. 379-85, 2011.
4. Lindner, JR, et al., *J Am Soc Echocardiogr*, vol. 15, pp. 396-403, 2002.

Extracorporeal Acute Cardiac Pacing by a Multi Harmony High Intensity Focused Ultrasound: The Role of Cavitation, Insights from In-vivo Pacing and Modeling of a Left Ventricle Cardiomyocyte

Amit Livneh, Eitan Kimmel, Dan Adam

*Department of Biomedical Engineering, Technion-Israel Institute of Technology, Haifa, Israel
Corresponding author email address: amitl@bm.technion.ac.il*

Extracorporeal acute cardiac pacing by high intensity focused ultrasound (HIFU) could be a disruptive technology in the field of cardiology. This suggested modality may be clinically applied for reducing morbidity and mortality amongst heart failure patients by offering preoperative screening before cardiac resynchronization therapy (CRT) where currently no noninvasive optimization method is available and the current CRT nonresponse rate is 20-40%; As well as offering a method of emergency medicine cardiac pacing that may prevent a sudden cardiac arrest from becoming sudden death. Although ultrasonic cardiac stimulation was first applied in 1929, the mechanisms of ultrasonic cardiac pacing are yet unknown. Our work aims to unveil the mechanisms of HIFU cardiac pacing, using a combined experimental and modeling approach.

Recently, we published results demonstrating HIFU extra systole induction in whole anesthetized rats. Extrasystole induction was demonstrated temporally throughout the entire cardiac cycle beyond the absolute refractory period and spatially across the entire left ventricle. Passive Cavitation Detection (PCD) was applied in conjunction with US imaging on a gel phantom, and on rats. The gel phantom was sonicated with a HIFU pacing sequence, PCD positive cavitation indication was correlated with observed hyperechoic imaging. Similar PCD indications were recorded during in-vivo HIFU pacing, while hyperechoic imaging was not observed. Example PCD recordings results in vitro and in vivo are shown in panels A-E below. Analysis of these experimental results suggests membrane currents as the dominant cellular level mechanism and cavitation as the dominant ultrasound tissue interaction mechanism.

The hypothesis we test here through modeling and simulation is that HIFU induced intramembrane cavitation could induce Premature Action Potentials (PAPs) in a model of a cardiomyocyte by altering the membrane capacitance.

The Livshitz & Rudy guinea pig LV cardiomyocyte model and O'Hara et al. human LV cardiomyocyte model were adapted to include variable capacitance induced ionic currents and membrane voltage alterations. Numerical simulation in Matlab was applied to calculate the temporal membrane capacitance changes due to simulated HIFU insonation, and the resulting ion and membrane voltage dynamics. The simulated HIFU insonation reconstructed the minimal peak negative pressure that was observed to be required for HIFU pacing in rats.

Numerical simulation results demonstrated HIFU PAP induction throughout the entire diastole. Membrane depolarization was gradual, and the ion dynamics composition was similar to that of normal sinus rhythm. The temporal offset between insonation onset and the resulting PAP replicated the in-vivo observations. Moreover, PAP induction was demonstrated to occur also during insonation. Highlights of the simulation result are shown in panels F-H in the figure below.

The simulation results of a small animal model reproduced our in-vivo observations. This supports our hypothesis of the suggested dominant mechanisms. The simulation results of a human

cardiomyocyte model share similar characteristics and attributes to those of the small animal model, offering the prediction that HIFU pacing could be performed in humans with the same pacing patterns that were applied on whole anesthetized rats.

The presented results offer new insights to the study of HIFU pacing and predict that HIFU pacing may be performed in human subjects without membrane disruption.

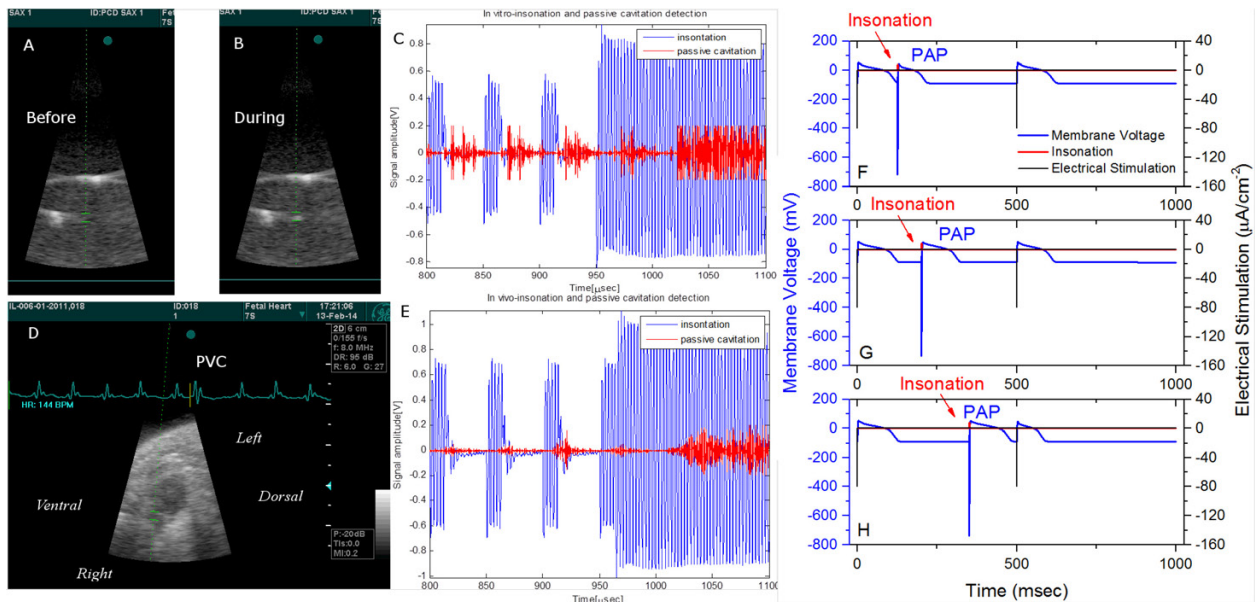


Figure 1 Result highlights. Gel phantom Passive Cavitation Detection (PCD) and US imaging: (A) the gel phantom before insonation, the HIFU focus is marked by the cursor a previous insonation lesion is seen to the left of the focus. (B) Immediately after insonation is triggered a hyperechoic region is imaged at the HIFU focus (C) a PCD trace that was recorded during the insonation shown in panel B, the blue trace shows the input voltage of the HIFU's 350 KHz amplifier channel, the red trace shows the PCD recorded signal, the positive PCD readouts are correlated with the input signal and the time of flight to the focus and back. (D) A short axis view of In vivo HIFU induced Premature Ventricular Contraction (PVC) as show on the imager ECG trace. (E) a PCD trace that was recorded during the insonation that produced the PVC shown in panel D, The color scheme is the same as in panel C, the PCD positive readouts are correlated similarly to the input signal and time of flight to the focus and back, yet lower intensity is recorded as would be expected due to a larger in-vivo attenuation in comparison to the attenuation in the gel phantom. **Simulated ultrasonic pacing in a small animal model:** Ultrasonic pacing at (F) 125ms (G) 200ms (H) 350ms, post an electrically paced action potential. Premature Action Potentials (PAPs) were paced throughout the entire diastole (evaluated by the temporal offset from the preceding AP peak of the membrane voltage trace). The applied acoustic pattern reconstructed the threshold pressure values at which extra-systoles were induced by extracorporeal HIFU pacing in anesthetized rats. The membrane potential is shown in blue. A baseline sinus rhythm was produced by electrical stimulation at 2Hz, the electrical stimulation is noted by the down facing black bars at 0 and 500ms. Ultrasonic pacing was applied at different times during the diastole, the ultrasonic pacing is noted by the upward facing red bars.

Microbubbles electrostatically adherent to tumor vasculature: positively charged bubbles provide tumor-specific contrast ultrasound imaging.

Alexander L. Klibanov, Zhongmin Du, Galina B. Diakova

Cardiovascular Division and Robert M. Berne Cardiovascular Research Center, University of Virginia School of Medicine, Charlottesville VA 22908, USA

Introduction

Targeted contrast ultrasound imaging of tumor vasculature is actively investigated; microbubble contrast agents targeted to endothelial biomarkers are successfully applied in animal models [1,2,3]. Targeted microbubbles (e.g., BR55, specific for VEGF Receptor 2) have already reached clinical trials.

At the same time, a universal method of targeting tumor vasculature independent of specific ligands may be desirable, for tumor tissue ultrasound imaging. We report the use of electrostatic interaction to achieve adherence of positively charged microbubbles to tumor vasculature and respective tumor delineation by contrast ultrasound imaging.

Methods and Materials

Microbubbles were prepared by sonication or by Vialmix amalgamation from C₄F₁₀ gas and stabilized with a lipid monolayer. Lipid composition was DSPC and PEG-stearate; it also included a positively charged lipid, distearoyl trimethylammoniumpropane (DSTAP)[4], which has been widely used for microbubble-ultrasound-assisted transfection; large doses of DSTAP-microbubbles have been injected in the experimental animals intravenously, without complications. Microbubble size was assessed by Coulter. Zeta potential was assessed with a Malvern Zetasizer. As an *in vivo* imaging model, murine colon adenocarcinoma tumor was used. MC38 cells (generously provided by Dr. J. Schlom, NIH) were inoculated in the hind leg of C57BL/6 mice, and a subcutaneous tumor was generated. Contrast ultrasound imaging was performed under isoflurane anesthesia (Acuson Sequoia c512, 15L8 probe, CPS mode, 7 MHz, 1 Hz, MI 0.2). Transducer was positioned to monitor the tumor and contralateral leg muscle; contrast signal was monitored for 30 min following an intravenous bolus of 2.10⁷ microbubbles. Images were analyzed with ImageJ.

Results

Mean bubble diameter was ~1.6-2 μm; 99.9% were <5 μm, to prevent blocking blood flow in capillaries. Following intravenous bolus, control microbubbles, lacking positive charge, cleared bloodstream within ~10 min; they did not accumulate in the tumor or in the normal muscle (contralateral leg). In the absence of the positively charged lipid component, microbubbles were electrostatically neutral; as positively charged lipid was added as a microbubble shell component, positive zeta potential on the particles was observed. For microbubbles containing DSTAP, contrast signal was persistent for over 30 min after injection. As we increased the fraction of positively charged lipid in the bubble shell, adherent contrast signal in the tumor increased, but accumulation of DSTAP-microbubbles in normal muscle also increased. For bubbles with most positive charge we tested, DSTAP:DSPC molar ratio 1:4, at 10 min the contrast signal difference between the tumor and

muscle was not significant ($p>0.3$). At 30 min tumor/muscle contrast signal ratio was just 2.1. For DSTAP:DSPC 1:13, tumor/muscle signal ratio exceeded 3 only at 30 min. DSTAP:DSPC ratio 1:22 was optimal for tumor targeting: at 10 min, tumor/muscle contrast ultrasound signal ratio was >7 ($p=0.00015$); at 20 min, >15 ($p=0.0034$); at 30 min, >16 ($p=0.00011$), sufficient for tumor delineation.

Conclusions

Positively charged microbubbles can selectively accumulate in the tumor vasculature. These microbubbles can provide target-to-muscle contrast ratio exceeding an order of magnitude. Therefore, positively charged microbubbles could become a universal ultrasound contrast agent for tumor imaging.

References:

1. Ellegala DB, Leong-Poi H, Carpenter JE, et al. Imaging tumor angiogenesis with contrast ultrasound and microbubbles targeted to $\alpha(v)\beta_3$. *Circulation*. 2003;108:336-341.
2. Anderson CR, Rychak JJ, Backer M, et al. scVEGF microbubble ultrasound contrast agents: a novel probe for ultrasound molecular imaging of tumor angiogenesis. *Invest Radiol*. 2010;45:579-585
3. Pochon S, Tardy I, Bussat P, Bettinger T, Brochot J, von Wronski M, Passantino L, Schneider M. BR55: a lipopeptide-based VEGFR2-targeted ultrasound contrast agent for molecular imaging of angiogenesis. *Invest Radiol*. 2010;45(2):89-95
4. Christiansen JP, French BA, Klibanov AL, et al. Targeted tissue transfection with ultrasound destruction of plasmid-bearing cationic microbubbles. *Ultrasound Med Biol*. 2003;29(12):1759-1767.

Partial support of this study is via NIH R21 EB016752.

Empirical and theoretical study of the interaction between plasmonic-nanoparticle coated microbubbles and nanosecond pulsed laser excitation.

Adam J. Dixon, Song Hu Ph.D., Alexander L. Klibanov Ph.D., John A. Hossack Ph.D.

Department of Biomedical Engineering, University of Virginia, Charlottesville, VA USA

Background, Motivation and Objective

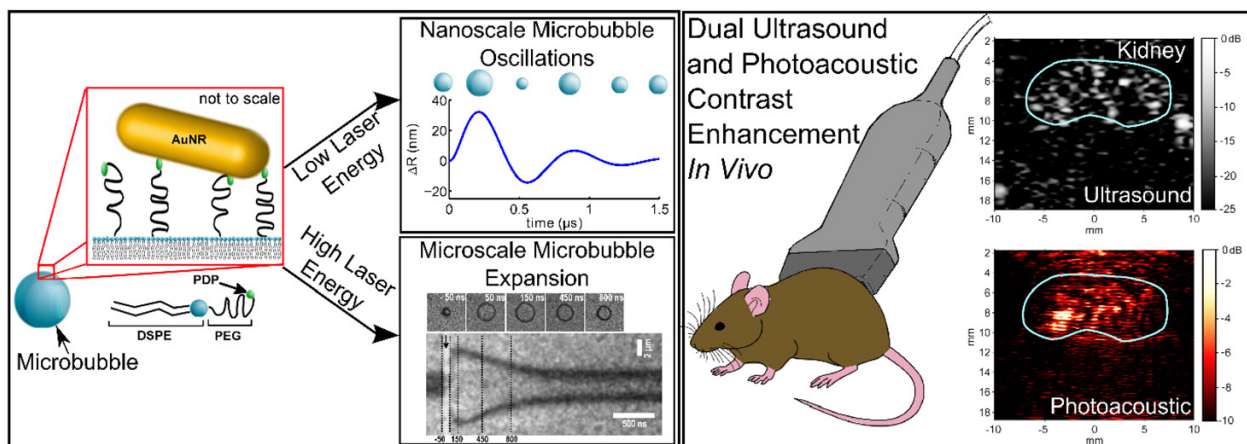
We present the design of a multimodality contrast agent for ultrasound and photoacoustic imaging consisting of microbubbles coated with optically absorbing gold nanorods (AuMBs). We hypothesized that attaching nanorods to the microbubble shell would drive thermal expansion of the microbubble's gaseous core and result in an amplified photoacoustic emission following excitation by nanosecond pulsed laser irradiation. Results of both in vivo and in vitro ultrasound/photoacoustic dual-modality imaging are presented.

Methods

Gold nanorods were attached to the microbubble shell using a gold-thiol bond. The behavior of single AuMBs following excitation by a single nanosecond-duration laser pulse was characterized by high-speed video microscopy, analysis of the photoacoustic emission, and finite element numerical modeling.

Results and Discussion

We identified two-distinct AuMB responses to pulsed laser excitation. At low laser fluence (below approximately 5 mJ/cm²), microbubble wall motion was not detectable via high speed microscopy and photoacoustic emissions were relatively weak. At higher laser fluences, microbubble diameters expanded by several hundred nanometers and photoacoustic emissions were over 10-fold greater than photoacoustic emissions from comparable concentrations of freely dispersed gold nanorods. Rapid microbubble expansion was hypothesized to result from water vapor formation at the gold nanorod-water interface. Thermal modeling of the gold nanorod/water/microbubble system confirmed that temperatures sufficient for water vaporization were reached at the nanorod surface (above 600 K). Finally, we demonstrated 9 dB photoacoustic contrast enhancement derived from the presence of AuMBs in the murine kidney.



Quantitative differences are present between the first and second injection of contrast agent in contrast-enhanced ultrasonography of feline kidneys.

E. Stock¹, K. Vanderperren¹, H. Haers¹, L. Duchateau², M. Hesta³, J.H. Saunders¹

¹*Department of Veterinary Medical Imaging and Small Animal Orthopedics, Faculty of Veterinary Medicine, Ghent University, Merelbeke, Belgium*

²*Department of Comparative Physiology and Biometrics, Faculty of Veterinary Medicine, Ghent University, Merelbeke, Belgium*

³*Department of Nutrition, Genetics and Ethology, Faculty of Veterinary Medicine, Ghent University, Merelbeke, Belgium*

Introduction

Repeated injections of contrast agent are most often required. The first injection sometimes used to optimize image settings. Multiple lesions may be present, urging for several injections of contrast agent to be able to study all lesions. In the assessment of diffuse renal disorders, both kidneys should be imaged. Additionally, patient motion during the study, may induce the need for multiple injections of contrast agent. Several authors already mentioned that tissue enhancement after the first injection of microbubbles is subjectively less bright in comparison with subsequent contrast agent injections (Haers et al. 2013; Pey et al. 2011; Salwei et al. 2008). A study on CEUS of liver and aorta in human subjects confirmed this finding quantitatively (Skrok, 2007). In contrast, no significant differences were found between the first and second injection of contrast agent in mice liver and tumor tissue (Rix et al. 2014). Thus far, it remains unclear if there are significant differences between the first and second injection of contrast agent. Nevertheless, it is of major importance to know if differences are present between both injections as this could influence study results.

Therefore, the purpose of this study was to compare several perfusion parameters between the first and second injection in the left feline kidney and spleen.

Materials and methods

The experiments were approved by the Local Ethical Committee of Ghent University (EC2014/38).

Contrast-enhanced ultrasound of the left kidney and spleen was performed in 7 healthy purpose-bred laboratory cats. All cats were anesthetized with propofol (Propovet®, Abbott Lab), 6 mg/kg intravenous, maintained with additional boluses of 1 mg/kg on effect.

A commercial contrast agent (Sonovue®, Bracco) was administered at 0,15 mL per bolus, immediately followed by a 1 mL saline bolus. The cats received 2 consecutive injections. In-between the injections, the microbubbles were destroyed by setting the acoustic power at the highest value and scanning the aorta, liver, and spleen for approximately 2 minutes.

A linear array transducer of 5-7.5 MHz on a dedicated ultrasound machine (MyLab 30 CV, Esaote), equipped with CnTI-contrast tuned imaging technology, was used. Machine settings were kept

constant between the injections (mechanical index 0.09, gain setting was adapted to a value just suppressing signals before arrival of contrast agent).

Quantitative analysis was performed using an off-line image analysis program (Image J). The curves were analyzed for blood flow parameters representing blood volume (baseline intensity (BI), peak intensity (PI), area-under-curve (AUC)) and blood velocity (arrival time (AT), time-to-peak (TTP), wash-in/out (W_{in}/W_{out})). Wash-out was not calculated for the spleen, as only the first part of the wash-out occurred within the time the clip was captured (120s). Baseline intensity was defined as the intensity measured the first 3 seconds after contrast agent injection. Arrival time set at the point where the curve reached a value at least 5 mean pixel intensity values higher than BI. Wash-in was calculated from data points between 10% higher than BI and 90% of PI; wash-out from points between 90% of PI and T=120s (end of the study). Peak intensity and AUC were corrected for the BI.

Results

Area-under-the-curve was significantly ($P < 0.05$) higher for the second injection compared to the first injection for both the renal cortex and medulla. The PI was also higher for the second injection; this was only significant for the renal cortex. A trend was present for the renal medulla ($P = 0.055$). Additionally, for the renal cortex, the W_{in} and W_{out} were less steep for the first injection compared to the second. No significant differences were present between the first and second injection for AT and TTP.

Similarly, the PI and AUC in the splenic parenchyma were significantly higher for the second injection compared to the first.

The BI was consistently comparable for the first and second injection.

Perfusion parameter	Renal cortex		Renal medulla		Spleen	
	1 st injection	2 nd injection	1 st injection	2 nd injection	1 st injection	2 nd injection
BI	2.50 ± 0.35	2.96 ± 0.35	1.72 ± 0.14	1.74 ± 0.14	2.70 ± 0.39	3.13 ± 0.39
PI	34.95 ± 4.58 ^a	51.13 ± 4.58 ^a	26.83 ± 3.97 ^b	39.91 ± 3.97 ^b	46.06 ± 4.70 ^a	59.60 ± 4.70 ^a
AT	7.51 ± 0.61	6.86 ± 0.61	20.59 ± 1.47	18.29 ± 1.47	7.22 ± 0.55	7.38 ± 0.55
TTP	41.75 ± 2.36	39.61 ± 2.36	43.61 ± 2.76 ^b	35.90 ± 2.76 ^b	61.03 ± 1.29	62.91 ± 1.19
W_{in}	1.17 ± 0.19 ^a	1.90 ± 0.19 ^a	1.58 ± 0.32 ^b	2.37 ± 0.32 ^b	1.74 ± 0.45	1.85 ± 0.45
W_{out}	-0.30 ± 0.04 ^a	-0.43 ± 0.04 ^a	-0.28 ± 0.04	-0.33 ± 0.04	-	-
AUC	2340.50 ± 492.91 ^a	3769.82 ± 492.91 ^a	1077.03 ± 322.53 ^a	1983.53 ± 322.53 ^a	3770.93 ± 477.01 ^a	5235.02 ± 477.01 ^a

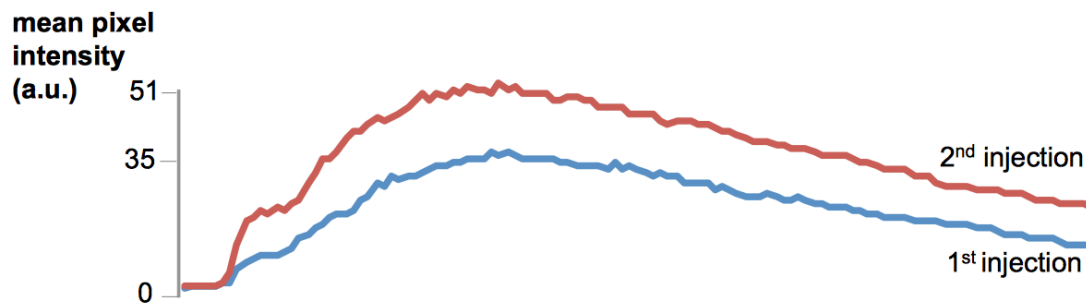
Table 1. Means and Standard Errors of perfusion parameters calculated from the renal cortex, renal medulla and splenic parenchyma in healthy cats, for the first and second injection of contrast agent.

^a value represents a significant ($P < 0.05$) effect

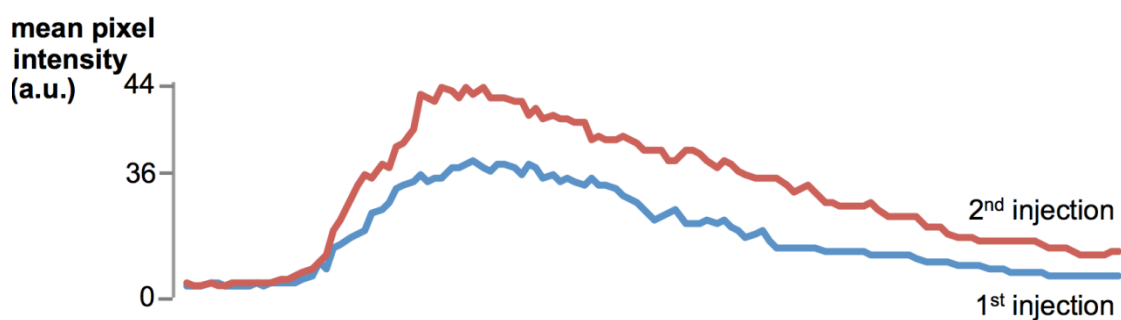
^b value represents a tendency ($0.10 > P > 0.05$)

(BI baseline intensity, PI peak intensity, AT arrival time, TTP time-to-peak, W_{in} wash-in, W_{out} wash-out, AUC area-under-curve)

A. Renal cortex



B. Renal medulla



C. Splenic parenchyma

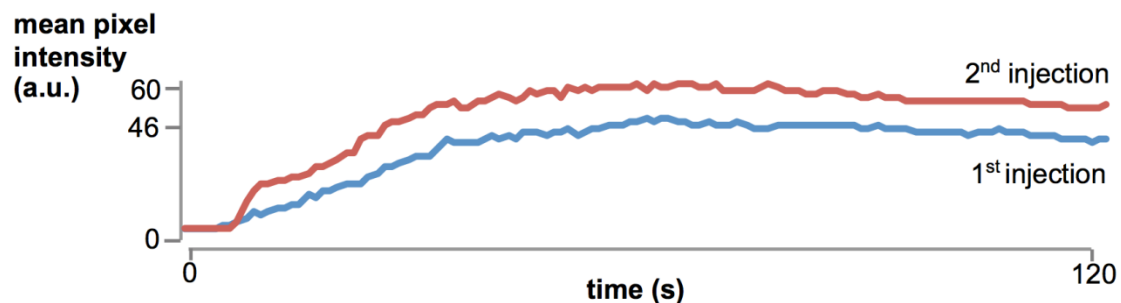


Figure 1. Mean time-intensity curves calculated from the renal cortex (A), renal medulla (B) and spleen (C) demonstrating the higher peak intensity, larger area-under-the-curve for the second injection of microbubbles.

Discussion

There are clear differences between the first and second injection. The most reproducible differences between the two injections are a higher PI and AUC for the second injection, seen in the renal cortex, renal medulla and splenic parenchyma. For the renal cortex, the wash-in and wash-out were also steeper.

This is an agreement with results obtained in a study on human liver (Skrok, 2007) and corresponds well with findings in mice, where a tendency towards a higher PI after consecutive microbubble

injections was noted in tumors. In the later study, the opposite effect, i.e. a decreasing PI after consecutive injections, was observed in the liver (Rix et al. 2014).

The reason for this increased enhancement after the second injection with microbubbles remains unclear. Multiple hypotheses rise. There were no significant differences in BI between the first and second injection, indicating that no residual microbubbles were remaining in tissue of interest. Nevertheless, it cannot be excluded that some contrast agent was still present in other organs and/or the circulation. Some residual microbubbles might also be present in the three-way stopcock or catheter.

In mice, an increased heart rate has been after the first injection, possibly causing the bolus to be more concentrated, resulting in a higher PI (Rix et al. 2014). Also in mice, short-term accumulation of microbubbles in the liver sinusoids and spleen might induce a higher PI in other tissues (Rix et al. 2014). Another explanation for the stronger enhancement after the second injection might be saturation of the lung macrophages by the microbubbles (Skrok, 2007). This would allow more microbubbles to pass the lung and finally reach the systemic circulation.

In conclusion, clear differences are present between the first and second injection of contrast agent. Generally, less bright enhancement is achieved by the first injection. It is of major importance to be aware of this when performing quantifications of consecutive injections. It is recommended to exclude the first injection for quantification regarding the less favorable enhancement.

REFERENCES

1. Granata A., Zanoli L., Insalaco M., Valentino M., Pavlica P., Di Nicolo P., Scuderi M., Fiorini F., Fatuzzo P., Bertolotto M. Contrast-enhanced ultrasound (CEUS) in nephrology: Has the time come for its widespread use? *Clin Exp Nephrol* 2014 (ePub ahead of print)
2. Haers H., Vignoli M., Paes G., Rossi F., Taeymans O., Daminet S., Saunders J.H. Contrast harmonic ultrasonographic appearance of focal space-occupying renal lesions. *Vet Radiol Ultrasound* 2010; 5: 516-522.
3. Haers H., Daminet S., Smets P.M.Y., Duchateau L., Aresu L., Saunders J.H. Use of quantitative contrast-enhanced ultrasonography to detect diffuse renal changes in Beagles with iatrogenic hypercortisolism. *Am J Vet Res* 2013; 74: 70-77.
4. Pey P., Vignoli M., Haers H., Duchateau L., Rossi F., Saunders J.H.. Contrast-enhanced ultrasonography of the normal canine adrenal gland. *Vet Radiol Ultrasound* 2011; 52: 560-567.
5. Piscaglia F, Bolondi L. The safety of SonoVue in abdominal applications: retrospective analysis of 23188 investigations. *Ultrasound Med Biol* 2006; 32: 1369-1375
6. Rix A., Palmowski M., Gremse F., Palmowski K., Lederle W., Kiessling F., Bzyl J.. Influence of repetitive contrast agent injections on functional and molecular ultrasound measurements. *Ultrasound in Med & Biol* 2014; 40: 2468-2475.
7. Salwei R.M., O'Brien R.T., Matheson J.S.. Characterization of lymph nodes in dogs using contrast harmonic and power Doppler ultrasound. *Vet Radiol Ultrasound* 2005; 46: 411-416.
8. Seiler, G.S., Brown, J.C., Reetz, J.A., Taeymans, O., Bucknoff, M., Rossi, F., Ohlerth, S., Alder, D., Rademacher, N., Drost, T., et al., 2013. Safety of contrast-enhanced ultrasonography in dogs and cats: 488 cases (2002–2011). *Journal of the American Veterinary Medical Association* 242, 1255–1259.
9. Skrok J. 2007. Markedly increased signal enhancement after the second injection of SonoVue compared to the first – a quantitative normal volunteer study. Conference proceedings 12th European symposium on Ultrasound Contrast Imaging, Rotterdam, the Netherlands.
10. Szebeni J., Muggia F., Gabizon A., Barenholz Y. Activation of complement by therapeutic liposomes and other lipid excipient-based therapeutic products: prediction and prevention. *Adv Drug Deliv Rev* 2011; 45: 573-578.
11. Weskott H.P.. Emerging roles for contrast-enhanced ultrasound. *Clin Hemorheol Microcirc* 2008; 40: 51-71.

Bio-physical insight into the mechanisms of ultrasound-stimulated microbubble sonoporation

Brandon Helfield¹, Xucai Chen¹, Simon C. Watkins², Flordeliza S. Villanueva¹

¹Center for Ultrasound Molecular Imaging and Therapeutics, University of Pittsburgh, PA, USA

²Department of Cell Biology, Center for Biologic Imaging, University of Pittsburgh, PA, USA

Background

Ultrasound-stimulated microbubbles are emerging as novel target-specific non-viral gene/drug delivery vectors for the treatment of cancer and vascular disease, *e.g.* to deliver VEGF plasmid DNA to promote arteriogenesis. The nature of the microbubble-target cell interactions that facilitate nucleic acid delivery across cell membranes, and hence strategies to optimize the efficiency of this platform, are poorly understood. The objective of this study was to gain mechanistic insight into microbubble-mediated increases in cell membrane permeability.

Methods

Individual phospholipid coated microbubbles were allowed to lay adjacent to cultured human umbilical vein endothelial cells (HUVEC) at 37C. Propidium iodide (PI) was diluted into the media (125 μ M) before US exposure to assess membrane permeability *i.e.* a sonoporation marker. Individual microbubble-cell pairs ($n=351$) were exposed to a single US pulse at 0.5, 1, or 2 MHz, with a duration of 4, 8 or 16 μ s and pressures between 0.1-0.8 MPa. Simultaneous ultrafast microscopy (~ 11 Mfps) via the UPMC-Cam and standard (15 fps) epi-fluorescence imaging were performed in order to directly correlate individual microbubble oscillations with sonoporation dynamics. A subset of microbubble-cell pairs was interrogated with 3D real-time confocal microscopy and the resulting pore features were visualized via a fluorescent cell membrane probe.

Results

The maximum absolute microbubble expansion and associated shear stress were strong threshold indicators of sonoporation. For an 8 μ s pulse, the oscillation (shear stress) threshold above which HUVECs porate was 3.9, 2.6, and 1.4 μ m (7.8, 14.5, 22.7 kPa) at 0.5, 1 and 2 MHz respectively. At a given US frequency, increases in pulse duration decreased the required excursion and shear stress. Real-time confocal microscopy highlights that microbubbles exposed to a single, 8 μ s pulse can generate large, heterogeneous pore patterns that may re-seal out-of-plane, as measured by PI cessation despite persistent evidence of cell perforation (Fig. 1a&b), and that such a sonoporation event does not affect cell viability.

Conclusions

Sonoporation is related to absolute microbubble expansion and its associated shear stress and can occur with various US parameters and microbubble sizes. Once sonoporation is achieved, membrane perforation areas are generated that may close via apical-to-basal membrane resealing. This data has implications on intelligent ultrasound-microbubble design for their use as payload delivery vehicles, as well as in the elucidation of biophysical sonoporation mechanisms.

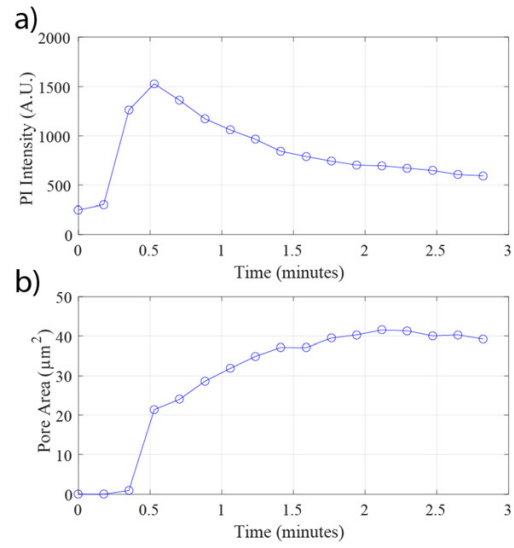


Figure 1: Ultrasound-stimulated microbubble sonoporation. An individual microbubble adjacent to a HUVEC was insonicated with a single, 1 MHz, 8 cycle pulse at 400 kPa. The quantification of (a) PI uptake within the cell and (b) membrane pore area highlight that intracellular delivery has ceased despite the consistent presence of membrane perforation.

In situ Activation of monomethylauristatin E (MMAE) using Ultrasound-Triggered Release of Composite Droplets

*Marine Bezagu*³, *Jonathan Clarhaut*^{4,5}, *Fabrice Monti*¹, *Patrick Tabeling*¹, *Janine Cossy*², *Sébastien Papot*⁴, *Olivier Couture*³, *Mickael Tanter*³, *Stellios Arseniyadis*².

¹MMN (ESPCI, CNRS, UPMC), Paris, France

²LCO (ESPCI, CNRS, UPMC), Paris, France

³Institut Langevin (ESPCI, CNRS, INSERM), Paris, France

⁴IC2MP (Université de Poitiers, CNRS), Poitiers, France

⁵CHU Poitiers, Poitiers, France

marine.bezagu@gmail.com

We previously established that composite droplets comprised of a nanoemulsion of water loaded with fluorescein and encapsulated in a perfluorohexane matrix (4 μm in diameter) could release their content by acoustic vaporization (Couture *et al. Medical Physics*, **2011** and **2012**). As two-third of the droplets is payload, large doses of active agents could thus be potentially delivered. However, like other conventional delivery strategies, the carriers also accumulate in healthy organs and tend to release their content in a non-specific manner. For this reason, we recently introduced the concept of chemistry *in-situ*, whereby an active agent would be created at the ultrasound focus by inducing a chemical reaction after the release of the droplets' content (Bezagu *et al. J. Am. Chem. Soc.*, **2014**).

Such targeted chemistry could be applied to the localized in-vivo activation of a drug that would be either too toxic or unstable to be directly injected. In this perspective, we studied the in vitro localized release of a monomethylauristatin E (MMAE) prodrug and its subsequent activation by a specific enzyme, the β -glucuronidase, leading to the localized production of the parent MMAE.

The demonstration was achieved by encapsulating a solution of MMAE-glu (MMAE's glucuronide prodrug) at 0.1 mM into composite droplets of perfluorohexane, and releasing their content in a 96-well plate containing adherent KB cancer cells. The β -glucuronidase, an endogenous enzyme specifically localized in the tumor extracellular microenvironment, was used in solution in the culture medium to activate the released prodrug. Four acoustic pulses of five cycles at 1.5 MHz were focused in each well using a single-element transducer. Cell proliferation was recorded after a 72 h incubation time using a XTT colorimetric assay.

In the presence of the β -glucuronidase enzyme, in the following 72 h upon the release of the droplets, cell proliferation was as low as $21\pm 2\%$ when compared to the non-treated cells. In comparison, cell proliferation was comparable ($91\pm 6\%$) to non-treated cells when MMAE-glu was released in the absence of the enzyme, thus confirming the specific production of the cytotoxic MMAE drug when both reactants are allowed to be in contact. Moreover, it is worth noting that a 80% gain of cytotoxicity is observed when applying the acoustic pulses compared to the sole effect of the leakage. In summary, we managed to 1) initiate the *in vitro* conversion of a MMAE prodrug to the active drug by locally releasing it in a medium containing the β -glucuronidase, and 2) induce a significant toxicity on KB cancer cells. We expect that such targeted chemistry will lead to a new approach to chemotherapy.

Graphene PVA Microbubbles: a New Hybrid Ultrasound–Photoacoustic Imaging Contrast Agent.

Yosra Toumia¹, Dmitry Grishenkov², Barbara Cerroni¹, Fabio Domenici^{1,3}, Silvia Orlanducci¹, Philippe Trochet⁴, and Gaio Paradossi¹

¹Dipartimento di Scienze e Tecnologie Chimiche, Università di Roma Tor Vergata, Rome, Italy, ²Karolinska Institutet, Stockholm, Sweden, ³Dipartimento di Fisica, Università di Roma Sapienza, P.^{1e} Aldo Moro, Rome, Italy, ⁴Fuji Film, Visual Sonics, Amsterdam, Netherland

Ultrasound Imaging (US) is one of the most widely used technologies in medicine. A recent extension of US imaging, i.e. the photoacoustic imaging (PAI), is emerging as a new diagnostic modality for small size animals combining enhanced resolution, real time analysis, and oxygen functional detection. In the perspective to enhance PAI diagnostic abilities and to translate this preclinical diagnostic approach into a clinical one, many particulate systems absorbing in the near infrared (NIR) spectral region, such as gold nanorods and fluorophores were developed in the recent years.^[1,2] NIR is the spectral region emitting pulsed laser used in PAI because of the low absorbance of water and tissues. Graphene, a 2D honeycomb carbon material with unique optical and mechanical properties, has been used in biomedical applications including imaging and theranostics.^[3] From visible to NIR spectral range, the pristine form of graphene exhibits a strong absorbance almost independent from the wavelength of the radiation. This feature makes graphene a more effective candidate with respect to other investigated systems. Herein, we present a new hybrid injectable contrast agent with high chemical versatility, for both US and PAI, based on poly(vinyl-alcohol) (PVA) air filled microbubbles (PVA MBs) as US efficient scatterer coupled with pristine mono- and few-layers graphene sheets with the aid of a surfactant^[4,5] with two functionalities: one stabilizing graphene in aqueous medium and the other bearing a moiety which allows the tethering to PVA MB shells. The system is able to capture NIR radiation activating the graphene sheets by thermoelastic expansion and transfer the collected energy to the PVA MBs, which resonate in the ultrasound region. These hybrid MBs were characterized by Raman spectroscopy and electron microscopy, and their cytotoxicity was evaluated by incubation with NIH 3T3 fibroblasts. To assess the potential of the hybrid Graphene-PVA MBs in PAI, they were tested *in vitro* and *in vivo*.

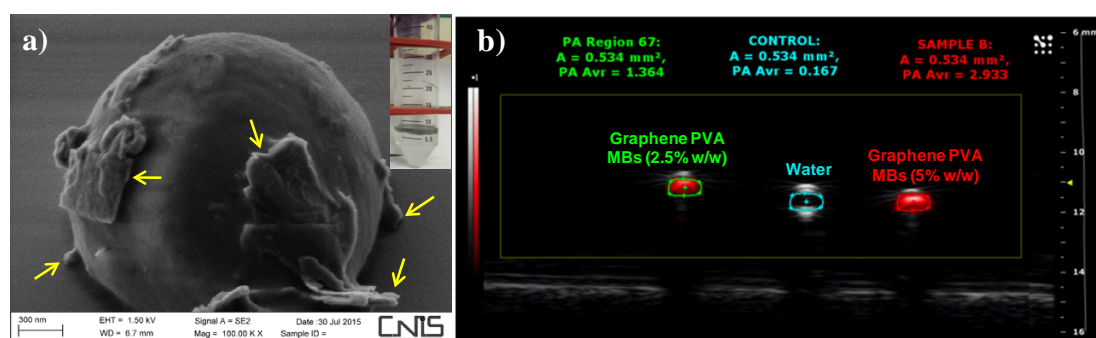


Figure 1. a) Field emission scanning electron microscopy of Graphene-PVA MBs, arrows indicate graphene flakes on the shell; inset: MBs aqueous dispersion. b) *in vitro* phantom PA enhancement of Graphene-PVA MBs at 2.5 % (w/w) and 5% (w/w)

References

1. Cheng, Y. S.; Frey, W.; Kim, S.; Kruizinga, P.; Homan, K.; Emilianov, S. *Nano. Lett.* **2011**, *11*, 348.
2. Krumholz, A.; Shcherbakova, D. M.; Xia, J.; Wang, L. V.; Verkhusha, V. V. *Sci. Rep.* **2014**, *4*, 3939.
3. Patel, M. A.; Yang, H.; Chiu, P. L.; et al. *ACS Nano* **2013**, *7*, 8147.
4. Toumia, Y.; Orlanducci, S.; Basoli, F.; Licoccia, S.; Paradossi, G. *J. Phys. Chem. B.* **2015**, *119*, 2051.
5. Cavalieri, F.; El Hamassi, A.; Chiessi, E.; Paradossi, G. *Langmuir* **2005**, *21*, 8758.

Acknowledgement

The research leading to these results has received funding from the European Union Seventh Framework Programme FP7/2007-2013 under grant agreement n. 602923 “TheraGlio”.

Quantification of cancer angiogenesis by modeling the binding kinetics of targeted ultrasound contrast agents

S. Turco¹, P. J. A. Frinking², H. Wijkstra^{1,3}, M. Mischì¹

¹Department of Electrical Engineering, Eindhoven University of Technology, the Netherlands

²Bracco Suisse S.A., Geneva, Switzerland

³Department of Urology, Academic Medical Center, University of Amsterdam, the Netherlands

Background

Tumor growth and development are supported by angiogenesis, i.e., the formation of a vascular network feeding the tumor and enabling metastatic spread [1]. Imaging of angiogenesis holds thus great potential for cancer detection and management. In dynamic contrast enhanced ultrasound (DCE-US), contrast agents consisting of microbubbles (MBs) able to travel throughout the whole circulation are used to probe angiogenic tumor vasculature. Analysis of time-intensity curves (TICs) obtained at each pixel and reflecting MB concentration enables the assessment of the vascular changes occurring during cancer angiogenesis by perfusion and dispersion quantification [2, 3]. In recent years, *in-vivo* assessment of angiogenesis at the molecular level has also become possible thanks to the introduction of novel targeted ultrasound contrast agents (tUCAs) [4]. These consist of microbubbles that have been decorated with targeted ligands able to bind specifically molecular expressions of angiogenesis, thus causing selective enhancement especially in the late phase several minutes after injection.

In this context, Bracco Suisse S.A. (Geneva, Switzerland) has recently developed the first clinically translatable tUCA, BR55, targeting the vascular endothelial growth factor receptor 2 (VEGFR2), which is over-expressed in angiogenic tumor vasculature in various organs (e.g., prostate, breast, ovaries, pancreas, colon, and rectum) [5]. Differentiation between free and bound MBs is essential to assess the degree of binding and thus to quantify angiogenesis. Conventionally, MB binding is assessed by looking at the late phase enhancement or at the differential targeted enhancement (dTE), i.e., the difference in acoustic intensity before and after a high-pressure pulse has been applied to destroy all the MBs in the acoustic field [6, 7]. However, these methods are not-quantitative, they require long acquisition times (10-30 min) and, in case of the dTE, the application of a destructive pulse raises concerns for damages to the endothelium [8].

To overcome these limitations, here we propose a novel method for quantitative assessment of angiogenesis by modeling the MB binding kinetics during the tUCA first-pass. The feasibility of the method is investigated in three prostate tumor-bearing rats injected with BR55. Quantitative estimation and short acquisition makes this method particularly attractive for antiangiogenic therapy monitoring, in which several repeated measurements are compared.

Methods

First-pass binding model

The total concentration of a tUCA in a pixel of tissue $C_t(t)$ can be described as the weighted sum of the concentrations of free MBs, $C_f(t)$, and bound microbubbles, $C_b(t)$, as

$$C_t(t) = v_f C_f(t) + v_b C_b(t), \quad (1)$$

where v_f and v_b are the fractional volumes of free and bound MBs, respectively.

By describing the kinetics of the free MBs with the modified local density random walk (mLDRW) model [9], and under the assumptions of high flow and of negligible unbinding in the first pass of the contrast bolus, the first-pass binding (FPB) model is obtained as

$$C_t(t) = \alpha \sqrt{\frac{\kappa}{2\pi}} \left[v_f (t-t_0)^{-1/2} e^{-\frac{\kappa(t-t_0-\mu)^2}{2(t-t_0)}} + K_{BI} \int_0^t (\tau-t_0)^{-1/2} e^{-\frac{\kappa(\tau-t_0-\mu)^2}{2(\tau-t_0)}} d\tau \right], \quad (2)$$

where α is multiplicative factor depending on the injected dose and the blood flow, μ is the mean transit time of free MBs, t_0 is the theoretical injection time, κ is the dispersion parameter; and K_{BI} is the first pass binding rate.

Data acquisition

Three Copenhagen rats were injected with G Dunning R-3327 tumor cells to establish prostate adenocarcinoma in one side of the prostate. All animal procedures were approved by the Cantonal Veterinary Office in Geneva.

Ultrasound molecular imaging was performed after injection of a 50- μ L bolus of BR55 contrast agent with a Sequoia scanner (Siemens Medical Solutions, Mountain View, CA) in Cadence Pulse Sequencing (CPS) mode [10], with a 15L8 linear array probe working at 7 MHz. The temporal resolution was 1s for the first 53s of acquisition, and 15s for the remaining 12 minutes of recording. Imaging was performed at mechanical index MI=0.25 until about 10 minutes, when a high-pressure destructive burst (MI=1.9) was applied. After the burst, imaging at low MI was resumed for about 3 minutes.

Data analysis

Parametric maps of the dispersion parameter κ and the first-pass binding rate K_{BI} were estimated by fitting each pixel TIC by the FPB model in (2). These were compared with the late-enhancement map, calculated as the gray-level (G.L.) value for $t=500$ s, and the dTE map, obtained as the difference between the average gray-level value before ($300 < t < 600$ s) and after ($660 < t < 750$ s) the application of the destructive burst.

Regions-of-interest (ROIs) marking benign and malignant tissue were obtained in each rat prostate. The ability of the estimated parameters of detecting cancer angiogenesis was investigated by testing the significance of the difference between the parameters' values in the ROIs with a paired Student t-test (level of significance $\alpha=0.05$).

Results

Figure 1 shows the estimated parametric maps of the dispersion parameter, κ , and the first-pass binding rate map, K_{BI} . These are compared with the dTE and late-enhancement maps. Table I reports the mean and standard deviation of the parameters' values in the benign and malignant ROIs, and the *p-value* of the paired Student t-test performed on the parameters' value difference between the ROIs.

Table I. Parameters' values in benign and malignant tissue

	Benign	Malignant	<i>p-value</i>
K_{BI} [min-1]	1.47±0.79	2.53±0.78	<<0.05
κ [s⁻¹]	1.31±0.92	2.10±1.30	<<0.05
dTE [G.L.]	12.60±11.08	56.52±16.62	<<0.05
Late-enhancement [G.L.]	41.07±14.53	83.83±19.52	<<0.05

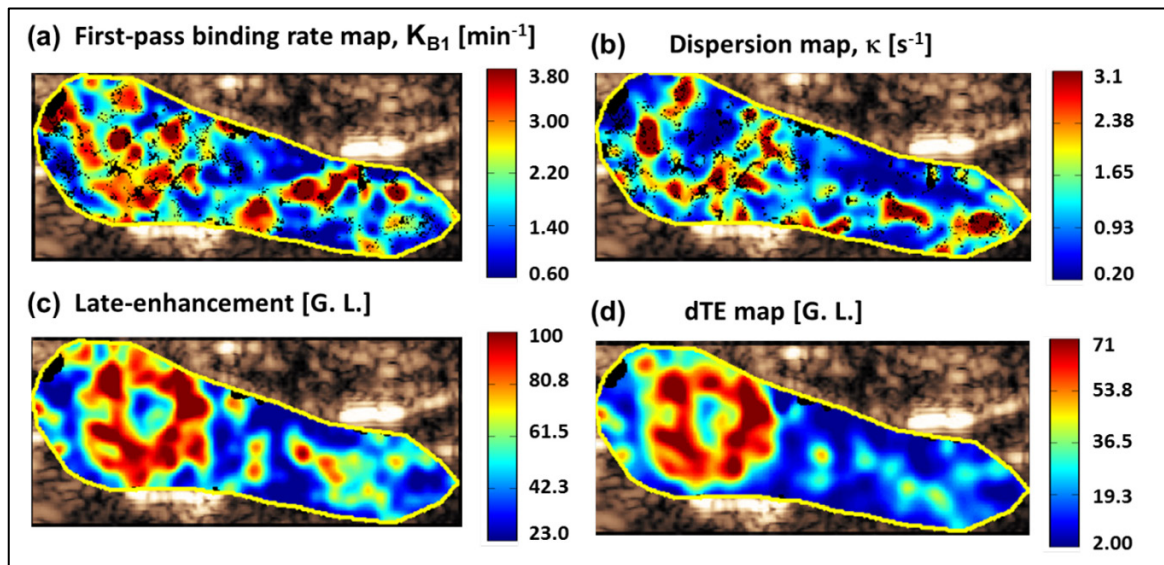


Fig. 1 Parametric maps of (a) first-pass binding rate K_{B1} , (b) dispersion κ , (c) late-enhancement, and (d) dTE.

Conclusions

In this work, a novel mathematical model describing the binding kinetics of the tUCA first pass was presented and tested on three prostate-tumor bearing rats injected with BR55. Parametric maps of the first-pass binding rate, K_{B1} , and the dispersion parameter, κ , showed agreement with the late-enhancement and dTE maps, and provided good discrimination between malignant and benign areas (p -value $\ll 0.05$), with shorter acquisition time (1 vs. ~ 10 min) and no need for a destructive pulse. In future work, further validation against immunohistological quantification of biomarker concentration will be performed to confirm the promising role of the proposed parameters for quantitative MB binding assessment in the context of cancer diagnostics and therapy monitoring.

1. P. Cameriet, "Angiogenesis in life, disease and medicine," *Nature*, vol. 438, pp. 932-936, 2005.
2. D. Cosgrove, "Angiogenesis imaging – ultrasound," *The British Journal of Radiology*, vol. 76, pp. S43-S49, 2003.
3. M. P. J. Kuenen, T. A. Saidov, H. Wijkstra, and M. Mischi, "Contrast-Ultrasound Dispersion Imaging for Prostate Cancer Localization by Improved Spatiotemporal Similarity Analysis," *Ultrasound in Medicine and Biology*, vol. 39, pp. 1631-1641, 2013.
4. F. Tranquart, M. Arditi, T. Bettinger, P. Frinking, J. M. Hyvelin, A. Nunn, et al., "Ultrasound contrast agents for ultrasound molecular imaging," *Z Gastroenterol*, vol. 52, pp. 1268-76, Nov 2014.
5. L. Abou-Elkacem, S. V. Bachawal, and J. K. Willmann, "Ultrasound molecular imaging: Moving toward clinical translation," *European journal of radiology*, 2015.
6. P. J. Frinking, I. Tardy, M. Théraulaz, M. Arditi, J. Powers, S. Pochon, et al., "Effects of acoustic radiation force on the binding efficiency of BR55, a VEGFR2-specific ultrasound contrast agent," *Ultrasound in medicine & biology*, vol. 38, pp. 1460-1469, 2012.
7. J. r. K. Willmann, R. Paulmurugan, K. Chen, O. Gheysens, M. Rodriguez-Porcel, A. M. Lutz, et al., "US Imaging of Tumor Angiogenesis with Microbubbles Targeted to Vascular Endothelial Growth Factor Receptor Type 2 in Mice 1," *Radiology*, vol. 246, pp. 508-518, 2008.
8. D. L. Miller, "Overview of experimental studies of biological effects of medical ultrasound caused by gas body activation and inertial cavitation," *Progress in Biophysics and Molecular Biology*, vol. 93, pp. 314-330, 1// 2007.
9. M. P. J. Kuenen, M. Mischi, and H. Wijkstra, "Contrast-Ultrasound Diffusion Imaging for Localization of Prostate Cancer," *IEEE T Med Imaging*, vol. 30, pp. 1493 - 1502, 2011.
10. P. Phillips and E. Gardner, "Contrast-agent detection and quantification," *European radiology*, vol. 14, pp. P4-P10, 2004.

Effect of viscosity and thrombus composition on sonoreperfusion efficacy in a model of microvascular obstruction

Xucaï Chen, John J. Black, Francois T. H. Yu, Rick G. Schnatz, Brandon Helfield, Flordeliza S. Villanueva, John J. Pacella

Center for Ultrasound Molecular Imaging and Therapeutics, University of Pittsburgh Medical Center, Pittsburgh, PA 15213, USA

Background

Distal embolization of microthrombi during stenting for myocardial infarction (MI) causes microvascular obstruction (MVO). We have previously shown that sonoreperfusion (SRP), a microbubble (MB)-mediated ultrasonic (US) therapy, resolves MVO from venous microthrombi *in vitro* in saline. However, blood is more viscous than saline and arterial thrombi that embolize during stenting are mechanically distinct from venous clot. Therefore, we tested the hypothesis that greater US energy is required for effective SRP during MVO created with arterial microthrombi with blood viscosity perfusate in an *in vitro* model of MVO. To gain mechanistic insight into the sonoreperfusion results, ultra-high speed microscopy of individual MB oscillations was performed.

Methods

Lipid MBs suspended in plasma with adjusted viscosity (1.1 or 4.0 cP) were passed through 4-mm tubing bearing a mesh with 40 μm pores at a rate of 1.5 ml/min to simulate a microvascular cross-section; upstream pressure reflected thrombus burden. To simulate MVO, the mesh was occluded with microthrombi to increase upstream pressure to 40 ± 5 mmHg. Therapeutic long-tone-burst US (1 MHz, 5 ms pulse duration, 0.33 Hz PRF) with peak negative acoustic pressures of 0.6 MPa, 1.0 MPa, and 1.5 MPa was delivered to the occluded area for 20 min. Upstream pressure was monitored continuously during US treatment to assess the efficacy of the SRP. The slope of the pressure vs time curve over the initial 3 min was defined as the lytic rate. Additionally, MB cavitation activity was recorded with a passive cavitation detector (PCD). A subset of individual MBs was placed in either the low or high viscosity medium ($n=111$ at 1cP, $n=109$ at 4 cP) and imaged under ultra-high frame rate microscopy (~ 10.8 Mfps) during insonification with a single, 8-cycle, 1 MHz pulse at acoustic pressures of 0.5 MPa, 1.0 MPa and 1.5 MPa. The percentage of fragmented MBs was determined for each acoustic pressure.

Results

MVO caused by arterial microthrombi at blood viscosity resulted in less upstream pressure drop with SRP therapy, compared to venous thrombi at plasma viscosity (Figure 1). Arterial microthrombi had lower lytic rate than venous microthrombi at both blood and plasma viscosity at each acoustic pressure tested, reaching statistical significance at $P=0.6$ MPa in both blood and plasma viscosity, and at $P=1.5$ MPa in blood viscosity. There was a trend toward reduced lytic rate with arterial microthrombi in both blood and plasma viscosity at 1.0 MPa, and in plasma viscosity at 1.5 MPa.

PCD showed a decrease in inertial cavitation when viscosity was increased at each acoustic pressure tested, demonstrating that increased viscosity dampens the cavitation of MBs in response to US. Ultra-high frame rate recordings corroborate these results, revealing a larger fragmentation threshold for MBs in 4 cP fluid medium as compared to 1 cP fluid. Specifically, at pressures of 0.5 MPa, 1.0 MPa and 1.5 MPa, all MBs in 1 cP fluid were shown to fragment over similar size ranges. In 4 cP fluid medium, there was a marked reduction in the percentage of MBs demonstrating fragmentation at each acoustic pressure compared to MBs in the low viscosity fluid medium (3.1%, 21.9% and 70.9% of MBs, for 0.5, 1.0 and 1.5 MPa, respectively, $p < 0.002$).

Conclusions

These data suggest that arterial thrombi require higher acoustic pressures than venous thrombi to achieve similar SRP efficacy, and that increased viscosity further increases US acoustic energy requirements by decreasing MB cavitation activity and MB fragmentation. These findings could help guide the selection of acoustic parameters for optimization of SRP.

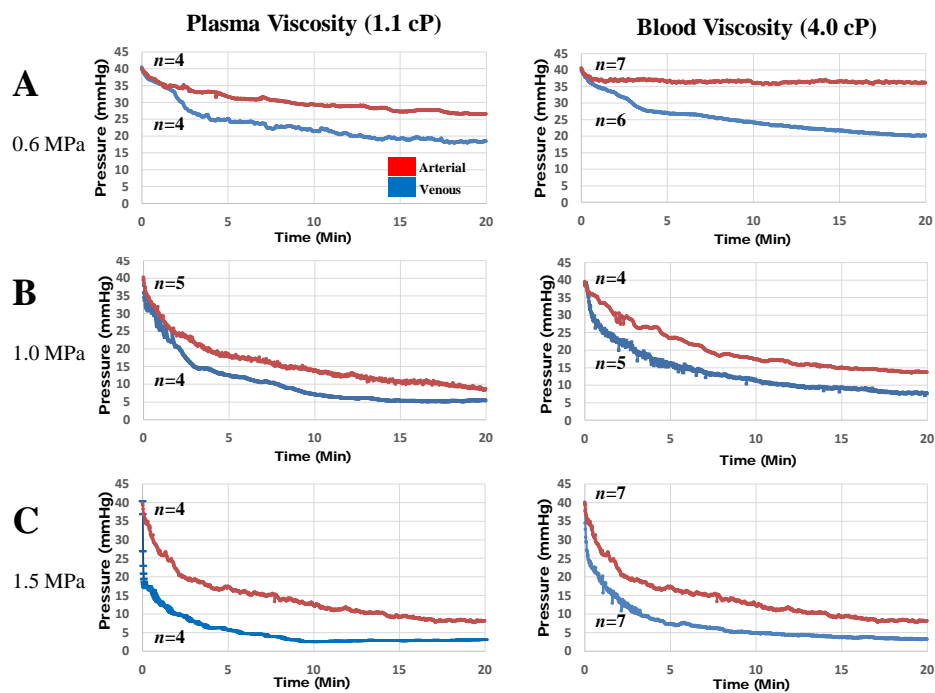


Figure 1. Pressure upstream of mesh occluded with either arterial (red) or venous thrombi (blue) at plasma viscosity (left column) or blood viscosity (right column) during SRP therapy (0.6, 1.0, 1.5 MPa acoustic pressure).

Ultrasound propagation through contrast agent suspensions

J-P. O'Brien¹, N.C. Ovenden¹, E. Stride²

¹*Department of Mathematics, University College London, Gower Street, London WC1E 6BT, U.K.*

²*Institute of Biomedical Engineering, Department of Engineering Science, Old Road Campus Research Building, University of Oxford, Oxford OX3 7DQ, U.K.*

Gas microbubbles stabilised by a surfactant or polymer coating have been in clinical use as contrast agents for ultrasound imaging now for several decades. They are widely used in echocardiography and, increasingly, for quantitative studies of tissue perfusion. It is the highly nonlinear response of microbubbles to ultrasound excitation that makes them such effective contrast agents. It is this property also, however, that leads to significantly nonlinear propagation through regions of tissue containing microbubbles and both to image artefacts and difficulties in obtaining accurate quantitative information.

There are very few theoretical models describing the response of a contrast agent population that take into account both the nonlinear behaviour and multiple bubble interactions. Most quantitative imaging algorithms rely on empirically derived correction factors and assume backscatter and attenuation respond linearly with concentration. One fully nonlinear numerical approach in use was originally proposed by Hamilton & Blackstock [1], and is based on a nonlinear wave equation derived by Commander & Prosperetti [2] which takes the form

Here, p is the pressure, c_0 and ρ_0 are the wave speed and density of the surrounding fluid respectively, $n(R_0) dR_0$ is the concentration of bubbles present with initial radii between R_0 and $R_0 + dR_0$ and the radii of such bubbles at time t is given by $R(t, R_0, \mathbf{x})$.

Computational complexity arises when the medium contains a polydisperse bubble population because, to close the model above, a RPNNP -type ordinary differential equation (ODE) governing the bubble response must be computed for the current radius of each bubble size R_0 present at each spatial location at every time step [1,2]. Sonovue, a commercial contrast agent, has a range of bubble sizes from less than $0.5 \mu\text{m}$ to $5 \mu\text{m}$ [3] and, at a ultrasound frequencies of clinical interest, these bubble types exhibit a variety of differing behaviours. This can mean that 30-40 ODEs need to be computed at every space and time step to determine the integral on the right hand side of the equation, which unfortunately makes the numerical model impractical for real-time clinical use.

In 2007, an approximation was proposed by Hibbs et al [4] whereby the ODE of only a single bubble type was computed at every space-time point, with the initial bubble size at each point in space being chosen randomly at the start of the computation, according to a probability distribution dependent on the concentration $n(R_0) dR_0$. Such an approximation reduces the computation of the nonlinear wave

equation significantly, but it also raises some questions about the validity of such an approximation and how accurate this simpler computation might be under different conditions.

In this talk, we present an analysis of the Hibbs approximation above in terms of the geophysical theories of layered media [5] and demonstrate that the accuracy of this approximation can vary greatly from very poor to acceptable depending on the grid spacing and how the bubble sizes are randomly chosen. Our analysis, in turn, indicates how a reasonable accurate approximation of this nature can be obtained and our modified approximation is tested by running an ensemble of 40 computations of the modified approximation, an ensemble of 40 computations of the original Hibbs approximation and then directly comparing them to the full computation of the wave equation (where all bubble sizes are computed at every space and every time step). Figure 1 shows the spread of the attenuation spectra from each ensemble for the original (v1) and for the modified (v3) approximations in the case of a Gaussian-enveloped incident pulse at two different incident frequencies propagating through a polydisperse bubble population. The spread is quite wide for the original approximation but is greatly improved with the approximation guided by the layer-theory analysis. Indeed the modified approximation appears able to capture the attenuation of the fundamental, second harmonic and subharmonic spectra within 4-5dB for 2MHz and to even greater accuracy for the higher incident frequency.

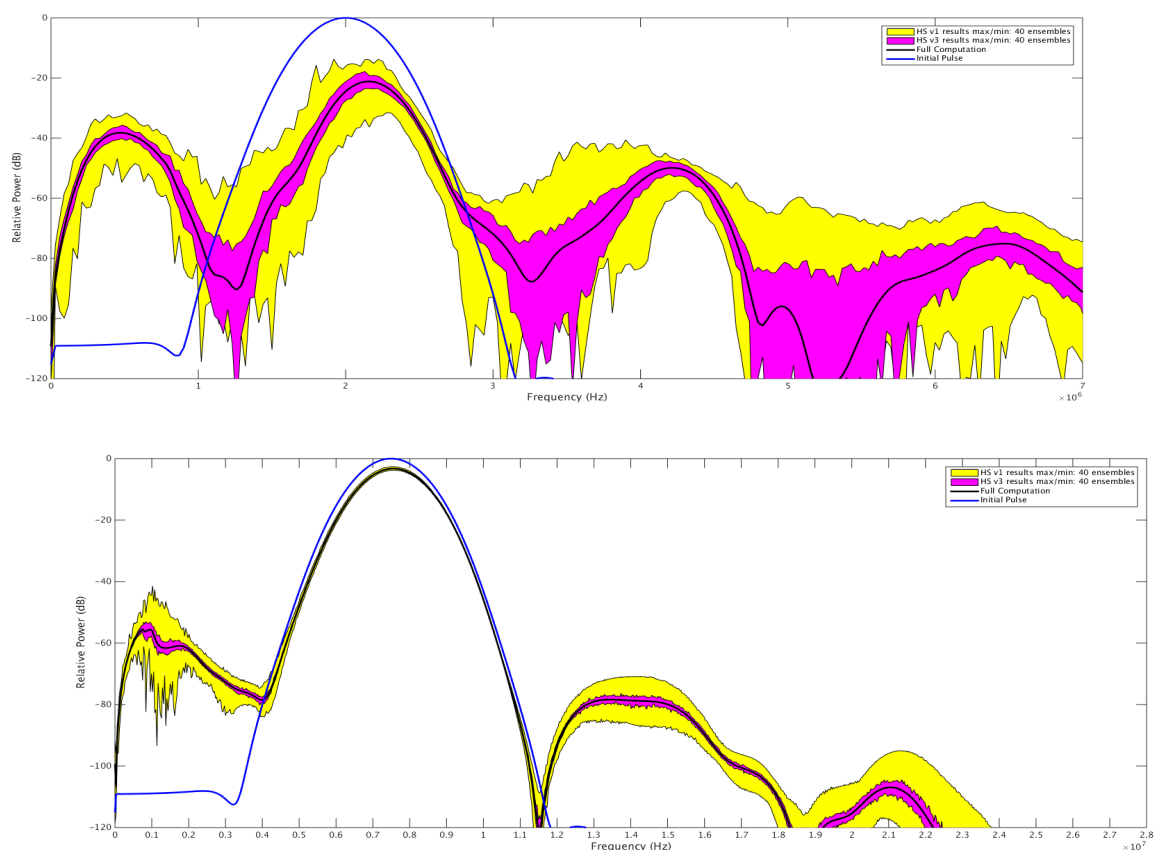


Figure 1: Attenuation spectra of propagation through a Sonovue at $1e11$ per m^3 concentration with an eight-cycle Gaussian enveloped incident pulse of peak negative pressure 200kPa at frequency 2MHz (top) and 7.5MHz (bottom). The blue line shows the initial pulse spectra, the black line the attenuated pulse spectra computed by the full computation at a distance of 2cm. The yellow shaded

area shows the maximum and minimum extent of 40 ensembles of the approximation originally proposed by Hibbs et al and the magenta shaded area shows 40 ensembles of the improved approximation based on a layered-theory analysis.

References

1. Commander, K. W., & Prosperetti, A. (1989). Linear pressure waves in bubbly liquids: Comparison between theory and experiments. *The Journal of the Acoustical Society of America*, 85(2), 732-746.
2. Hamilton M, Blackstock D. (1998). *Non-linear acoustics*, Academic Press. ISBN 0-12-321860-8
3. Gorce, J. M., Arditi, M., & Schneider, M. (2000). Influence of bubble size distribution on the echogenicity of ultrasound contrast agents: a study of Sonovue™. *Investigative radiology*, 35(11), 661-671.
4. Hibbs, K., Mari, J. M., Stride, E., Eckersley, R. J., Noble, A., & Tang, M. X. (2007). P4D-7 Nonlinear Propagation of Ultrasound Through Microbubble Clouds: A Novel Numerical Implementation. In *Ultrasonics Symposium, 2007. IEEE* (pp. 1997-2000). IEEE.
5. Griffiths, D. J., & Steinke, C. A. (2001). Waves in locally periodic media. *American Journal of Physics*, 69(2), 137-154.

A Contrast Enhanced Ultrasound imaging system with diverging waves for cardiac imaging – initial evaluation on a beating phantom

M Toulemonde, V Papadopoulou, MX Tang

*Department of Bioengineering, Imperial College London, Exhibition Road, London, SW7 2AZ, UK
mengxing.tang@imperial.ac.uk*

Introduction

There is currently significant interest in cardiac imaging with ultrasound (US) and new ultrafast techniques for increased frame rate using diverging transmission (Papadacci et al., 2014) (Moore et al., 2015). However there has been to date no specific investigation reported, as far as we are aware, for Contrast Enhanced Ultrasound (CEUS) cardiac imaging using ultrafast ultrasound and diverging waves. Ultrafast imaging may improve perfusion imaging. The perfusion imaging of organs with Ultrasound Contrast Agents (UCAs) has been applied to various clinical applications. In the case of cardiac imaging, disruption replenishment is obtained by transmitting a burst of high-intensity to destroy UCAs, then measuring the replenishment of the UCAs in that region as a function of time. Several models have been proposed to quantify the disruption replenishment (Hudson, Karshafian and Burns, 2009).

The aim of this study is to develop an ultrafast diverging wave imaging system using a cardiac probe and pulse inversion, and demonstrate its feasibility for heart perfusion applications. In the first instance the imaging is demonstrated on a simple test phantom in the laboratory. This simple, cheap and fast “DIY” set-up for testing cardiac CEUS imaging before going in-vivo also allows controlled repeatable experiments and testing beamforming strategies, motion correction, etc.

Methods

Ultrafast diverging transmission

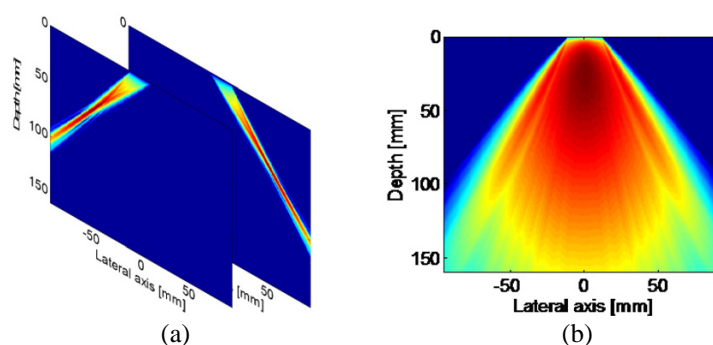


Figure 1: Log compressed pressure field with a 20 dB dynamic simulated by the Verasonics Platform for (a) focalization and (b) diverging transmissions. For the focalization imaging, several transmissions are required to obtain an image whereas for the diverging imaging, one transmission is enough.

For linear arrays, plane wave transmission has been developed in order to reach thousands of frames per second. Plane wave compounding was proposed to improve image quality (Montaldo et al., 2009), which consist of transmitting steered plane waves which cover a sector angle. After post processing, the radio frequency images from the different transmissions are averaged thereby improving contrast, signal-to-noise ratio and resolution.

For cardiac application, diverging transmissions have been proposed by several groups using different approaches (Hasegawa and Kanai, 2011) (Papadacci et al., 2014) (Tong et al., 2012). A virtual point source is created behind the probe creating a diverging beam which enlarge the region illuminated. Moreover, as for plane wave imaging, several diverging waves are successively transmitted in order to improve the image quality. However the acoustic pressure decreases more with propagation distance than for plane wave.

The classic focalization and diverging transmissions for cardiac applications are shown in Figure 1. Compared to the focalization transmission, the acoustic pressure of diverging imaging cover a larger region of interest. However its pressure is lower. For CEUS imaging, diverging imaging should be less sensible to movement than the focalization approach due to the higher frame rate.

Perfusion

In order to evaluate the diverging transmission for disruption replenishment of the myocardium, a real time disruption transmission was developed for the Verasonics Platform. The mechanical index (MI) is determined using a Precision Acoustic 0.2mm needle hydrophone and an oscilloscope. A focused long burst in the central frequency of the P4-1 phased array probe was used for bubble disruption. This transmission is compared to a short diverging pulse which is used during imaging of the replenishment. The transmission parameters are given in Table 1 and the received pulses are shown in Figure 2. The MI for both signals is 0.04 and 0.58 in water for the diverging and focalization transmission, respectively.

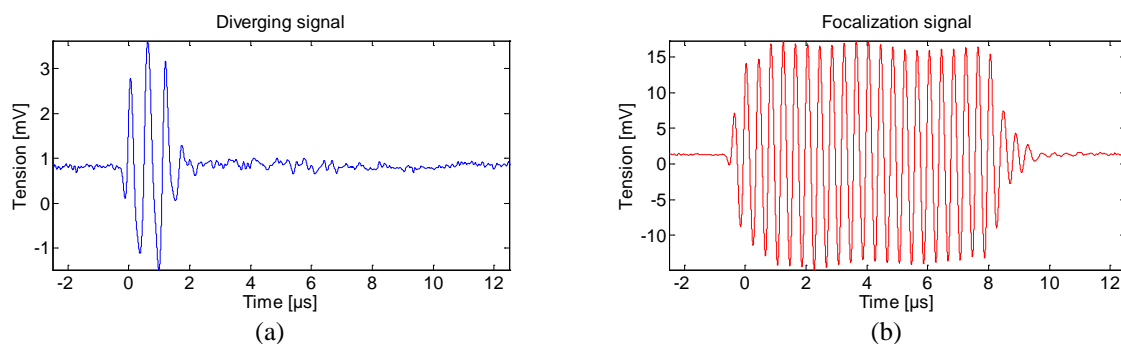


Figure 2: Signals received at 80 mm for (a) diverging and (b) focalization transmission. The diverging transmission was a 1-cycle (Verasonics definition) 1.5 Mhz sinusoidal signal and the focalization transmission is a 21-cycle 2.5 MHz sinusoidal signal.

Beating phantom set-up and Tissue Mimicking Material (TMM) preparation

A Tissue Mimicking Material (TMM) solution with 0.3% agar concentration was prepared by modifying a liquid phantom recipe (Madsen, Frank and Dong, 1998) in order to get a flexible phantom.

The beating phantom is formed using two balloons on top of each other held around a lid with a water entry and exit point connected to the pumping system shown in Figure 3.a. The region between the two balloons is filled with TMM. The inside of the inner balloon, which is pre-filled from the syringe in Figure 3.b, is the section that is part of the water circulation loop with a piston pump and thus allows the beating movement, Figure 3.c. The tap is also used in order to inject UCAs.

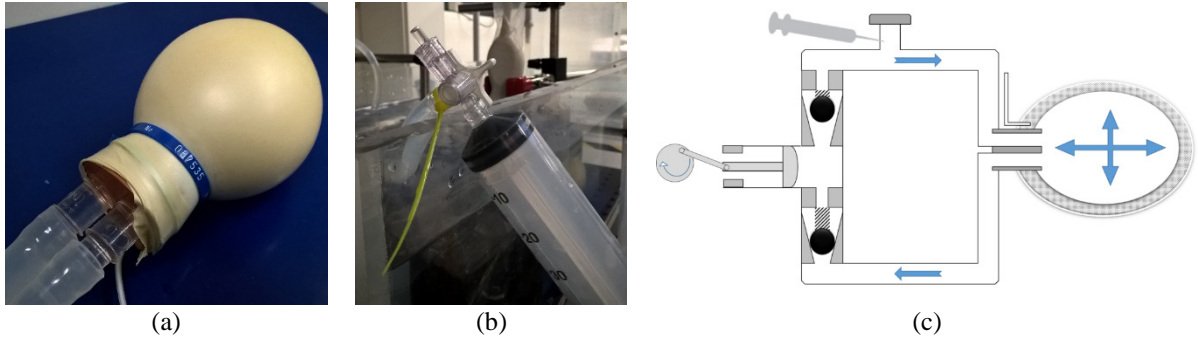


Figure 3: Beating phantom composed of (a) two balloons with tissue mimicking material between balloons, (b) tap in order to pre-fill balloon and introduce UCAs and (c) experimental set-up schematic showing the piston pump driven closed flow system that expands and contracts the beating phantom. The tube between the two balloons allows to add TMM.

Experiments

The ultrafast PI diverging perfusion was evaluated using the beating phantom described in Figure 3.c. PI consists of a successive positive and negative pulse transmission for each steered angle. In reception or during the beam forming, the backscattering echoes of the two transmissions for the same angle are averaged in order to filter the harmonic signal. The pump piston used during experiments is a Harvard Apparatus pulsatile blood pump for rabbits allowing heartbeat rates of 60-180bpm. A concentration of 0.4 ml/L of Sonovue UCAs was injected through the syringe, Figure 3.b. The acquisitions were performed using the Verasonics research Platform and a P4-1 phased probe. The transmission parameters are given in Table 1 and the Figure 4 shows the perfusion of the beating phantom at different time as well as the replenishment time-intensity curve. The frame rate chosen is 3 times higher than the harmonic imaging with standard echographic scanner. Moreover, using this frame rate and saving 500 frames, it is possible to have 4 full beats.

	Number of angles	Focus	Angle range	Frequency	Cycles	Frames	Frame rate
Diverging (pre-Flash)	11 ($x2$ PI)	80 mm	30°	1.5 MHz	1	4	107.7 Hz
Focalization	128		40°	2.5 MHz	21	2	18.5 Hz
Diverging (post-Flash)	11 ($x2$ PI)		30°	1.5 MHz	1	500	107.7 Hz

Table 1: Transmission parameters for the diverging pre-Flash, the microbubble destruction with focalization and the diverging post-flash.

Results

In the Figure 4.a, using PI diverging transmissions with a MI of 0.04 shows that before the destruction there are UCAs inside the balloon and some free gas in the surrounding water. Figure 4.b is the first frame of the UCA destruction. The focused long burst with a MI of 0.58 has created bright signals from the UCAs in the balloon and also the free gas bubbles in the surrounding water during the disruption. In the first frame after the UCAs destruction, Figure 4.c, there are no UCAs left in the balloon and most of the free gas in the water has also been destroyed. After a few seconds, the balloon again fills with UCAs as demonstrated by Figure 4.d.

The replenishment time-intensity curve in Fig. 4.e has a similar shape as perfusion usually obtained for the myocardium. It was fitted with the Hudson reperfusion model (Hudson, Karshafian and Burns, 2009). Moreover, starting at 2.5s post UCA-destruction it is possible to see clearly the beating pattern in backscatter intensity induced by the pump as shown in Fig. 5. This periodic variation in intensity is also present in real myocardia (heart beating) (Averkiou et al., 2003).

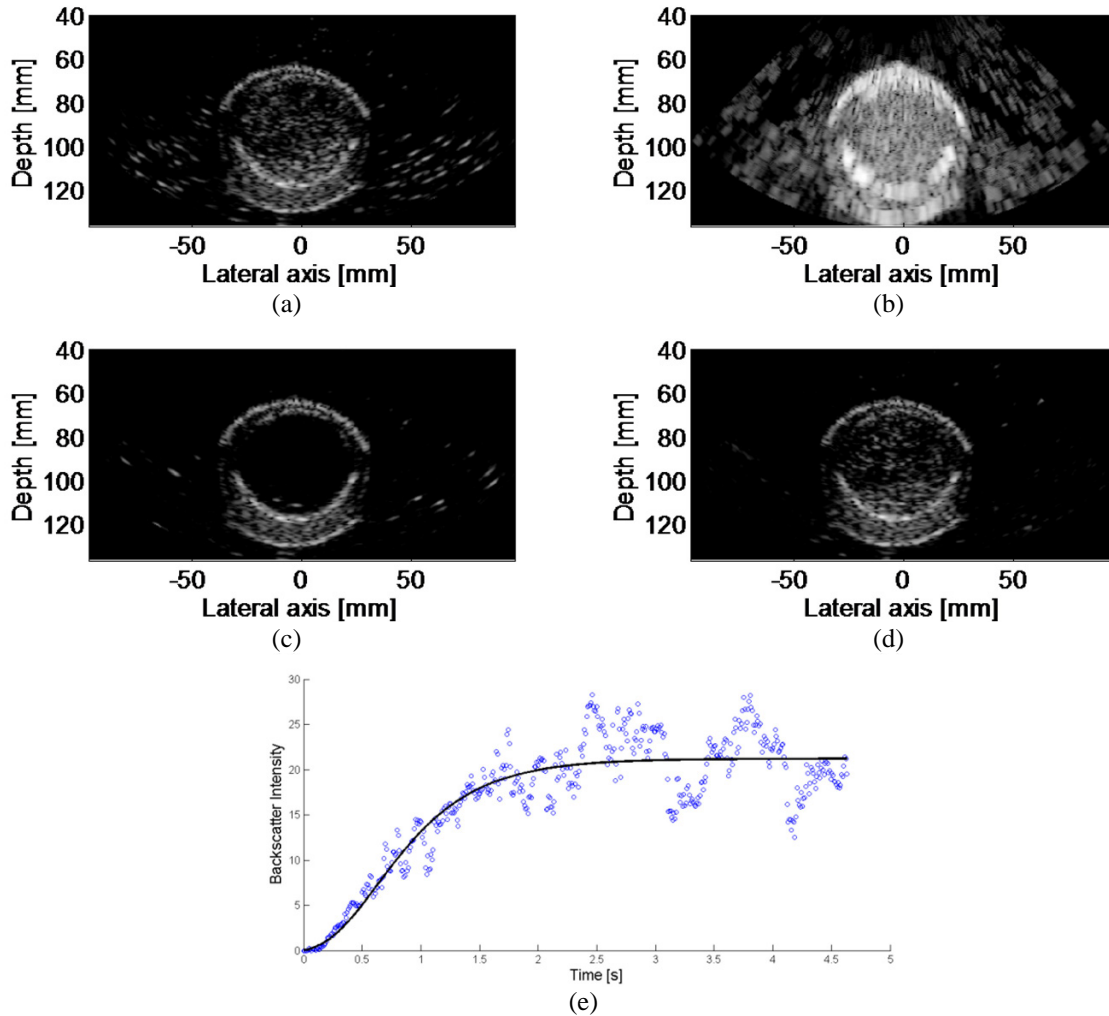


Figure 4: Perfusion image and graphic analysis. (a) PI diverging image before the disruption, (b) focalization image of the disruption (Time = 0), (c) 1st PI diverging image of the replenishment (Time = 0.0093s), (d) 300th PI diverging image of the replenishment (Time = 2.7855s) and (e) replenishment time-intensity curves in the beating phantom.

Discussion/Conclusion

This paper reports the development of a CEUS system for imaging perfusion using diverging transmissions and pulse inversion and initial evaluation on a simple beating phantom in the laboratory. It shows the possibility to use the Verasonics Platform to transmit a long burst signal with a high MI in order to destroy UCAs and then to transmit PI diverging waves for perfusion analysis. The replenishment time-intensity curves obtained has a similar profile as myocardial perfusion.

Another way to improve the perfusion precision is the frame rate. It may be possible to improve the frame rate by reducing the number of transmitted angles (11 here) at the cost of reduces the image quality. An optimisation of the angle transmission and motion correction for misalignment between PI transmissions may allow a higher frame rate with a good image quality, a first investigation of which is shown by Figure 5.

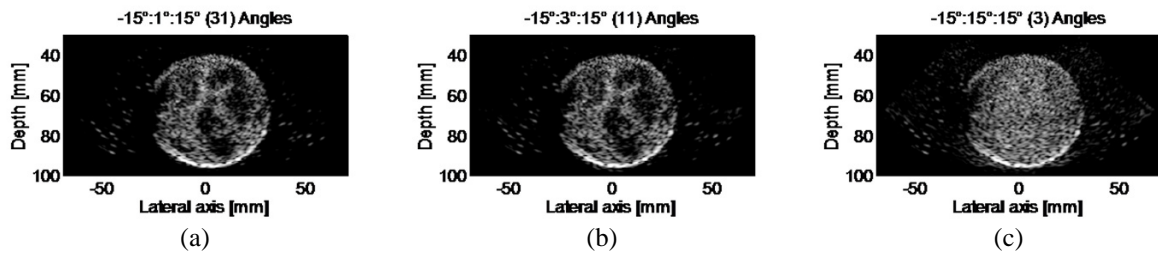


Figure 5: PI diverging images of beating phantom using (a) 31, (b) 11 and (c) 3 angles during beamforming.

PI diverging transmission has been evaluated in experiments using the same beating phantom. 31 steered angles have been transmitted with an angle range of 30° (-15° to 15° each 1°). During beam forming, different angle compounding have been used in order to evaluate their impact on the image quality. Comparing 31 with 11 angles, Figure 5.(a-b), the images look similar with a frame rate improvement of 3 folds for 11 angles. However, using 3 angles, it is difficult to differentiate the microbubbles. This first investigation shows the importance of the choice of angle transmissions with respect to the heart application, high frame rate or image quality objective, although further optimisation should be conducted a more realistic heart phantom or in vivo.

Acknowledgements

The authors would like to acknowledge the help of Prof. Kim Parker in the development of the beating phantom, as well as Dr Robert Eckersley and Prof. David Cosgrove for useful discussions on this work.

References

1. Averkiou, M., Powers, J., Skyba, D., Bruce, M. and Jensen, S. (2003) 'Ultrasound contrast imaging research.', *Ultrasound Q*, vol. 19, no. 1, Mar, pp. 27-37.
2. Hasegawa, H. and Kanai, H. (2011) 'High-frame-rate echocardiography using diverging transmit beams and parallel receive beamforming', *Journal of Medical Ultrasonics*, vol. 38, no. 3, pp. 129-140, Available: <http://dx.doi.org/10.1007/s10396-011-0304-0>.
3. Hudson, J.M., Karshafian, R. and Burns, P.N. (2009) 'Quantification of Flow Using Ultrasound and Microbubbles: A Disruption Replenishment Model Based on Physical Principles', *Ultrasound in Medicine & Biology*, vol. 35, no. 12, pp. 2007-2020, Available: <http://www.sciencedirect.com/science/article/pii/S0301562909013970>.
4. Madsen, E.L., Frank, G.R. and Dong, F. (1998) 'Liquid or Solid Ultrasonically Tissue-Mimicking Materials with Very Low Scatter', *Ultrasound in Medicine & Biology*, vol. 24, no. 4, pp. 535-542, Available: <http://www.sciencedirect.com/science/article/pii/S0301562998000131>.
5. Montaldo, G., Tanter, M., Bercoff, J., Benech, N. and Fink, M. (2009) 'Coherent plane-wave compounding for very high frame rate ultrasonography and transient elastography', *Ultrasonics, Ferroelectrics and Frequency Control, IEEE Transactions on*, vol. 56, no. 3, pp. 489-506, Available: ISSN: 0885-3010 DOI: 10.1109/TUFFC.2009.1067.
6. Moore, C., Castellucci, J., Andersen, M.V., Lefevre, M., Arges, K., Kisslo, J. and von Ramm, O.T. (2015) 'Live high-frame-rate echocardiography', *Ultrasonics, Ferroelectrics, and Frequency Control, IEEE Transactions on*, vol. 62, no. 10, October, pp. 1779-1787, Available: ISSN: 0885-3010 DOI: 10.1109/TUFFC.2015.007203.
7. Papadacci, C., Pernot, M., Couade, M., Fink, M. and Tanter, M. (2014) 'High-contrast ultrafast imaging of the heart', *Ultrasonics, Ferroelectrics, and Frequency Control, IEEE Transactions on*, vol. 61, no. 2, February, pp. 288-301, Available: ISSN: 0885-3010 DOI: 10.1109/TUFFC.2014.6722614.
8. Tong, L., Gao, H., Choi, H.F. and D'hooge, J. (2012) 'Comparison of conventional parallel beamforming with plane wave and diverging wave imaging for cardiac applications: a simulation study', *Ultrasonics, Ferroelectrics, and Frequency Control, IEEE Transactions on*, vol. 59, no. 8, August, pp. 1654-1663, Available: ISSN: 0885-3010 DOI: 10.1109/TUFFC.2012.2371.

Acoustic quantification of microbubble populations in a branched microvasculature phantom

*Shengtao Lin, Claudia Feldman, Samira Jamalain, Yesna Yildiz, Virginie Papadopoulou, Martin Ward, Robert Eckersley, James Moore, Meng-Xing Tang**

mengxing.tang@imperial.ac.uk

Background, Motivation and Objective

The behaviour of microbubbles is affected by wall proximity or confinement in vessels, although there is a lack of in-depth understanding of this effect and its implications in contrast-enhanced ultrasound perfusion imaging and microbubble-mediated therapy. Existing number of mathematical models look at microbubble behaviour near a wall or in the presence of geometrical confinement [1,2]. Experimentally, measurements have also been made in vessels of different sizes on individual microbubbles. However the existing measurements which are optical for the most part suffer from the difficulty of finding microvessels of different sizes made of the same material [3,4]. Furthermore, the response of microbubble populations in these vessels has not been extensively studied. We report the acoustic quantification of the response of microbubble populations in microvessels of different sizes (50 μ m, 100 μ m, 200 μ m) in a custom designed branched PDMS microvascular phantom.

Statement of Contribution/Methods

Figure 1 shows the branching structure of the polydimethylsiloxane (PDMS) microvasculature phantom. PDMS was chosen because its elastic modulus can be controlled through its composition to reflect that of soft tissue. All the vessel branches have the same height of 50 microns but different widths. The biggest branch is 400 μ m in width and branches out into two 200 μ m ones, each connected to two 100 μ m vessels that each lead into two final 50 μ m branches. A microbubble solution with a physiologically relevant flow rate filled the phantom and the acoustic response was collected using pulse-inversion imaging with a phased array probe with a central frequency of 2MHz and a mechanical index of 0.15. The scattered amplitude of microbubble was calculated based on the averaged pixel intensity from the chosen region of interest divided by the known number of microbubble (concentration \times volume) in the same region to obtain a scattering per microbubble measure.

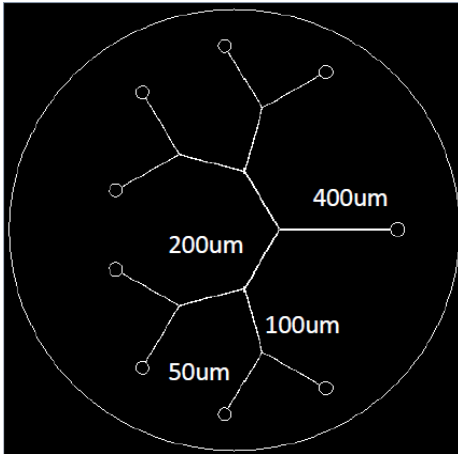


Figure 1. Schematic representation of the branched PDMS microvasculature tissue mimicking phantom (not to scale).

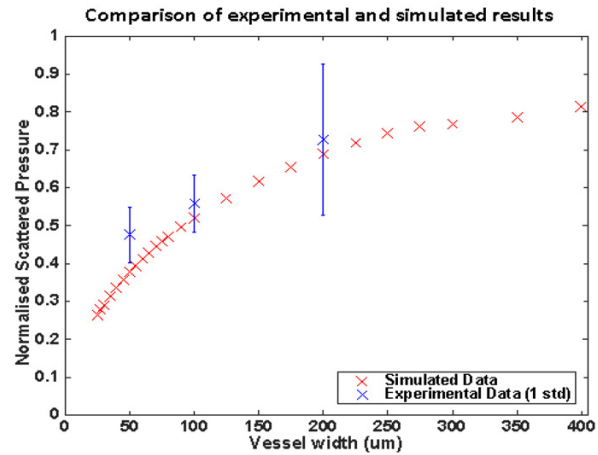


Figure 2. Normalised scattered amplitude of microbubbles in different size vessels. Blue: experimental data; red: simulated data.

Results/Discussion

The scattered amplitude of microbubbles in 50 μm , 100 μm and 200 μm vessels were normalised to that measured on free microbubbles (in a beaker without geometry confinement) and were plotted as a function vessel size (Figure 2.blue). The scattered pressure response from microbubbles increased as the microvasculature size increases. This positive increasing trend shows a good agreement with an independent simulation result (Figure 2.red) using mathematical modelling [5] with the same geometry as the microvasculature phantom and weighting average response from different size of microbubbles (same size distribution as experiment). The results show about a 40% decrease in average bubble population scattering amplitude when the vessel size decreases from 200 microns to 50 microns. It should be noted that this decrease could be underestimated as only one dimension of the vessel size was varied in this study.

In conclusion, a custom designed microvascular phantom has been developed and acoustic quantification of microbubble populations has shown a significant reduction of averaged microbubble population scattering as the vessel size decreases.

1. Doinikov AA, Bouakaz A. Interaction of an ultrasound-activated contrast microbubble with a wall at arbitrary separation distances. *Physics in Medicine and Biology* 60.20 (2015): 7909.
2. Qin S, Ferrara KW. Acoustic response of compliant microvessels containing ultrasound contrast agents. *Physics in medicine and biology* 51.20 (2006): 5065.
3. Thomas DH, Sboros V, Emmer M, Vos H, De Jong N. Microbubble oscillations in capillary tubes. 2013 UFFC IEEE
4. Caskey CF, Kruse DE, Dayton PA, Kitano TK, Ferrara KW. Microbubble oscillation in tubes with diameters of 12, 25, and 195 microns. *Applied Physics Letters* 88.3 (2006): 033902.
5. Ward M, Yildiz Y, Papadopoulou V, Eckersley RJ, Tang M-X. Modelling of ultrasound contrast agent oscillations in vessels based on an infinite mirror image method. 2015 IUS IEEE

Observations of the Doppler Twinkling Artifact of Kidney Stones are Bubble Related

Matthew Bruce,¹ Bryan Cunitz,¹ Charles Tremblay-Darveau,² Julianna Simon,¹ Barbrina Dunmire,¹ Mike Bailey¹

1. University of Washington, USA

2. Sunnybrook Health Sciences Centre, Toronto, Ontario, Canada

Kidney stone disease is a growing US and worldwide health issue.[1-3] Abdominal computed tomography (CT), the most common initial imaging test to diagnose the presence of kidney stones is expensive and uses ionizing radiation, increasing long term cancer risk and limiting pediatric and repeated use. Ultrasound is an alternative initial imaging technique having a much lower cost, no radiation and much wider availability, but as currently applied suffers a lower and variable sensitivity (78-90%) and specificity (31-100%) of stone detection compared to CT. [4]

A key reason for the lower sensitivity and specificity in the ultrasound detection of kidney stones relative to CT is that conventional ultrasound imaging modes have been used. The conspicuity of kidney stones from surrounding renal structures with ultrasound can be problematic especially for smaller stones.

A broadband Doppler signal specific to kidney stones, commonly referred to as the twinkling artifact, has been observed since the 1990's.(Fig 1) [5]



Fig 1

While the source of this Doppler signal from kidney stones has been debated, the artifact has still been used to improve the ultrasound detection and classification of stones.[6] However, the twinkling artifact is not reliably visualized with conventional color Doppler. Improved understanding of the source of these transient broadband Doppler signals could improve the sensitivity and specificity of ultrasound in the detection of kidney stones and thus reduce the need for CT. Our group has observed

growing evidence the twinkling signal is possibly due to small submicron bubbles trapped in the crevices of the stone surface.[7,8] One of the key observations was from continually scanning an ex-vivo stone in a hydraulic pressure chamber.(Fig 2)[7]

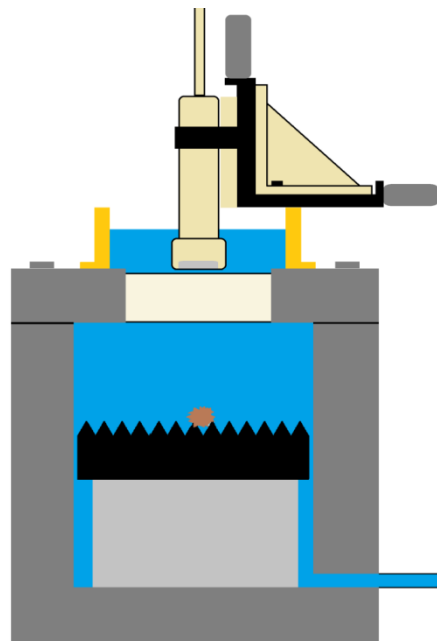


Fig 2



a) Before overpressure b) During overpressure c) After overpressure

Fig 3

Overpressure of the chamber removed the twinkling artifact, which then returned after the overpressure was removed.

The following observations have been made with regard to the Doppler twinkling artifact on kidney stones:

1. Overpressure reduces the twinkling artifact.
2. Under-pressure increases the twinkling artifact.
3. Increased intake of carbon dioxide of a porcine model with implanted stones has suppressed the twinkling artifact.
4. Transient Doppler signals similar to those observed from the disruption of microbubbles used in ultrasound contrast agents.

1. Tang J, Mettler P, McFann K, Chonchol M. The association of kidney stone disease with mortality in US adults: the national health and nutrition examination survey III, 1988-1994. *Am J Nephrol.* 2013;37(5): 501–506.
2. Pearle MS, Calhoun EA, Curhan GC. Urologic diseases in America project: urolithiasis. *J Urol* 2005;173: 848-57.
3. Fwu CW, Eggers PW, Kimmel PL, Kusek JW, Kirkali Z. Emergency department visits, use of imaging, and drugs for urolithiasis have increased in the United States. *Kidney Int* 2013;83:479-86.
4. Ray AA, Ghiculete D, Pace KT. Limitations to ultrasound in the detection and measurement of urinary tract calculi. *Honey RJ. Urology* 2010; 76:295-300.
5. Rahmouni A, Bargoin R, Herment A, Bargoin N, Vasile N. Color Doppler twinkling artifact in hyperechoic regions. *Radiology* 1996; 199:269–271.
6. Kielar AZI, Shabana W, Vakili M, Rubin J. Prospective Evaluation of Doppler Sonography to Detect the Twinkling Artifact Versus Unenhanced Computed Tomography for Identifying Urinary Tract Calculi. *J Ultrasound Med.* 2012 Oct;31(10):1619-25.
7. Lu W, Sapozhnikov OA, Bailey MR, Kaczkowski PJ, Crum LA. Evidence for trapped surface bubbles as the cause for the twinkling artifact in ultrasound imaging. *Ultrasound Med Biol.* 2013 Jun;39(6):1026-38.
8. Sapozhnikov O, Lu W, Bailey MR et al., Bubbles trapped on the surface of kidney stones as a cause of the twinkling artifact in ultrasound imaging. *Proc Meet Acoust.* 2013 Jun 2;19.

Two-step, single chip, microfluidic production of hybrid Microbubble-Nanodroplet architectures for enhanced hydrophobic drug delivery

Victoria Mico, Sally A. Peyman and Stephen D. Evans*

Molecular and Nanoscale Physics, School of Physics and Astronomy, University of Leeds, UK py11vme@leeds.ac.uk

Lipid coated microbubbles (MBs) have proven to be reliable vehicles for drug delivery [1]. Their ultrasound properties (US) provide them with the ability to retain drugs until a destruction pulse is applied, therefore allowing for spatial and temporal control over drug release. Conveniently, these US properties can simultaneously be used for diagnostic purposes, turning MBs loaded with drugs into *theranostic* agents. The implementation of microfluidics for MB production allowed for fine control over the sizes of the MBs, and also facilitated the construction of more complex, drug loaded MB structures. Improvements made towards the production of high concentrations of therapeutic MBs, as well as the reduction of production times, makes them attractive, inexpensive candidates for the delivery of numerous drugs. Notably, there are a high percentage of new pharmaceuticals that show poor water solubility or are hydrophobic. This leads to problems for their delivery *in vivo*, from reduced efficacy to toxicity. Given that a number of these drugs have shown promising results against malignancies *in vitro*, there is an urgency to develop robust methods to deliver them *in vivo*.

We are developing hybrid MB-Nanodroplet architectures as a new route for hydrophobic drug delivery. Lipid Oil Nano-Droplets (LONDs) are attolitre oil volumes stabilised with a lipid monolayer that are capable of storing hydrophobic drug molecules and protecting them from the aqueous environment of the body, thus maintaining drug functionality and reducing aggregation. MB-LONDs architectures retain the ultrasound properties of the MBs, but also incorporate the drug delivery benefits of the LONDs. Functionalization of the LONDs shell with neutravidin allows the formation of the architectures via the biotin-neutravidin linker chemistry. MB-LONDs are assembled in a microfluidic device in a two-step process, in which MBs are first formed in the spray [2] regime and LONDs are incorporated to the solution further downstream. Current work is investigating MB destruction via a high energy US pulse to assist the spatial release of LONDs from the MB surface. We expect that the energy released during this process will also improve cellular uptake of the drug cargo by causing localised sonoporation effects in cell walls.

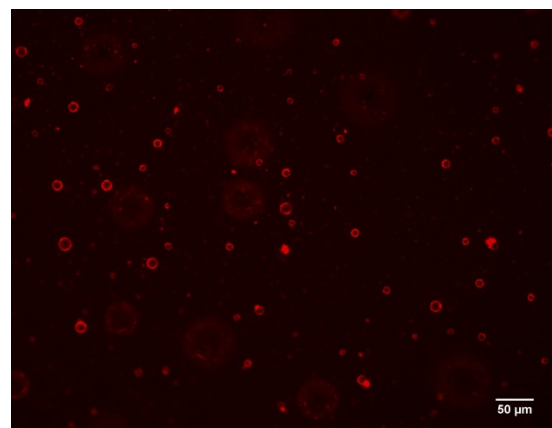
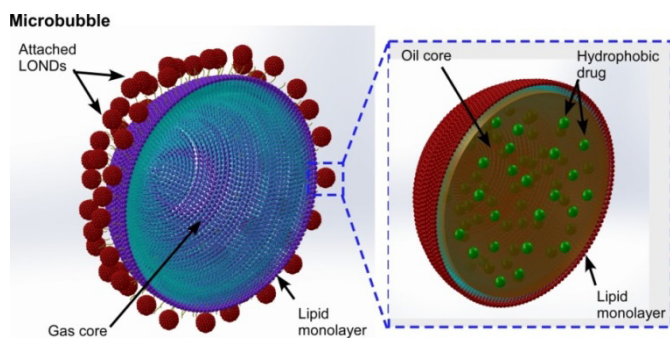


Figure 1: (Left) Schematic of MB-LOND architecture. Neutravidin functionalization of the LONDs surface allows them to bind to MBs. (Right) Fluorescence imaging of MB-LONDs. The red halo around the MBs corresponds to attached LONDs whose shells contain fluorescently tagged phospholipids

1. A. Kheiriloom, et al. (2007) *J. Controlled Release*, **118** (3), 275-284
2. S. A. Peyman, et al. (2012) *Lab Chip*, **12** (21), 4544–4552

Theoretical and Experimental Investigation of Magnetic targeting to Enhance Microbubble Delivery in an Occluded Microarterial Bifurcation

*Marie de Saint Victor¹, Dario Carugo¹, Lester Barnsley¹,
Constantin-C. Coussios¹, Eleanor Stride¹*

University of Oxford, Institute of Biomedical Engineering, Oxford, UK

Ultrasound in combination with microbubbles has emerged as a promising method to accelerate the breakdown of blood clots compared to conventional pharmaceutical treatments [1]. However, its clinical translation is still limited in part by inefficient microbubble delivery to the thrombus [2]. Notably, formation of laminar vortices and abrupt reduction of blood flow within occluded vessels [3] make it difficult to deliver sufficient numbers of microbubbles to the target vascular region.

In this study, we investigated whether magnetic targeting can overcome the limitations imposed by the fluid dynamic conditions and improve microbubble delivery in an occluded vessel. Specifically we examined the effect of a magnetic field on the distribution of magnetic microbubbles in a model of a microarterial bifurcation with an occluded branch, using both computational and experimental methods.

Two-dimensional (2D) numerical modelling was performed using Comsol Multiphysics[®] (Comsol Ltd, UK) in order to determine: (i) the fluid dynamic field in the blood vessel with inlet velocities ranging from 1 to 100 mm.s⁻¹ and (ii) the flow behaviour of microbubbles of varying sizes. *In vitro* experiments were carried out in a PDMS-glass microfluidic device coupled with an inverted microscope (at 40x magnification). Experimental characterisation of the fluid flow field was performed using 2- μ m diameter FITC-labelled polystyrene beads. Lipid-shelled microbubbles loaded with 10-nm iron oxide nanoparticles were labelled with DiI for visualisation and tracking. The magnetic field was applied using a single 12.7 mm cubic permanent magnet element (N52 grade NdFeB, with a magnetization value of 1.09×10^6 A/m).

Formation of laminar vortices within the fluid cavity formed by a complete vascular occlusion (i.e., a thrombus) was observed. In the absence of a magnetic field, the microbubbles remain trapped in the vortex within 250 μ m from the opening of the occluded branch. Importantly, microbubbles did not reach the clot under these conditions. The number of microbubbles trapped within the vortex decreased as the inlet velocity increased, but was independent of microbubble size in the clinically-relevant 0.6 to 5 μ m diameter range.

Application of the magnetic field enabled delivery of microbubbles to the clot and the number of microbubbles delivered increased with bubble size and with decreasing inlet velocity. There was a good agreement between *in vitro* and *in silico* observations.

1. M. de Saint Victor, C. Crake, C-C. Coussios and E. Stride, *Expert Opin Drug Deliv.*, 1(2):187-209 (2014)
2. W. Culp, T. Porter, F. Xie, et al., *Cardiovasc Intervent Radiol*, 24(6):407-12 (2001)
3. D. Carugo, L. Capretto, B. Roy et al., *J Control Release*, 214, 62-75 (2015)

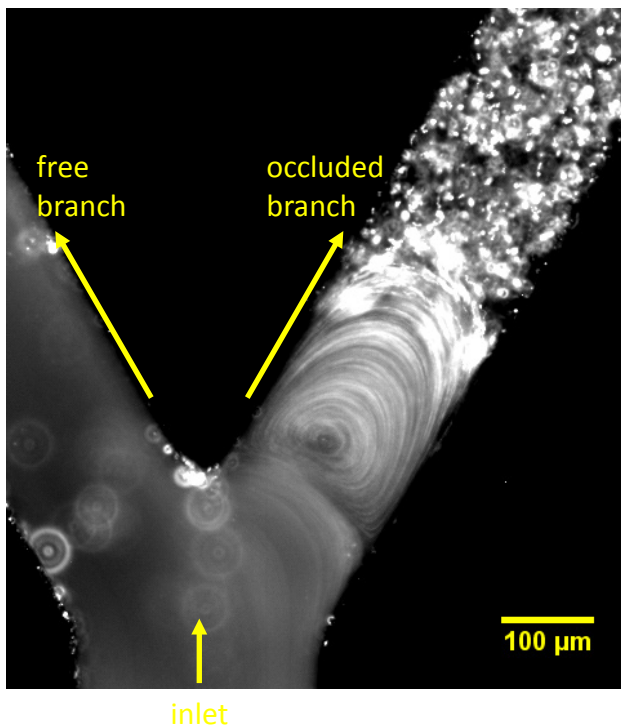


Figure 1: Vortex formation in the occluded micro-arterial bifurcation model. Fluorescent microbeads were employed to visualise the flow field

In this example, the inlet velocity is 10 mm/s.

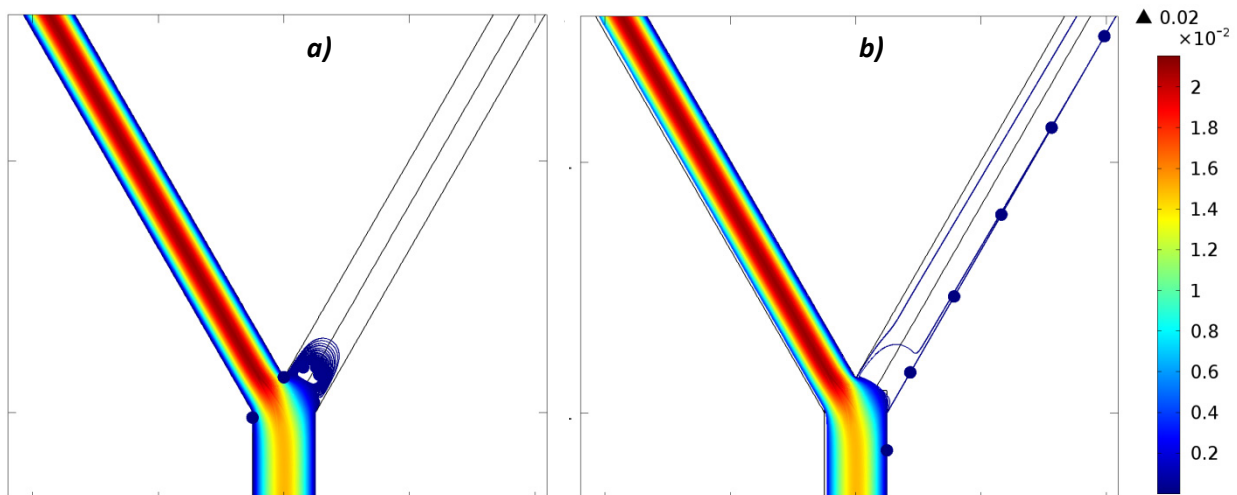


Figure 2: Magnetic microbubble trajectories in the bifurcation

a) without a magnetic field and b) with a magnetic field, determined from numerical simulations.

In this example, the trajectories of 300 microbubbles were simulated over 150 seconds after injection at the inlet. The microbubbles had a diameter of 2.4 μm and the mean inlet velocity was set to 10 mm/s. The colour scale represents microbubble velocity. The dots represent individual microbubbles, the lines represent their trajectories.

Poly(vinyl alcohol) based microbubbles: A study on the chemical and mechanical ageing

Fabio Domenici^{‡, &}, Letizia Oddo[‡], Francesco Brasili[&] and Gaio Paradossi[‡]

[‡]Dipartimento di Scienze e Tecnologie Chimiche, Università di Roma “Tor Vergata”, 00133 Rome, Italy.

[&]Dipartimento di Fisica, Università di Roma “Sapienza”, 00100, Rome, Italy.

One of the assets of crosslinked polymer shelled microbubbles (MBs) as potential ultrasound contrast agent (UCA) is the robustness of the shell, combined with the versatility in modifying the surface with ligands and/or drugs. The stiffness of the shell is usually paid with a decreased echogenicity and a trade off should be searched to accomplish polymer based UCAs with good acoustic and surface performances. A major feature of polymer crosslinked based MBs is their stability. Despite the long shelf-life, subtle modifications occur in the MBs shells reflecting shifts in the acoustic and mechanical properties.

A correlation between the mechanical, acoustic behaviour and structural features is framed within the ageing process of the shell. In this framework, our work is primarily focused on understanding the effect of ageing on the mechanical parameters (i.e. resonance frequencies, Young modulus etc.) of crosslinked polyvinyl alcohol (PVA) shelled MBs, a basic platform for some of the most intriguing diagnostic tools based on ultrasound [1].

In this perspective, we carried out acoustic attenuation and AFM combined tests on MBs with different ageing. At first, we studied the frequency dependence of the attenuation of the ultrasonic waves (Fig.1, left panel) propagating through a suspension of fixed concentrations of several millions of PVA MBs, at different ageing time, from zero to three months. We then combined the acoustic results with a more comprehensive topographical surface and nanomechanical AFM analysis of single MBs (Fig.1, right panel) extracted from the same ensemble.

We found that the increase of the MBs ageing corresponds to an increase of the resonance frequency together with a broadening of the profile of ultrasound attenuation of the bubbles, although the overall shape of MBs remains preserved over several months. In this contribution the changes will be discussed in terms of thickness, roughness and stiffening of the PVA MB shell, according to both the comparative theoretical attenuation spectra calculated from the Church model and the response to nanomechanical stimuli.

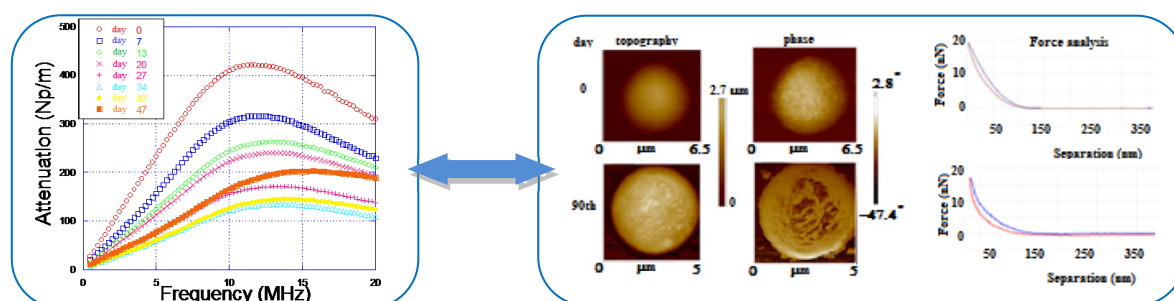


Fig. 1. Representative responses to acoustic vibration (left) and to nanomechanical stimulus (right) of PVA-shelled MBs followed at different ageing time by ultrasonic attenuation and AFM measurements, respectively.

Reference

1. F. Cavaliere, A. El Hamassi, E. Chiessi, G. Paradossi “Stable Polymeric Microballoons as Multifunctional Device for Biomedical Uses: Synthesis and Characterization” *Langmuir*, 2005, 21, 8758-8764.

High-throughput production of clinically-relevant microbubbles using microfluidic architectures

Dario Carugo†, Richard J Browning†, Paul Rademeyera, and Eleanor Stridea

*a*Department of Engineering Science, Institute of Biomedical Engineering, University of Oxford,
Oxford OX3 7DQ, United Kingdom

† Authors have equally contributed to the work in this study.

Gas-filled microbubbles stabilised by a surfactant or polymer coating are routinely used in medical imaging as ultrasound (US) contrast agents, being capable of enhancing ultrasound backscatter from blood by several orders of magnitude. The microbubble core usually consists of a high molecular weight gas (i.e., perfluorocarbon or sulphur hexafluoride) to enhance sample stability both in vivo and during handling or storage [1]. In clinical formulations, the outer coating is usually constituted of saturated phospholipids or denatured albumin. Moreover, the microbubble shell can be employed as a scaffold for transporting biologically active compounds or targeting agents in the haematic circulation, which has opened the way for the use of microbubble as a vehicle in therapeutic applications such as drug delivery or gene therapy.

The acoustic response and therefore the clinical utility of microbubbles are profoundly influenced by their physical characteristics, including size, size distribution, and mechanical/rheological properties of the coating layer [2]. These have been observed to depend on the chemical formulation of the microbubble shell and on the production technique [3].

A variety of different methods have been developed for batch production of microbubbles, including sonication, high shear emulsification, membrane emulsification, and coaxial electrohydrodynamic atomisation [4]. Sonication is the most commonly employed method in both academic and industrial laboratories, and involves dispersing gas or liquid in a suspension of a coating material using high intensity ultrasound [4]. The size distribution of microbubbles obtained from sonication is however relatively broad, which makes it necessary to perform additional, time-consuming post-production procedures (i.e., fractionation or filtration) in order to remove any large bubbles which could cause vascular occlusion after intravenous injection. Furthermore, the lack of process automation makes this technique highly operator dependent and difficult to reproduce faithfully over multiple iterations.

More recently, microfluidic-based techniques have been proposed as an alternative to batch methods for producing relatively monodisperse microbubbles [5-10]. A typical microfluidic device consists of a cross-flow (i.e., flow focusing) or T-junction architecture, in which gas and fluid streams are forced to flow into a confined microenvironment where break-up of the gas stream into individual microbubbles occurs. Depending on the geometrical properties of the microenvironment and the fluid dynamic field, different microbubble production regimes have been demonstrated. However, the narrower size distribution is frequently accompanied by low production rates, the need for chemical additives to adjust fluid viscosity and surface tension, and in some cases lower microbubble stability [3]. These factors have hindered the adoption of microfluidics as a viable technology for industrial production of microbubbles for clinical usage.

In order to overcome these limitations, we developed a two-step microfluidic-based device capable of rapidly producing microbubbles with clinically relevant mean size, composition, concentration and stability.

Syringe pumps (World Precision Instruments Inc., Florida, USA) were employed to control the fluid flow through the microfluidic device, whilst the nitrogen gas employed for microbubble production was provided by a pressurised cylinder, and the pressure measured using a digital manometer (2023P Digitron, Elektron Technology, Cambridge, UK). The fluid phase corresponded to a suspension of 1,2-Distearoyl-sn-glycero-3-phosphocholine (DSPC, from Avanti Polar Lipids, Alabama, USA) and polyoxyethylene (40) stearate (PEG40, from Sigma

Aldrich, Gillingham, UK), at a molar ratio of 9:1, in phosphate buffered saline (PBS, from Thermo Fisher Scientific Inc., Massachusetts, USA).

Microbubble size, concentration and stability were measured from microscope images acquired using a Leica DM500 microscope (Leica Microsystems GmbH, Wetzlar, Germany) coupled with a CCD camera (MicroPublisher 3.3 RTV, QImaging, Surrey, Canada). Microbubble response to ultrasound excitation was instead determined using a high-throughput co-axial flow focusing apparatus combining optical and acoustic detection [11]. A representative microbubble size distribution plot is reported in Figure 1 (total number of bubbles = 11904), showing the absence of larger microbubbles typical of conventional batch sonication approaches. Notably, the dimensional properties are comparable to those of lipid-shelled microbubbles currently used in the clinic (i.e., SonoVue®).

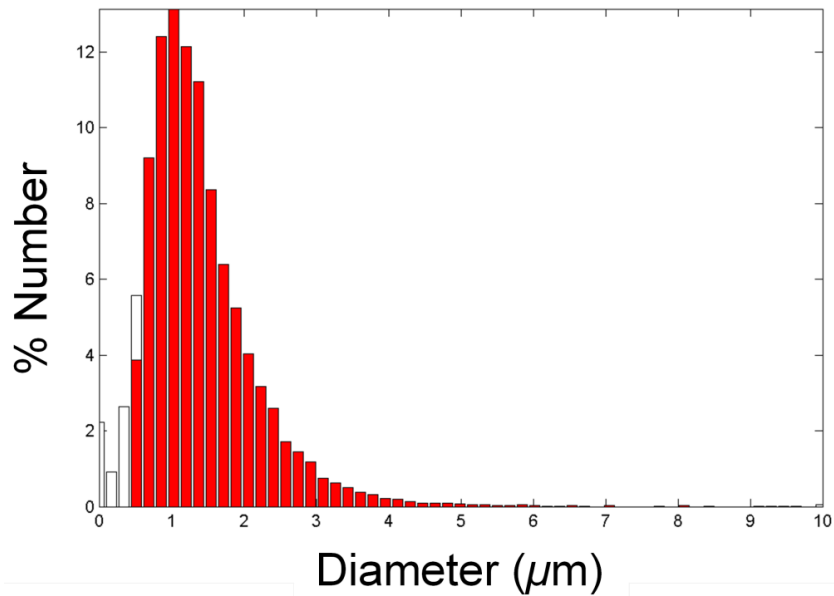


Figure 1. Representative size distribution plot of microbubbles obtained using the developed microfluidic system (total number of bubbles = 11904). The mean microbubble diameter is equal to $1.45 \pm 0.77 \mu\text{m}$, and microbubble concentration is equal to 2.17×10^8 microbubbles/mL.

Table 1. Minimum obtainable Mean Diameter (\pm Standard Deviation, in μm) and corresponding Production Rate (in bubbles/sec) respectively for different microfluidic-based microbubble production techniques, compared to the method described in the present study (highlighted in red).

* Please note that at the optimised operating conditions this device can produce 1.6×10^6 bubbles/sec, with a mean microbubble diameter of $\sim 1.7 \mu\text{m}$.

Operation Principle	Mean Diameter \pm SD (μm)	Production Rate (bubbles/sec)
Microfluidic device	1.45 ± 0.76	2.1×10^6
Micro-spray [5]*	1.7 ± 0.07	$\sim 1.0 \times 10^5$
Flow focusing I [6]	$\sim 5.0 \pm 0.1$	1.0×10^6
Flow focusing II [9]	~ 5.0	$\sim 1.5 \times 10^5$
Sonication-Microfluidics [7]	~ 10.0	NA
T-junction [10]	~ 4.5	7.5×10^3

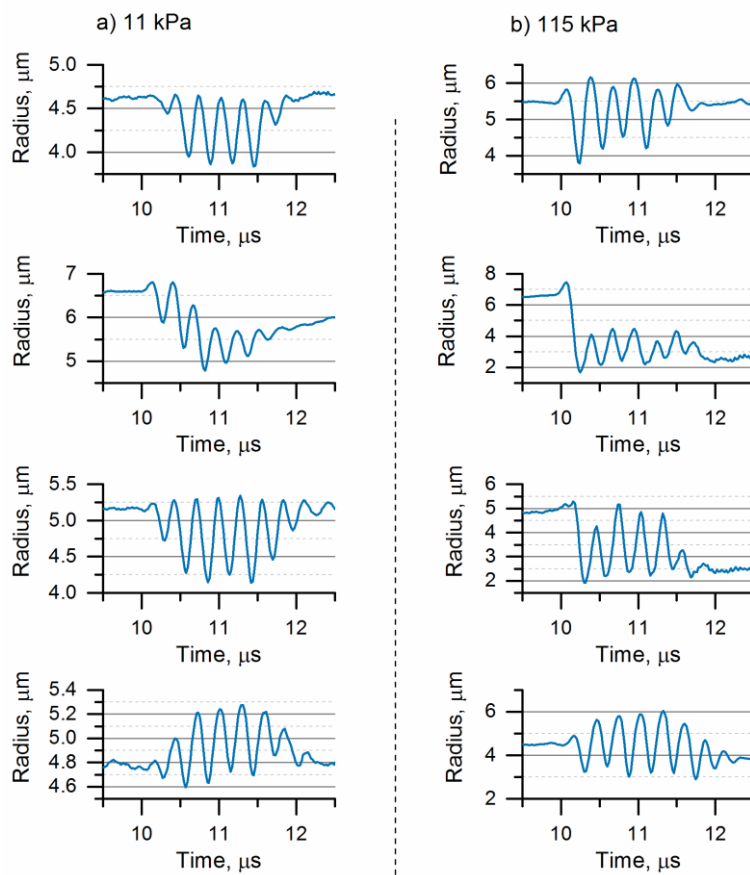


Figure 2. Examples of microfluidic microbubble radial responses, driven at 3.5 MHz, pulse length of 5 cycles and peak negative pressures of a) 11 kPa and b) 115 kPa.

In Table 1 are reported the minimum obtainable mean diameter and corresponding production rate for microbubbles generated using different microfluidic-based techniques, compared to the method described in the present study. Notably, compared to state-of-the-art microfluidic-based technologies (i.e., usually based on flow-focusing or T-Junction architectures), our system produces microbubbles having both clinically-relevant size (i.e., $\sim 1.5 \mu\text{m}$ mean diameter, compared to $1.58 \mu\text{m}$ for SonoVue[®] [12]) and concentration (i.e., $\sim 2.5 \times 10^8$ microbubbles/mL, compared to $\sim 4.1 \times 10^8$ microbubbles/mL for SonoVue[®] [12]). The throughput (i.e., number

of microbubbles generated per unit time) is also higher than conventional microfluidic approaches (i.e., up to $\sim 2 \times 10^6$ microbubbles/sec). Compared to other microscale systems our system provides superior performance (in terms of microbubble size and concentration) and, importantly, does not require exogenous particles (i.e., cavitation nuclei) which could limit the range of applicable microbubble formulations and may compromise the clinical usability of the finished product.

Figure 2 shows typical radial responses measured using laser scattering at a driving frequency of 3.5 MHz, pulse length of 5 cycles and driving peak negative pressures of 11 kPa and 115 kPa. The expected compression and expansion dominated behaviour is observed, as well as sudden reductions in size at the higher pressure.

In summary, the microbubble production method described in the present study provides the following advantages compared to the other technological approaches:

- (i) Large microfluidic channels, resulting in faster priming, higher operating flow rates, and reduced likelihood of channel clogging. The latter results in a significant increase in device lifetime, and therefore reduced cost;
- (ii) Device fabrication is performed using a low-cost and facile replica moulding technique, which makes it attractive for a wide range of laboratory settings;
- (iii) High-throughput microbubble production, at concentration, composition and mean size comparable to those of clinical formulations;
- (iv) Direct microbubble production (i.e., no need for additional post-production steps);
- (v) Chemical additives or exogenous cavitation nuclei are not required to facilitate or trigger microbubble formation;
- (vi) Higher control over the properties of the physical environment compared to batch sonication, potentially allowing for improved reproducibility between experiments and narrower microbubble size distributions;

References

- [1] K. Ferrara, R. Pollard, M. Borden, Ultrasound microbubble contrast agents: fundamentals and application to gene and drug delivery, *Annu. Rev. Biomed. Eng.*, 9 (2007) 415-447.
- [2] E.C. Unger, T. Porter, W. Culp, R. Labell, T. Matsunaga, R. Zutshi, Therapeutic applications of lipid-coated microbubbles, *Advanced drug delivery reviews*, 56 (2004) 1291-1314.
- [3] N.A. Hosny, G. Mohamedi, P. Rademeyer, J. Owen, Y. Wu, M.-X. Tang, R.J. Eckersley, E. Stride, M.K. Kuimova, Mapping microbubble viscosity using fluorescence lifetime imaging of molecular rotors, *Proceedings of the National Academy of Sciences*, 110 (2013) 9225-9230.
- [4] E. Stride, M. Edirisinghe, Novel microbubble preparation technologies, *Soft matter*, 4 (2008) 2350-2359.
- [5] S.A. Peyman, R.H. Abou-Saleh, J.R. McLaughlan, N. Ingram, B.R. Johnson, K. Critchley, S. Freear, J.A. Evans, A.F. Markham, P.L. Coletta, S.D. Evans, Expanding 3D geometry for enhanced on-chip microbubble production and single step formation of liposome modified microbubbles, *Lab on a Chip*, 12 (2012) 4544-4552.
- [6] K. Hettiarachchi, E. Talu, M.L. Longo, P.A. Dayton, A.P. Lee, On-chip generation of microbubbles as a practical technology for manufacturing contrast agents for ultrasonic imaging, *Lab Chip*, 7 (2007) 463-468.
- [7] H. Chen, J. Li, W. Zhou, E.G. Pelan, S.D. Stoyanov, L.N. Arnaudov, H.A. Stone, Sonication-Microfluidics for Fabrication of Nanoparticle-Stabilized Microbubbles, *Langmuir*, 30 (2014) 4262-4266.
- [8] J.L. Chen, A.H. Dhanaliwala, A.J. Dixon, A.L. Klibanov, J.A. Hossack, Synthesis and characterization of transiently stable albumin-coated microbubbles via a flow-focusing microfluidic device, *Ultrasound in medicine & biology*, 40 (2014) 400-409.
- [9] E. Castro-Hernández, W. van Hoeve, D. Lohse, J.M. Gordillo, Microbubble generation in a co-flow device operated in a new regime, *Lab on a Chip*, 11 (2011) 2023-2029.
- [10] C. Chen, Y. Zhu, P.W. Leech, R. Manasseh, Production of monodispersed micron-sized bubbles at high rates in a microfluidic device, *Applied Physics Letters*, 95 (2009) 144101.
- [11] P. Rademeyer, D. Carugo, J.Y. Lee, E. Stride, Microfluidic system for high throughput characterisation of echogenic particles, *Lab on a Chip*, 15 (2015) 417-428.
- [12] C.A. Sennoga, V. Mahue, J. Loughran, J. Casey, J.M. Seddon, M. Tang, R.J. Eckersley, On sizing and counting of microbubbles using optical microscopy, *Ultrasound in medicine & biology*, 36 (2010) 2093-2096.

Lactadherin specifically detects phosphatidylserine on the surface of clinically available ultrasound contrast agent

Kentaro Otani

*Department of Regenerative Medicine and Tissue Engineering,
National Cerebral and Cardiovascular Center Research Institute, Suita, Japan*

Background and Aim

Lactadherin is an endogenous protein which serves as a mediator between the phosphatidylserine (PS)-expressing apoptotic cells and integrin $\alpha_v\beta_3$ -expressing macrophages. Recently, we reported the feasibility of integrin $\alpha_v\beta_3$ -targeted bubbles preparation based on the PS-containing clinically available ultrasound contrast agent (Sonazoid) and lactadherin. However, the specificity of binding between Sonazoid and lactadherin was still unknown. In this study, we examined whether Sonazoid binds with other protein, which has a similar chemical property to lactadherin.

Methods

Angiopoietin-like 5 (ANGPTL5), which has a similar molecular weight and isoelectric point to lactadherin, but has no binding site for PS, was utilized to clarify the specificity of binding with Sonazoid (**Table**). Sonazoid was incubated with R- phycoerythrin (PE) labeled-ANGPTL5 or lactadherin for 10 minutes at room temperature. After washes and centrifugations, bubbles were analyzed by FACSCalibur. Sonazoid incubated with PE-dye was served as control.

Results

By incubating with PE labeled-lactadherin, the fluorescence intensity of Sonazoid was markedly increased (Sonazoid: 2.78 ± 0.04 vs. Lactadherin: 191.77 ± 35.87) (**Figure 1**). On the other hand, the fluorescence intensity of Sonazoid after incubating with PE labeled-ANGPTL5 was significantly lower than that after incubating with PE-lactadherin (ANGPTL5: 47.07 ± 2.07). Additionally, the fluorescence intensity of Sonazoid after incubating with PE-ANGPTL5 was almost identical to that of control (PE-dye: 45.20 ± 0.53).

Conclusion

Our study demonstrated that the lactadherin specifically detected the PS on the surface of Sonazoid. In the near future, the development of simplified method to achieve the lactadherin-bearing Sonazoid only by mixing them would be of benefit for the clinical translation of lactadherin-bearing Sonazoid.

Table. Chemical properties of Lactadherin and ANGPTL5

	Lactadherin	ANGPTL5
Predicted Molecular Weight	41.6kDa	42.3kDa
Isoelectric point	6.7	6.7

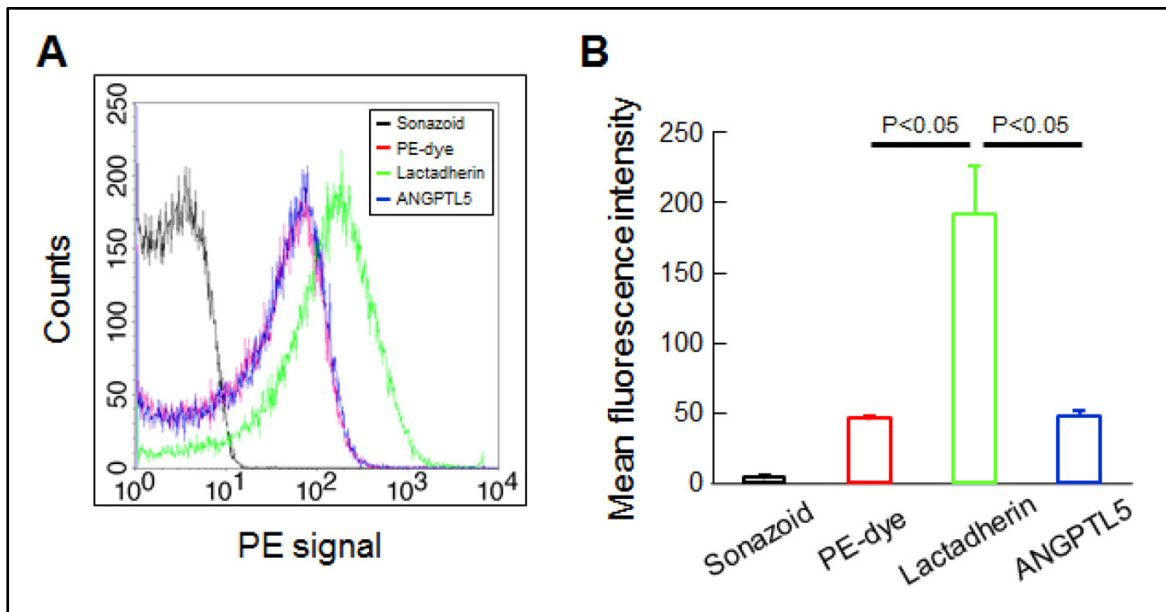


Figure 1. A) Representative FACS histograms of Sonazoid with or without conjugation with PE-labelled protein. B) Summary of quantitative data of FACS analysis.

Sonophorable polyelectrolyte multi-layer shelled nanobubbles for enhancing 'on demand' drug release

Monica Argenziano¹, Sara Zullino², Caterina Guiot², Roberta Cavalli¹
[*roberta.cavalli@unito.it](mailto:roberta.cavalli@unito.it)

¹Dipartimento di Scienza e Tecnologia del Farmaco, Università di Torino, Via P. Giuria 9, 10125 Torino

²Dipartimento di Neuroscienze, Università di Torino, Corso Raffaello 30, 10125 Torino

Polymer-shelled nanobubbles (NBs) are versatile multifunctional nanocarriers for the delivery of gases, drugs and genes. The application of US to NBs may increase the therapeutic index of drugs favoring their administration by sonophoresis and their 'on demand' release in the target tissues. NBs can be loaded with either hydrophilic or lipophilic drugs and different technological approaches have been proposed to associate molecules within the bubble structures. A common strategy consists of association of charged drugs with the shell via electrostatic interaction, when anionic/cationic lipids or polymers are present.

Polyelectrolyte multi-layered coatings could be used to increase the amount of charged drug incorporated in the NBs and to enhance the *in vivo* half-lifetime of the system. Here, NBs were formulated using perfluoropentane as inner core component and dextran sulfate and hyaluronic acid for the shell. Doxorubicin, a positive charged anticancer drug, was chosen as model. The layer-by-layer self-assembly technique was used to adsorb sequentially the two oppositely charged polyelectrolytes on the bubble surface. Doxorubicin was included in negative charged layer of the shell to obtain the drug-loaded NBs.

Different NBs formulations, either blank or drug-loaded, were *in vitro* characterized by size, surface charge determination and morphology analyses, using transmission electron microscopy (TEM). Drug loading and encapsulation efficiency were determined through HPLC analyses. Moreover, *in vitro* drug release kinetics was investigated in the presence and in the absence of ultrasound.

Finally, multilayer shelled NBs could be a promising strategy to enhance drug loading and improve their stability in circulation.

Detection of tumoral Netrin-1 protein levels using ultrasound microbubble contrast agents: *in vitro* validation

Jennifer Wischhusen^{1,2*}, Jean-Guy Delcros^{2,3}, Patrick Mehlen^{2,3}, Frederic Padilla^{1,2}

¹ LabTAU, Inserm U1032, Lyon, France

² LabEx DEVweCAN of the University of Lyon, Lyon, France

³ CRCL, Inserm U1052, Lyon, France

*Jennifer.Wischhusen@inserm.fr

Introduction

Netrin-1 is a ligand of dependence receptors inducing survival in presence of ligand and apoptosis in absence of ligand. In breast cancer, overexpression and secretion of netrin-1 enables apoptosis evasion. Hence, a netrin-1/receptor-disrupting therapy has been developed to reactivate apoptosis signaling. But patient response is dependent on the intra-tumoral netrin-1 expression level and distribution creating the need for a reliable diagnostic tool for patient stratification. Ultrasound (US) microbubble (MB) contrast agents can be targeted to proteins that are presented on the vascular endothelium. Thus, MB present an excellent potential tool for the detection of tumoral netrin-1 using so-called US molecular imaging. The objective of the present study is the *in vitro* validation of MB targeting netrin-1 protein under stresses resembling those of physiological conditions: presence of plasma, shear stress, temperature.

Method

US MB contrast agents (Vevo MicroMarker Target-Ready, VisualSonics) are composed of a gas core stabilized by a lipid monolayer containing avidin. Anti-netrin-1 antibody (Ab) (Netris-Pharma) was biotinylated and coupled to the MB surface via avidin-biotin chemistry. MB were characterized for surface charge (Zeta Sizer), size distribution and concentration (Malassez counting chamber, Leitz Laborlux S, Matlab). MB binding specificity was evaluated on cells (HeLa cells transfected with sleeping beauty system for overexpression of netrin-1 and UNC5B) and protein (netrin-1-Fc; R&D Systems), in presence and absence of plasma (Innovative Research), at different shear stresses (parallel plate flow chamber) and temperatures using light microscopy (Leitz LaborluxS and Nikon Eclipse Ti-S). For control of netrin-1 expression on cells, flow cytometry was used (BD FACSCalibur). MB echogenicity was studied using a gel phantom and a Vantage Verasonics imaging system.

Results

On average, 4.7 biotin molecules were added per Ab and 10 µg/mL of Ab were coupled to 1.6×10^9 MB without leaving free Ab in solution. Static binding assays showed specific binding of MB diluted in both 0.9% of NaCl and 50% of plasma. Although absolute numbers of bound MB were lower in the presence of plasma, the signal-to-noise ratio was higher in this condition. The reduced number of attached MB was associated with the degradation of MB diluted in plasma. Dynamic binding of anti-netrin-1-MB at physiological shear stresses of 1 and 2 dynes/cm² was specific and increased with ongoing inflow of MB. The HeLa model cell line presented netrin-1 on the cell surface in presence and absence of its dependence receptor UNC5B, although the netrin-1 signal was strongly reduced in the latter condition. Binding on cells was specific and the density of bound MB correlated with netrin-

1 expression as quantified by flow cytometry. MB showed a good signal-to-noise ratio in US contrast imaging.

Conclusion

In our study, anti-netrin-1 MB were functional in *in vitro* binding assays reflecting *in vivo* physiological conditions. Binding capacity and specificity were considered satisfactory to enter the second phase of the project: a pre-clinical study to evaluate the feasibility of US molecular imaging of netrin-1 overexpression in a breast cancer animal model. In contrast to previous studies, this US molecular imaging approach targets a diffusible protein secreted by the tumor tissue and not by the tumor microenvironment. The translation of our *in vitro* findings into an *in vivo* study will promote the application of US molecular imaging to a broader field of targetable proteins.

Reproducible quantification of active vascular density in human lower limbs through temporal and spatial analysis of contrast enhanced ultrasound images

¹W.K. Cheung, ²K.J. Williams, ³K. Christensen-Jeffries, ²B. Dharmarajah, ³R.J. Eckersley, ²A.H. Davies, ¹M.X. Tang (mengxing.tang@imperial.ac.uk)

¹ Department of Bioengineering, Imperial College, Exhibition Road, London, SW7 2AZ

² Section of Surgery, Imperial College, Charing Cross Hospital, Fulham Palace Road, W6 8RF

³ Division of Imaging Sciences & Biomedical Engineering, King's College London, SE1 7EH

Objectives

Contrast enhanced ultrasound (CEUS) using microbubble contrast agents has shown great promise in visualising and quantifying active vascular density. Most existing approaches for perfusion quantification using CEUS are calculated based on image-intensity, and are susceptible to confounding factors and imaging artefact [1-4]. Poor reproducibility is a key challenge to clinical translation. In this study a new automated temporal and spatial signal analysis approach is developed for reproducible microbubble segmentation and quantification.

Materials and Methods

This is evaluated *in vitro* on phantoms and *in vivo* in lower limbs of healthy volunteers before and after physical exercise. In this approach perfusion is quantified based on the relative areas microbubbles occupy instead of their image intensity. Temporal features of the CEUS image sequences are used to identify pixels that contain microbubble signals. A microbubble track density (MTD) measure, the ratio of the segmented microbubble area over the whole tissue area, is calculated as a surrogate for active capillary density.

Results

In vitro results show a good correlation ($r^2 = 0.89$) between the calculated MTD measure and the known bubble concentration. For in vivo results, the segmentation results and destruction and replenishment analysis of subject 1 before and after exercise on day 2 is displayed in Figure 1. Also, Figure 2A shows the average microbubble track density of all subjects on day 2 and Figure 2B shows the average blood flow of all subjects on day 2. Moreover, Table 1 shows the percentage change of first day scan vs second day scan by Microbubble track density quantification. A significant increase (129% in average) in the MTD measure is found in lower limbs of healthy volunteers after exercise, with excellent repeatability over a series of days (ICC = 0.96). This compares to the existing state-of-art approach of destruction and replenishment analysis on the same subjects (ICC \leq 0.78).

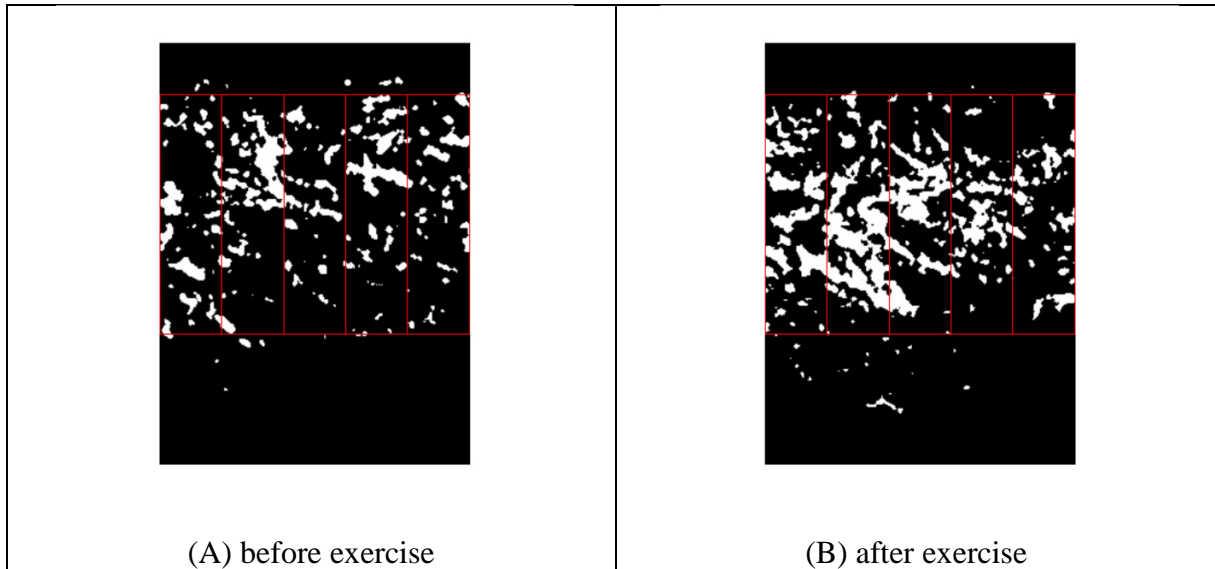


Figure 1: The CEUS segmentation results of a human subject taken from gastrocnemius before (A) and after (B) exercise

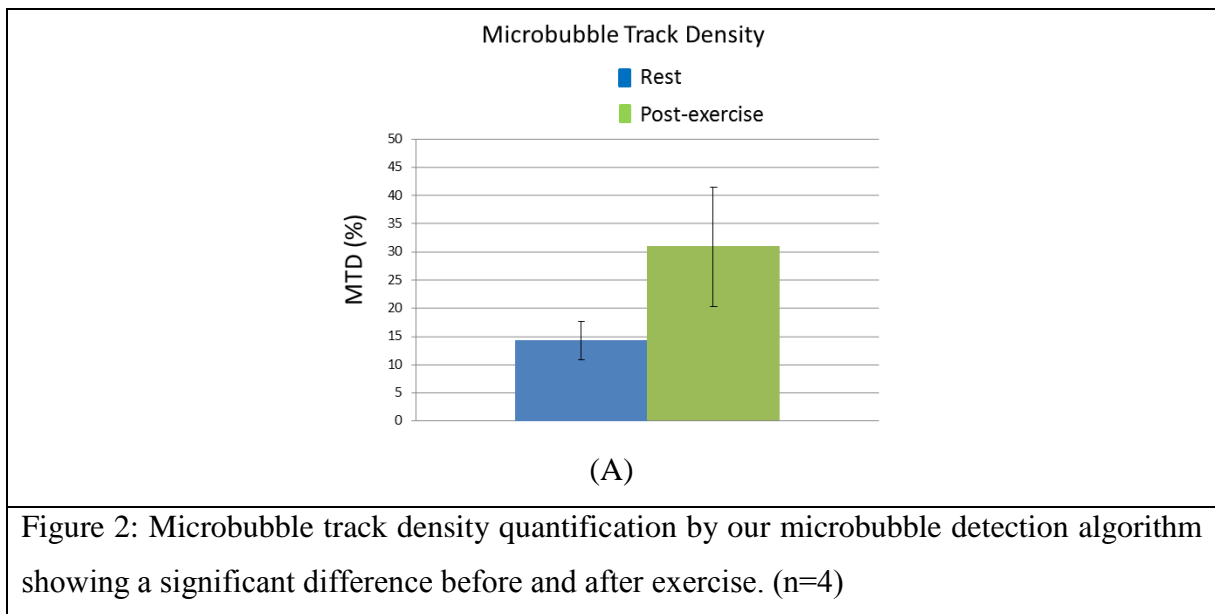


Figure 2: Microbubble track density quantification by our microbubble detection algorithm showing a significant difference before and after exercise. (n=4)

Table 1: The percentage change of first day scan vs second day scan by Microbubble track density quantification, generating an intra-class correlation coefficient (ICC) of 0.96 ($p < 0.01$)

	Day 1	Day 2
Subject 1	51.34 %	43.55%
Subject 2	232.20%	177.27%
Subject 3	171.33%	163.90%
Subject 4	97.91%	92.69%

Conclusions

The proposed new approach demonstrates great potential as an accurate and highly repeatable clinical tool for quantification of active vascular density.

References

1. MX. Tang, H. Mulyana, T. Gauthier et al., *Quantitative contrast-enhanced ultrasound imaging: a review of sources of variability*, *Interface Focus*, August 6, 2011 1:520-539
2. E Stride, MX Tang and RJ Eckersley, *Physical phenomena affecting quantitative imaging of ultrasound contrast agents*, *Applied Acoustics*, 2009 Vol 70(10), SI Pages: 1352-1362
3. Lindner JR, Womack L, Barrett EJ, et al. *Limb stress-rest perfusion imaging with contrast ultrasound for the assessment of peripheral arterial disease severity*. *JACC Cardiovascular imaging*. 2008;1(3):343-50.
4. Akkus Z, Hoogi A, Renaud G et al. *New quantification methods for carotid intra-plaque neovascularization using contrast-enhanced ultrasound*. *Ultrasound Med Biol* 2014;40:25-36

Dosimetric assessment of calcein sonoextraction from cells in vitro

M. Maciulevičius¹, M. Tamošiūnas¹, B. Jakštys¹, R. Jurkonis², M. Venšlauskas¹, S. Šatkauskas¹

¹*Biophysical research group, Vytautas Magnus University, Kaunas, Lithuania*

²*Biomedical Engineering Institute, Kaunas University of Technology, Lithuania*

Introduction

Ultrasound contrast agents, microbubbles (MBs), exposed to ultrasound can significantly enhance cell membrane permeability by mechanisms attributed to transient pore formation and/ or endocytosis [1]. This can be exploited for therapeutic biocompound delivery or extraction from cells. Our previous studies have shown that electroporation can be successfully used for calcein extraction from calcein-preloaded cells. Moreover, it was proved that by controlling electric field parameters high calcein release efficiency could be achieved while maintaining high cell viability [2]. Thus, the aim of this study was to relate calcein release efficiency from calcein-preloaded cells to MB cavitation activities in the intensive and temporal dimensions of the acoustic field by simultaneously monitoring scattered and attenuated US signals.

Materials and methods

Sonoporation experiments were performed using Chinese hamster ovary cells, preloaded with calcein-AM. Calcein release was evaluated using spectrofluorimetry. Cell viability was evaluated using cell clonogenic assay. US excitation waveform was 1 MHz central frequency, 1 kHz pulse repetition frequency, 10 % duty cycle (100 μ s on, 900 μ s off), 0 - 380 kPa peak negative (PNP) acoustic pressures, 0 - 2 s exposure duration. The experimental parameters were set according to pre-performed optimisation leading to cell reversible permeabilisation. Passive cavitation detection system was used to record MB scattering and attenuation signals. Root mean square (RMS) was calculated in 1.5 – 1.75 and 0.9 – 1.1 MHz frequency ranges for subsequent differential RMS and attenuation quantifications by subtracting –MB group from +MB and calculating logarithmic ratio of +MB to –MB, respectively. Differential RMS was used to calculate sonoporation metric, inertial cavitation dose (ICD). Attenuation was used to predict the time needed to achieve complete MB sonodestruction.

Results and discussion

Differential ICD vs. calcein fluorescence graph (Fig. 1) shows that the amount of released calcein has linear part in 0 - 0.18 $V \times s$ ICD range (Fig. 1 insert), then slowly enters saturation.

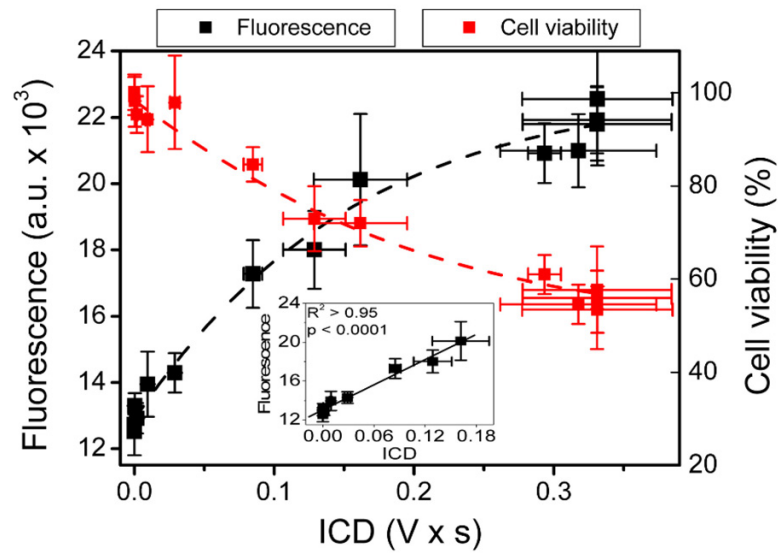


Fig. 1. Calcein fluorescence and cell viability dependence on ICD

Similarly cell viability was decreasing linearly up to $0.18 \text{ V} \times \text{s}$ and had strong significant correlation. At Further ICD increase cell viability entered saturation as well.

RMS and attenuation curves in timescale show the approximate simultaniety of differential RMS decrease to 0 V and attenuation increase to 0 dB indicate that the major cavitation activity had already occurred with complete MB sonodestruction achieved (Fig. 2).

Time-scale sonoporation experiments were performed at 380 kPa acoustic pressure. (Fig. 2). As it can be seen from differential RMS and attenuation curves, main cavitation activity and MB sonodestruction occurs up to $\sim 1.25 \text{ s}$. During this period calcein release and cell viability reached plateau levels. Moreover, this data shows the difference between sonoporation and electroporation as increased electric field pulse number induces calcein release and cell viability [2]. This difference arises because sonoporation is mostly dependent on MB behaviour not only on the acoustic field properties.

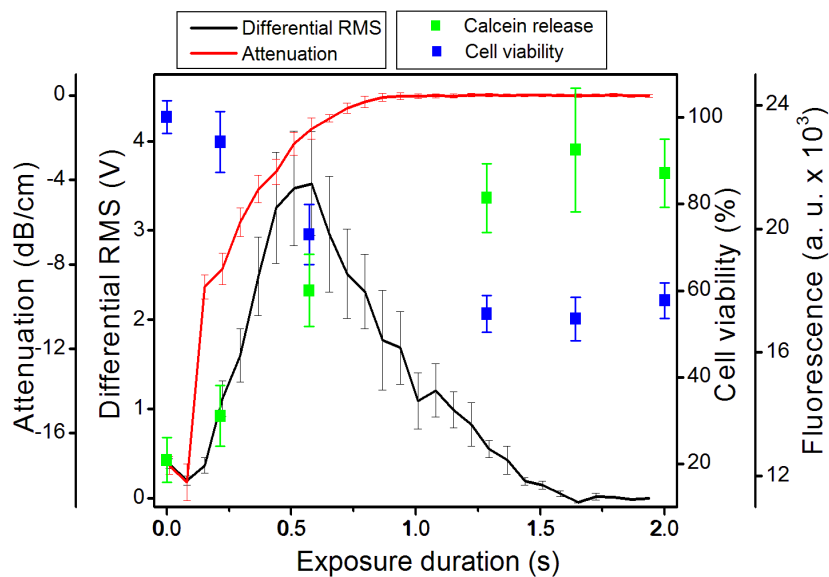


Fig. 2. Temporal dynamics of attenuation, differential RMS, calcein fluorescence and cell viability

The results of this study show that the efficiency of the extraction of calcein molecules from cells as well as cell viability decrease are associated to MB cavitation activity and can be accurately predicted using inertial cavitation dose. In addition to this, neither additional calcein release nor cell viability decrease were observed after complete MB sonodestruction was achieved. This indicates the optimal exposure duration for maximal sonoextraction efficiency to coincide with the time needed to achieve complete MB sonodestruction. These results demonstrate the importance of MB inertial cavitation in sonoextraction. To our knowledge, this work is the first with the scope to: 1) investigate small molecule extraction from cells using sonoporation and 2) relate extraction processes to the physical aspects of MB cavitation.

Acknowledgements

This work was funded by Research Council of Lithuania project SVE-08/2014.

References

1. Meijering B.D., Juffermans L.J., van Wamel A., Henning R.H., Zuhorn I.S., Emmer M., Versteilen A.M., Paulus W.J., van Gilst W.H., Kooiman K., de Jong N., Musters R.J., Deelman L.E., Kamp O. *Ultrasound and microbubble – targeted delivery of macromolecules is regulated by induction of endocytosis and pore formation.* *Circ. Res.* 2009, 104(5). 679-687.
2. Rajeckaitė V., Rafanavičius A., Jakštys B. and Šatkauskas S. *Electroporation-assisted extraction of molecules from cells in vitro.* *1st World Congress on Electroporation and Pulsed Electric Fields in Biology, Medicine and food & Environmental Technologies.* 2015, September. Portoroz, Slovenia.

Interaction of laser-activated polymeric microcapsules with cells

Tom van Rooij¹, Guillaume Lajoinie², Ilya Skachkov¹, Nico de Jong^{1,3}, Klazina Kooiman¹, Michel Versluis²

¹ Department of Biomedical Engineering, Thorax Center, Erasmus MC, Rotterdam, the Netherlands

² Physics of Fluids Group, MIRA Institute for Biomedical Technology and Technical Medicine, University of Twente, Enschede, the Netherlands

³ Laboratory of Acoustical Wavefield Imaging, Faculty of Applied Sciences, Delft University of Technology, Delft, the Netherlands

Introduction

Cavitation of ultrasound contrast agents can be used to enhance therapeutic effects by increasing the membrane permeability. Next to microbubbles, polymer microparticles can also induce these cavitation effects [1]. One of the advantages of these agents is their increased stability. Next to that, light absorbing dyes can be embedded into their shell, which opens up possibilities for photoacoustic imaging. We have previously shown that single polymeric capsules can be triggered by a laser, resulting in a cavitation bubble [2]. In the present study we used two types of light-absorbing polymeric microcapsules: one type is loaded with a high boiling point oil (hexadecane) and the second type contains a low boiling point oil (perfluoropentane, PFP) [3]. We studied the effects of the laser-induced cavitation bubbles generated by these agents on human endothelial cells to evaluate their potential for imaging and therapeutic applications.

Materials & Methods

Hexadecane-loaded polymethylmethacrylate (PMMA-hexadecane, Sudan Red) microcapsules and poly(lactic-coglycolicacid) Resomer RG502 (Resomer-PFP, Sudan Red) microcapsules were prepared by an emulsion solvent evaporation technique, using microsieve emulsification [4].

Human umbilical vascular endothelial cells (HUVECs) were cultured on one side of an OptiCell. Forty minutes prior to the experiment, the cells were incubated with calcein-AM (final concentration of 0.4 $\mu\text{g}/\text{mL}$) for labeling live cells. Then Hoechst (5 $\mu\text{g}/\text{mL}$) was added to stain all cell nuclei, propidium iodide (PI, 25 $\mu\text{g}/\text{mL}$) was added to measure disruption of the cell membrane (i.e., poration), and Resomer-PFP capsules or PMMA-hexadecane capsules were added to the OptiCell. The OptiCell was placed in a 37 °C water bath with the cells on top for the floating PMMA-hexadecane capsules, whereas the cells were on the bottom for the sinking Resomer-PFP capsules. Upon laser-activation (8 ns, 532 nm, pulsed laser, Quantel Evergreen 150 mJ), the Brandaris 128 ultrahigh-speed camera [5] recorded the cavitation events at 10 Mfps, whereas a Photron SA2 color high-speed camera was simultaneously used for imaging PI uptake. The ultrasound signals produced by the cavitation bubbles were measured using a single-element focused 1-MHz transducer (C302, Panametrics). Snapshots of calcein-AM and Hoechst staining were taken before laser activation and after the recording of PI. Analysis of the data was performed in Matlab.

Results & Discussion

After laser activation, the PMMA-hexadecane capsules produced two different types of bubbles: cavitation bubbles located outside the capsule, and ‘internal’ bubbles which remain confined within the capsule (Fig. 1A). When an internal bubble is produced, the PMMA coating does not break open, as previously reported [3]. The internal bubble dynamics were nonviolent and did not lead to significant poration as PI uptake was negligible, but their acoustic signal could be detected. The ultrahigh-speed Brandaris recordings showed that single capsules had a higher probability of producing internal bubbles than capsule clusters, which implies that lower concentrations of bubbles could be beneficial for imaging purposes.

The oscillation of the PMMA-hexadecane cavitation bubbles stopped after the laser had been turned off and these bubbles disappeared within microseconds. Time-intensity curves of PI uptake showed almost five times more poration for large bubbles (35 – 45 μm in diameter) than for the smaller bubbles (5 – 15 μm in diameter). In addition, when the cavitation bubbles were in contact with a cell, the signal of the calcein after activation was lower than before due to calcein efflux, as reported by Fan et al. [6]. In contrast, after activation of the Resomer-PFP capsules, the oscillation of the bubbles sustained after the laser had been turned off and they remained on top of the cells where they kept on growing. These growing bubbles did not float up, which suggests that they had adhered to the underlying cell layer. When the PFP bubbles were close to a cell the calcein signal completely vanished. This suggests destruction of the cell membrane and even the nuclear membrane.

Based on PI influx and calcein efflux, PMMA-hexadecane cavitation bubbles porated ~50% more cells than the Resomer-PFP bubbles at equal bubble size (5 – 30 μm in diameter). The PMMA-hexadecane cavitation bubbles vaporize the surrounding water, which is in direct contact with the cell membrane. These cavitation bubbles are therefore more violent than the Resomer-PFP bubbles that only vaporize the low boiling point oil in their core [3]. Another explanation can be found in the activation energy of the capsules; to generate a water vapor bubble a higher energy is required than to vaporize a PFP bubble of the same size [3]. In addition, more heat deposition in the system results in a higher thermal shock, which may induce more poration and thus PI uptake.

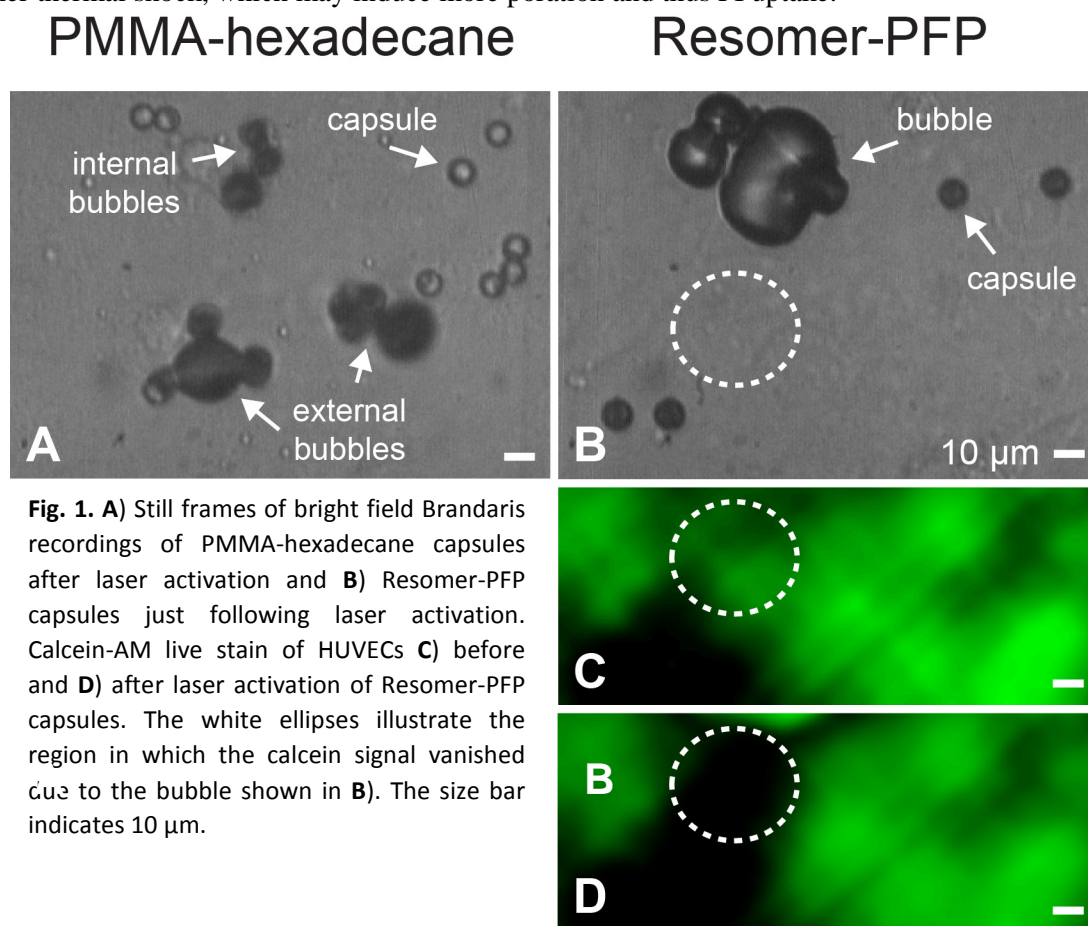


Fig. 1. A) Still frames of bright field Brandaris recordings of PMMA-hexadecane capsules after laser activation and B) Resomer-PFP capsules just following laser activation. Calcein-AM live stain of HUVECs C) before and D) after laser activation of Resomer-PFP capsules. The white ellipses illustrate the region in which the calcein signal vanished due to the bubble shown in B). The size bar indicates 10 μm .

Conclusion

In this study we investigated the cavitation effects of laser-activated polymeric microcapsules on human endothelial cells. Single floating PMMA-hexadecane capsules produced internal bubbles that did not induce poration, but did produce a measurable acoustic signal. The PMMA-hexadecane capsules may therefore offer opportunities for imaging. However, the concentration of capsules and the laser intensity should be low enough to ensure that only internal bubbles are produced. The vaporization of the Resomer-PFP capsules is too violent for imaging, but can be used for therapeutic effects where cell death is desired, such as tumor treatment.

References

1. Kooiman, K, et al., *Adv Drug Deliv Rev*, vol. 72C, pp. 28-48, 2014.
2. Lajoinie, G, et al., *Nat Commun*, vol. 5, p. 3671, 2014.
3. Lajoinie, G, "Ultrasound Contrast Agents - Bubbles, Drops and Particles," *PhD thesis, Physics of Fluids, University of Twente, Enschede, 2015.*
4. Loxley, A, et al., *J Colloid Interface Sci*, vol. 208, pp. 49-62, 1998.
5. Chin, TC, et al., *Rev Sci Instrum*, vol. 74, pp. 5026-5034, 2003.
6. Fan, Z, et al., *Proc Natl Acad Sci U S A*, vol. 109, pp. 16486-91, 2012.

In vivo activation, imaging dynamics and delivery effectiveness of an acoustic cluster therapy (ACT) agent

Nigel Bush¹, Andrew Healey³, Per Christian Sontum³, Svein Kvåle³, Gary Box¹, Sue Eccles¹, Annemieke van Wamel², Catharina de Lange Davies², Jeffrey Bamber¹

¹*The Institute of Cancer Research, London, UK;* ²*Dept. of Physics, NTNU, Trondheim Norway;* ³*Phoenix Solutions AS, Oslo, Norway.*

Introduction

The limitations of conventional microbubbles for enhancing drug delivery in combination with ultrasound (US) include low drug carrying capacity (on the bubble surface), small and brief local dose enhancement (the released drug flows downstream) and limited ability to interact with the vascular endothelium to increase permeation (due to small surface area). Here we present studies using a novel acoustic cluster therapy (ACT) agent, designed to overcome these disadvantages, consisting of a dispersion of positively charged oil microdroplets (which could carry a dissolved drug within its volume rather than on its surface) electrostatically bound to negatively charged microbubbles. When ACT is delivered intravenously and exposed to relatively low acoustic pressures, bubble-to-droplet energy transfer ‘activates’ (vaporises) the droplets to produce large (>20 µm) bubbles which occlude microvessels to briefly (< 15 minutes) trap released or co-injected drug. Finally, drug delivery is completed in a delivery enhancement phase, which uses a low frequency acoustic field to gently resonate the activated bubbles and increase vascular permeability by generating shear forces at the bubble-endothelium interface. Further details of the concept may be found in [1], [2] and [3], and in a companion paper at this conference [4].

To effectively deploy ACT, imaging methods are needed to (a) monitor accumulation of non-activated agent for dosimetry, (b) confirm and quantify activation and its spatial distribution, and (c) monitor delivery and duration of the delivery. Here we present results of in vivo pre-clinical imaging experiments designed to better understand the ACT agent behaviour for the first two of these imaging requirements. These results enabled the design of further experiments to study the improvement of substance delivery, in this case a fluorescent dye, using co-injected and activated ACT. The latter experiments employed the same enhanced permeation and retention (EPR) infrared (IR) dye, namely 800CW PEG (LI-COR Biosciences), as employed in a previous study of the effectiveness of ACT [5], but were carried out independently in a different laboratory using a different tumour model, different US imaging and treatment configuration and different US equipment. Such independent verification is an important part of thorough scientific research.

Materials and Methods

Imaging and activation of ACT were achieved with a Toshiba Aplio XG standard clinical US scanner and a 1204BT linear array capable of simultaneous interleaved, non-linear contrast mode and fundamental mode imaging at 8 MHz. Delivery enhancement employed a 300 kHz single element focused transducer mounted beside the imaging array in an open polyethylene water bath above the animal and directed at the tumour, with acoustic coupling gel between the water bath and the animal. Athymic mice were used, each bearing an SLC-B (a sub-line of SK-OV3, ovarian carcinoma)

subcutaneous human tumour xenograft on the lower right flank. This arrangement, which mimicked a potential clinical set-up, differed completely from the system used previously [5], where a tumour-bearing hind limb of the animal was immersed into a sound tank and imaged with a high frequency preclinical scanner. Here, raw radiofrequency (RF) data and video image sequences were acquired, for both fundamental and non-linear contrast modes, before, during and up to 15 minutes after intravenous contrast injection.

Initial studies confirmed that non-activated ACT agent could be imaged at low mechanical index (MI) using the nonlinear contrast-specific mode. Then, by increasing the MI, the agent was activated. Above an MI of 0.1, stationary echoes were observed to appear in fundamental US images of the tumour, which previously had shown little or no contrast enhancement, consistent with the production of large trapped bubbles. To test the hypothesis that these stationary echoes are uniquely associated with ACT activation, echo time-intensity curve (TIC) properties were measured of Sonazoid™ microbubbles [6] and ACT (clusters) using simultaneous nonlinear contrast and fundamental modes for a range of MI values up to 0.4. An image sequence processing method was developed to segment stationary from moving echoes using thresholded images of echo temporal correlation computed after respiratory motion compensation using speckle tracking. This allowed novel TICs to be generated for tumour regions of interest (ROI) separately for mobile and stationary components of both types of agent.

Having confirmed ACT activation in vivo, studies of the delivery of IR dye CW800 to tumour tissue were conducted with the same SK-OV3, human ovarian carcinoma xenografts, equipment and experimental arrangement as described above. Repeated measurements were made using an IVIS™ Spectrum CT of dye epifluorescence in the tumour ROI compared to a background ROI (contralateral thigh of the mouse) following tail vein injection of 100 µl (2 nmol), with or without the injection of ACT agent following dye injection. ROI's were drawn with the aid of X-ray CT images co-registered with the epifluorescence images. ACT was administered in 50 µl doses, with 5 minute intervals between doses, and activated at the tumour site for 45 s immediately after injection using the Toshiba Aplio™ at 8 MHz in interleaved (10 frames/s) non-linear contrast mode and fundamental B-mode, MI = 0.4. Each administration of activated ACT was followed by insonification for delivery enhancement for 45 s using 300 kHz, 2-cycle pulses of US, pulse repetition frequency of 2 kHz and MI = 0.12.

Results and Discussion

Stationary echoes uniquely accumulated in tumours following ACT injection and US activation, but were not detected when imaging Sonazoid™ microbubble injections at any MI (e.g. Figure 1). The peak number of stationary activated ACT bubbles increased as a function of MI from MI = 0.1 to 0.4. Stationary echoes were observed consistently and with good signal level in fundamental imaging mode but not in nonlinear contrast mode, providing further evidence that they were due to large bubbles rather than microbubbles. Clear differences were observed in the temporal dynamics of Sonazoid™, ACT, and ACT moving and stationary components, as a function of MI. The peak for Sonazoid™ mobile contrast accumulation in tumours was 5 to 10s post-injection, compared with 30s to 2 minutes for activated ACT. Sonazoid™ washed out within 6 minutes but the segmented stationary ACT component failed to wash out during the observation time, further confirming that the bubble echoes were stationary.

ACT was seen to significantly enhance the uptake of CW800, as measured by fluorescence in the tumour relative to background, even though this dye is designed for use as an EPR agent (Figure 2). The level of enhancement using ACT seen here was comparable to that observed elsewhere [5] with the same IR dye but using a different tumour model and experimental arrangement.

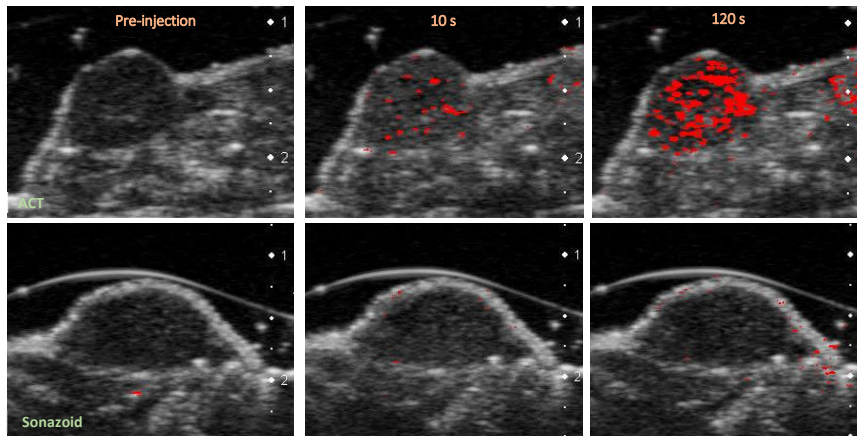


Figure 1. Example frames from image sequences at MI = 0.4, overlaid with contrast echoes segmented as stationary (red). Left: pre-injection. Middle: 10 s after injection. Right: 120 s after injection. Top: ACT. Bottom: Sonazoid™.

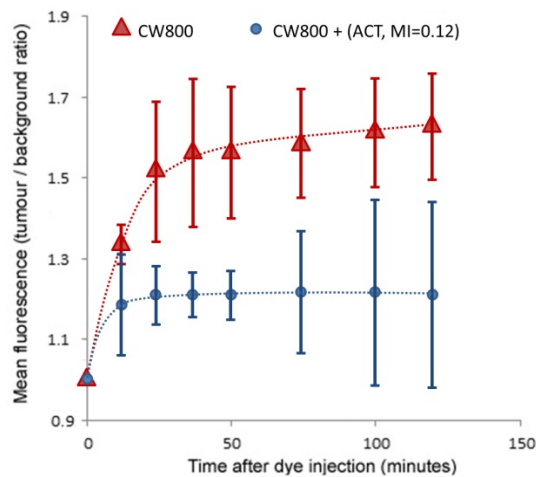


Figure 2. IR dye uptake enhancement using ACT. Tumour : background epifluorescence is compared for CW800 dye alone and CW800 dye followed by activated ACT agent and delivery enhancement with pulsed 300 kHz US, MI = 0.12. (Means, \pm 1 st.dev., for 3 mice, each cohort.)

Conclusions

All observations during the activation and imaging dynamics studies were consistent with the hypothesis that stationary echoes observed in fundamental mode imaging provide a reliable signature for uniquely identifying activated ACT bubbles *in vivo*. Confirmation was provided of the ability of ACT to significantly enhance uptake of an IR dye, demonstrating reproducibility of the observations between laboratories and using different tumour models and experimental arrangements. The novel methods developed to automatically segment stationary from moving bubble echoes in the presence of respiratory motion, and their use in time-intensity curve analysis of mobile and stationary vascular contrast agents, may be of value in other fields such as the study of molecularly targeted microbubbles.

References

1. P.C. Sontum, A. J. Healey, S. Kvåle; *Ultrasound Mediated Delivery of Drugs*, patent application PCT/NO2014/050177.
2. P.C. Sontum, S. Kvåle, A. J. Healey, R. Skurtveit, R. Watanabe, M. Matsumura, J. Østensen, *Acoustic Cluster Therapy (ACT) – a novel concept for ultrasound mediated, targeted drug delivery*, *Int J of Pharmaceutics*, Vol. 495 (2) (2015): 1019–1027. <http://dx.doi.org/10.1016/j.ijpharm.2015.09.047>.
3. A. J. Healey, P. C. Sontum, S. Kvåle, M. Eriksen, R. Bendiksen, A. Tornes and J. Østensen, *Acoustic Cluster Therapy (ACT) – in-vitro and ex-vivo measurement of activated bubble size distribution and temporal dynamics*, submitted to *Ultrasound Med Biol*, 2015.
4. P. Sontum, A. Healey, S. Kvåle, N. Bush, J. Bamber, C. de Lange Davies and A. van Wamel. *Acoustic Cluster Therapy – A Novel Approach for Ultrasound Mediated Targeted Drug Delivery: Technology Basics and Proof of Concept*, submitted to 21st European Symposium on Ultrasound Contrast Imaging, Rotterdam, Jan 21-22, 2016.
5. A. Van Wamel, A. Healey, P. C. Sontum, S. Kvåle, N. Bush, J. Bamber and C. de Lange Davies, *Acoustic Cluster Therapy (ACT) – pre-clinical Proof of Principle for local drug delivery and enhanced uptake effects*, submitted to *J Cont. Release*, 2015. [6] P.C. Sontum; *Physicochemical characteristics of Sonazoid™, a new contrast agent for ultrasound imaging*, *Ultrasound Med. Biol.*, Vol. 34 (5), (2008) 824-833.

High-resolution Estimation of Local Perfusion Parameters While Compensating for Substantial Respiratory Motion

Avinoam Bar-Zion¹, Melissa Yin², Elizabeth Kuczynski^{3,4}, Robert S. Kerbel^{3,4}, Dan Adam¹ and F. Stuart Foster^{2,4}

¹ *Department of Biomedical Engineering, Technion - Israel Institute of Technology, Haifa, Israel.*

² *Physical Sciences, Sunnybrook Research Institute, Toronto, Ontario, Canada.*

³ *Biological Sciences, Sunnybrook Research Institute, Toronto, Ontario, Canada.*

⁴ *Department of Medical Biophysics, University of Toronto, Toronto, Ontario, Canada.*

BACKGROUND

Dynamic contrast-enhanced ultrasound (DCEUS) imaging enables the estimation of blood flow and perfusion in tissue, allowing for early detection and treatment monitoring in different cancers. However, current analysis of DCEUS scans is limited, due to motion artifacts induced by respiratory movements. Therefore, motion compensation is necessary for reliable analysis of DCEUS scans. Although B-mode based image registration can partially compensate for in-plane movement, frames acquired outside of the main imaging plane contain non-relevant information and should be excluded. However, currently, since common DCEUS processing methods are not designed for processing non-uniformly sampled data, clips that contain considerable motion artifacts are discarded. Here, we present a method that facilitates the estimation high resolution perfusion parametric maps even when a significant percentage of the frames are excluded due substantial respiratory motion artifacts.

METHODS

In-plane movements were compensated for by rigid registration, applied to anatomic B-mode clips. Out-of-plane frames were automatically detected using a clustering algorithm. The log-transformed single-pixel DCEUS time-traces were processed within the framework of *reconstruction of non-uniformly sampled signals in shift-invariant (SI) spaces* [1]. The Gaussian kernel, being compactly supported and a popular generator for SI spaces, was used. This kernel can represent a broad range of time-intensity curve shapes, encountered in DCEUS imaging. An iterative algorithm was used for the estimation of the SI representation coefficients. In order to enhance the signal-to-noise (SNR) of the data, a log-normal model was fitted to the estimated signals with and without spatial averaging. The proposed method was validated in a series of numerical simulations and *in vivo* bolus injection scans. An orthotropic mouse model of hepatocellular carcinoma (HCC, n=22) was used to test the algorithm under substantial motion artifacts. Scans were made before and during treatment with sorafenib, an anti-angiogenic drug.

RESULTS AND DISCUSSION

In silico - The width of the selected Gaussian kernel was narrow enough to enable proper depiction of the fast contrast agent wash-in, but still sufficiently broad to remove the speckle noise from the data. The simulated log-normal perfusion curves (without noise) were represented with $R^2=0.99$, and the normalized root mean square error (NRMSE) was also 0.99. The proposed method was able to estimate the noisy simulated time-intensity curves with mean NRMSE of 0.14 at 25 frames per second. When 50% of the samples were removed, the NRMSE increased by only 0.05, to 0.19. The processed HCC scans included up to 55% out-of-plane frames. However, all of the scans were

analyzed successfully and none of the scans was entirely discarded. In the in vivo experimental data, local parametric curve fitting with small averaging filters (e.g. 3x3 pixels) had significantly lower MSE compared to large averaging filters ($\geq 10 \times 10$ pixels, $p < 0.005$). A significant reduction in the mean PE signal was observed in the treated group. In contrast to the spatially homogeneous PE maps of the tumors in the control group, the PE maps of the treated tumors were very non-uniform (Fig. 1, C and D respectively). This trend continued, and after 5 weeks of treatment, well resolved blood vessels were observed inside the treated tumors (Fig. 1, E). Analysis of tumor sections immunostained for CD31, showed that sorafenib treatment resulted in a significant 78.6% reduction in microvessel density (Fig. 2). A non-significant increase in tumor necrosis (from 4 to 12% of the total tumor area) was observed. Results from both the ultrasound data and histology suggest that following sorafenib induced pruning of small vessels, the remaining vasculature, spread throughout the HCC tumors, continue to support these tumors.

CONCLUSION

The proposed method enabled high-resolution quantification of scans containing substantial motion artifacts, thus extending the usability of DCEUS imaging. The high-resolution parametric maps that were obtained enabled the visualization of morphological changes in tumors, and revealed important information on the outcome of the antiangiogenic treatments. DCEUS imaging allowed for high-resolution monitoring of drug induced changes in the tumors, with close correlations to standard histology measurements.

REFERENCES:

1. A. Aldroubi and K. Gröchenig, "Nonuniform Sampling and Reconstruction in Shift-Invariant Spaces," *SIAM Rev.*, vol. 43, no. 4, pp. 585–620, Jan. 2001.

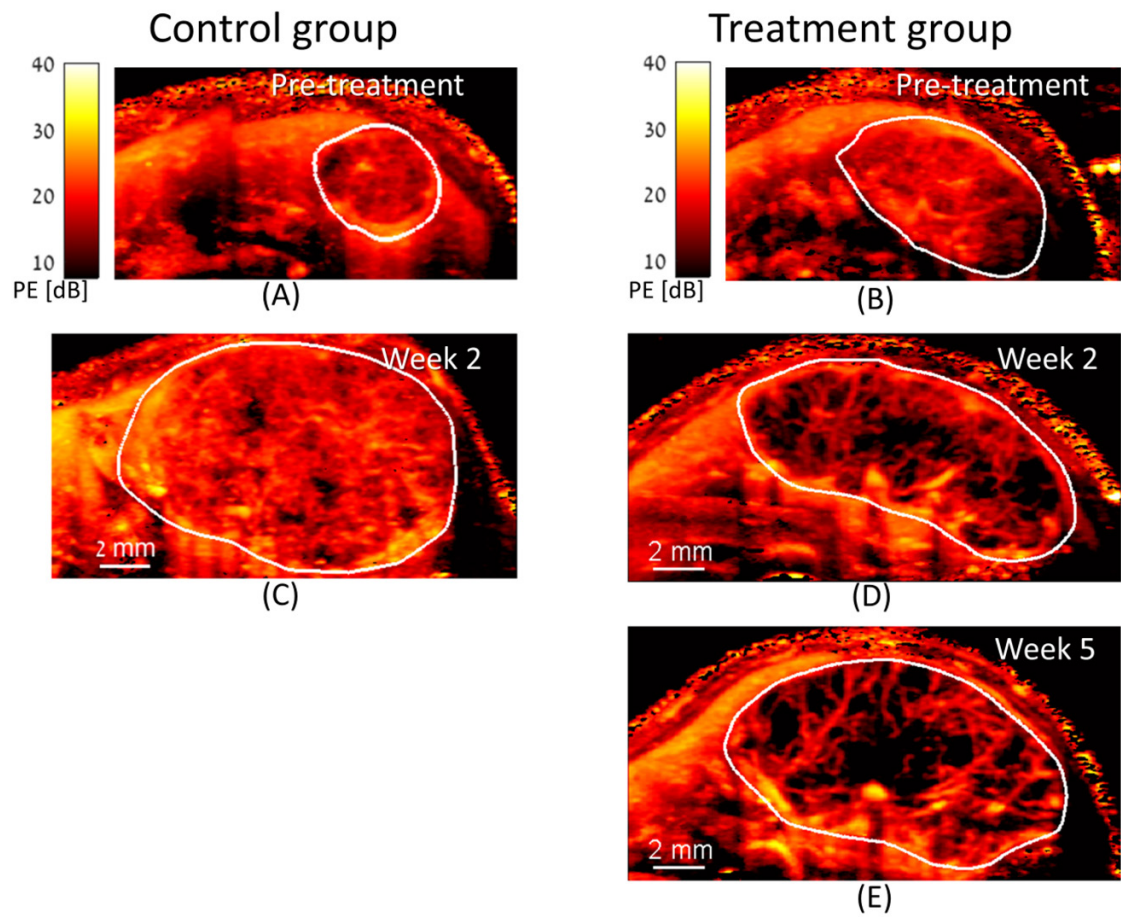


Figure 1: HCC Parametric Maps – Sorafenib Treatment

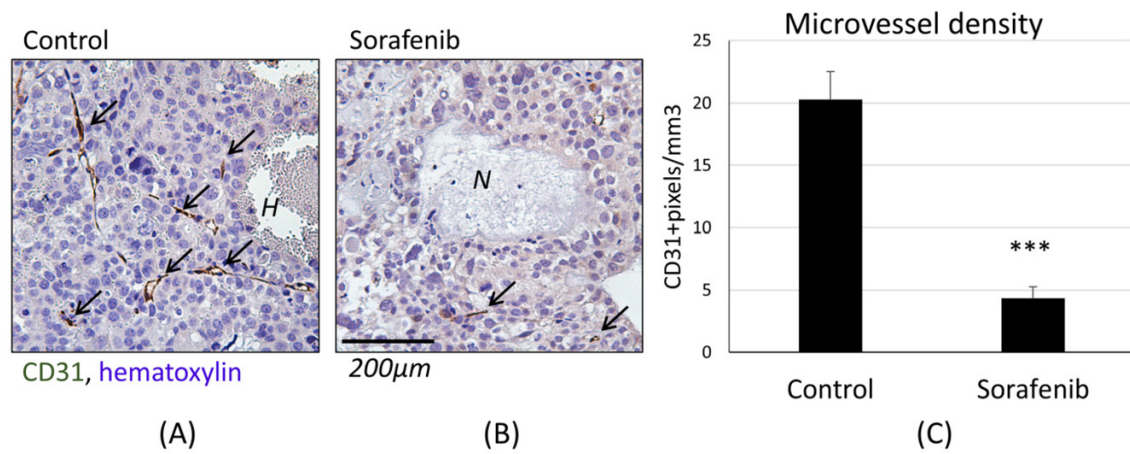


Figure 2: HCC Microvessel Density. Here 'N' represents a necrotic region and 'H' an area of hemorrhage (blood pool).

Impact of gas composition on subharmonic emission from phospholipid contrast agents

Emma Kanbar, Damien Fouan, Charles Sennoga, Ayache Bouakaz

UMR Inserm U930, Université François Rabelais de Tours, 10 ter Bd Tonnellé, 37032 Tours, Cedex 1, France

Introduction

Subharmonic (SH) signals, backscattered from gas-filled microbubbles can be used to improve the detection and specificity of contrast-enhanced ultrasound imaging. This enhancement is due to significant differences between SH signals emanating from microbubbles as compared to tissue [1], [2]. However, SH emissions are characterised by variable and time-dependent generation which has not been elucidated [3]. Deciphering microbubble features that influence the onset of SH emissions is needed not only to better develop new microbubble compositions, but also to develop dedicated SH imaging modes. In this study, we investigated the impact of microbubble gaseous composition on the SH response of phospholipid contrast agents.

Material and Methods

Four phospholipids contrast agents with different gas compositions were studied: Sonovue (SF_6), BR 14 (C_4F_{10}), BG 7725 (C_4F_{10}) and Definity (C_3F_8). Agents were activated according to the manufacturer's instructions, were dispersed in air-stabilised PBS and promptly characterised. Bulk dispersions of the contrast agents were acoustically excited at intervals of 180 seconds for a time period of 90 minutes using a focused transducer at a driving frequency of 10 MHz (450 kPa; 50 cycles; 500 ms). The scattered signal was acquired using a focally matched transducer at 5 MHz to acquire subharmonic signals. All 4 agents were characterized with their original gas and then re-characterized following substitution of the original gas with air, SF_6 or C_4F_{10} .

Results

Figure 1 shows the temporal evolution of the fundamental (10 MHz) and SH (5 MHz) emissions of BR 14, BG 7725, Definity and Sonovue microbubbles. A measurable change in the intensity of SH emissions was recorded followed by a progressive increase in SH emissions of the order 10-15 dB. Microbubbles with SF_6 gas (Sonovue) exhibited negligible delay in the onset of SH emissions. On the contrary, BR 14, BG 7725 and Definity which are agents with C_3F_8 and C_4F_{10} gases exhibited a delay in the onset of SH emissions. Substitution of SF_6 and C_4F_{10} with air (before reconstitution) showed absence of the earlier observed delay (Figure 2). Significantly, substitution of SF_6 for C_4F_{10} revealed a delay in the onset of SH emissions, while substitution of C_4F_{10} for SF_6 eliminated the earlier observed delay (Figure 2); clearly suggesting that the type of gas contained in the microbubble influenced SH emissions in a time-dependent manner. However, the substitution of the gas did not affect the trend and the amplitude of the fundamental response.

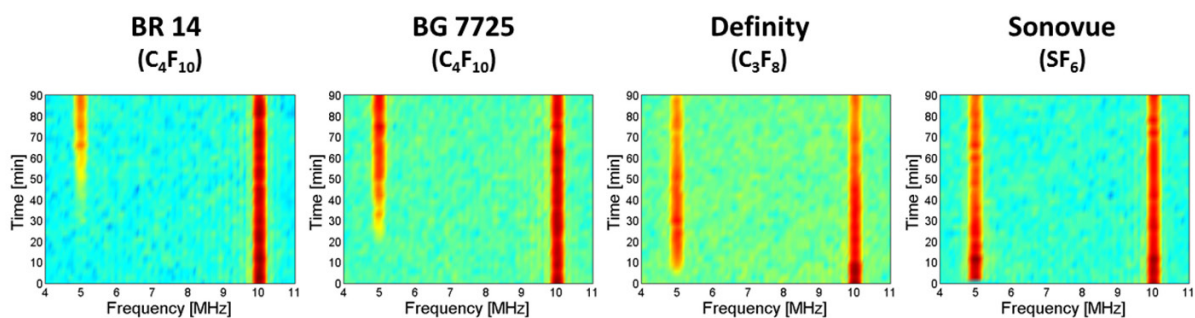


Figure 1: Subharmonic and fundamental evolution over 90 minutes from BR 14, BG 7725, Definity and Sonovue microbubbles.

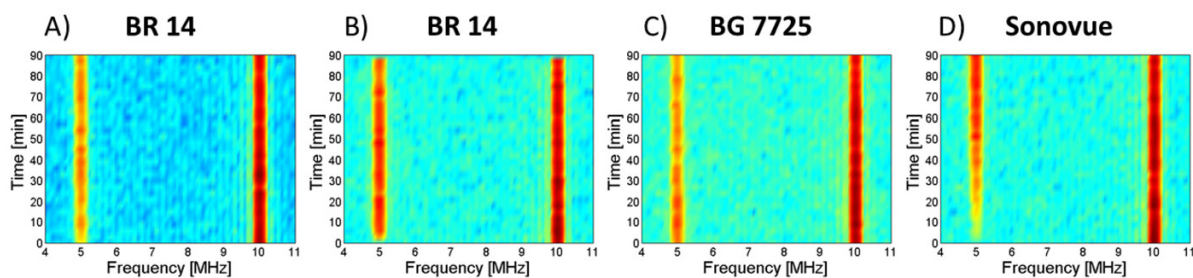


Figure 2: Subharmonic and fundamental evolution over 90 minutes from BR 14 when C_4F_{10} is substituted with air (A) and SF_6 (B), from BG 7725 when C_4F_{10} is substituted with Air (C) and from Sonovue when SF_6 is substituted with C_4F_{10} (D).

Discussion and Conclusion

We have shown that agents filled with gaseous SF_6 exhibit a negligible delay (< 180 seconds) in the evolution and onset of SH emissions while agents filled with C_3F_8 and C_4F_{10} showed a delay of 360 ± 30 seconds and 1800 ± 600 seconds, respectively. In contrast, complete saturation of the agents with air exhibited no delay in the corresponding SH emissions, presumably because substitution of SF_6 , C_3F_8 , C_4F_{10} gases with air leads to improved microbubble compressibility. To corroborate our hypothesis, we substituted SF_6 for C_4F_{10} and successfully changed the SH behavior of the resultant agents. Since the agents are dispersed in air-saturated PBS, these results suggest that the diffusivity of the gas within the agent is correlated with the onset and time-dependent evolution of SH emissions. This is clearly demonstrated by the progressive decrease in the diffusion coefficients of the corresponding gas compositions of $2.05 \times 10^{-9} \text{ m}^2 \text{ s}^{-1} > 1.2 \times 10^{-9} \text{ m}^2 \text{ s}^{-1} > 7.45 \times 10^{-10} \text{ m}^2 \text{ s}^{-1} > 6.9 \times 10^{-10} \text{ m}^2 \text{ s}^{-1}$, as we move from air, SF_6 , C_3F_8 and C_4F_{10} , respectively. The same trend is again noticeable in the Ostwald coefficients of $5.4 \times 10^{-3} > 5.2 \times 10^{-4} > 2.02 \times 10^{-4}$ as we move from SF_6 , C_3F_8 and C_4F_{10} , respectively [4]. Similar results obtained at different frequencies and acoustic pressures will be

presented as well. This study highlighted the role of the gas composition in the onset and evolution of SH emission for phospholipid microbubbles, a finding that has important implications for future diagnostic exploitation of SH imaging.

Acknowledgments

The authors acknowledge Bracco SA Geneva for supplying the contrast agents.

References

1. P. M. Shankar, P. Dala Krishna, and V. L. Newhouse, "Advantages of subharmonic over second harmonic backscatter for contrast-to-tissue echo enhancement.," *Ultrasound Med. Biol.*, vol. 24, no. 3, pp. 395–9, Mar. 1998.
2. F. Forsberg, W. T. Shi, and B. B. Goldberg, "Subharmonic imaging of contrast agents," *Ultrasonics*, vol. 38, no. 1–8, pp. 93–98, Mar. 2000.
3. H. Shekhar, I. Awuor, K. Thomas, J. J. Rychak, and M. M. Dooley, "The delayed onset of subharmonic and ultraharmonic emissions from a phospholipid-shelled microbubble contrast agent.," *Ultrasound Med. Biol.*, vol. 40, no. 4, pp. 727–38, 2014.
4. K. Sarkar, A. Katiyar, and P. Jain, "Growth and dissolution of an encapsulated contrast microbubble: effects of encapsulation permeability.," *Ultrasound Med. Biol.*, vol. 35, no. 8, pp. 1385–96, Aug. 2009.

The Superharmonic Microbubble Doppler Effect in Ultrasound Therapy: An Observation Useful for Monitoring Velocities

A.N. Pouliopoulos¹, J.Bezer², J.J. Choi¹

¹Noninvasive Surgery and Biopsy laboratory, Department of Bioengineering, ²Department of Physics, Imperial College London, London, SW7 2AZ, United Kingdom

OBJECTIVE

The use of microbubbles in focused ultrasound therapies has catalysed the introduction of a diverse range of non-invasive technologies. Microbubbles are used in sonoporation to deliver drugs into cells, in sonothrombolysis to dissolve blood clots, and in blood-brain barrier opening to deliver drugs into the brain. In contrast with the short pulses used in ultrasound imaging, therapeutic pulses can be very long (>10,000 cycles) leading to a rapid and continuous reorganisation of the microbubble distribution due to primary and secondary acoustic radiation force effects. Current methods for monitoring this movement have been limited to position by passive acoustic mapping and cavitation mode by spectral analysis. Here, we introduce a new feature that can be monitored in real-time: microbubble velocity.

METHODS

Previous studies have shown that echoes from short imaging pulses had a Doppler shift that was produced by the movement of microbubbles. Here, we analysed the Doppler shift during long therapeutic ultrasound pulses using a passive cavitation detector. A population of microbubbles (5×10^4 - 5×10^7 microbubbles/ml) was embedded in a vessel (inner diameter: 4mm) and sonicated using a 0.5MHz focused ultrasound transducer (peak-rarefactional pressure: 147-366kPa, pulse length: 50,000 cycles or 100ms) within a water tank. Microbubble acoustic emissions were captured during ultrasound exposure with a coaxially aligned 7.5MHz passive cavitation detector and were spectrally analysed to detect the Doppler shift for multiple harmonics above the 10th harmonic (i.e., superharmonics). We also evaluated the superharmonic Doppler effect *in silico* through computational modelling of microbubbles translating under the influence of the primary Bjerknes force.

RESULTS

A Doppler shift was observed on the order of tens of kHz with respect to the primary superharmonic peak. This is due to the axial movement of the microbubbles. The position, amplitude and width of the Doppler peaks depended on the acoustic pressure (figure 1) and the microbubble concentration. Higher pressures increased the effective velocity of the microbubbles up to 3m/s, prior to the onset of broadband emission, which is an indicator for high magnitude inertial cavitation. Although the reorganisation of microbubble distribution was shown to persist for the entire sonication period in dense populations, it was constrained

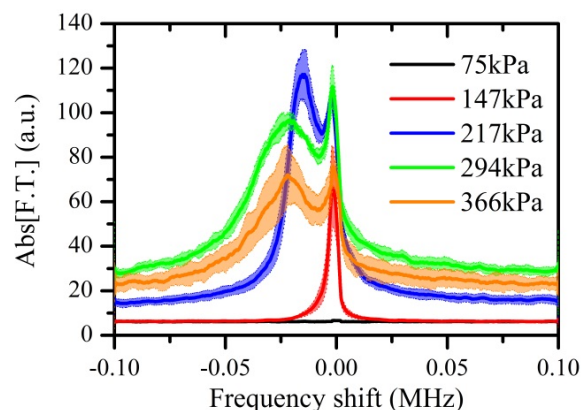


Figure 1: Microbubble superharmonic Doppler frequency shift across the acoustic pressures (10th harmonic). The position, amplitude, and width of the Doppler peak changed with pressure, indicating different microbubble kinetics within the sonicated area.

in the first few milliseconds in lower concentrations. Computational modelling confirmed that microbubbles sonicated with long-pulse and low-frequency therapeutic ultrasound can yield frequency shifts on the order of tens of kHz, due to their translational movement in the direction of the ultrasound propagation.

CONCLUSIONS

In conclusion, superharmonic microbubble Doppler effects can provide a quantitative measure of velocities of a sonicated microbubble population and could be used for monitoring ultrasound therapy in real-time.

Study of the Colloidal Properties of Phospholipids Microbubbles

Tereza Pilgrová^{1,2}, Filip Mravec¹, Marek Orban², Miloslav Pekar¹

¹*Brno University of Technology, Faculty of Chemistry, Institute of Physical and Applied Chemistry
Purkyňova 464/118, 61200 Brno, Czech Republic*

²*International Clinical Research Center, St. Anne's University Hospital Brno, Brno, Czech Republic*

This work was supported by European Regional Development Fund - Project FNUSA-ICRC (No.CZ.1.05/1.1.00/02.0123) and by project Materials Research Centre at FCH BUT- Sustainability and Development, REG LO1211, with financial support from National Programme for Sustainability I (Ministry of Education, Youth and Sports).

Microbubbles are currently used as contrast agents in combination with ultrasound and are proposed for drug delivery applications. A development of a new drug carrier requires identification of microbubble formation process and basic physical properties of the system. A new physico-chemical approach to characterization of phospholipid microbubbles was found. Dynamic light scattering method and maximum bubble pressure tensiometry was used for study of colloidal properties of phospholipids aggregates in relation to the microbubble applications. Size distribution and surface activity of SonoVue[®] contrast agent and analogous phospholipid system were studied for evaluation of an effect of a system composition on final properties and stability of the system.

It was found that surface properties of phospholipid systems are significant for microbubble formation and stability of contrast agents and that preparation method influences size distributions of the system in contrast with surface tension of the system. Prepared systems are more polydisperse in comparison with SonoVue[®] agent. Roles of individual components of SonoVue[®] agent were characterized. We present results of a study of colloidal properties of ultrasound contrast agents. Selected techniques and characterization methods are very useful for study of surface properties and formation process of ultrasound contrast agents.

Keywords: hyaluronan, surfactant, nanoparticles, fluorescence spectroscopy, pyrene, dynamic light scattering

Spherical and translational dynamics of a collapsing cavitation bubble cluster

N. Sugita and T. Sugiura

Department of Mechanical Engineering, Keio University, Japan

Background

The cluster bubble dynamics is of particular interest for ultrasound applications because the bubbles in a cluster present complex collective behavior due to strong nonlinear interactions. Although the radial dynamics of a cluster has been addressed for many years, global dynamics such as deformation and translational motion of a bubble cluster is still inadequate. We conducted optical observation using a high-speed video camera in order to investigate the translational stability of a collapsing bubble cluster driven in a vibrating water vessel. We restrict our interest to the attractive force between hemi-spherical bubble clusters attracted to a wall and observe the translational motion of the cluster due to the secondary Bjerknes force from its mirror image clusters.

Material and Methods

A rectangular acrylic vessel (inside dimension: 40×40×100 mm, thickness: 5 mm) filled with tap water of 90 mm height is fixed on a vibration generator (EMIC, 513-BS/Z08). A vacuum pump is connected to the vessel through a valve in order to reduce the hydrostatic pressure in the vessel to near that of vapor pressure. This allows large pressure amplitude to be developed in the liquid at low driving amplitude and frequency of hundreds of Hz. The recording system consists of a high-speed video camera (Photron, FASTCAM SA-5), a distortion-less macro lens and LED backlight. A millimeter sized gas bubble as a cavitation nucleus is injected by a needle through a silicon plug of 5 mm diameter located at 30 mm above the vessel bottom and 20 mm away from the side wall. As the driving acceleration is exerted on the water vessel, pressure gradient is generated in the vertical direction, and the cavitation nucleus undergoes violent collapse to evolve to a collapsing bubble cluster.

Results

Image sequence of a typical collapsing bubble of initial radius 1.02 mm is shown in Fig. 1. The cluster departs from the silicone plug and violently collapses as a result of large amplitude oscillation, producing a number of fission fragments which coalesce again during the next expansion phase. The driving frequency is 300 Hz and the pressure amplitude is about 1.1 kPa at the center of the cluster. The recorded images are analyzed using MATLAB (R2014b, Mathworks Inc.) based on the binarization to a 8-bit grayscale image using a thresholding technique. The positions of the cluster centroid, (X, Y) corresponding to horizontal and vertical direction, respectively, and area of the bounding box, A_{box} which encloses the contour of the cluster with the minimum area are obtained for the recorded image sequences and plotted in Fig. 2. Here, we defined the area-equivalent mean radius as $R_m = \sqrt{A_{\text{box}}/\pi}$. Strongly nonlinear oscillation with the maximum radius of about 3.77 mm which is about 3.7 times larger than the initial bubble nucleus is experienced. We also found that for this case the period of the mean radius curve is twice the driving period. Therefore, the primary resonance frequency of the collapsing bubble can be estimated to be around 150 Hz. As the separation distance

between the cluster and the side wall decreases, the oscillation amplitude gradually decays and the velocity in the X direction gradually accelerates due to the secondary Bjerknes force exerted from its mirror image. (Fig. 2(b))

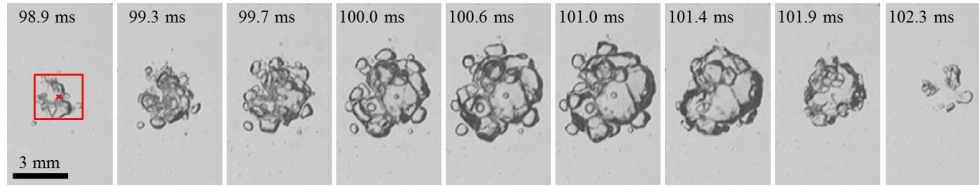


Figure 1: The recorded image sequence of a collapsing bubble cluster. The bounding box obtained from image processing is also shown by a red rectangle at the first image. The driving frequency is 300 Hz, and the pressure amplitude is about 1.1 kPa at the position of the cluster. The frame rate of the camera is set to 7000 fps, and every 3 frames are shown from left to right.

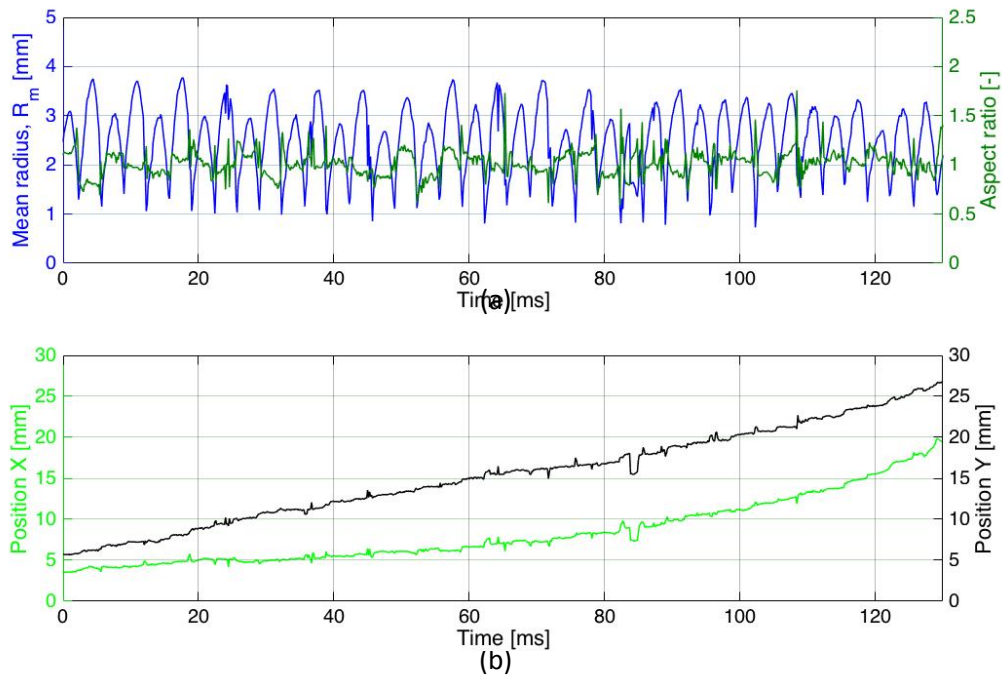


Figure 2: Time histories of (a) Area-equivalent mean radius, $R_m = \sqrt{A_{\text{box}}/\pi}$ and the aspect ratio of the bounding box where A_{box} is the area of the bounding-box calculated in the image processing based on the binarization of a 8 bit grayscale thresholding technique and (b) Temporal positions of the cluster center. Time is set to zero when the cluster gets completely detached from the wall. The cluster is attracted to the acrylic wall located at $X = 20$ mm due to the secondary Bjerknes force exerted from the mirror image cluster.

Acoustic characterization of a novel cell culture platform for ultrasound-mediated drug delivery

Inés Beekers^{1,2}, Shreyas B. Raghunathan³, Tom van Rooij², Varya Daeichin², Nico de Jong^{2,3}, Klazina Kooiman², Sebastiaan J. Trietsch¹

¹Mimetas B.V., Leiden, the Netherlands

²Department of Biomedical Engineering, Thorax Center, Erasmus MC, Rotterdam, the Netherlands

³Laboratory of Acoustical Wavefield Imaging, Department of Imaging Physics, Faculty of Applied Sciences, Delft University of Technology, Delft, the Netherlands

Introduction

Ultrasound insonification of gas filled microbubbles can be used to locally enhance drug delivery, as the oscillating microbubbles increase the endothelial permeability of the vascularization, i.e. sonoporation [2]. To better understand the underlying mechanisms of sonoporation, the ideal *in vitro* endothelial cell model consists of an optimal environment for 3D cell culture, flow, and cell-to-cell interactions. Therefore, we propose to use the OrganoPlate™ (Mimetas BV, Leiden): an elaborate microfluidic channel structure (Fig. 1) incorporated into a standard 384-well microtiter plate [3]. However, as the OrganoPlate™ has never been used for studies involving ultrasound, its acoustic properties are unknown. Since microbubble behavior highly depends on the acoustic pressure and frequency, the ultrasound transmission through the microchannels needs to be fully characterized. Here, we study the feasibility of using OrganoPlates™ for *in vitro* ultrasound-mediated drug delivery research in terms of modeling the acoustic pressure and frequency transmission, experimentally validating the model, and studying the distribution of microbubbles inside the OrganoPlate™.

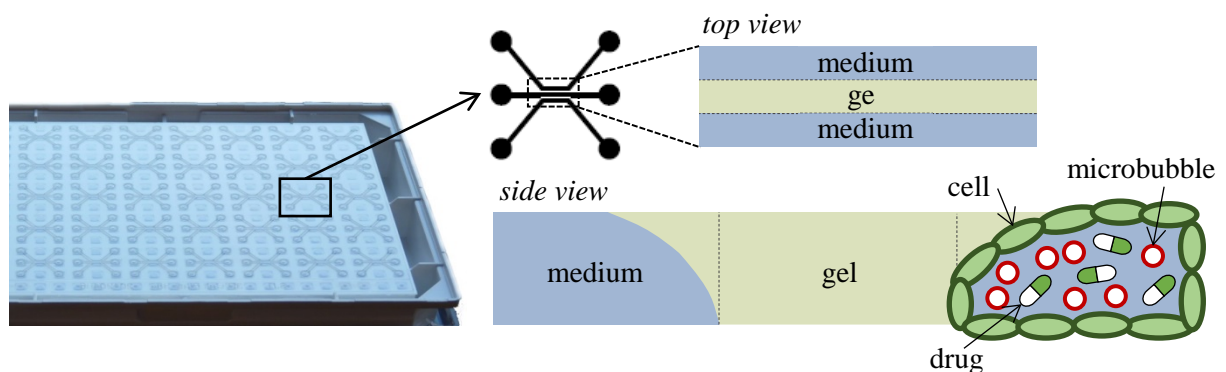


Figure 1: Bottom of the OrganoPlate™ [1] revealing the microchannel structure. The top view sketch shows the three adjacent lanes, two for medium perfusion and one containing gel, allowing for culture on soft boundaries. The side view sketch shows the gel meniscus formed in the medium channels. The bottom right illustration shows the desired *in vitro* setup with cultured endothelial cells and a flow of microbubbles and therapeutic agent in one of the medium channels.

Materials and methods

The propagation of acoustic pressure through an OrganoPlate™ was modeled with a finite element tool known as *PZFlex* [4]. We developed a 2D model of the microchannels, for both a channel width of 200 and 400 μm (Fig. 2). The ultrasound insonification was simulated by a 45° incident plane wave excitation from the bottom of the channels. The input function is a 10-cycle sine wave burst at a frequency of 1 MHz. In addition, ultrasound reflection and hydrophone transmission measurements

were performed on an OrganoPlate™ to experimentally verify the acoustic wave transmission modeled using *PZFlex*. Finally, we introduced fluorescently labeled (DiI) microbubbles with a C₄F₁₀ gas core and a DSPC (1,2-distearoyl-sn-glycero-3-phosphocholine) based shell [5] in the OrganoPlate™, next to a channel filled with gel.

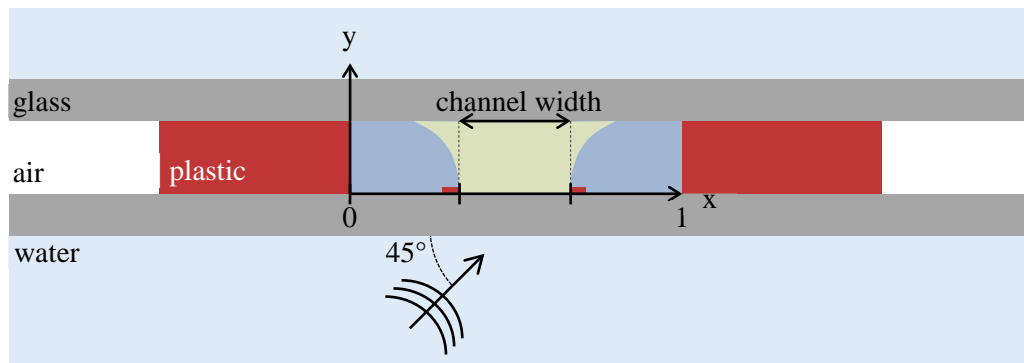


Figure 2: Sketch of the 2D model of the OrganoPlate™ insonified at 45°. The microchannels are bound by plastic walls and incorporated between two glass plates. The entire OrganoPlate™ was submerged in water. The x-axis is defined such that $x=0$ corresponds to the boundary of the plastic wall on the left and $x=1$ to the boundary on the right.

Results

The modeled transmission showed a more homogeneous pressure field in the case of a channel width of 400 μm (Fig. 3A). In addition, when comparing the two medium channels, the smallest variation in pressure was observed at the side of insonification. Also, we found a preserved frequency content after transmission into the microchannels. Although small inhomogeneities developed at the boundaries, the frequency remained uniform within the medium channels (Fig. 3B). Further, modeled amplitudes of transmission and reflection of the OrganoPlate™ were substantiated by experimental results. Finally, the microbubbles were successfully introduced into the OrganoPlate™. As expected, fluorescent imaging revealed that the bubbles floated to the highest point in the channel due to buoyancy (Fig. 4).

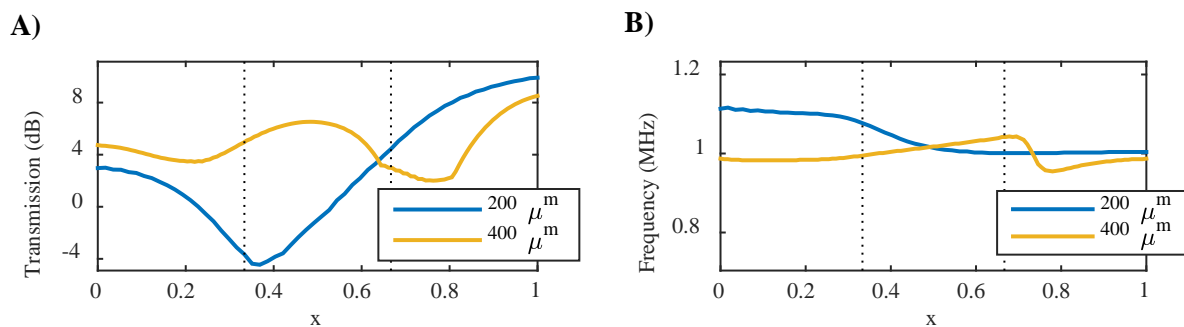


Figure 3: The modeled propagation of the acoustic pressure wave through an OrganoPlate™ having a channel width of 200 or 400 μm . **A)** Transmission, defined as the maximum amplitude relative to the incident pressure. **B)** Frequency at which most of the pressure was transmitted. Both quantities are represented as a function of the horizontal position inside the channels (see Fig. 2 for the x-axis definition). The dotted lines are the boundaries between the channels.

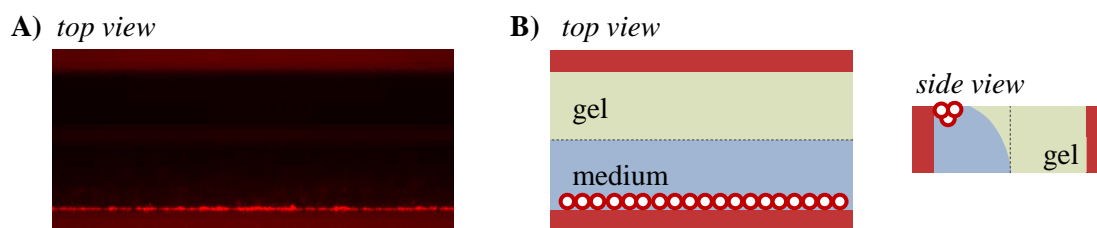


Figure 4: **A)** Fluorescent image showing two channels (horizontally), the top channel contained the gel and the bottom channel was filled with microbubbles. The microbubbles floated to the side away from the gel channel. **B)** Sketches corresponding to the fluorescent image. The microbubbles float to the highest point in the medium-filled channel.

Conclusions

The homogeneous acoustic pressure and frequency in the OrganoPlate™ demonstrates its potential to create an ideal *in vitro* model for ultrasound-mediated drug delivery. Our experimentally validated finite element model showed that the design with channels of 400 μm resulted in the most homogeneous pressure and frequency transmission. Moreover, it revealed optimal uniformity in the medium channel on the side of insonification. Therefore, we would recommend using that specific channel for cell culture, and the perfusion and insonification of microbubbles. We also observed that microbubbles in an OrganoPlate™ float up to one side of the medium channel. To achieve a more homogeneous distribution over the endothelial layer, we suggest using targeted microbubbles. Their binding capability to endothelial cells will prevent them from floating up, additionally rotating the OrganoPlate™ during the binding process will ensure a more homogeneous distribution.

Acknowledgements

The authors would like to thank Koen Sweering, Lana Keijzer and Nick Stigter for their contributions to the experimental setups.

References

1. Lellouche, J. *Future Organ-on-a-chip Global Leader MIMETAS raised 4 Million euros. The European Biotech News Website 2014 [cited 2015 Nov 10th]; Available from: <http://labiotech.eu/4-million-euros-raised-benefit-mimetas-organ-chip-technology/>.*
2. Kooiman, K., et al., *Acoustic behavior of microbubbles and implications for drug delivery. Advanced drug delivery reviews, 2014. 72: p. 28-48.*
3. Trietsch, S.J., et al., *Microfluidic titer plate for stratified 3D cell culture. Lab Chip, 2013. 13(18): p. 3548-3554.*
4. Vaughn, D. and J. Mould, *PZFlex Time Domain Finite Element Analysis Package. Los Altos, CA: Weidlinger Associates, Inc, 2001.*
5. Kooiman, K., et al., *DSPC or DPPC as main shell component influences ligand distribution and binding area of lipid-coated targeted microbubbles. European Journal of Lipid Science and Technology, 2014. 116(9): p. 1217-1227.*

Poly(vinyl alcohol) Microbubbles for Ultrasound Molecular Imaging

Barbara Cerroni[‡], Rosella Cicconi[&], Letizia Oddo[‡], Maurizio Mattei[&] and Gaio Paradossi[‡]

[‡] *Dipartimento di Scienze e Tecnologie Chimiche, Università di Roma Tor Vergata, 00133 Rome, Italy*

[&] *Centro Servizi Interdipartimentale-Stazione per la Tecnologia Animale, Università di Roma Tor Vergata, 00133 Rome, Italy*

Poly(vinyl alcohol) based microbubbles (PVA-MBs) can be considered a platform for searching new roads toward a multifunctional contrast agent.

In this contribution, we focus on an early detection of the intravascular marker of atherosclerosis by coupling α ICAM-1 antibody on the surface modified PVA-MBs. Targeted microbubbles will allow molecular imaging of the diseased endothelium by locally visualizing the protein expression over the time and following the outcome of the therapeutic treatment.

PVA shell has a longer stability than the lipid microbubbles.¹ The endurance of polymer crosslinked microbubbles to high mechanical index (nearly three times more than lipid MBs), without bursting, provides potentially higher quality images and time-lasting echographic observation. Surprisingly, PVA-MBs display an echogenicity comparable to the lipid ones, probably due to the plasticizing action of water in the hydrated polymer network constituting the shell.² Decoration of MB surface is quite handy as long as the chemistry used for the coupling with functional molecules is carried out in aqueous media.³

Here, we present a concept of surface derivatization which can be modified and customized according to the addressed pathology. The strategy used for antibody tethering consists in the use of biotin-streptavidin-biotin as strong non covalent assembly between the PVA-MB and the α ICAM-1 antibody or the non specific isotype.

The targeting efficiency was evaluated on mouse b.END5 brain endothelioma cells (ECs) and leukemic monocyte macrophage (M ϕ) RAW264.7 cells inflamed for 18 hours using TNF α and lipopolysaccharides, respectively. In vitro analysis by confocal microscopy and cytofluorimetry (Fig.1) shows that both in static and dynamic conditions, α ICAM-1 and fluorescent labeled MBs can effectively discriminate between non-inflamed and inflamed ECs and monocyte/macrophages.

In vivo tests on CD-1 mice with inflammation-induced footpad were also carried out and results will be highlighted in the poster.

1. F. Cavalieri, A. El Hamassi, E. Chiessi, G. Paradossi. *Stable Polymeric Microballoons as Multifunctional Device for Biomedical Uses: Synthesis and Characterization*. *Langmuir*, 21(19), 8758-8764 (2005)
2. D. Grishenkov, L. Kari, L.-Å. Brodin, T.B. Brismar and G. Paradossi. *In vitro contrast-enhanced ultrasound measurements of capillary microcirculation: Comparison between polymer- and phospholipid-shelled microbubbles*. *Ultrasonics*, 51(1), 40-48 (2011)
3. F. Cavalieri, A. El Hamassi, E. Chiessi, G. Paradossi, R. Villa, N. Zaffaroni. *Tethering Functional Ligands onto Shell of Ultrasound Active Polymeric Microbubbles*. *Biomacromolecules*, 7, 604-611 (2006)

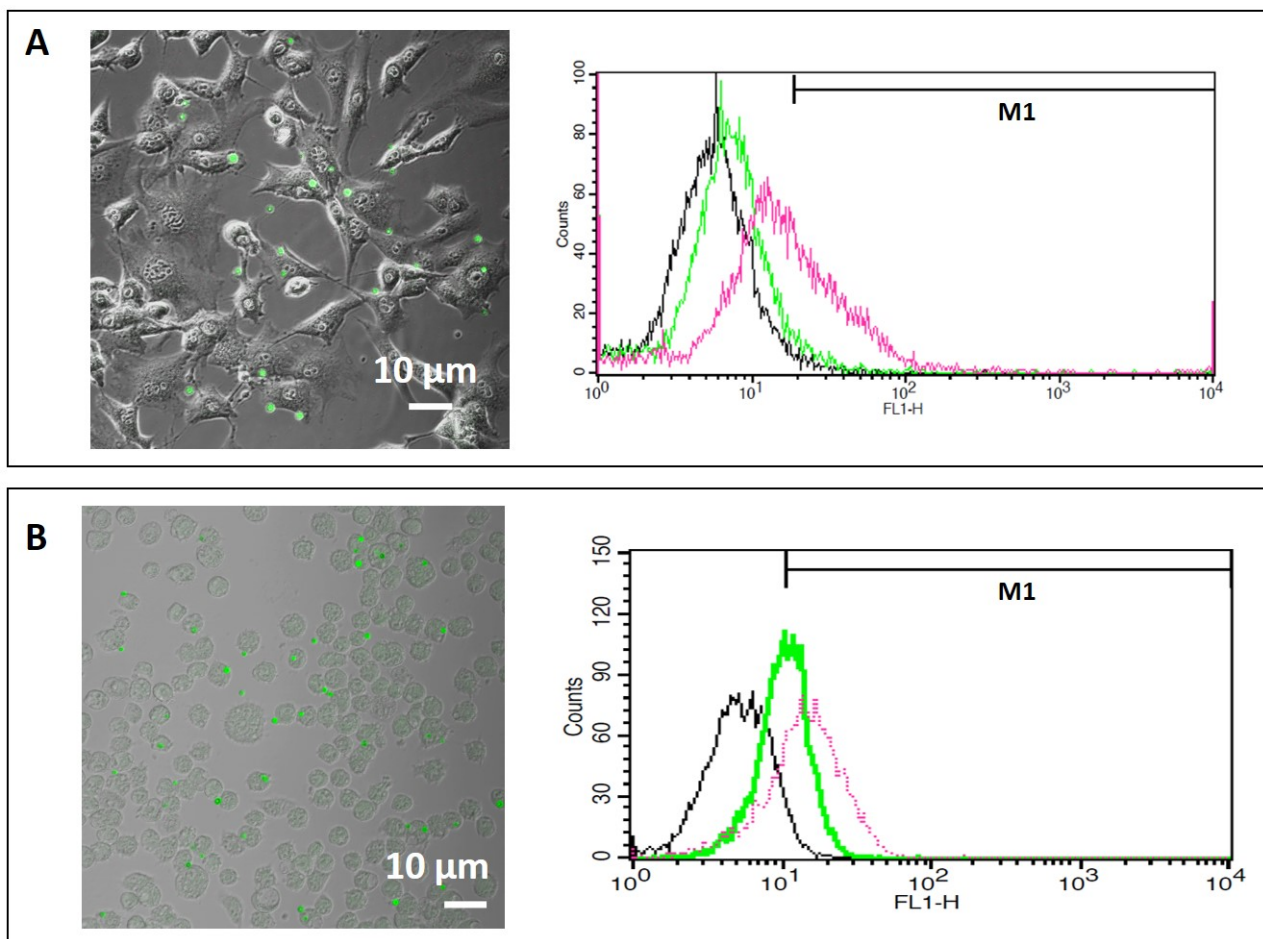


Figure 1. Left: merged (transmission and confocal imaging) micrographs of inflamed ECs (A) and Mφ (B) with fluorescein (green) labeled anti ICAM-1 MBs. Right: cytofluorimetry analysis of inflamed cells treated with no MBs (black lines), isotype MBs (green line) and α ICAM-1 MBs (pink lines).

Polymeric nanoparticles for enhancing HIFU ablation

Edyta Swider¹, Dylan Eikelenboom¹, Martijn Hoogenboom², Olga Koshkina¹, Jurgen Futterer², Gosse Adema¹, Mangala Srinivas¹

¹Department of Tumor Immunology, Radboud Institute for Molecular Life Sciences, Nijmegen, The Netherlands, ²Department of Radiology and Nuclear Medicine, Radboud University Medical Center, Nijmegen, The Netherlands

Introduction

High Intensity Focused Ultrasound (HIFU) is gaining more popularity as a tumour ablation technique in the clinic, where it has been used to treat a variety of solid malignant tumors. HIFU has the advantages of being non-invasive, with low post-treatment complications. However, the small focal volume results in a long treatment time which is a major problem. There have been several reports on the use of microbubbles in reducing the treatment time or increasing the lesion area. The downside of microbubbles is that they could result in cavitation effects, making it difficult to control the ablation area. Here, we present the effect of non-microbubble agents on MRI-guided HIFU thermal ablation.

Methods

Here, perfluoro-15-crown-5-ether was entrapped in 200 nm particles consisting of poly-lactic-co-glycolic acid (PLGA) or polyethylene glycol-PLGA (PEG-PLGA). The particles were then homogeneously distributed in a gel phantom. Ablations were carried out on a gel phantom either with or without particles, using 3 different ablation settings. To study the particle stability, particles were incubated in a thermo-block for 2 hours at 70°C. The results of particle stability were confirmed using dynamic light scattering, electron microscopy and ¹⁹F NMR.

Results

We show the effect of polymer-entrapped liquid perfluorocarbons on the temperature change and the size of the ablation. PLGA particles resulted in a maximal temperature change of around 30°C over controls without the presence of particles. The size of the ablation was larger in gel with particles as compared to empty control. The results of stability test show no change in particle diameter or fluorine content.

Conclusions

Particles used in this study were originally designed for ¹⁹F MRI and will be tested in the clinic for cell imaging in 2016. The advantage of our polymeric particles is that they are more stable than microbubbles and they may give the ability to control the ablation area. The preliminary results indicate that a HIFU treatment can be improved by the presence of polymeric particles in the ablated area.

Investigation of Polymer-Shelled Microbubbles Motions in Acoustophoresis

Dmitry Grishenkov^a, Satya Kothapalli^a, Martin Wiklund^b, Birgitta Janerot-Sjoberg^c

^a*Department of Medical Engineering, KTH Royal Institute of Technology, Stockholm, Sweden.*

^b*Department of Applied Physics, KTH Royal Institute of Technology, Stockholm, Sweden*

^c*Department of Clinical Science, Intervention and Technology, Karolinska Institute, Stockholm, Sweden.*

The objective of this study is to explore the trajectory motion of polymer-shelled microbubbles by the radiation force in standing wave acoustic fields. The experimental set-up consists of microfluidic chip coupled to a piezoelectric crystal (PZT) having a resonance frequency of about 2.8 MHz. The microfluidic channel includes a rectangular chamber with the width, w , corresponding to one wavelength. This in turn corresponds to one full wave ultrasound standing wave pattern with two pressure nodes at $w/4$ and $3w/4$, and three anti-nodes at 0 , $w/2$, and w respectively. The peak-to-peak amplitude of electrical potential over the PZT was varied between 1 and 10 Volts. From Gorkov's potential equation, the acoustic contrast factor, Φ , for the polymer-shelled microbubbles was calculated to about -100. Experimental results demonstrate that the polymer-shelled microbubbles are translated and accumulated at the pressure anti-nodal planes. First the primary radiation forces dragged polymer-shelled microbubbles into close proximity to each other at the pressure anti-nodal planes, then the secondary radiation force causing them to aggregate at different clusters along the channel. Experiments were performed at flow varied from 0 to 100 ul/min. Worth noting that the relocation time for polymer-shelled microbubbles is 40 times shorter than for solid polyamide microbeads of the same size. Furthermore, the polymer-shelled microbubbles can be actuated even at a driving voltage (which is proportional to radiation force) as low as 1 Volt, which is not the case for solid microbeads. In a conclusion, the polymer-shelled microbubbles demonstrate the behavior attributed to the negative acoustic contrast factor particles and thus can be trapped at the anti-nodal plane. This phenomenon could be utilized to explore in future applications, such as bio-assay, bio-affinity, and cell interaction studies *in vitro* in controlled environment.

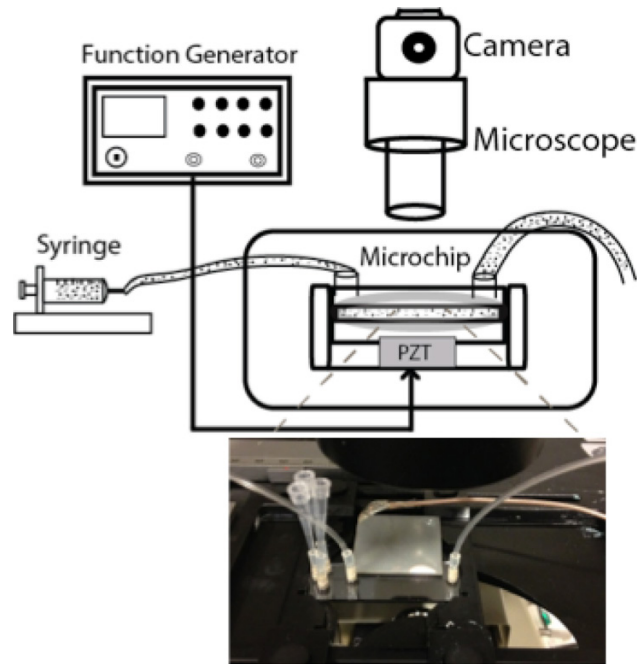


Figure 1. Schematic representation of experimental setup that consists of the silicon/glass microchip connected to PZT transducer mounted under the microscope and the CCD camera.

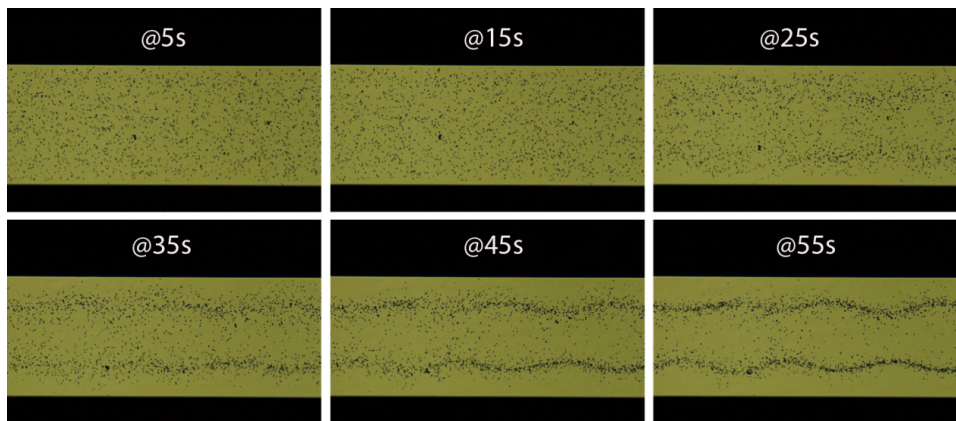


Figure 2. The microscopic images of 5 μm solid polyamide microbeads (represented in black dots) at different time intervals. Microbeads are positioned at pressure nodes.

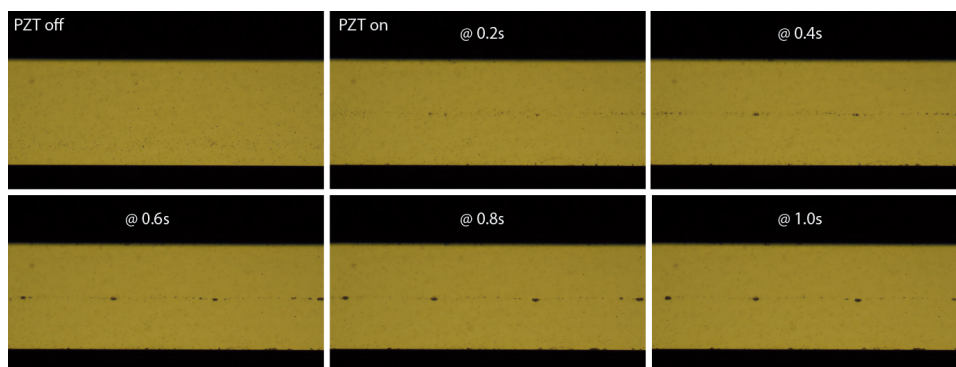


Figure 3. The microscopic images of polymer-shelled microbubbles (represented in black dots) at different time intervals. Microbubbles are positioned at pressure antinodes.

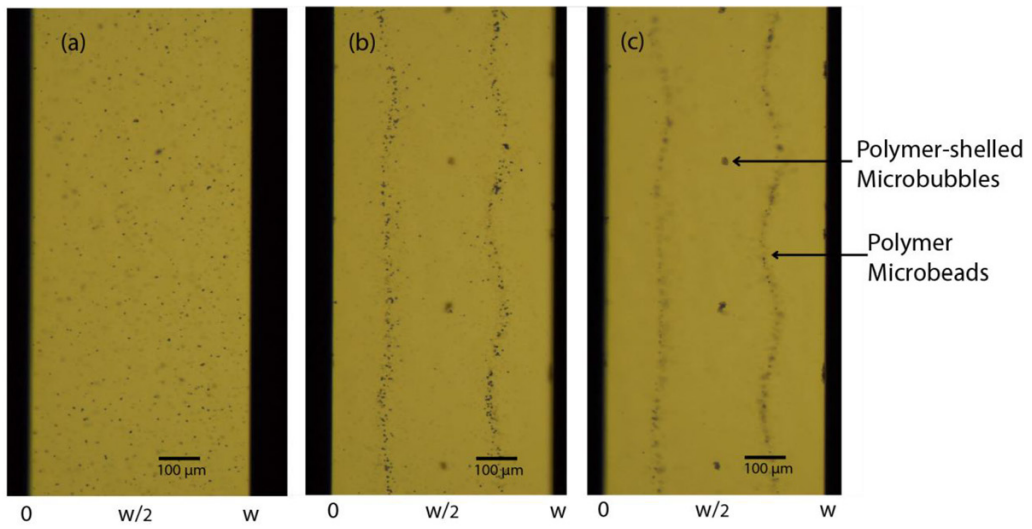


Figure 4. Microscopic images of combined polymer-shelled microbubbles and microbeads suspension in the microchip (a) before and (b) after subjected to standing wave acoustic fields.

Contrast-Enhanced Ultrasound Elastography: A Novel Method for using Acoustic Particle Palpation (APP) to Image Tissue Elasticity

*Hasan Koruk^{1,2}, Niloufar Saharkhiz¹, Ahmed El Ghamrawy¹,
Antonios N Pouliopoulos¹, James J Choi¹.*

¹Imperial College London, Royal School of Mines Building, South Kensington Campus, London, SW7 2AZ, United Kingdom, ²MEF University, Istanbul, 34396, Turkey.

Acoustic radiation force (ARF) was introduced in 1997 as a method to ‘palpate’ tissue and measure its elasticity. When the same stress was applied, soft tissue deformed more than stiffer tissue. ARF in elasticity imaging has rapidly evolved over the last two decades and is now the most prolifically used noninvasive stress source for measuring elasticity (e.g., acoustic radiation force impulse imaging and shear wave elasticity imaging). Despite this success, the resolution and sensitivity of ARF-based methods are fundamentally limited by the size and magnitude of the palpation volume, which is on the order of tens of millimetres cubed. We propose here, a novel stress source that uses acoustically-responsive particles (e.g., microbubbles) driven by ultrasound (US) to palpate tissue deep in our body. In contrast to ARF-based palpation, acoustic particle palpation (APP) can displace at a smaller resolution and higher magnitude. We will demonstrate the feasibility of APP as a stress source and present initial findings for the first contrast-enhanced ultrasound elastography technique.

We administered lipid-shelled microbubbles (MBs) (mean diameter: $1.3 \pm 0.8 \mu\text{m}$) into a wall-less 0.8-mm-in-diameter tunnel of a tissue-mimicking material (1.2%, 5%, 7.5%, 10% gelatin) so that they were compartmentally separate from the surrounding tissue. US pulses (f_c : 1, 3, 5 MHz) forced the MB against the tissue wall to cause a transient deformation, which was observed with high-speed optical microscopy. A range of acoustic pressures was evaluated for different concentrations of MBs (1X, 10X clinical dose) while optical observations were recorded before, during, and after sonication with and without MBs present.

Without the presence of MBs in the tunnel, no tissue deformation was observed. However, when MBs were administered, a net displacement of MBs was observed in the direction of wave propagation (figure), which ultimately caused the tissue to deform in the same direction. The deformation magnitude increased with peak-rarefactional pressure and MB concentration. We also observed shear waves propagating away from the region of palpation at a velocity of $0.39 \pm 0.03 \text{ m/s}$ for a 2.5% gelatin phantom and $0.71 \pm 0.07 \text{ m/s}$ for a 5% gelatin phantom. This resulted in an estimated Young’s modulus of $0.46 \pm 0.06 \text{ kPa}$ and $1.54 \pm 0.32 \text{ kPa}$ for the 2.5% and 5% gelatin phantoms, which was in good agreement with values found in the literature. Clinically relevant US and MB parameters were used and our future work will incorporate APP into elasticity imaging systems by palpating (impulse, quasi-static, harmonic) and imaging deformations on- and off-site (impulse, shear wave imaging). To our knowledge, APP is the first stress source that uses clinically relevant acoustic particles to measure tissue elasticity and could be the first contrast-enhanced ultrasound elasticity imaging method.

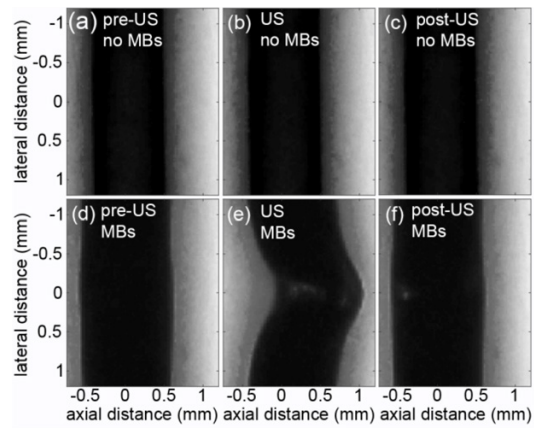


Figure. Feasibility of Acoustic Particle Palpation. A wall-less vessel phantom (1.2% gelatin) contained (a, b, c) water only or (d, e, f) microbubbles. The images are zoomed into the focal volume (a, d) before, (b, e) during, and (c, f) after ultrasound exposure (f_c : 5MHz, P_{neg} : 400kPa). US propagated left to right and produced (b) no displacement with ultrasound alone, and (e) a large displacement with microbubbles.

Development of a branched microfluidic platform for acoustic quantification of microbubble populations

Samira Jamalian, Shengtao Lin, Claudia Feldman, Yesna Yildiz, Virginie Papadopoulou, Martin Ward, Robert Eckersley, Meng-Xing Tang, James Moore

james.moore.jr@imperial.ac.uk

The lymphatic system is the route of metastatic spread for all of the deadliest forms of cancer. Accurate assessment of lymphatic flow pathways from tumour regions is crucial for prognosis. In breast cancer patients, sentinel lymph node (SLN) excision biopsy is the traditional procedure for axillary staging. However, about 35% of patients show nodal metastasis and require additional surgery after excision biopsy. Recent studies suggest that lymphatic vessels and SLNs could be dynamically visualized using microbubble contrast agents for preoperative biopsy of SNL in breast cancer patients [1]. By performing ultrasound-guided biopsies only patients with SNL metastasis proceed to axillary lymph node dissection and unnecessary SNL excision biopsies are prevented. More work is required to improve ultrasound mapping of tumor lymphatic drainage to facilitate preoperative lymph node assessment and surgical planning.

The ability to determine vessel size from acoustic response of microbubbles in ultrasound imaging can significantly improve the diagnostic power of such imaging techniques [2]. In addition to detecting lymphatic vessels that lead to lymph nodes, identifying vessel size specific behaviours is useful for detecting microvasculature of tumors as well as small blood vessels around arterial plaques. We have developed a novel microfluidic platform with a branched network of microchannels of different sizes, built within a layer of PolyDimethylSiloxane (PDMS) with elastic properties close to soft tissue. Importantly, this system enables us to exclusively identify the effect of channel size on acoustic behaviour as a single microbubble solution is pushed through the microchannel network, while material properties remain unchanged. Previous measurements of microvessels of different sizes focused on single vessels and did not have control over material properties [3,4]. Thus, the microfluidic system described here provides us with the required tool to expand our understanding of microbubble populations' response in microvascular networks.

We designed and constructed a microfluidic mold containing a symmetric bifurcating network (Fig. 1) using soft lithography technique. The inlet channel is 400 μm wide; the channel width is halved after each branching point, resulting in 200, 100, and 50 μm channel sizes. The feature height is 50 μm throughout the network. To capture the physiological elastic properties, we used a combination of Sylgard 184 and Sylgard 527 (Dow corning) to create PDMS substrates for fabrication of the microfluidic device [5]. Sylgard 184 was prepared with 10:1 ratio of base to curing agent, and Sylgard 527 with 1:1 ratio of part A and B (according to manufacturer's instructions). Each Sylgard was thoroughly mixed and let to de-bubble in a desiccator for 15-20 minutes until bubble free. To create the final blend, pure Sylgards, prepared as described above, were mixed with the desired mass ratio followed by an additional de-bubbling step.

Among several mass ratios tested, we found that a 1:4 ratio of Sylgard 184:527 provided the optimal functionality (in terms of imaging and mechanical properties for fabrication of the device) with Young's modulus of around 250 kPa. The final blend was poured in a 12 mm

petri dish with the microfluidic mold placed and secured at the bottom, to create 4 mm thick PDMS substrates with the branched microchannel structure. The PDMS solution was left in the oven at 65 °C to cure for 24h. After removal from the oven, PDMS layer was carefully detached from the mold and inlet and outlet reservoirs were pierced through the substrate. To make the second piece for the microfluidic device, the same PDMS mixture (prepared as described above) was poured in an empty 12 mm petri dish. After curing in the oven at 65 °C for 50 minutes, the detached and cured substrate was carefully positioned on the partially cured piece and let to fully cure in the oven for an additional 24h at 65 °C. The 50-minute period was found to be the sufficient time required for the two PDMS pieces to fully attach without blocking the channels (Fig. 2).

Pulse-inversion imaging with a phased array probe with a central frequency of 2MHz and a mechanical index of 0.15 was used to collect acoustic response of microbubbles. Microbubble solution filled the microfluidic system at a physiologically relevant flow rate using a syringe pump. The number of microbubbles was calculated from the known concentration and volume (concentration \times volume). The scattered amplitude of microbubble (scattering per microbubble measure) in a region of interest was calculated by dividing the average pixel intensity and number of microbubbles in that region. Preliminary results indicated that the scattered pressure response from microbubbles is dependent on the channel size and considerably decreases in smaller microchannels (about 40% decrease from 200 μ m to 50 μ m vessel) [6].

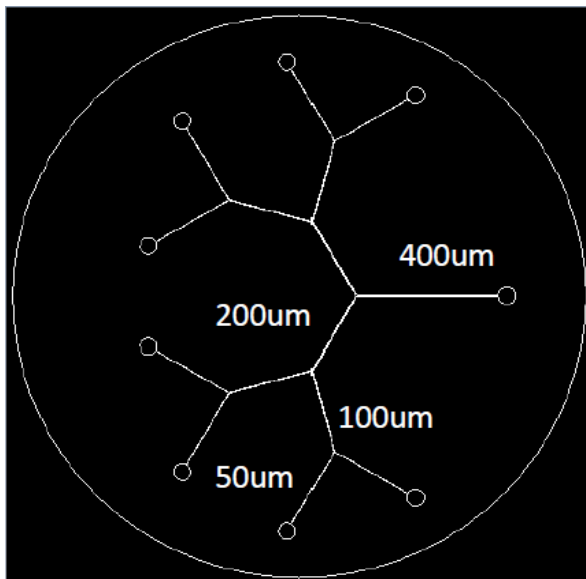


Figure1. Schematic representation of the bifurcating network of microchannels.

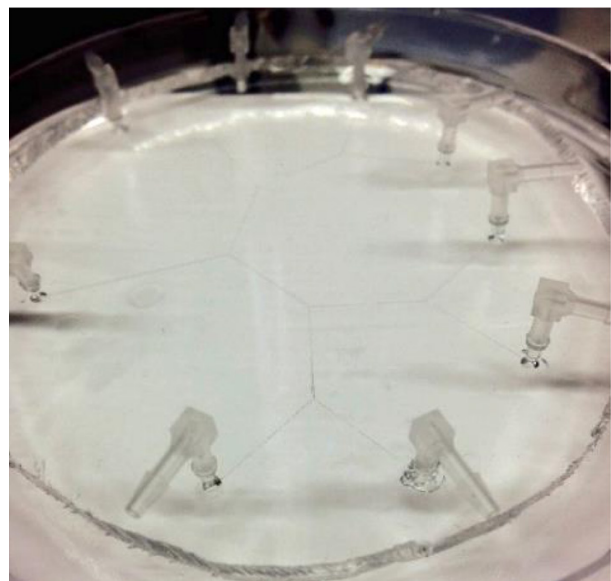


Figure2. Image of the microfluidic platform, with a view of branched channels formed between the two PDMS pieces.

References:

1. Sever AR, Mills P, Jones SE, Cox K, Weeks J, Fish D, Jones PA. Preoperative sentinel node identification with ultrasound using microbubbles in patients with breast cancer. *AJR Am J Roentgenol* (2011) 196(2):251-6. doi: 10.2214/AJR.10.4865
2. Butler MB, Dermitzakis A, Thomas D, Looney P, Pye S, Sboros V. Single microbubble acoustics in small tubes. 2010 ICA
3. Thomas DH, Sboros V, Emmer M, Vos HJ, De Jong N. Microbubble oscillations in capillary tubes. 2013 UFFC IEEE
4. Caskey CF, Kruse DE, Dayton PA, Kitano TK, Ferrara KW. Microbubble oscillation in tubes with diameters of 12, 25, and 195 microns. *Appl. Phys. Lett.* 88, 033902 (2006). doi: 10.1063/1.2164392
5. Palchesko RN, Zhang L, Sun Y, Feinberg AW. Development of Polydimethylsiloxane Substrates with Tunable Elastic Modulus to Study Cell Mechanobiology in Muscle and Nerve. *PLoS ONE* (2012) 7(12): e51499. doi: 10.1371/journal.pone.0051499
6. Ward M, Yildiz Y, Papadopoulou V, Eckersley RJ, Tang M-X. Modelling of ultrasound contrast agent oscillations in vessels based on an infinite mirror image method. 2015 IUS IEEE

Estimation of Medical Microbubble and Liquids Properties by Acoustic Resonance Interference Spectroscopy

Spencer, S.J.

*Manufacturing – CSIRO - Sydney, NSW, Australia
steven.spencer@csiro.au*

Contrast-enhanced ultrasound (CEUS), based on the acoustic response of encapsulated microbubbles, is now in clinical usage in many countries. Targeted CEUS (molecular imaging), utilising selective binding of microbubble conjugated ligands to receptors expressed in regions of abnormal or diseased tissue, is under preclinical investigation. This approach is also being investigated for targeted delivery of therapeutics loaded on microbubble surfaces. CEUS exploits the enhanced echogenicity of microbubbles with respect to surrounding tissue to generate high contrast sonograms. However, the acoustic response of microbubbles to insonation across a range of frequencies can be used to gain additional information relevant to the properties of both the microbubbles themselves and the surrounding liquid medium. This spectral information potentially allows new CEUS imaging modalities to be developed.

The method of *acoustic resonance interference spectroscopy* (ARIS) is described for estimation of encapsulated microbubble and surrounding liquid properties¹. A modified ‘Rayleigh-Plesset’-like non-linear equation is used to model the radial oscillation of the wall of an encapsulated microbubble loaded with attached mass, subject to excitation by an acoustic source. Perturbation theory is used to derive approximate analytical solutions for bubble radius small-amplitude response in terms of harmonic oscillations. The perturbation method approximate solution for acoustic pressure generated by the bubble at a hypothetical receiver in an incompressible liquid is found as a function of the frequency of acoustic excitation. Analytical solutions for the frequencies of the fundamental resonance maximum, source – bubble response interference minimum and second harmonic resonance maximum in total pressure power at the receiver are found as a function of the properties of the bubble, liquid medium, acoustic source and system geometry. Unique solutions to the inverse problem for estimation of system properties such as microbubble equilibrium radius, attached mass and encapsulating layer dilatational viscosity; and liquid medium viscosity and density are found in terms of the frequencies of these acoustic spectroscopic features.

This paper will describe some details of the ARIS technique as relevant to medical microbubbles. The theoretical ARIS signatures of several commercially available ultrasound contrast agents (UCAs) are demonstrated. The possibility of using commercially available UCAs as diagnostic tools for estimating the rheological properties of biological liquids is explored. The potential sensitivity of the method for detection of the progressive delivery of therapeutic agents loaded on microbubbles is also discussed.

¹ *Spencer, S.J. , Journal of the Acoustical Society of America* **2015** 137(5), 2623-2641.

High Throughput Characterisation of Single Contrast Agent Microbubbles – Towards Optimisation of Contrast Enhanced Imaging

Paul Rademeyer, Dario Carugo, Richard Browning, Eleanor Stride

Institute of Biomedical Engineering, Department of Engineering Science, University of Oxford, Old Road Campus OX3 7DQ

The utility of microbubble agents in a variety of diagnostic and therapeutic ultrasound techniques has been widely demonstrated, most notably in Contrast Enhanced Ultrasound (CEUS) imaging. There remains, however, considerable scope for optimisation, in particular in the development of quantitative imaging techniques e.g. for perfusion imaging and treatment monitoring.

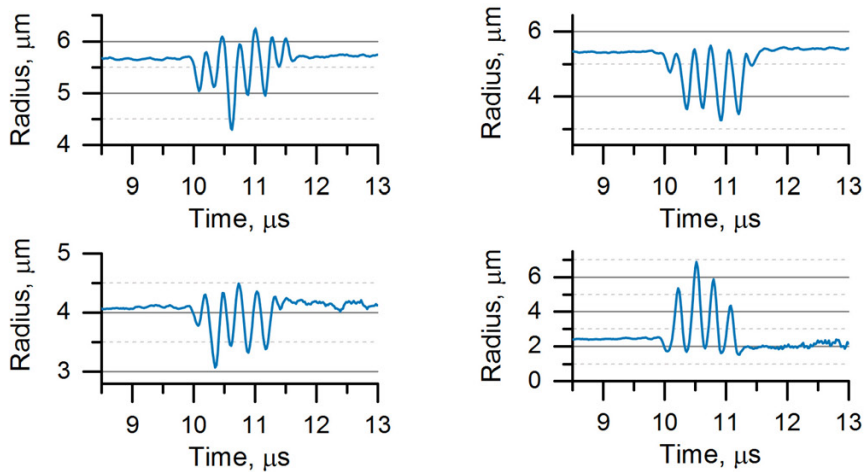
A major challenge lies in the current lack of understanding and hence predictability of the response of microbubbles to ultrasound excitation. Whilst vital insights have been gained from characterisation techniques such as ultra high speed imaging, these methods are limited by the need to confine microbubbles against a rigid surface and their complexity which limits the number of bubbles that can be analysed in a single experiment. The authors have previously presented a new experimental technique¹ that is able to overcome these limitations and perform high throughput measurements of single microbubbles hydrodynamically isolated from physical boundaries using light scattering. The aim of this study was to apply the technique to characterise the response of large samples of a clinical contrast agent, SonoVue®, under different ultrasound conditions.

The responses of several thousand microbubbles were recorded for each set of conditions. Examples of the radial responses of isolated microbubbles obtained are shown in figure 1a. There were a number of interesting findings:

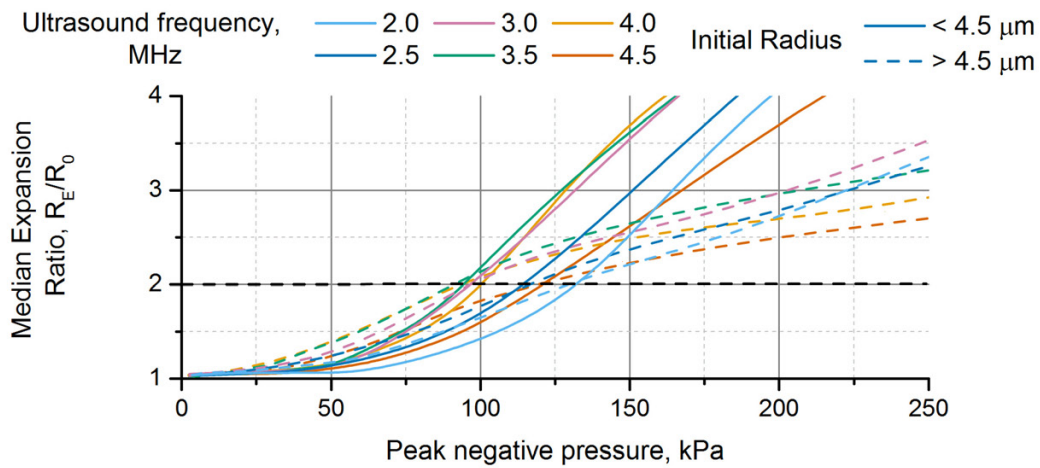
- (i) The measurements confirmed that for all sizes of microbubble there is considerable variation in response which complementary measurements of microbubble surface properties indicates is likely to be due to a lack of uniformity in microbubble coating.
- (ii) At peak negative driving pressures of 50kPa or above there was found to be a proportional relationship between driving pressure and the scattered acoustic power from the microbubbles with no observable resonance effects when the response of the population was examined as a whole.

¹ Rademeyer, P., Carugo, D., Lee, J.Y. and Stride, E., *Microfluidic system for high throughput characterisation of echogenic particles, Lab on a Chip*, 2015,15, 417-428

a) Example radial traces



b) Size dependent expansion ratio as a function of peak negative pressure



c) Estimated backscattered acoustic pressure compared to stability

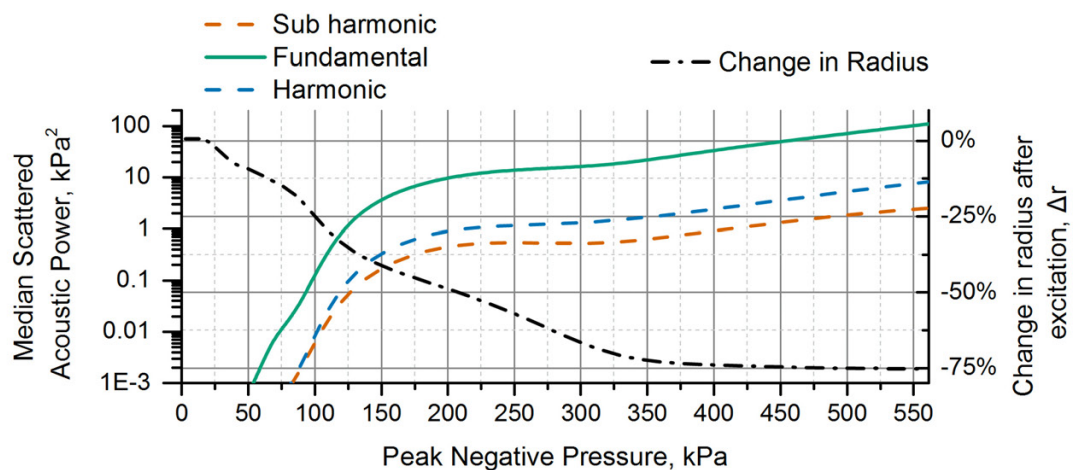


Figure 1. a) Example radial responses of SonoVue microbubbles measured using light scattering, b) there is a trade off between back scattered pressure and microbubble stability and c) median expansion ratio for various microbubble compositions demonstrates significant effect of adding nano-particles during fabrication.

(ii) Non-linear responses were observed as compression and expansion dominated behaviours at pressures as low as 6 kPa and there was a transition from compression to expansion dominated behaviour as the peak negative driving pressure increases from 50 kPa upto 100 kPa (figure 1b).

(iii) Up to peak negative pressures of 100 kPa the expansion ratio (R_{max}/R_o) was found to be proportional to initial microbubble radius, but above this pressure it became inversely proportional.

(iv) Evidence of lipid shedding was observed as a change in microbubble size after ultrasound excitation (figure 1c) and there was found to be a linear relationship between peak negative pressure and decrease in size; with the effect increasing with the number of cycles in the driving ultrasound pulse.

(v) 'Inertial Cavitation' defined as a microbubble expanding twice its initial radius was found to occur at peak negative pressures of ~ 100 kPa for the majority of microbubbles at all frequencies tested (figure 1b). Above this threshold microbubbles smaller than $4.5 \mu\text{m}$ show higher expansion ratios than those larger than $4.5 \mu\text{m}$ which is the opposite trend to below this pressure. This was found to agree well with theoretical predictions.

The implications of these findings for the design and optimisation of contrast imaging strategies and potential bioeffects will be discussed.

Laser driven microbubbles as multimodal contrast agents

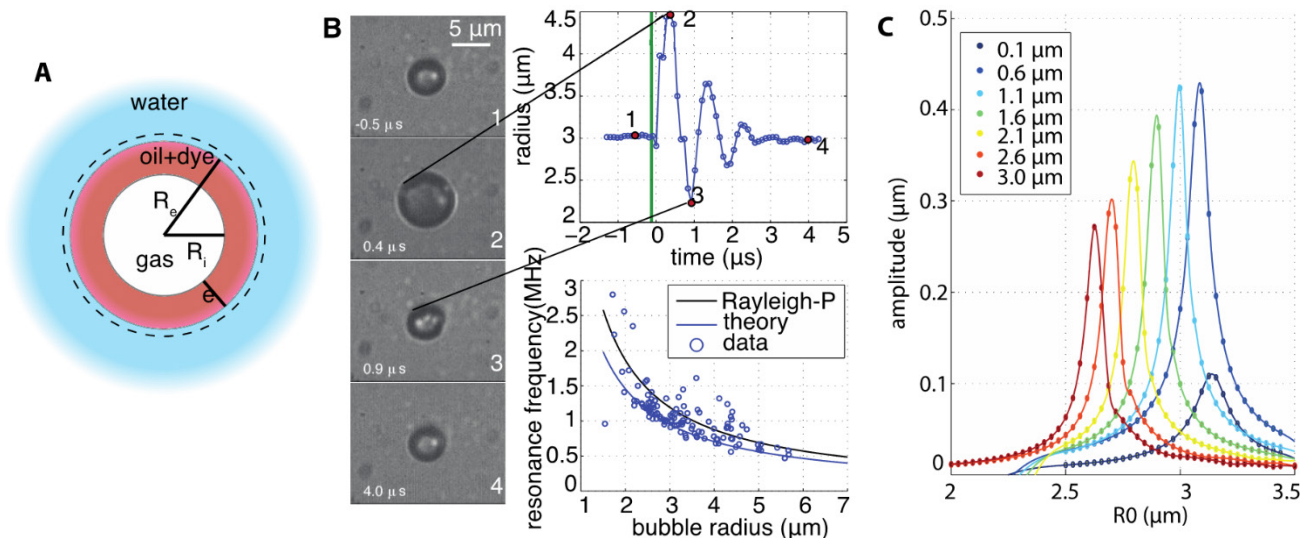
Guillaume Lajoinie¹, Jeong-Yu Lee³, Erik Linnartz¹, Joshua Owen³, Pieter Kruizinga², Gijs van Soest², Nico de Jong², Eleanor Stride³ and Michel Versluis¹

¹*Physics of Fluids Group, MIRA Institute for Biomedical Technology and Technical Medicine and MESA+ Institute for Nanotechnology, University of Twente, P.O. Box 217, 7500 AE Enschede, The Netherlands*

²*Biomedical Engineering, Erasmus MC, P.O. Box 2040, 3000 CA Rotterdam, The Netherlands*

³*Institute of Biomedical Engineering, Department of Engineering Science, University of Oxford, Old Road Campus, Oxford OX3 7DQ, UK.*

Our ability to remotely probe soft tissue in the human body is a focus for medical imaging research. Improved imaging quality and higher sensitivity leading to an earlier diagnosis are our best chance in fighting a number of diseases such as cancer. Ultrasound imaging has been established as a safe and affordable technique to probe structures deep into tissue with a high resolution but at relatively low contrast. Although bound by a more superficial penetration, light presents a very specific interaction with matter. In order to allow the simultaneous use of both acoustical and optical modalities, we present a micron-sized agent consisting of a gas core encapsulated by a lipid layer, itself loaded with a dye. The resulting laser light absorption can then be used to thermally drive the bubble at its resonance in the MHz range. The agents can be driven in a pulsed excitation scheme, as well as amplitude modulated by an AOM continuous wave laser. We developed a full theoretical description of these new agents as well as an experimental proof of concept showing quantitative agreement.



A. Schematic representing the proposed agent: a bubble coated with an absorbing oil layer.

B. Example response of a single bubble to a pulsed laser. **C.** Theoretical resonance curves of bubbles coated with an oil layer of variable thickness. The bubble is driven using a 1MHz modulated CW laser.

Can bolus wash-in/washout analysis measure flow changes in the liver microvasculature?

Mike Averkiou¹, Christina Keravnou^{1,2}, Maria-Louisa Izamis² and Ed Leen³

¹University of Washington, Department of Bioengineering, Seattle, WA, USA

²University of Cyprus, Department of Mechanical Engineering, Nicosia, Cyprus

³Imperial College, Hammersmith Hospital, London, UK

Objective:

To evaluate dynamic contrast enhanced ultrasound (DCEUS) as a tool for measuring blood flow in the macro- and micro-circulation of an ex-vivo machine-perfused pig liver. Confirm the ability of DCUES to accurately detect induced flow rate changes so that it could be then used as a clinical tool for monitoring flow changes in liver tumors.

Materials and Methods:

Three fully functioning, machine-perfused pig livers were used in the present study. Flow changes were induced by the pump of the machine perfusion system and they naturally propagated to the liver macro- and micro-vasculature. The induced flow changes were of clinical relevance (150-400 ml/min for the hepatic artery and 400-1400 ml/min for the portal vein) and similar to those taking place during tumor growth or during therapeutic procedures targeting tumor angiogenesis. From DCEUS image loops after bolus injections in either the hepatic artery or the portal vein, time-intensity curves were formed and the Local Density Random Walk indicator dilution model was fitted on the data. From the fitted model various quantification parameters [rise time (RT), mean transit time (MTT), area under the curve (AUC) and peak intensity (PI)] were extracted in order to evaluate whether the induced flow changes were reflected in these parameters. The quantification parameters are related to flow with known indicator dilution relationships.

Results:

A linear relationship between the image intensity and the microbubble concentration was confirmed first ($R^2=0.8-0.93$ for PV injections and $R^2=0.72-0.93$ for HA injections), while time parameters (rise time and mean transit time) were found to be independent of concentration. This result enables the use of indicator dilution methods for measuring flow in the liver vasculature. The induced flow changes which propagated from the larger vessels to the parenchyma and the hepatic vein tree were successfully reflected in the quantification parameters extracted from the indicator dilution model. Specifically, RT, MTT and area AUC correlated with flow rate changes (curve fits with $0.81 < R^2 < 0.93$ for HA and PV main vessels, $R^2=0.91$ for HV, and $R^2=0.66$ for parenchyma) while the PI stayed constant. The above results are in agreement with the indicator dilution relationships.

Conclusion:

Ex-vivo machine perfused pig liver is an excellent test-bed for DCEUS quantification approaches for measuring flow changes in the macro- and micro-circulation and it allows for the study of the hepatic vascular networks. Bubble concentration does not affect time quantification parameters and thus variations in the amount of injected microbubbles in the clinic will not affect the quantification results. DCEUS quantification parameters (RT, MTT, and AUC) can measure relative flow changes of about 20% and above in the liver vasculature. DCEUS quantification is a promising tool for real-time monitoring of therapeutic applications which target the vascular network of tumors.

Contrast ultrasound dispersion imaging in prostate cancer: an update

M. Mischì¹, S. Turco¹, R. van Sloun¹, S. Schalk¹, L. Demi¹, H. Wijkstra^{1,2}

Biomedical Diagnostics Lab, Electrical Engineering Dept, Eindhoven University of Technology, the Netherlands

Urology Dept, Academic Medical Center University of Amsterdam, the Netherlands

In Western countries, Prostate Cancer (PCa) is the most common form of cancer in men, accounting for 26% of new cancer cases and 9% of cancer-related deaths; yet the available diagnostic options are limited by the lack of reliable imaging solutions [1]. Dynamic Contrast-Enhanced UltraSound (DCE-US) is a diagnostic tool that is suitable for analysis of the vascularization, by imaging an intravenously-injected bolus of ultrasound contrast agents. The localization of angiogenic vascularization associated with cancer growth is of particular interest for the diagnosis of aggressive cancer [2]. Recently, methods for the analysis of the bolus convective-dispersion process have shown promise to localize angiogenesis. These are implemented by fitting the modified local density random walk model to time-intensity curves (TICs) measured at each pixel [3], or by estimating the similarity between neighboring TICs [4-6]. Several similarity measures have been adopted ranging from spectral coherence [4-5], to temporal correlation [6], up to nonlinear measures such as mutual information [7]. More recently, extension to 3D has also been shown, enabling the analysis of the full prostate volume by the injection of a single bolus of ultrasound contrast agents [8].

By all these methods, independent estimation of dispersion was not possible due to the ambiguity between convection and dispersion. Here a new method is presented that provides the separate estimation of convection and dispersion by identification of the local (linear) dilution system. To this end, model-based parameter estimation is employed. The method also permits generating maps of the Péclet number (Pe), a physics parameter characterizing the dilution system [9]. Clinical evaluation using data recorded from 25 patients (61 planes) at the Academic Medical Center, University of Amsterdam (the Netherlands), shows that the proposed method can be applied effectively to DCE-US, and is able to locally characterize the hemodynamics, yielding promising results for prostate cancer localization. Comparison of the resulting Pe maps with the histological results following radical prostatectomy showed an area under the ROC curve of 0.84, superior to all the other methods.

In addition, use and modeling of ultrasound contrast agents that are targeted to angiogenic expressions (BR55, Bracco Suisse), such as the vascular endothelial growth factor receptor 2 (VEGF-R2), are tested in rat models of human prostate cancer. A convective-dispersion model is used to describe the kinetics of circulating bubbles while a single-compartment model is used to describe bubble binding/unbinding kinetics. Identification of the proposed analytical model enables the assessment of both vascular and molecular features, determined by the dispersion and binding kinetics of the agent, showing promise for future applications aimed at PCa localization. In general, the proposed methods for angiogenesis imaging are not specific to prostate cancer only, and future extension to other types of cancer can also be envisaged.

1. *Cancer Facts & Figures*, American Cancer Society, 2015.
2. Weidner N, Carroll PR, Flax J, Blumenfeld W, Folkman J. Tumor angiogenesis correlates with metastasis in invasive prostate carcinoma. *American Journal of Pathology* 1993;143:401-9.
3. Kuenen MP, Mischi M, Wijkstra H. Contrast-ultrasound diffusion imaging for localization of prostate cancer. *IEEE Transactions on Medical Imaging* 2011;30:1493-502.
4. Mischi M, Kuenen MP, Wijkstra H. Angiogenesis imaging by spatiotemporal analysis of ultrasound contrast agent dispersion kinetics. *IEEE Trans Ultrason Ferroelectr Freq Control* 2012;59:621-9.
5. Kuenen MP, Saidov TA, Wijkstra H, Mischi M. Contrast-ultrasound dispersion imaging for prostate cancer localization by improved spatiotemporal similarity analysis. *Ultrasound Med Biol* 2013;39:1631-41.
6. Kuenen MP, Saidov TA, Wijkstra H, de la Rosette JJ, Mischi M. Spatiotemporal correlation of ultrasound contrast agent dilution curves for angiogenesis localization by dispersion imaging. *IEEE Trans Ultrason Ferroelectr Freq Control* 2013;60:2665-9.
7. Mischi M, Bouhouch N, Demi L, et al. Contrast-ultrasound dispersion imaging of cancer neovascularization by mutual-information analysis. *2014 IEEE International Ultrasonics Symposium (IUS) 2014*:1148-51.
8. Schalk SG, Demi L, Smeenge M, Mills DM, Wallace KD, de la Rosette JJ, Wijkstra H, Mischi M. 4-D spatiotemporal analysis of ultrasound contrast agent dispersion for prostate cancer localization: a feasibility study. *IEEE Trans Ultrason Ferroelectr Freq Control* 2015;62:839-51.
9. Mischi M, "Contrast Echocardiography for Cardiac Quantifications", PhD Thesis, Eindhoven University of Technology, 2004.

Cumulative Phase Delay Imaging

Libertario Demi¹, Ruud J.G. Van Sloun¹, Hessel Wijkstra^{2,1}, Massimo Mischi¹

¹*Department of Electrical Engineering, Lab. of Biomedical Diagnostics, Eindhoven University of Technology, the Netherlands*

²*AMC University Hospital, Amsterdam, the Netherlands.*

Introduction

As cancer needs nutrients and oxygen to grow and spread, it triggers angiogenesis and neovascularization. Consequently, there is growing interest in developing imaging modalities able to detect, localize, and visualize these processes. To this end, dynamic contrast-enhanced ultrasound (DCE-US) represents a valuable option. Unfortunately, performing handheld DCE-US is challenging for the breast as, unlike X-ray CT or MRI, DCE-US imaging of the breast is highly operator dependent.

Based on our recent discovery of a new marker for ultrasound contrast agents (UCAs) [1-2], we are currently developing a novel imaging technique named cumulative phased delay imaging (CPDI). CPDI could potentially lead to the development of three-dimensional contrast-enhanced ultrasound computed tomography (3D CEUS-CT), providing a radiation-free imaging modality that enables visualization of the whole breast vascular architecture in 3D. Such an imaging modality would open new horizons for the detection and localization of breast cancer.

Method

A (positive) cumulative phase delay (CPD) between the second harmonic (2H) and fundamental (F0) component is observable for ultrasound (US) propagating through UCA. This delay is dependent on agent concentration, propagation path length through UCA, pressure field amplitude, and insonating frequency. Most importantly, this delay is absent in tissue, and clearly observable at frequencies (2.5 MHz) and pressure regimes ($0.05 < MI < 0.2$) of interest for clinical application [1-2]. Consequently, variations in the total time delay between 2H and F0 can be exploited to image and detect UCAs.

Results

Numerical and *in-vitro* studies confirmed the applicability of CPDI for contrast specific US imaging [2-3], with CPDI showing superior capabilities in detecting and localizing UCA, as compared to speed-of-sound and dispersion-based US tomography [3-4]. Furthermore, phantom experiments showed how cavities of different size (filled with UCA and surrounded by tissue-mimicking material), which were down to 1 mm in diameter, could clearly be detected [3] (see Figure 1). CPD image values relate to the measured delay, which is here expressed in cycles/m.

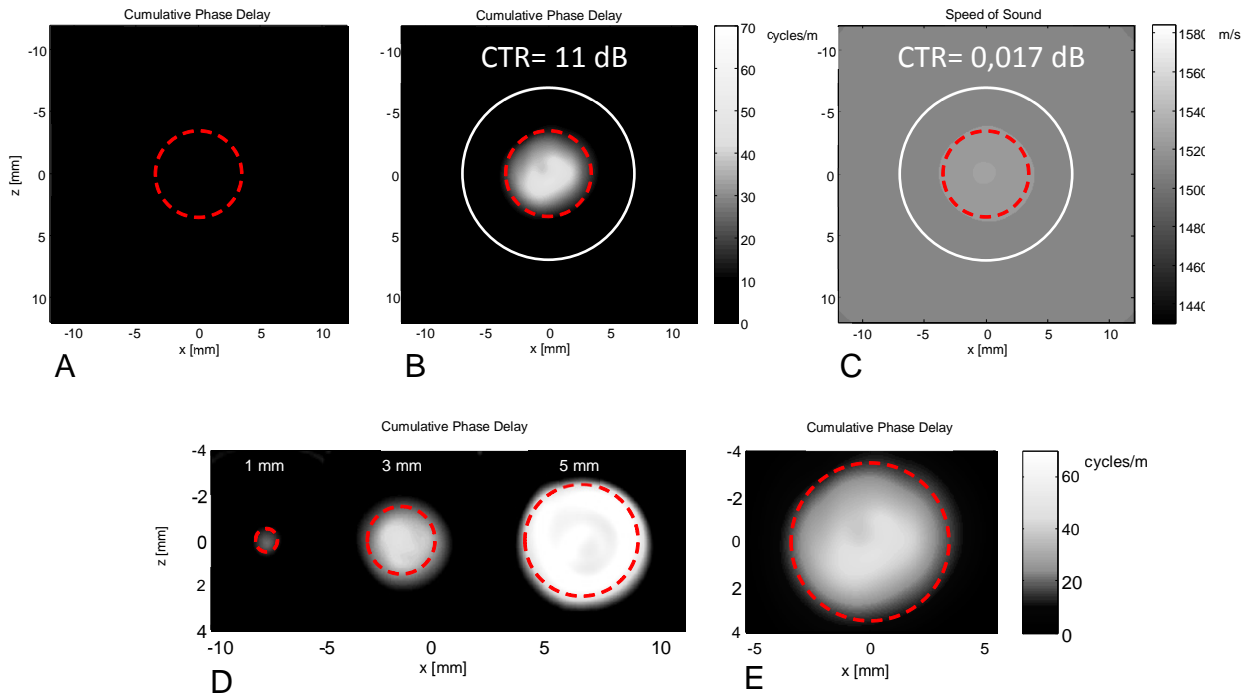


Figure 1: CPD images of a tissue-mimicking phantom containing a 7-mm cavity filled with (A) only saline and (B) SonoVue®. (C) Speed of sound tomographic image as obtained for the same intra-cavity UCA concentration. Contrast to tissue ratio (CTR) values are also shown. CPD images of tissue-mimicking phantoms containing (D) three cavities (measuring from 1 to 5 mm in diameter) and (E) a single 7-mm cavity filled with SonoVue® [3].

Conclusion and Discussion

CPDI may find relevant application to the development of contrast enhanced ultrasound tomography of the breast aimed at angiogenesis imaging for cancer detection and localization. To this end, investigating the performance of CPDI in estimating UCA flow dynamics and imaging more complex and heterogeneous targets will be the focus of future work.

References

1. L. Demi, G. Russo, H. Wijkstra, and M. Mischi "Observed Cumulative Time Delay Between Second Harmonic and Fundamental Component of Pressure Wave Fields Propagating Through Ultrasound Contrast Agents", *Proceedings of Meetings on Acoustics 20*, San Francisco, 075002, 2013.
2. L. Demi, H. Wijkstra, and M. Mischi "Cumulative phase delay between second harmonic and fundamental components - A marker for ultrasound contrast agents", *Journal of the Acoustical Society of America*, 136, pp. 2968 - 2975, 2014.
3. L. Demi, R. J.G. Van Sloun, H. Wijkstra, and M. Mischi, "Cumulative phase delay imaging for contrast-enhanced ultrasound tomography", *Physics in Medicine and Biology*, vol. 60, no. 21, pp. L23 L33, 2015.
4. L. Demi, R. J.G. Van Sloun, H. Wijkstra, and M. Mischi, "Contrast enhanced ultrasound tomography by means of the cumulative phase delay between second harmonic and fundamental component", *International Ultrasonics Symposium IEEE*, Taipei, Taiwan, 2015.

The chicken embryo chorioallantoic membrane model for studying microbubbles *in vivo*

Ilya Skachkov¹, Antonius F.W. van der Steen^{1,2}, Nico de Jong^{1,2}, Klazina Kooiman¹.

¹ Dept. of Biomedical Engineering, Thoraxcenter, Erasmus MC, Rotterdam, the Netherlands

² Laboratory of Acoustical Wavefield Imaging, Faculty of Applied Sciences, Technical University Delft, Delft, the Netherlands

To study microbubble behavior for ultrasound imaging and drug delivery, a simple, cheap, and relevant model is desired. All the existing models can be divided into three big groups: *in vitro*, *ex vivo*, and *in vivo*. To optically study microbubble behavior *in vivo* several models are available such as the mouse or rat cremaster muscle, rat mesentery, hamster cheek pouch, dorsal skin-fold chamber [1, 2], and chicken embryo chorioallantoic membrane (CAM) model [3]. The CAM model has several advantages over the other *in vivo* models as it is cheap, does not fall under strict animal experiment legislation regulations if used before day 14 after fertilization, and CAM vessel endothelial cells uniformly express the important angiogenic marker $\alpha_v\beta_3$ -integrin [4]. These features make the CAM model very well suited to study ultrasound imaging, ultrasound molecular imaging, and targeted microbubble-mediated drug delivery of angiogenesis, relevant to both tumors and atherosclerosis.

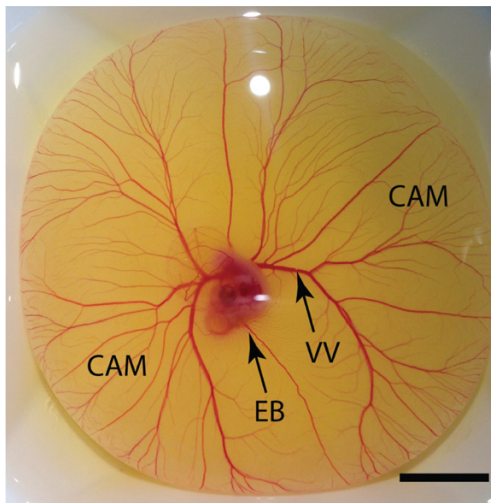


Figure 1. Six-day old chicken embryo extracted from the egg shell. CAM – chorioallantoic membrane, EB – embryo body, VV – vitelline vein. Scale bar: 1 cm.

Over the last three years we have successfully used the CAM of 5 to 6-day old chicken embryo's to characterize microbubble behavior [5], image the microvasculature using IVUS [6], sonoporate endothelial cells [7], and manipulate StemBells, i.e. stem cells encased by microbubbles, towards the vessel wall [8].

Acknowledgments

This research was financially supported by the Dutch Technology Foundation STW (2007 Simon Stevin Meester grant and project 10507), and the FP7 Sonodrugs Project (NMP-2008-213706). The authors would like to thank Telli Faez, David Maresca, Tom Kokhuis, Ying Luan, Guillaume Renaud, Krista Jansen, and Gijs van Soest from the Dept. of Biomedical Engineering, Erasmus MC, the Netherlands, and Michel Versluis from the Physics of Fluids Group, University of Twente, the Netherlands for their valuable contributions to the microbubble CAM model studies.

References

1. M. Schneider et al., *Microcirculation*, 2012; 19: p. 245-59;
2. S. Bowry et al., *Circulation*, 2007; 116, p. II-546;
3. S. M. Stieger et al., *Radiology*, 2007; 243: 112-21;
4. S. M. Jilani et al., *J Histochem Cytochem*, 2003; 51: p. 597-604;
5. T. Faez et al., *Ultrasound Med Biol*, 2012; 38: p. 1608-17;
6. D. Maresca et al., *Ultrasound Med Biol*, 2014; 40: p. 1318-28;
7. I. Skachkov et al., *IEEE Trans Ultrason Ferroelectr Freq Control*, 2014; 61: p. 1661-7;
8. T. J. Kokhuis et al., *Biotechnol Bioeng*, 2015; 112: p.220-7.

Micro-ultrasound molecular imaging in mice: Live observation of atherosclerosis plaque disruption in ApoE^{-/-} mouse

Verya Daeichin^a, Klazina Kooiman^a, Ilya Skachkov^a, Hans Bosch^a, Ben Janssen^b, Mat Daemen^c, Ton van der Steen^{a,d}, Nico de Jonga^{a,d}, And Judith Sluimer^e

^a Dept. of Biomedical Engineering, Erasmus MC, Rotterdam, the Netherlands; ^b Dept. of Pharmacology, Maastricht University Medical Center, Maastricht, the Netherlands; ^c Dept. of Pathology, Academic Medical Center, Amsterdam, the Netherlands; ^d Lab of Acoustical Wavefield Imaging, Delft University of Technology, Delft, the Netherlands; ^e Dept. of Pathology, Maastricht University Medical Center, Maastricht, the Netherlands.

Introduction

Angiogenesis is a critical feature of plaque development in atherosclerosis and might play a key role in both the initiation and later rupture of plaques. The precursory molecular or cellular events that initiate plaque growth and that ultimately contribute to plaque instability, however, cannot be detected directly with any current diagnostic modality. This study is designed to investigate the feasibility for micro-ultrasound molecular imaging of endothelial $\alpha_v\beta_3$ expression in vitro and in vivo using the $\alpha_v\beta_3$ -targeted ultrasound contrast agents (UCA). Meanwhile, we observed symptom implying plaque disruption during micro-ultrasound molecular imaging of a 50-week old ApoE^{-/-} transgenic 33 g mail mouse¹. Plaque disruption mechanism, in which a structural defect occurs in a thin fibrous cap overlying an inflamed atherosclerotic lesion, is of major interest for researchers and development of therapy in the field of atherosclerosis. While human plaques histopathology provides valuable data on cellular and histochemical properties of ruptured plaques, there is still an urgent need for representative animal models where prospective examination of the events leading up to plaque rupture and the rupture process itself can be performed. In the past decade, features suggestive of plaque rupture in ApoE^{-/-} mice with spontaneously developed unstable atherosclerosis have been reported. However, this topic has remained controversial up to now.

Material and method

In the in vitro study, $\alpha_v\beta_3$ expression were confirmed by Western blotting in murine SVEC cells and tracked by using the targeted UCA and further imaged under ultrasound imaging system at 18 MHz transmit frequency. In vivo, hypercholesterolemic male ApoE^{-/-} mice (n=7) derived from a C57/BI6 background from an in-house breeding colony was fed chow until the age of 50 weeks. UCA was prepared from Target-Ready Vevo MicroMarker contrast agent (VisualSonics Inc. Toronto, Canada) according to the manufacturer's instruction. Microbubbles were targeted with biotinylated antibodies against $\alpha_v\beta_3$ -integrin (BD Biosciences, San Jose, CA, USA) for making targeted UCA. Inactive form of biotinylated IgG(κ) (BD Biosciences) were used for making control UCA. A micro-ultrasound scanner, with a 256-element linear array transducer (Vevo 2100 with MS250 probe, VisualSonics Inc., Toronto, ON, Canada) was operated at 18 MHz. Details of the imaging setup, pulse sequences and quantification methods have been published earlier^{2, 3}. At sacrifice, blood was drawn from the

right ventricular apex. Subsequently the mice were gently perfusion fixed via the left cardiac ventricles with 20 ml sodium nitroprusside, followed by 1% paraformaldehyde (PFA). The right carotid arteries and salivary glands were excised, fixated in 1% PFA for 24 hours, and paraffin-embedded. The right carotid arteries and salivary glands were sectioned, and stained with Hematoxylin and Eosin (HE, Sigma-Aldrich) for microscopical examinations. Serial sections were subjected to heat-induced epitope retrieval and stained with rat anti-mouse MAC3 for one hour at RT, to show plaque macrophages. Slides were subsequently incubated with biotin-conjugated rabbit-anti-rat secondary, followed by horse-radish (HRP) peroxidase ABC and staining was visualized using 3,3-diaminobenzidin tetrahydrochloride. Endothelial cells were stained overnight at 4°C with CD31 primary antibody after trypsin treatment for 20min at 37°C⁴ for epitope retrieval. Slides were further incubated with mouse-absorbed rabbit-anti rat (vector), hrp-conjugated anti rabbit to amplify signal and visualized using DAB.

Results

Our results showed that endothelial $\alpha_v\beta_3$ expression was significantly higher in the carotid wall artery containing atherosclerosis lesions compared with parts without any lesions (Figure.1). We also showed that the salivary gland can be used as an internal positive control for successful binding of targeted UCA to $\alpha_v\beta_3$ integrin (Figure. 1). Moreover, during live contrast enhanced ultrasonography of one of the animals (a 50-week old ApoE^{-/-} male mouse), symptoms suggesting plaque disruption in the right brachiocephalic artery were observed. Quantifications of carotid walls motions, blood flow information, perfusion parameters in the gland and surrounding tissues (Figure. 2) and immunohistological data of advanced atherosclerotic lesions in this animal will be discussed in this presentation. These observations demonstrate evidence of plaque instability and possibly spontaneous plaque disruption in ApoE^{-/-} mice.

Conclusions

This study demonstrated the successful preparation of the $\alpha_v\beta_3$ -targeted microbubbles and the potential of target-specific ultrasound contrast agent to detect the expression of $\alpha_v\beta_3$ -integrin in vitro and in vivo. Our initial experience in molecular ultrasonography using the $\alpha_v\beta_3$ -targeted microbubble has shown that it may enable in vitro and in vivo molecular imaging of $\alpha_v\beta_3$ expression on actively sprouting vascular endothelium and macrophages. This imaging modality may provide reference values of relative expression of $\alpha_v\beta_3$ and information likely to be very useful to address the detection, prognosis, vulnerable potential of atherosclerosis or susceptibility to anti-atherosclerosis drugs. In addition, for the first time, possible spontaneous plaque disruption in the right brachiocephalic artery of an ApoE^{-/-} mouse was observed real-time with contrast enhanced ultrasonography.

References

1. Daeichin V, Sluimer JC, van der Heiden K, Skachkov I, Kooiman K, Janssen A, Janssen B, Bosch JG, de Jong N, Daemen MJAP, van der Steen AFW. Live Observation of Atherosclerotic Plaque Disruption in Apolipoprotein E-Deficient Mouse. *Ultrasound International Open* 2015; 01:E67-E71.
2. Daeichin V, Bosch JG, Needles A, Foster FS, van der Steen A, de Jong N. Subharmonic, non-linear fundamental and ultraharmonic imaging of microbubble contrast at high frequencies. *Ultrasound Med Biol* 2015; 41:486-97.
3. Daeichin V, Akkus Z, Hoogi A, Bosch JG, Needles A, Kooiman K, Skachkov I, Sluimer J, Janssen B, Daemen MJAP, van der Steen AFW, de Jong N. 2013 Quantification of targeted microbubbles in contrast enhanced ultrasound. *Ultrasonics Symposium (IUS), 2013 IEEE International*, 1825-28.
4. Muchir A, Shan J, Bonne G, Lehnart SE, Worman HJ. Inhibition of extracellular signal-regulated kinase signaling to prevent cardiomyopathy caused by mutation in the gene encoding A-type lamins. *Hum. Mol. Genet.* 2009; 18:241-47.

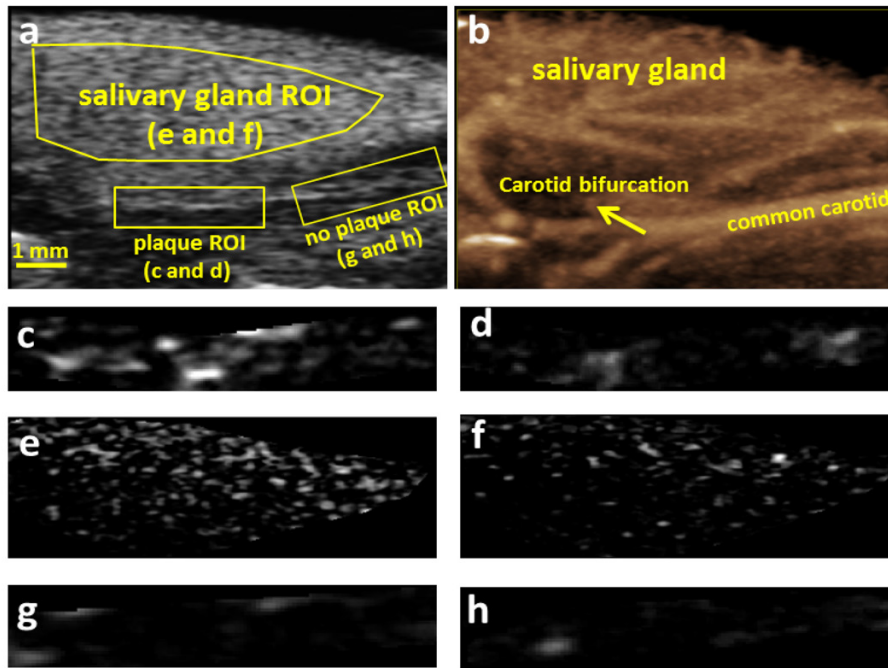


Figure 1. Molecular sonogram of carotid artery vessels and salivary gland: a) Bmode image of the right carotid and right salivary gland with region of interest in the salivary gland, around the plaque at the carotid bifurcation and around the common carotid artery where there is no plaque present; b) corresponding nonlinear contrast mode image (maximum intensity projection over 100 frames); c, e and e) Detected bound microbubbles after injection of targeted microbubbles; d, f and h) Detected bound microbubbles after injection of control microbubbles.

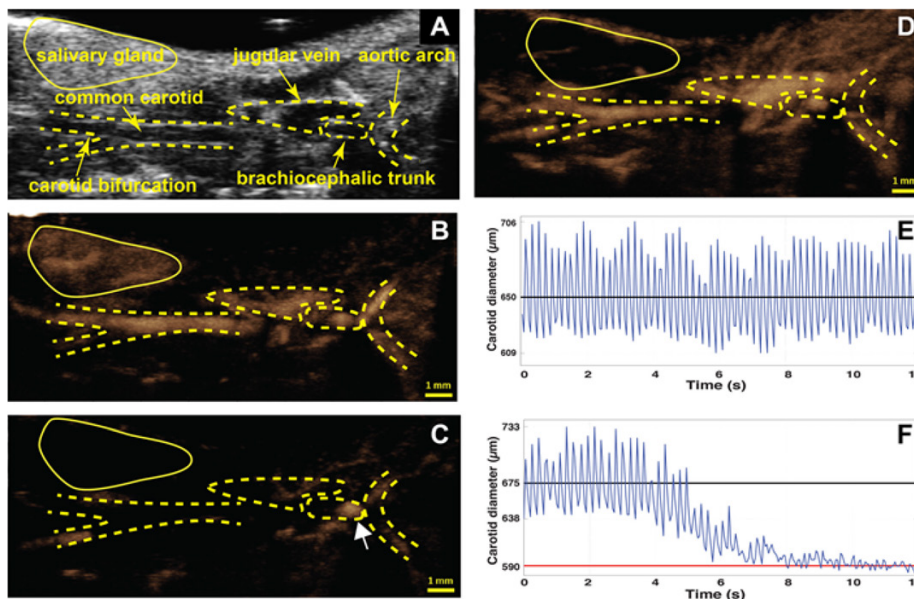


Figure 2. Dynamics of plaque disruption , imaged with contrast enhanced ultrasound A) B-mode image B) Maximum Intensity Projection (MIP) over 100 frames after arrival of UCA (first injection) in the aortic arch showing the trajectory of the aortic arch, carotid artery, and the perfused salivary gland. C) MIP over 100 frames after arrival of UCA (third injection) in the aortic arch showing the accumulation of UCA in beginning of brachiocephalic trunk (white arrow) and significant reduction of the blood flow in the carotid artery and no perfusion of the UCA in the salivary gland. D) Longer MIP of the sequence in c showing the return of the UCA in the common carotid but still no perfusion of the UCA in the salivary gland. E) Normal pulsation of the common carotid walls before plaque disruption. F) Pulsation of the common carotid walls during plaque disruption showing the decrease in common carotid pulsation followed by vessel constriction.

Clinical oncology therapy with microbubbles and ultrasound: The future

A. Bouakaz¹, J.M. Escoffre¹ and T. Lecomte²

- 1. Inserm U930, Imagerie et Cerveau, Université François Rabelais, Tours, FRANCE*
- 2. Service d'Hépatogastroentérologie et de Cancérologie Digestive, CHRU Trousseau, Tours, FRANCE*

Ultrasound in combination with gaseous microbubbles has come into focus as a potential new drug delivery technology. Commonly referred to as sonoporation, this approach is a delivery technique for which high-frequency sound waves are used with microbubbles to enhance the permeability of biological barriers while allowing co-administered therapeutic chemicals, drugs, or nucleic acids to be introduced into targeted biological cells and tissues. In this way, the extravasation of the therapeutic compound is potentiated and by that its bioavailability in the targeted region.

Sonoporation offers real promises as a drug delivery tool with potential of alleviating the limitations encountered by traditionally available therapeutic arsenal. It is interesting to note that considerable work has been performed, showing the potential benefit of this new therapeutic approach to deliver drugs locally using into individual cells and in preclinical situations. Moreover, numerous basic and more advanced investigations have provided an increased understanding of the interaction of ultrasound waves, microbubbles and biological tissue. Despite all these vigorously pursued studies since a number of years now, this technology has not been adopted yet as a clinical tool, probably because efficacy and safety have not been evaluated and the relevant protocols/parameters leading to its efficient use remain inadequately defined and thus broadly unregulated.

Before reaching its imperative outcome - the clinical practice, it is crucial to address the inherent challenges of this drug delivery approach, particularly related to controlling the efficacy and safety which will undeniably provide a broad range of potential clinical applications.

We will discuss the principles of delivering drugs using ultrasound waves in combination with microbubbles in both in-vitro and in-vivo scenarios for oncology indications. The talk will approach optimization aspects of sonoporation directed drug delivery including ultrasound parameters, treatment protocols, microbubble properties and ways of administration.

Ultrafast and programmable ultrasound scanners, a new paradigm applied to contrast imaging

Olivier Couture, Yann Desailly, Claudia Errico, Jean-Michel Correas, Mickael Tanter

(Institut Langevin (CNRS, INSERM, ESPCI), 1 rue Jussieu, Paris. Olivier.couture@espci.fr)

The quest to attain frame rates beyond 1000 fps with ultrasound imaging started almost 40 years ago with Bruneel et al. [APL, 1977]. This group already highlighted the interest for ultrasound imaging to breach the line-by-line frame rate limit to explore fast phenomena in the body, such as heart motion. Today, ultrafast scanners, which are also programmable, have triggered a paradigm-shift in the field of ultrasound. In this presentation, we will present a short review of its concepts, history and implications, placed in the context of ultrasound contrast imaging.

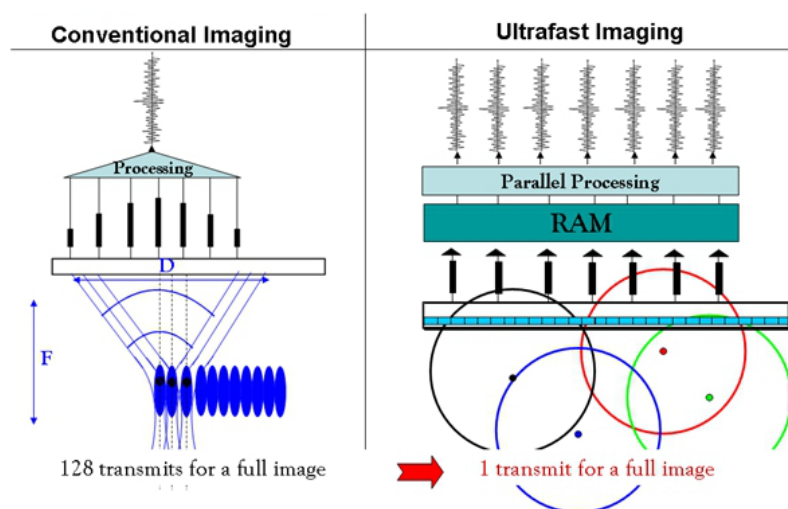


Figure 1: Concept of ultrafast imaging. In conventional imaging, a pulse-echo experiment is performed for each line, which takes in the order of $100 \mu\text{s}$, making such that the frame rate is limited to about 50 Hz. In ultrafast imaging, plane-waves are generated and the signal received by each element is recorded to create one image for each pulse-echo, leading to 10,000 images per second.

The Explososcan, proposed by Shattuck et al. [JASA, 1984] introduced parallel processing of multiple ultrasonic beams in reception. Combined with the emission of unfocused beams, this concept would become the foundation of ultrafast imaging. Indeed, high frame rates are attained by first emitting pulses that insonify the entire region of interest and, then, by collecting the echoes on multiple channels which allow the beamforming of a full image per emission (figure 1). The 4-channels Explososcan was followed by other beamforming approaches

with synthetic beamforming or limited diffraction beams [Cooley et al 1994, Karaman et al 1995, Lu 1998, Nikolov et al 2002]. For instance, the time-reversal mirrors introduced by Fink et al. [RPP, 2000] were already fully programmable, with independent arbitrary waveform generators and easy access to memory through software. This flexibility is the second key aspect of the ultrafast revolution. While optimization on conventional scanners often requires modification of the electronic and provide no access to the raw data, the programmable ultrafast scanner gave complete control over each phase of the ultrasound pulse-echo: emission, reception and synthetic beamforming. This flexibility over the sequence programming, which was inherent in the MRI field and the cause of its rapid evolution, lead to several new ultrasound techniques and applications.

Ultrafast imaging would find its first optimal application with transient elastography in the early 2000 [Sandrin et al 1999, Tanter et al 2002, Sandrin et al. 2002]. This method for measuring the elasticity of tissue, or tumors, relied on the tracking of the velocity of shear waves on all points in the image. As the shear waves propagate at several meter per second, frame rates beyond 1000 fps were necessary to sample the related displacement of tissue. The elasticity modification due to tumors, fibrosis or

dynamic muscular process could be imaged in real-time, providing a new form of remote palpation. The first clinical proof of concept of the clinical added value of ultrafast imaging was provided in 2008 in the framework of breast cancer diagnosis [Tanter et al 2008]. Early 2010, a first commercial clinical ultrafast scanner was introduced under the name Aixplorer (SuperSonic Imagine), after several major improvements such as beamforming with Graphical Processing Units (GPU). Since then, it has improved the specificity of ultrasound imaging toward malignant tumors, mainly in the breast, and reduce the number of biopsies [Evans et al. BJC, 2012].

Ultrafast imaging also improved Doppler drastically [Bercoff et al. IEEE, UFFC, 2011]. Conventional line-by-line pulsed-Doppler is generally limited by the ensemble length in the slow-time. For each line, motion can only be sampled a limited number of time to preserve a respectable frame rate. As it addresses each pixel of the image several thousand times a second, ultrafast imaging, brings the sensitivity of pulse-wave Doppler over the entire image. Moreover, very large blocks of data could also be acquired with sufficient memory, which allowed more powerful filtering and artefacts elimination. With the introduction of spatio-temporal filters, the sensitivity has reached a new level and blood flow in the order of 0.5 mm/s can be observed, even when much faster tissue or probe motion are present [Demene et al., IEEE, TMI2015]. Ultrafast Doppler is now exploited in preclinical and clinical imaging. For instance, it now gives an insight on the brain vasculature in prematured babies, a difficult task for MRI [Demene et al. JCBFM, 2014]. For an extensive review on ultrafast imaging in biomedical ultrasound, the interested reader can read [Tanter and Fink 2014, IEEE UFFC].

Ultrafast Doppler imaging also demonstrated that it can detect minute changes in blood flow without contrast agents. In fact, its sensitivity was sufficient to highlight the activity of the brain through the neurovascular coupling [Macé et al. Nature Methods 2011]. Since then, functional ultrasound (fUS) has been applied to functional targets difficult to attain with fMRI such as odor-evoked stimuli

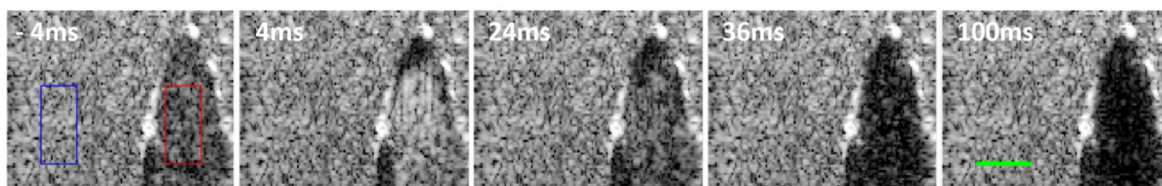


Figure 2: Millisecond time-scale evolution of microbubbles post-disruption in a wall-less vessels

[Osmanski et al. NeuroImage, 2014] or even awake animals [Sieu et al. Nature Methods, 2015].

Even though it proved to have an exceptional sensitivity to blood flow, ultrafast imaging has not killed contrast imaging. As a matter of fact, it actually started improving it. To our knowledge, the first implementation of plane-wave ultrafast imaging with microbubbles was in 2009 [Couture et al., UMB] where we demonstrated that the dissolution of microbubbles could be explored in the millisecond timescale, highlighting free bubble phenomena. Decorrelation (Doppler) and nonlinear ultrafast sequences were also introduced in this context. These sequences would rapidly prove to be useful in-vivo for tumor molecular imaging [Couture et al., MI, 2011]. Indeed, microbubbles imaged with plane-waves experience more pulses of lower amplitude than with conventional imaging. Therefore, a higher contrast with lower disruption can be obtained with Ultrafast Contrast [Couture et al. IEEE UFFC, 2012], which is particularly useful for targeted microbubbles. These developments triggered the interest of others groups which explored a dual-mode plane-wave imaging of microbubbles where both blood vessels and perfusion can be displayed [Tremblay-Darveau, IEEE UFFC, 2014, IEEE TMI, 2015]. Ultrafast Contrast is now being implemented on clinical systems and should improve our sensitivity to blood flow even more [Bruce et al. Rotterdam Symposium, 2014].

At the preclinical level, ultrafast imaging of contrast agents allowed functional ultrasound to be

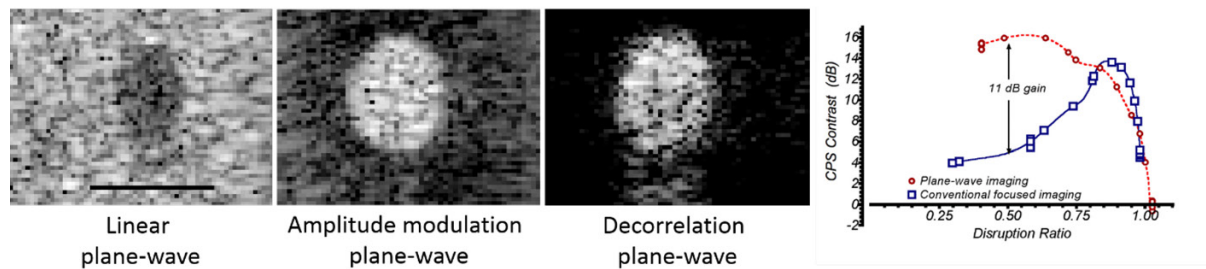


Figure 3: Ultrafast imaging with various pulse sequences of a wall-less vessel filled with microbubbles. Right Panel: Contrast-to-tissue ratio in Contrast-Pulse Sequence (CPS) for plane wave and focused imaging. To preserve 50% of the bubbles after 100 images, peak-negative pressure has to be reduced in conventional focused imaging, but not in plane-wave imaging

performed without the removal of the rat skull (Errico et al. NeuroImage, 2015a).

In parallel to contrast imaging, synthetic beamforming was also applied to cavitation detection, both passively [Gyongyi et al. JASA, 2010] and actively [Gateau et al., IEEE UFFC, 2011]. In therapy, we introduced an ultrafast monitoring technique for droplet vaporization, which highlights the creation of gas pockets during therapy in the microsecond time-scale, eliminating the static tissue background (Couture et al. 2011, 2012). This way, the same system can image, trigger the release and monitor the effect. Such a technique was later exploited by Puett et al. for the monitoring of nanodroplets vaporization [Ultrasonics 2014].

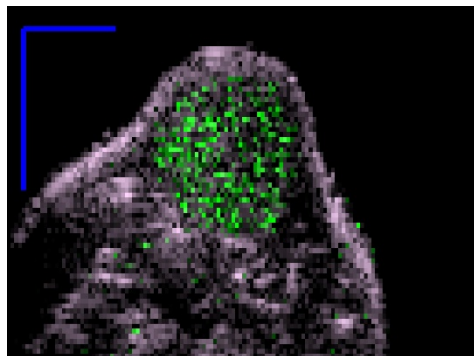


Figure 4 Ultrasound imaging of a tumor with targeted microbubbles. The green overlay is plane-wave amplitude modulation.

In our view, one of the best application for ultrafast imaging of microbubbles yet is ultrasound localization microscopy. Ultrasound super-resolution exploits the millisecond timeframe to separate multiple sources (Couture et al., Patent, 2010, Couture et al., IEEE UFFC symposium, 2011). Indeed, we discovered that, with the appropriate filters, microbubbles could individually blink frame by frame on an ultrasound movie even when injected at a high-concentration. This allows a close analogy with optical localization microscopy (FPALM for instance), where dense collections of fluorescent markers are made to blink separately on different frames. From clearly separated punctual sources, it is then trivial to find the center of the point-spread-function. The image is reconstructed based on the accumulation of a large number of super-localized microbubbles which highlights the vessels with a precision an order of magnitude better than the wavelength. Theoretically, images of the microvasculature could have a resolution of a few micrometers [Desailly et al. APL, 2015], which was demonstrated in-vitro in 3D [Desailly et al., PMB, 2013]. In-vivo, a resolution of 8 micrometers was achieved over the entire rat brain [Errico et al. Nature 2015]. In our

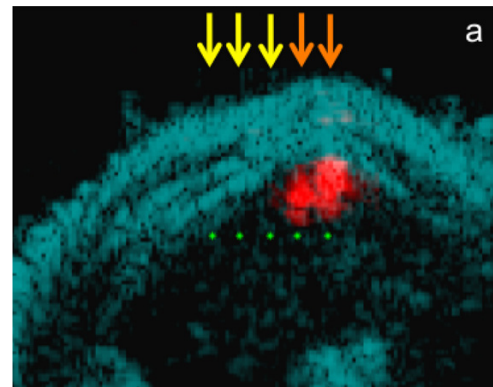


Figure 5 Ultrasound imaging using plane waves at 1.1 kHz frame-rate of the vaporization of drug-delivery agents.

mind, ultrafast is a key component of any practical ultrasound super-resolution technique as they require the detection and accumulation of millions of bubbles to reconstruct an appropriate image. Slower techniques relying on a low-concentration of contrast agents and line-per-line beamforming to separate microbubbles, which were adapted more recently [O'Reilly, Medical Physics, 2013, Viessman et al., PMB, 2013, Christensen-Jeffries, IEEE TMI, 2015] remain hampered preclinically or clinically by extremely long acquisitions as large concentrations of bubbles require the synergetic combination of a large field of view and ultrafast frame rate.

Today, ultrafast imaging is being applied to several organs, including the heart [Couade et al. IEEE TMI 2011], which confirms the hindsight of Brunel et al 38 years ago. It even fully became 3D with the introduction of 2D array driven by a set of 1024 pulser-receiver [Gennisson et al., IEEE UFFC, 2015]. The democratization of ultrafast ultrasound is on the way both in academic research labs and ultrasound companies. Several companies propose systems that can be easily programmed and that can acquire thousands of frames per second, including Supersonic Imagine, Verasonics, Cephasonics, Ultrasonix, Ula-Op, etc. We can only hope that such flexibility will accelerate the profound changes in ultrasound imaging that occurred in the last decade. From that point forward, very little can limit the creativity of ultrasound researchers.

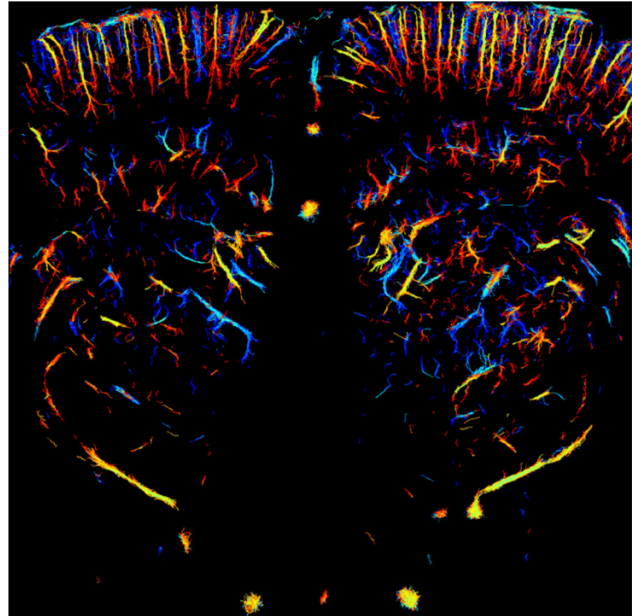


Figure 6: Ultrafast Ultrasound Localization Microscopy of the rat brain over an entire coronal plane. The resolution is 8 micrometers.

Principal curvature analysis in plane-wave contrast-enhanced Doppler imaging

*Charles Tremblay-Darveau¹, Ross Williams¹, Laurent Milot¹,
Paul Sheeran¹, Matthew Bruce² and Peter N. Burns^{1,3}*

¹ *Sunnybrook Health Sciences Centre, Toronto, Ontario, Canada*

² *University of Washington, USA*

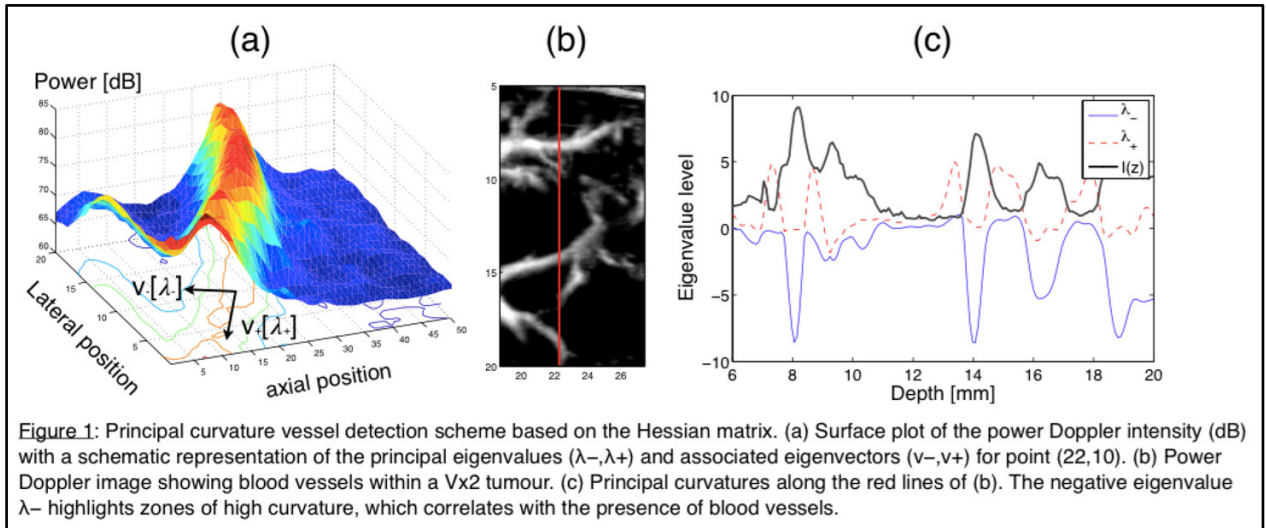
³ *Department of Medical Biophysics, University of Toronto, Toronto, Ontario, Canada*

Introduction

Recent breakthroughs in plane-wave ultrasound have triggered a veritable paradigm shift in Doppler ultrasound. The ability to acquire Doppler ensembles two orders of magnitude longer than conventional line-by-line imaging has enabled the duplexing of Doppler and bubble-specific contrast-enhanced imaging without sacrificing flow sensitivity or tissue motion rejection [1]. We propose that nonlinear Doppler is the best method to separate perfusion at the capillary level from conduit flow in the simultaneous presence of tissue motion. Nonetheless, the arbitration process separating pixels containing flow from noise and capillary perfusion regions (conventionally estimated by using thresholded power Doppler binary maps) still remains challenging, even when considering the significant SNR improvement provided by plane waves. This is partly due to the significant variation of background noise over the image arising with the clipping of the point spread function (PSF) from the finite transducer aperture and the main-lobe signal from a weak scatterer being often comparable in scale to the side lobe amplitude of a bright scatterer. This results in a trade-off where spatial resolution is often given up for sensitivity to small vessels during flow arbitration. One method which may further improve flow arbitration is to detect the principal curvature component of the Hessian matrix of the image, thus detecting and enhancing tubular structures. This is common practice in magnetic resonance angiography and X-ray computed tomography angiography [2]; however, until now, applying the method to ultrasound images has yielded poor results due to SNR constraints (from thermal/electronic and speckle noises). Here, we demonstrate that a principal curvature-based detector significantly improves the flow arbitration of contrast-enhanced Doppler ultrasound images created with plane waves, and enables fast quantitative estimates of morphological image metrics, such as fractal dimension and tortuosity, in the presence of tissue motion.

Method

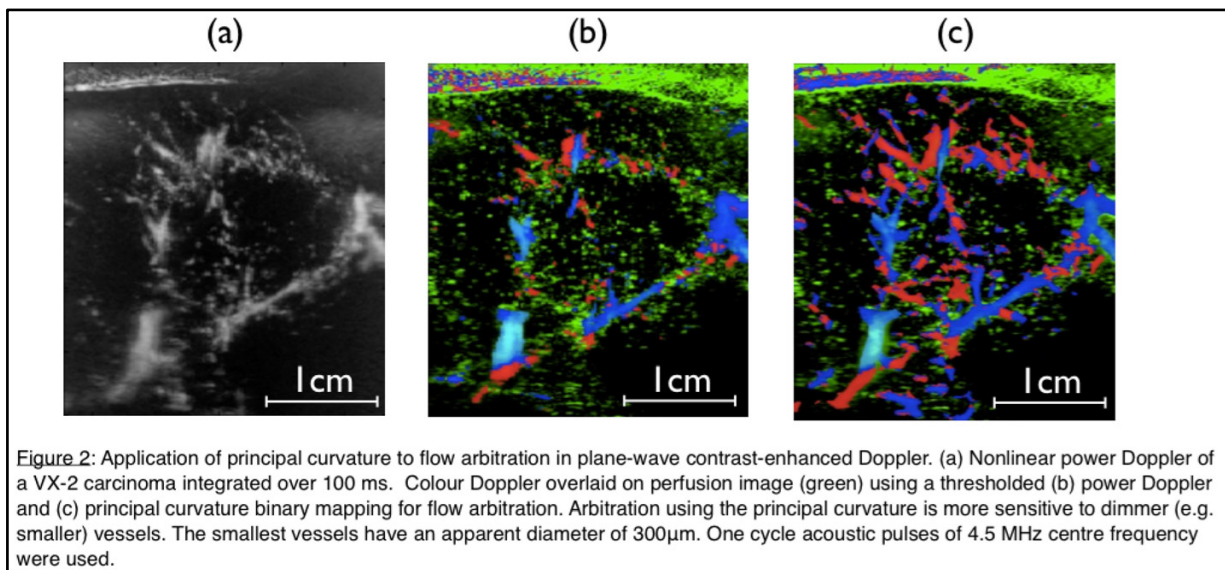
It is well known from differential geometry that an image (i.e. a 2D surface) can be locally described by its second order Taylor expansion. The Hessian, defined as $H_{i,j} = \partial^2 I / (\partial x_i \partial x_j)$, is a symmetric matrix which contains all information regarding the surface curvature. The associated eigenvalues λ_i are commonly referred to as the principal curvatures, and the corresponding eigenvectors \mathbf{v}_i are parallel and perpendicular to the tubular structure (see Fig 1). For the case of a bright blood vessel, the eigenvector corresponding to the lowest (negative) eigenvalue is perpendicular to the tube. To account for the effect of scale, the image was a priori blurred with a Gaussian kernel of width corresponding to the feature size.

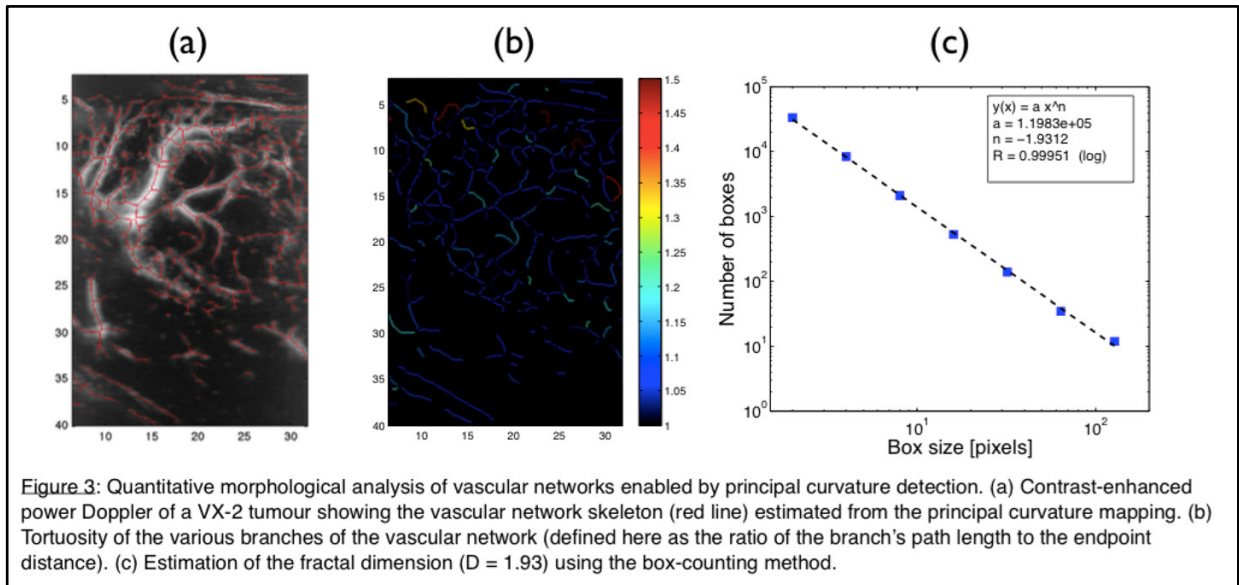


Results and discussion

Curvature-based detectors and plane-wave imaging:

The curvature operation involves the calculation of a second order derivative, and hence can amplify noise fluctuations. Conventional Doppler (via line-by-line imaging) provides little flexibility in compounding frames due to limitations in acquisition time (a Doppler ensemble of about 10 points is typical). Under such conditions, the principal curvature algorithm performs poorly, notably for the smaller scales. This occurs as there exists an inherent trade-off between the image SNR and the smallest scales that can be detected (smaller features are extracted from a Gaussian smoothing kernel of smaller footprint). Longer acquisitions enabled by plane-wave imaging reduce noise fluctuations in proportion to the square root of the Doppler ensemble length. Typically, Doppler ensembles of approximately 200 points are required to achieve a proper reduction of the thermal and speckle noises.





Application to power Doppler arbitration:

Figure 2 shows the colour Doppler overlaid on the perfusion image (green colourmap) where a thresholded (b) power Doppler and (c) principal curvature component was used for separating flow regions from clutter, noise and capillary perfusion. The arbitration based on the concavity mapping is significantly less susceptible to the noise background and the PSF side-lobes, and therefore provides a markedly superior sensitivity to colour Doppler.

Quantitative vascular morphology analysis using contrast-enhanced power Doppler:

The skeleton of VX-2 tumour arterioles and venules was estimated from the thresholded binary curvature mapping (Figure 3a). The skeleton representation reliably highlighted the structural hierarchy of the tumour. Such mapping enables real time quantitative analysis of the vascular network. For instance, Figures 3b and c demonstrate how the information can be used to estimate the tortuosity and the fractal index of the conduit flow.

Conclusion

Principal curvature segmentation techniques can be adapted to contrast enhanced Doppler when used in conjunction with the long acquisitions provided by plane waves. The method increases the sensitivity of the flow arbitration process compared to conventional power-based segmentation, and enables quantitative morphological analysis of the vein and artery network, as well as quantitative imaging of perfusion and flow velocity.

References

1. C. Tremblay-Darveau et al. *Visualizing the Tumour Microvasculature with a Nonlinear Plane-wave Doppler Imaging Scheme based on Amplitude Modulation. IEEE TMI (2015), In press.*
2. Frangi et al. *Multiscale vessel enhancement filtering. Med Image Comput Comput Assist Interv (1998) pp. 130-137*

Contrast enhancement by real-time spatiotemporal filtering of ultrafast images

*Yann Desailly, Jean-Michel Correas, Mickael Tanter *, Olivier Couture**

Institut Langevin (ESPCI, INSERM, CNRS), Paris, France

** MT and OC contributed equally*

Contrast enhanced ultrasound (CEUS) is taking advantage of the nonlinear behavior of injected microbubbles. These contrast techniques – Pulse Inversion (PI), Amplitude Modulation (AM), Contrast Pulse Sequence (CPS) – consist in suppressing the linear content of the backscattered echoes. Although the contrast enhancement reached is usually rather satisfying, nonlinear sequences still suffer some major drawbacks. First, most of the energy scattered by microbubbles lies in the fundamental, which implies a reduced signal-to-noise ratio for these techniques. Secondly, propagative harmonics or motion can diminish the efficiency of the linear cancellation, thus causing tissue artifacts. Finally, nonlinear sequences require detailed optimization of the electronic and pulses, which can affect other desirable features such as temporal and spatial resolution.

Ultrafast ultrasound imaging, which consists in reconstructing an entire image for each pulse-echo measurements, can reach 20,000 frames per second and lead to the development of fully-programmable ultrasound scanners. It became fundamental to the development of transient elastography (Sandrin *et al.* 2003), functional ultrasound imaging (Macé *et al.* 2011) and, more recently, ultrasound localization microscopy (Errico *et al.* 2015). In particular, it was shown to increase significantly Doppler sensitivity, giving access to flow at the millimeter/second scale (Bercoff *et al.* 2011). Further improvement in Doppler sensitivity was recently made through the use of spatiotemporal filters (Demene *et al.* 2015). Such filter exploits the high temporal resolution granted by ultrafast plane wave imaging. It separates features in the images on the basis of spatiotemporal coherence. Whereas tissues are strongly coherent both in time and space, blood display patterns that are far less coherent.

The use of ultrafast imaging has been proposed for contrast imaging (Couture *et al.* 2009, Couture *et al.* 2012) and drug-delivery monitoring (Couture *et al.* 2011a), implemented for preclinical imaging (Couture *et al.* 2011b, Tremblay-Darveau *et al.* 2014) and clinical imaging (Bruce *et al.* Rotterdam Contrast Symposium 2014). However, the pulse-sequence that was implemented exploited mostly the fact that ultrasound energy is spread all over the imaging plane rather than concentrated in the focal spot. This induces less destruction than focused imaging for similar CTR levels but is still based on nonlinear detection.

We believe that spatiotemporal filtering of ultrafast images with bubbles can yield high contrast levels without resorting to nonlinear techniques, hence avoiding artifacts and hardware issues.

To demonstrate the contrast improvement granted by this method, we performed ultrafast acquisition using a programmable ultrasound scanner (Aixplorer, Supersonic Imagine, France) driving a 6 MHz ultrasound probe (SL10-2 Supersonic Imagine, France; pitch 0.2 mm, elevation focus 35 mm, 96% bandwidth @ -6dB). Ultrasound contrast agents (Sonovue, Bracco, Switzerland) at a concentration of 10^5 /mL were pushed inside a 6 mm in diameter wall-less phantom (agarose gel with Sigmacell scatterers). The flow rate was controlled with a syringe pump (Harvard apparatus, USA) providing flow speeds between 5 mm/s and 30 mm/s.

Two different low-amplitude sequences ($MI = 0.05$; $ISPTA = 1 \text{ mW/cm}^2$) were tested: ultrafast plane wave CPS is compared with compound (3 angles: -3° , 0° , 3°) plane wave imaging with spatiotemporal filtering. The frame rate was set to 2 kHz for both of the imaging modalities. The ultrasound probe was mounted on a linear motor (PI translation stage VT-80, one directional) to enable transversal or longitudinal motion with respect to the phantom vessel. The probe motion velocity was set from 2 mm/s to 20 mm/s (with 2 mm/s incremental steps).

First attempts at in-vivo implementation of the technique were conducted on the human kidney with the same imaging setup. Only the frame rate was changed, set to 800 Hz. The patient was injected a bolus of 1.2 mL of non-diluted Sonovue. This observational study was approved by the institutional review board (CPP: 'Comité de Protection des Personnes', i.e., Committee for the Protection of Persons).

This kind of image processing not only allows the clean removal of the tissue in the image but also does not suffer from propagative harmonics artifacts. For low bubble concentration, the gain of contrast (in terms of CTR) can reach 20 dB in a wall-less phantom. In the human kidney, the spatiotemporal processing provides satisfying contrast levels with a good delineation of the vascular network.

Computation times being similar to the acquisition times, GPU computing in parallel with the acquisition could provide a real-time experience (30 frames/sec) on modern ultrasound scanners.

This new technique takes advantage of ultrafast imaging for enhancing contrast using only the fundamental mode. Thanks to the high temporal resolution, spatiotemporal filtering enables specific suppression of the signal from the tissues hence highlighting the bubble signal.

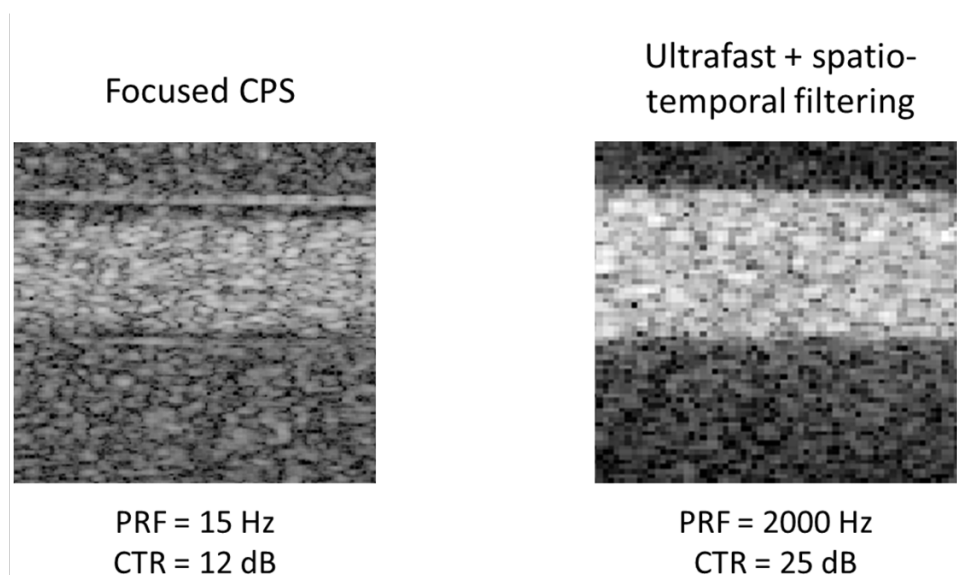


Figure 1: At low concentration of contrast agents (Sonovue by Bracco), the contrast reached by conventional CEUS – here CPS – is not performant enough (left panel); in comparison, the ultrafast images processed by spatiotemporal filtering yield a 13 dB improvement in terms of CTR.

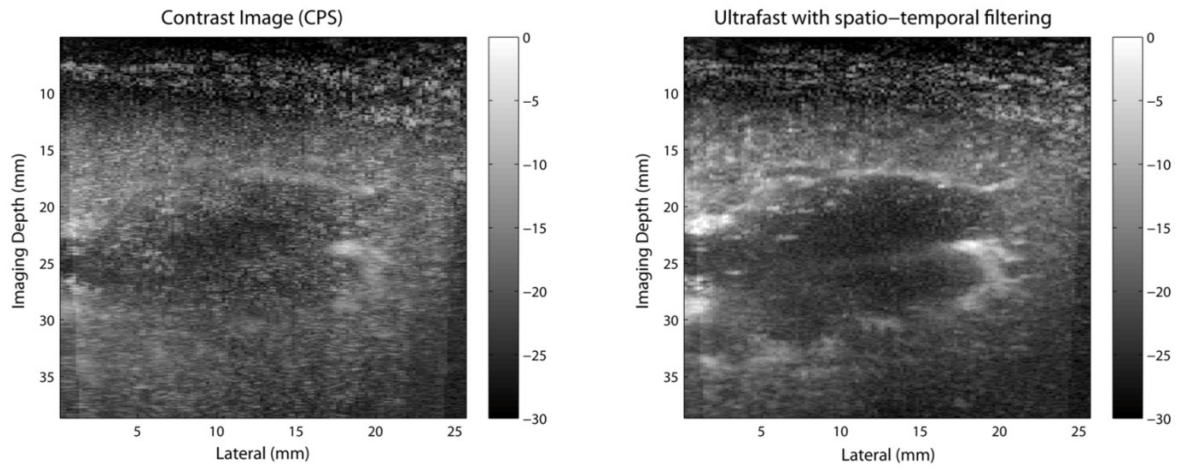


Figure 2: First attempt at in-vivo implementation of the technique (human kidney); not only higher CTR is yielded but the vascular network is also better delineated (mean over 30ms)

Fast and Background Free Super-Resolution Ultrasound Based on Fluctuation Statistics

Avinoam Bar-Zion¹, Charles Tremblay-Darveau^{2, 3}, Oren Solomon⁴, Tamir Bendory⁴, Dan Adam¹ and Yonina C. Eldar⁴

¹ *Department of Biomedical Engineering, Technion - Israel Institute of Technology, Haifa, Israel.*

² *Physical Sciences, Sunnybrook Research Institute, Toronto, Ontario, Canada.*

³ *Department of Medical Biophysics, University of Toronto, Toronto, Ontario, Canada.*

⁴ *Department of Electrical Engineering, Technion - Israel Institute of Technology, Haifa, Israel.*

BACKGROUND

Dynamic contrast-enhanced ultrasound (DCEUS) imaging enables the measurement of blood flow within the vasculature of the imaged tissue. The resolution of classic ultrasound scans is limited by the wavelength of the transmitted pulse in the axial direction and by the aperture of the transducer in the lateral dimension. In the past few years, different methods for achieving super-resolution using contrast-enhanced ultrasound were proposed ([1], [2], [3]). Currently, the temporal resolution is the main limitation of all ultrasound super-resolution methods. Similarly, acquisition of images with resolution below the diffraction limit is of great concern in the field of optical fluorescent microscopy. Recently, a method called super resolution optical fluctuation imaging (SOFI) [4] was introduced, in which the spatial resolution is improved over the diffraction limit, while maintaining good temporal resolution. The improvement is achieved by using the statistics of the blinking fluorophores. In this work, these statistical tools are applied to DCEUS signals in order to produce fast super-resolution acoustic scans. The scan duration required for the proposed method is a second or less while current super-resolution images require acquisition duration of several minutes. As a result, the proposed method can be applied during a breath-hold, while the others demand precise registration in order to compensate for motion artifacts in a clinical setting.

METHODS

Following the application of a high-pass clutter filter and in the spirit of SOFI, high-order statistical analysis of single-pixel DCEUS time-traces was performed. In this work, the temporal-mean, the 2nd and 4th order central cumulants and the 4th-order moments were calculated. The spatial map of the calculated moments and cumulants produced high resolution images of the underlying vasculature. The proposed method was evaluated using two New Zealand white rabbit models: normal vasculature was imaged in the kidneys of healthy rabbits and tumor vasculature was imaged in hind-limb intramuscular VX-2 tumors. *In-vivo* scans were performed using an Aixplorer diagnostic ultrasound system (Supersonic Imagine, France) with a 7.5MHz probe. Entire image planes are scanned using plane-wave pulse-inversion acquisitions at a PRF of 5 kHz. After the summation of the pre-beamformed data, separating the nonlinear component of the RF data, full images were reconstructed per plane-wave transmit. Definity, a commercial ultrasound contrast agent (UCA) with lipid shell, was used in all experiments. The UCA was administered in 0.5mL bolus injections with concentration of 10 μ L/kg.

RESULTS AND DISCUSSION

The different parts of the kidney's vasculature, observed in the unprocessed image, included a variety of sparsity levels: the main vessels are characterized by speckle patterns while single bubbles can be seen flowing in the smaller outer vessels. Both the 2nd and the 4th moment images improved the visualization of small vessels in the kidney model (see Figure 1). Using the high-order statistics, vessels that could not be resolved in the temporal-mean image were separated (Figure 1, dashed arrow). Additionally, smaller vessels in the periphery of the kidney were observed using the 4th moment (Figure 1, arrows). The background rejection capabilities of the high order statistics images in the proposed method are best seen in Figure 2. Furthermore, the ability of the method to separate adjacent small vessels is demonstrated by zooming on a bifurcation in the vasculature of the tumor that was not observed in the temporal-mean image but was resolved in the 4th cumulant image (see Figure 3). The kidney scan processed in this work included 150 frames compared to the 1000 frame long tumor scan. Estimation of high-order moments and cumulants requires long ensembles in order to achieve good signal to noise ratio (SNR). For example, in [4] 5000 frames were used to produce the SOFI images. Better SNR and background rejection could be achieved with ensembles of 1000 frames and more.

CONCLUSION

The methods studied in this work alleviate the tradeoff between spatial and temporal resolution in ultrasound-super resolution imaging: tens or hundreds of milliseconds are needed in order to produce these estimations compared to up to a few minutes using other ultrasound super-resolution methods ([1], [2], [3]). With this short acquisition time, using the proposed method, improved spatial resolution and background removal were presented. Improvement in the temporal resolution of super-resolution ultrasound could enable widespread use of this technique to enhance cancer and neuroscience research where blood-flow dynamics are of great importance.

REFERENCES

1. C. Errico, J. Pierre, S. Pezet, Y. Desailly, Z. Lenkei, O. Couture, and M. Tanter, "Ultrafast ultrasound localization microscopy for deep super-resolution vascular imaging," *Nature*, vol. 527, no. 7579, pp. 499–502, Nov. 2015.
2. K. Christensen-Jeffries, R. J. Browning, M.-X. Tang, C. Dunsby, and R. J. Eckersley, "In Vivo Acoustic Super-Resolution and Super-Resolved Velocity Mapping Using Microbubbles," *IEEE Trans. Med. Imaging*, vol. 34, no. 2, pp. 433–440, Feb. 2015.
3. M. A. O'Reilly and K. Hynynen, "A super-resolution ultrasound method for brain vascular mapping," *Med. Phys.*, vol. 40, no. 11, p. 110701, Nov. 2013.
4. T. Dertinger, R. Colyer, G. Iyer, S. Weiss, and J. Enderlein, "Fast, background-free, 3D super-resolution optical fluctuation imaging (SOFI)," *Proc. Natl. Acad. Sci.*, vol. 106, no. 52, pp. 22287–22292, Dec. 2009.

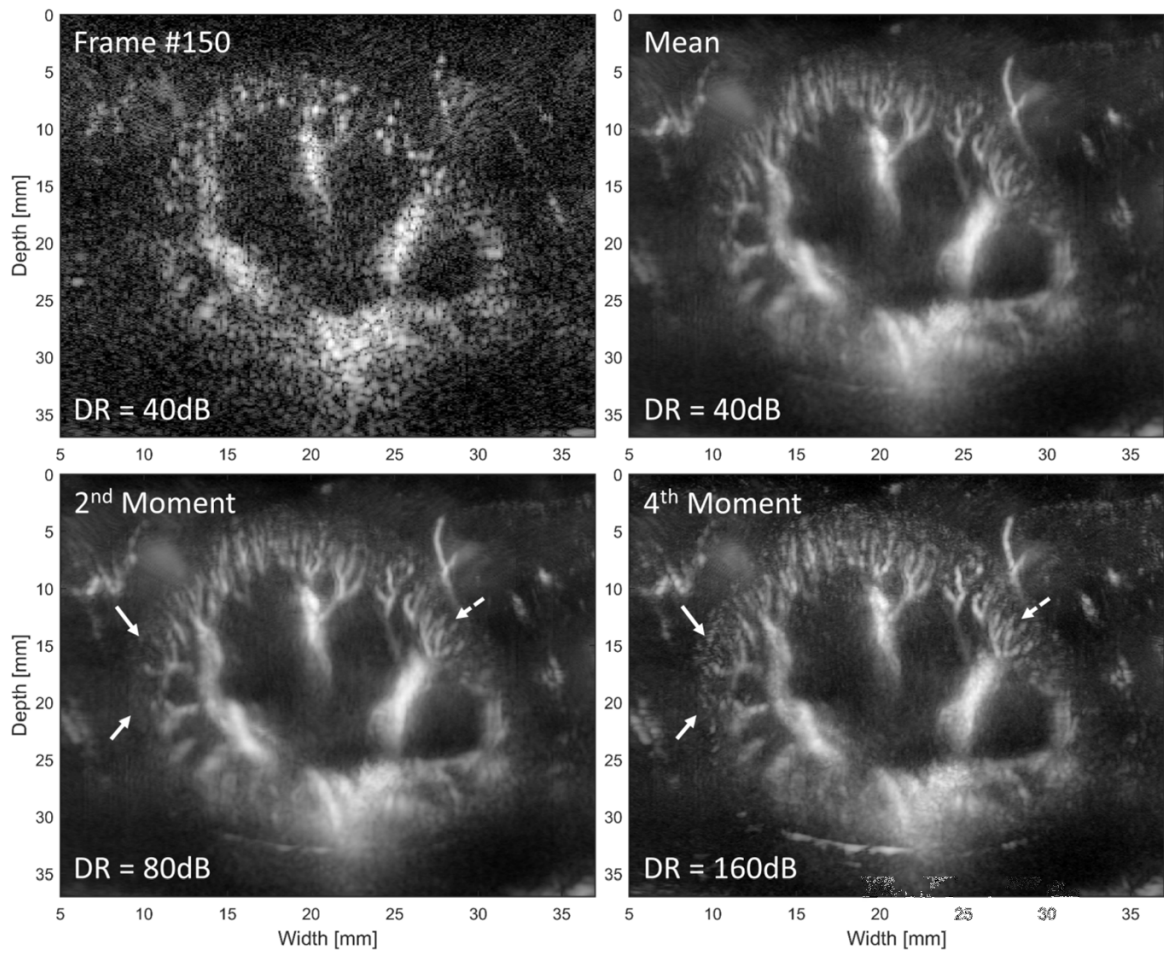


Figure 1: Kidney model. An ensemble of 150 frames was processed. The dynamic range (DR) of each image is specified.

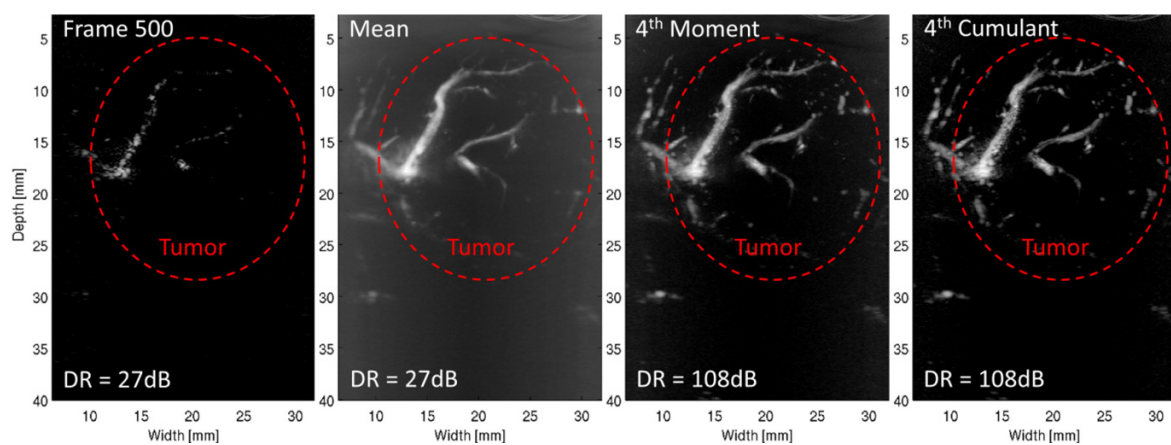


Figure 2: Tumor model. An ensemble of 1000 frames was processed. The dynamic range (DR) of each image is specified.

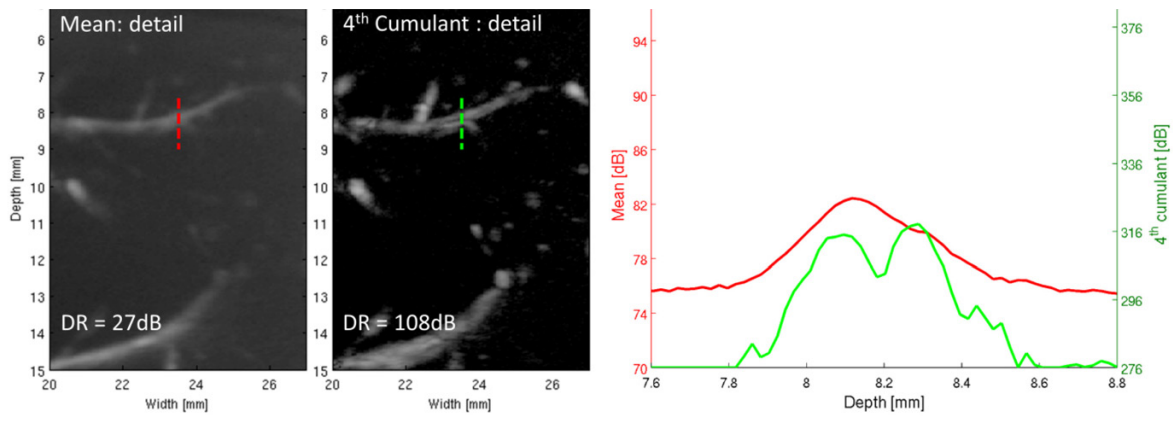


Figure 3: Tumor model - fine details. Cross-sections through the bifurcation, presented as red and green lines in the mean and 4th cumulant images respectively, demonstrate improvement in spatial resolution. An ensemble of 1000 frames was processed. The dynamic range (DR) of each image is specified.

Ultrafast ultrasound localization microscopy of the living brain vasculature at the capillary scale

Claudia Errico¹, Juliette Pierre¹, Sophie Pezet², Yann Desailly¹, Zsolt Lenkei², Olivier Couture^{1}, Mickael Tanter^{1*}*

1 Institut Langevin (ESPCI-ParisTech, CNRS UMR7587, INSERM ERL U979) 1 rue Jussieu, 75005, Paris

2 Brain Plasticity Unit (ESPCI-ParisTech, CNRS UMR 8249) 10 rue Vauquelin, 75005, Paris

** MT and OC contributed equally*

Introduction

The resolution of conventional ultrasound imaging is diffraction limited and corresponds roughly to the ultrasonic wavelength (100 μm). We have previously introduced the concept of ultrasound localization microscopy (ULM) by extracting precise positions for thousands of individual microbubbles per second from their punctual echo in ultrafast images [Couture et al. 2010, Couture et al. 2011, Desailly et al. 2013], allowing to surpass the diffraction-limit by an order of magnitude. Since intravenously injected microbubbles perfuse the entire vascular bed, the accumulation of their superlocalized echoes could precisely highlight the vasculature, *in vivo* at the microscopic scale. In this work, we show that ULM permits to overcome the trade-off between resolution and penetration, leading to a spatial reconstruction of the living rat brain vasculature down to the capillary level (<10 μm).

Material and Methods

The skull of anesthetized Sprague-Dawley rats was thinned and fixed in a stereotactic frame. Boluses of 200 μL microbubbles (2×10^9 microbubbles/mL) were delivered in the jugular vein. A linear array (15MHz, 128 elements) connected to an ultrafast clinical scanner (SSI, France) was placed coronally on the rat head at Bregma -1mm. Plane wave illumination continuously insonified the rat brain for 150s at 500Hz frame rate. Spatiotemporal filtering separated the fast decorrelation of the microbubble signal from the signals of slow moving blood and skull. Microbubbles were observed as unique and distinct sources. By deconvolving their individual point-spread-function, the axial position of microbubbles was localized one-by-one in depth. As the microbubbles could be observed over several images, their motion was also tracked over tens of milliseconds to determine the magnitude and orientation of their velocity vector (Figure 1).

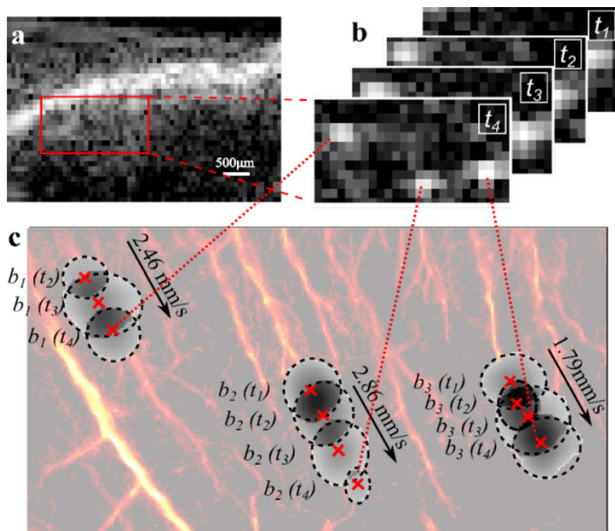


Figure 1. Super-localization of unique events in space and in time in the rat cortex. (a): B-mode image of the rat brain left hemisphere. The red box indicates a region of interest where uULM is performed. (b): Unique events are distinguishable in four representative frames acquired at 500 Hz. (c): uULM localizes in space and in time the microbubbles perfusing the rat brain cortex. Microbubbles tracking is performed to retrieve the blood flow speed in the cerebral vessels.

Results and Discussions

In the rat brain cortex, up to 1 million individual bubble events could be detected within 150 s. The resulting map of microbubble positions was reconstructed with a resolution of $\lambda/10$ (10 μm), down to 3.5 mm in depth. In a coronal plane, vessels between 15 and 65 micron diameter were highlighted by several passing microbubbles. Branching vessels could be resolved starting from 16 μm separation distance (Figure 2).

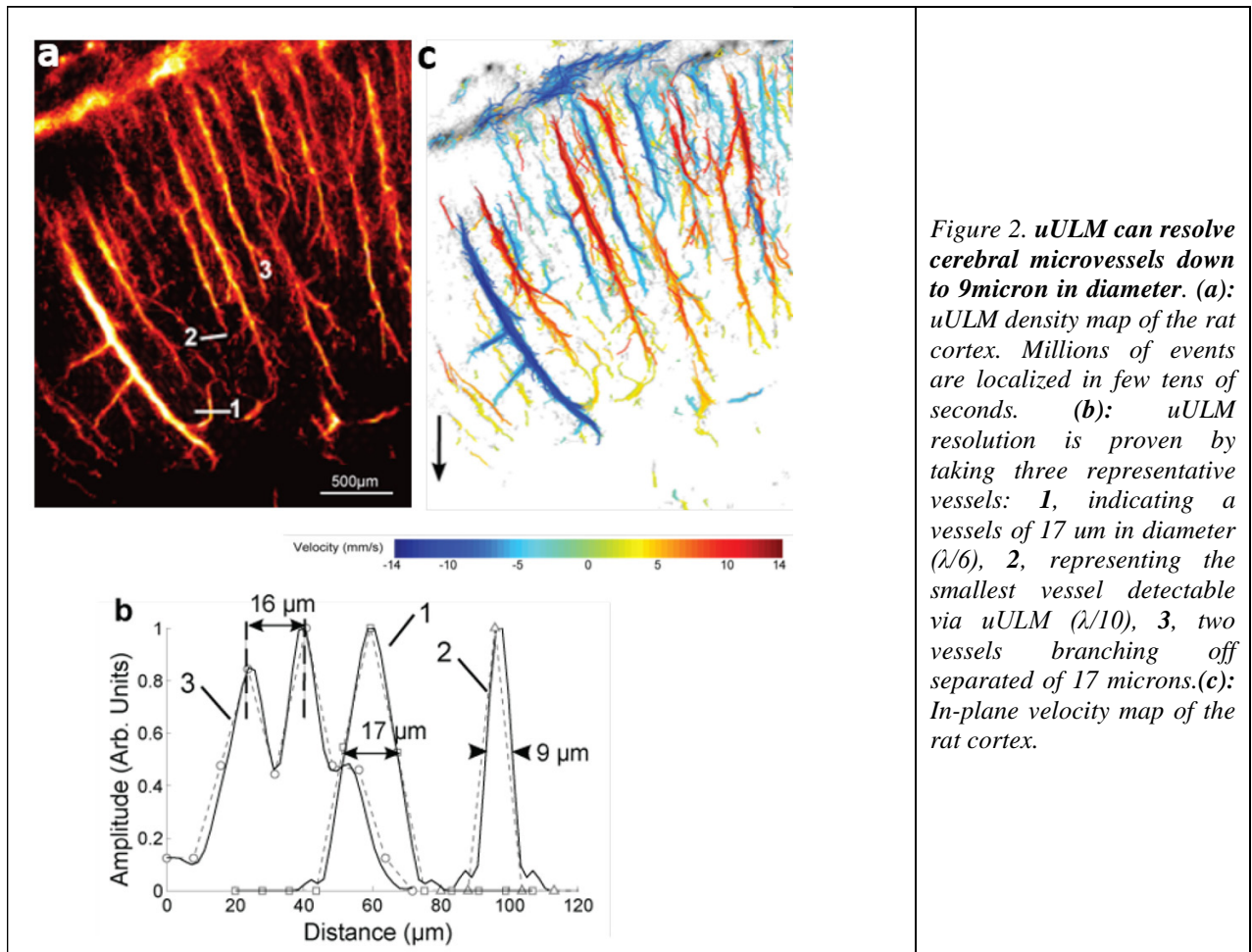


Figure 2. uULM can resolve cerebral microvessels down to 9micron in diameter. (a): uULM density map of the rat cortex. Millions of events are localized in few tens of seconds. (b): uULM resolution is proven by taking three representative vessels: 1, indicating a vessels of 17 μm in diameter ($\lambda/6$), 2, representing the smallest vessel detectable via uULM ($\lambda/10$), 3, two vessels branching off separated of 17 microns.(c): In-plane velocity map of the rat cortex.

The quantification of down and upstream flows further facilitated the discrimination between individual vessels. Bubble velocities ranged between 2 to 14 mm/s, which is consistent with the observed microvessels diameters.

In conclusion, the millisecond time-resolution combined with the micrometric spatial resolution of ULM allows the comprehensive reconstruction of the vascular map of entire organs within tens of seconds, paving the way to ultrasound localization microscopy in preclinical and clinical studies. More details in Errico et al., 2015a.

References

1. Couture, O., Tanter, M. & Fink, M. *Method and device for ultrasound imaging. Patent Cooperation Treaty (PCT)/FR2011/052810 (2010).*
2. Desailly, Y., Couture, O., Fink, M. & Tanter, M. *Sono-activated ultrasound localization microscopy. Appl. Phys. Lett. 103, 174107 (2013)*
3. Errico, C., Osmanski, B.-F., Pezet, S., Couture, O., Lenkei, Z. & Tanter, M. *Transcranial functional ultrasound imaging of the brain using microbubbleenhanced ultrasensitive Doppler. NeuroImage 124, 752–761 (2015)*

Temporal and spatial processing of high frame-rate contrast enhanced ultrasound data

Antonio Stanziola and Meng-Xing Tang

*Department of Bioengineering, Imperial College London, United Kingdom
(mengxing.tang@ic.ac.uk)*

Background

Contrast enhanced ultrasound (CEUS) has shown great promise in a range of clinical applications but at higher frequencies used in clinical peripheral tissue imaging it is often affected by its specificity (nonlinear artefact [1]) and signal to noise ratio (SNR). Ultrafast ultrasound allows for imaging at a frame rate of kHz, using e.g. plane waves and parallel processing. The large amount of data available afforded by this technique presents exciting opportunities for signal processing to improve image formation by combining data from multiple frames. This paper presents an explorative study on simple signal processing methods in both time and space for improved high-frame rate CEUS imaging.

Methods

In vivo measurements

High frame-rate CEUS Pulse Inversion (PI) data were acquired on a rabbit kidney using a linear array probe connected to a Veranosics system with plane wave transmission at 4MHz and 15 angle compounding. 1000 frames were acquired within ~ 1.5 second. 0.1 ul of Sonovue microbubble bolus was injected through the rabbit ear vein.

Averaging

The acquired data were processed in a number of ways detailed below. Firstly as a simple way to improve the resolution and contrast of the image, an average image was produced by averaging across the whole stack of B-mode images:

$$I(x, y)_{AVG} = \sum_{n=0}^{N-1} |I(x, t, n)|$$

where N is the number of frames and n the frame number. Here is the absolute value that makes this operation non linear, and allows for the despeckling of the image.

Temporal processing

Secondly to increase the specificity to contrast agents, some temporal features can be used. Here we process the individual pixel intensity over frames by summing up the changes over frames, fundamentally like the Power Doppler processing but on the high resolution compounded image data. This is done by convolving each pixel value over frames through a high-pass filter $h(n)$ (usually an high order filter such as a Butterworth [ref]) and then taking the power of the signal over the slow time

$$I_{PD}(x, y) = \sum_{n=0}^{N-1} \|I_{HP}\|^2 = \sum_{n=0}^{N-1} \|(I_{x,y} * h)(n)\|^2$$

Where * denotes convolution.

Next we explored the use of different high-pass filters in the above Power Doppler like processing and produced a differential image which is capable of separating fast from slow flow as below.

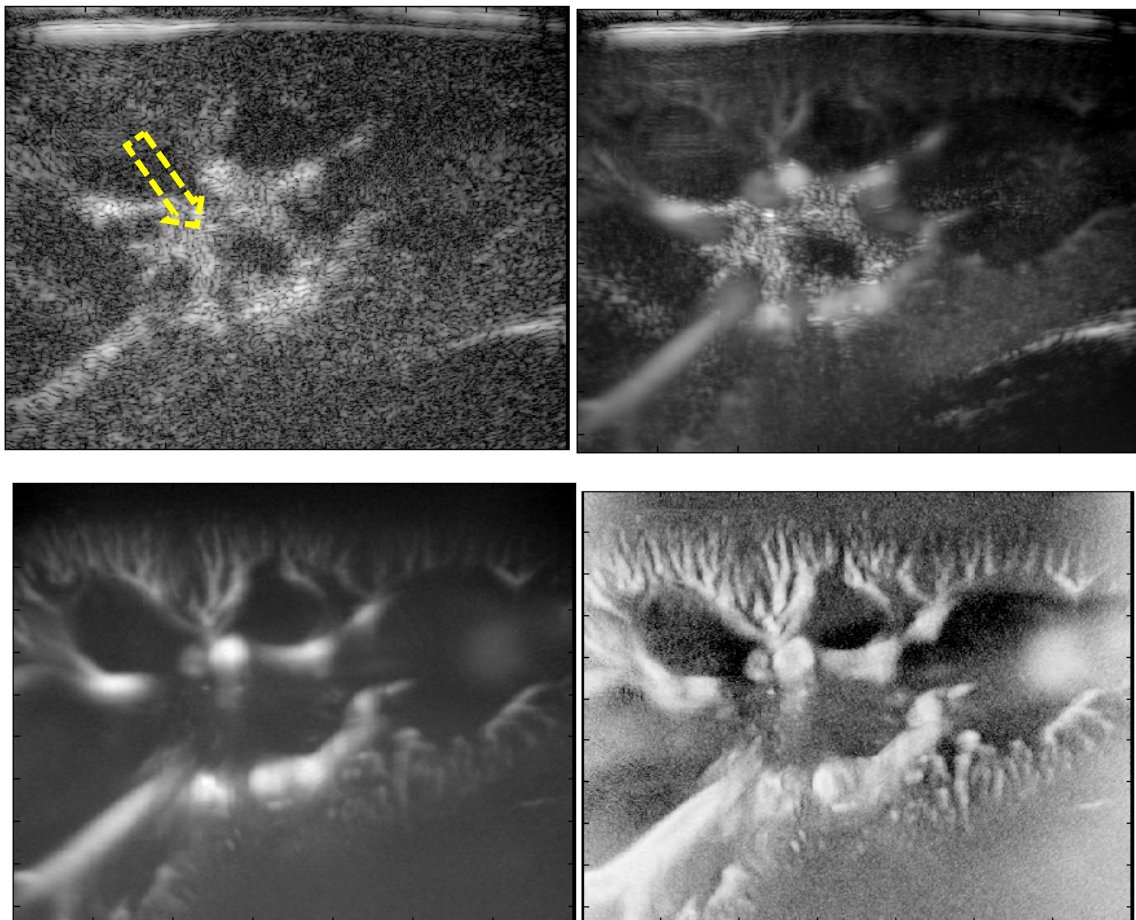
$$I_D(x, y) == \sum_{n=0}^{N-1} (\| (I_{x,y} * h_1)(n) \| - \| (I_{x,y} * h_2)(n) \|)$$

Spatial correlation processing

Finally we further explore this by looking at other non linear ways of processing ultrafast contrast signal. Power Doppler is limited in looking only at the temporal characteristic of a single image location, in this way it doesn't distinguish between variations of pixel intensity given by motion and contrast agent modification (deflation, destruction, fragmentation), and simple noise. This is shown by the blurring of smaller microvessels on the upper part of the kidney, where the signal is fainter.

We mitigate this problem by another non linear operation, which is spatial correlation between neighbouring pixels. The idea is that: if a pixel has to be considered a vessel (i.e. its intensity is given by contrast agent scattering), then not only its value has to vary fast over time but it also has to be accompanied by a neighbouring pixel which varies in a correlated way.

Results



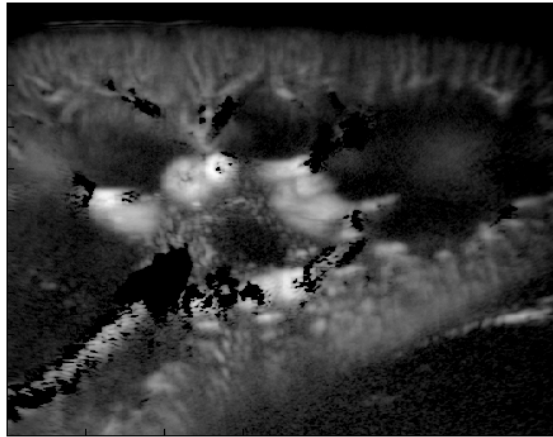


Figure 1: In vivo high frame-rate CEUS imaging of a rabbit kidney with different signal processing.

Top left: a single compounded image frame; Top right: averaged image over 1000 frames shows much improved SNR and some vessel details but with significant nonlinear tissue artefact (arrow). Middle left: Temporal Power Doppler processing on compounded high resolution images showing excellent details of vasclature; Middle right: Spatial correlation processing on compounded high resolution images showing excellent details of vasclature; Bottom: differential image showing separated slow flow. The boundary of the kidney is much better visualised than other images.

Conclusions

Through some simple signal processing methods (other than temporal averaging) it is possible to generate high sensitivity, specificity and resolution vascular images based on high frame-rate CEUS.

Acknowledgement:

We would like to thank members of the Ultrasound Laboratory for Imaging and Sensing (ULIS) group, Dr Robert Eckersley and Prof. David Cosgrove for their helpful discussion.

References

1. Tang, Meng-Xing et al. *Effects of Nonlinear Propagation in Ultrasound Contrast Agent Imaging*, *Ultrasound in Medicine and Biology*, Volume 36, Issue 3, 459 - 466
2. Charles Tremblay-Darveau · Ross Williams · Laurent Milot · Matthew Bruce · Peter N Burns, *Combined Perfusion and Doppler Imaging Using Plane-Wave Nonlinear Detection and Microbubble Contrast Agents*, *IEEE Transactions on Ultrasonics Ferroelectrics and Frequency Control* 12/2014; 61(12):1988-2000.

The 21st European Symposium on Ultrasound Contrast Imaging Rotterdam is sponsored by:

Philips Healthcare

John MacQuarrie
Senior Product Manager - Ultrasound
Philips Healthcare
22100 Bothell Everett Highway
Bothell, WA 98021 U.S.A.

Bracco Suisse SA

Marco Graf
Senior Communication Events Manager
Centro Galleria 2
Via Cantonale
CH-6928 Manno - Switzerland

GE Healthcare

Marta Gonzalez de Suso
Global Product Manager
Ultrasound Contrast Media
Life Sciences-Core Imaging
The Grove Centre, White Lion Road,
Amersham, HP7 9LL UK

SIEMENS Healthcare

Richard Medley
Product Manager
Ultrasound-EMEA
Sir William Siemens Square
Newton House
Frimley, Camberley, SY GU16 8QD – UK

Toshiba Medical Systems Europe BV

Jan de Bruijn
Marketing Communications Department
Zilverstraat 1
2718 RP Zoetermeer
The Netherlands

ZONARE

Ludwig Steffgen
Manager, International Clinical Marketing
Medical Systems GmbH
Henkestraße 91
91052 Erlangen – Germany

Visualsonics

Adrie Gubbels
Sales Manager Visualsonics
Joop Geesinkweg 140
1114 AB Amsterdam
The Netherlands

Oldelft Ultrasound

Stefan Roggeveen
Commercial Manager
Elektronicaweg 10
2628 XG Delft
The Netherlands

Samsung HME

Luc van Dalen
Account manager SEBN
Samsung Electronics Benelux
Gorinchem
The Netherlands

Coeur

Eric Boersma
Erasmus MC - Thoraxcenter
Dr. Molewaterplein 50
3015 GE Rotterdam
The Netherlands

Nederlandse Hartstichting

Mrs. E. Buitenhuis
Manager Research Department
P.O. Box 300
2501 CH Den Haag
The Netherlands

FIRST ANNOUNCEMENT 2017

**22nd EUROPEAN SYMPOSIUM ON
ULTRASOUND CONTRAST IMAGING**

19-20 JANUARY 2017

ROTTERDAM, THE NETHERLANDS

Information on the 22nd EUROPEAN SYMPOSIUM ON ULTRASOUND CONTRAST
IMAGING: Mieke Pruijsten, m.pruijsten@erasmusmc.nl



GE Healthcare



PHILIPS

TOSHIBA
Leading Innovation >>>

SIEMENS



 Oldelft
Ultrasound



SAMSUNG


ZONARE



The 21st European Symposium of Ultrasound Contrast Imaging, Rotterdam is sponsored by:



GE Healthcare

PHILIPS



TOSHIBA
Leading Innovation >>>



SIEMENS

SAMSUNG